

***INVESTIGATION OF LATE TIME RESPONSE
ANALYSIS FOR SECURITY APPLICATIONS***

SIMON JAMES HUTCHINSON

A thesis submitted in partial fulfillment of the
requirements of the Manchester Metropolitan University
for the degree of Doctor of Philosophy

Faculty of Science and Engineering
School of Engineering
The Manchester Metropolitan University

2015

This page intentionally left blank

ABSTRACT

The risk of armed attack by individual's intent on causing mass casualties against soft targets, such as transport hubs continues. This has led to an increased need for a robust, reliable and accurate detection system for concealed threat items. This new system will need to improve upon existing detection systems including portal based scanners, x-ray scanners and hand held metal detectors as these all suffer from drawbacks of limited detection range and relatively long scanning times.

A literature appraisal has been completed to assess the work being undertaken in the relevant field of Concealed Threat Detection (CTD). From this Ultra-Wide Band (UWB) radar has been selected as the most promising technology available for CTD at the present. UWB radar is provided by using Frequency Modulated Continuous Waves (FMCW) from laboratory test equipment over a multi gigahertz bandwidth. This gives the UWB radar the ability to detect both metallic and dielectric objects.

Current published results have shown that it is possible to use the LTR technique to detect and discriminate both single objects isolated in air and multiple objects present within the same environment. A Vector Network Analyser (VNA) has been used to provide the Ultra-Wide Band (UWB) Frequency Modulated Continuous Wave (FMCW) radar signal required for the LTR technique.

This thesis presents the application of the Generalized Pencil-of-Function (GPOF), Dual Tree Wavelet Transform (DTWT) and the Continuous Wavelet Transform (CWT), both real and complex valued, in Late Time Response (LTR) security analysis to produce a viable detection algorithm. Supervised and unsupervised Artificial Neural Networks (ANN) have been applied to develop a successful classification scheme for Concealed Threat Detection (CTD) in on body security screening. Signal deconvolution and other techniques have been applied in post processing to allow for extraction of the LTR signal from the scattered return. Data vectorization has been applied to the extracted LTR signal using an unsupervised learning based ANN to prepare data for classification. Classification results for both binary threat/non-threat classifiers and a group classifier are presented. The GPOF method presented true positive classification results approaching 72% with wavelet based methods offering between 98% and 100%.

Aims and Objectives of the Research Program

The aim of this project is to investigate the application of the Late Time Response (LTR) method to develop an algorithm that will reliably detect concealed objects in security environments. The objectives of this research are

- To develop a reliable method of detecting the LTR of a target in isolation and to develop a suitable algorithm for processing the test data. Work towards the completion of this objective has been presented in "Investigation of LTR analysis for Concealed Object Detection" at the Manchester Metropolitan University Science and Engineering day in 2013.
- To develop a system for detecting the LTR of multiple objects. Work towards the completion of this objective has been presented in "Investigation of LTR analysis for detection of multiple concealed objects" [1].
- To determine the capabilities of the LTR method in detecting concealed objects in different environments, such as with a larger complex geometric object in the background. Work presenting the completion of this objective has been submitted for publication in IEEE Microwave Theory and Techniques, title "A Morlet Based Continuous Wavelet Classification Regime" and Progress In Electromagnetic Research, title "Continuous versus complex wavelet analysis, a study in optimizing LTR security screening".

Contribution to knowledge and novelty of the work

The contribution to knowledge outlined in this work will include:

- The application of non-linear deconvolution, the CLEAN algorithm to improve Generalized Pencil-of-Function (GPOF) based LTR signal recovery in a noisy environment.
- The application of the Richardson-Lucy non-linear deconvolution algorithm to Continuous and Complex Wavelet Transform based LTR analysis.
- A study on the effects of multiple objects detected at the same range in the radar beam and the discrimination of one object from the other.
- A novel algorithm using Principal Component Analysis techniques leading to successful classification of targets using GPOF based LTR. The classification is performed using Artificial Neural Networks (ANN).
- A novel algorithm using Continuous and Complex Wavelet Transforms with Self Organizing Maps (SOM) and ANN for successful classification of LTR data with improved results over GPOF based LTR.
- A feasibility study on the application of the Dual Tree Wavelet Transform LTR analysis for successful classification for increased computational efficiency

TABLE OF CONTENTS

List of Figures	viii
List of Tables	xii
Abbreviations and Acronyms	xiii
Publications Relevant to this Work.....	xiv
Acknowledgements.....	xv
Chapter 1 Background and Introduction.....	1
1.1. Literature Appraisal	1
1.1.1. Background.....	1
1.2. Existing Concealed Weapon Detection methods.....	7
1.2.1. Introduction	7
1.2.2. Infra-red and Data Fusion based methods	8
1.2.3. Acoustic	9
1.2.4. Magnetic field.....	10
1.2.5. Portal and back scattering x-ray scanners	11
1.2.6. Millimetre wave and Microwave technology.....	12
1.2.7. Terahertz and Sub-millimetre wave technology.....	14
1.3. Signal processing techniques	15
1.3.1. Continuous wavelet transform based methods	15
1.3.2. The complex continuous wavelet transform.....	16
1.3.3. The dual tree wavelet transform	16
1.3.4. Empirical methods.....	18
1.4. Use of late time response in concealed weapon detection.....	19
1.4.1. Estimating Signal parameters	21
1.4.2. Other Applications of LTR.....	22
1.5. Definition of Aims and Objectives	25
1.6. Summary.....	25
Chapter 2 LTR Experimental setup and Optimization	27
2.1. RF emission safety.....	27
2.2. The Radar System.....	30
2.2.1. Ultra-Wideband Radar.....	30
2.2.2. VNA based LTR and scattering parameters	33
2.3. Experimental Algorithm	35
2.3.1. Setting up the experiment	36
2.3.2. Single and multiple target detection in isolation	37
2.3.4. Detection of targets attached to larger objects	40
2.4. Simulation procedures	42
2.5. EM propagation and scattering.....	44
Chapter 3 Clutter Reduction, Deconvolution and Classification Techniques	46

3.1. Signal Deconvolution	46
3.1.1. Signal deconvolution	46
3.1.2. Linear deconvolution	48
3.1.3. GPOF and Singular Variable Decomposition	53
3.2. Non-Linear deconvolution: The CLEAN approach	55
3.2.1. 1D signal analysis: The CLEAN algorithm	55
3.3. Filtering and Clutter reduction	60
3.3.1. Introduction to wavelets and the wavelet transform	60
3.3.2. Threshold filtering with the wavelet transform	66
3.3.3. Savitzky-Golay Filters	72
3.3.4. Background subtraction	74
3.3.5. Windowing of the signal	74
3.3.6. Supervised artificial neural networks	79
Chapter 4 Frequency Analysis techniques	82
4.1. Signal decomposition	82
4.1.1. Fourier	82
4.1.2. Complex natural resonances and the late time response	85
4.1.3. Model order	87
4.1.4. Principal Component Analysis	88
4.1.5. GPOF Results and Classification	91
4.2. GPOF classification results using Artificial Neural Networks	100
4.2.1. Operating conditions and Data structure	105
4.3. Overview of Algorithm 1: LTR using the GPOF method	107
Chapter 5 Real Valued Joint Time Frequency Wavelet Analysis techniques	110
5.1. Real valued wavelet analysis	110
5.1.1. Wavelet Families	110
5.1.2. Real valued wavelet Transforms	111
5.2. Self Organising Feature Maps	121
5.3. Algorithm 2: LTR using the wavelet method	123
5.4. Non-linear Deconvolved Wavelet Results	124
5.4.1. Non-Linear Deconvolution: The Richardson-Lucy approach	124
5.5. CWT classification results using Neural Networks	127
5.6. Some classical problems with real valued wavelets	133
Chapter 6 Complex Joint Time Frequency Analysis Wavelet techniques, a more accurate approach to LTR security screening	135
6.1. The Discrete Dual Tree Wavelet transform	135
6.1.1. Overview	135
6.1.2. DTWT Results and Classification	137
6.2. The continuous complex wavelet transform	147

6.2.1. Overview	147
6.2.2. CCWT Results and Classification	148
Chapter 7 Discussion and conclusions.....	164
7.1. Summary of work done	164
7.2. Assessment of how project objectives were addressed	165
7.3. Discussion.....	167
7.3.1. Signal smearing	167
7.3.2. Attenuation	168
7.3.3. Filtering and SNR.....	168
7.3.4. Feature extraction and classification	169
7.3.5. Process timescale.....	173
7.4. Future work and applications.....	174
7.4.1. Work program	174
References.....	176
Appendices.....	189
A.1. Gallery of target objects.....	189

LIST OF FIGURES

Figure 1: Example of a monostatic radar system.....	3
Figure 2: Example of a Bistatic radar system [14]	3
Figure 3: Example of a Synthetic Aperture Radar (SAR system) [16].....	4
Figure 4: Example of a phased array radar system [17]	5
Figure 5: Dual Tree Wavelet Transform Filterbanks.....	17
Figure 6: LTR waveform for a 6.5 cm needle	20
Figure 7. Block diagram outlining data flow	35
Figure 8. Block diagram for the single object in isolation experiment.....	39
Figure 9. Block diagram for the range resolution and discrimination of two objects at the same range experiment	40
Figure 10. Block diagram for detection of objects attached to larger objects experiment	41
Figure 11. Meshed volume for simulation of a 11 cm length, 1.2 cm diameter steel rod	43
Figure 12. Simulated relative electric field results for an 11 cm length, 1.2 cm diameter steel rod at 960 MHz.....	44
Figure 13: 6.5 cm needle original data grabbed by VNA, no signal processing, frequency domain, real part shown.....	49
Figure 14: 6.5 cm needle original data grabbed by VNA, no signal processing, time domain, real part shown.....	50
Figure 15: 6.5 cm needle data grabbed by VNA, deconvolved, time domain, real part shown.....	51
Figure 16: Pole plot results for 6.5 cm needle only with signal deconvolution.....	52
Figure 17: Pole plot results for 6.5 cm needle only without signal deconvolution	54
Figure 18: The CLEAN deconvolution technique applied to a 1D signal for creating the CLEAN components [3].....	56
Figure 19: CLEANed LTR signal for 6.5 cm needle.....	57
Figure 20: Pole plots for CLEANed 6.5 cm needle only	58
Figure 21: Flowchart of CLEAN non-linear deconvolution process.....	59
Figure 22: The Haar wavelet with the scaling function (ϕ) and the mother wavelet (ψ) which uses this scaling function [138]	61
Figure 23: Gaussian4 / Mexican hat wavelet.....	63
Figure 24: Morlet wavelet.....	65
Figure 25: Initial 10 Hz signal with no noise.....	67
Figure 26: Signal with added Gaussian white noise	69
Figure 27: CWT of noisy signal.....	70
Figure 28: Reconstructed signal after wavelet filtering.....	72
Figure 29: Time domain 10 Hz signal with additive Gaussian noise	75
Figure 30: 10 Hz noisy signal with Time-gating applied	76
Figure 31: Results of GPOF analysis on the 6.5 cm needle using the two presented methods for locating the star of the LTR with the 1-18G Hz horns. Decay time against frequency is on the left and amplitude against frequency on the right.....	78

Figure 32: Waveform of the grabbed data for the 6.5 cm needle against both time and number of points axis.....	78
Figure 33: Signal containing 3 components at 2000, 3000 and 4500 Hz corrupted by noise.....	84
Figure 34: Fourier domain representation of the signal corrupted by noise.....	85
Figure 35: Plot of 6.5 cm waveform with reconstructions at different model orders..	87
Figure 37: GPOF plots including model orders up to 4 with the body with hands at side to left and hands behind back to right.....	92
Figure 38: GPOF plots including model orders up to 2 with the 6.5 cm needle only to the left and the 6.5 cm needle on body to the right.....	93
Figure 39: GPOF plots including model orders up to 4 with the steel rod only to left and the steel rod on body to right.....	94
Figure 40: GPOF plots including model orders up to 4 with the kitchen knife only to left and the kitchen knife on body to right.....	95
Figure 41: GPOF plots including model orders up to 4 with the replica .38 calibre revolver only to left and the replica .38 calibre revolver on body to the right.....	96
Figure 42: GPOF plots including model orders up to 4 with the gas powered target pistol only to the left and the gas powered target on body to the right.....	97
Figure 43: GPOF plots including model orders up to 6 with the replica .44 calibre revolver only to left and the replica .44 calibre revolver on body to right.....	98
Figure 44: GPOF plots including model orders up to 2 with the camera only to the left and the camera on body to the right.....	99
Figure 45: GPOF plots including model orders up to 4 with the keys only to the left and the keys on body to the right.....	100
Figure 46: GPOF output data for binary threat/non-threat classifier.....	101
Figure 47: GPOF classification for a binary threat/non-threat classifier.....	102
Figure 48: GPOF PCA ROC curve results for a binary threat/non-threat classifier....	104
Figure 49: Flowchart of FFT GPOF based LTR algorithm.....	107
Figure 50: CWT of body hands at side to the left with body hands behind back to the right.....	112
Figure 51: CWT of 6.5 cm needle only to the left with on body to the right.....	113
Figure 52: CWT of steel rod only to the left with on body to the right.....	114
Figure 53: CWT of kitchen knife only to the left with on body to the right.....	115
Figure 54: CWT of replica .38 revolver only to the left with on body to the right.....	116
Figure 55: CWT of gas powered target pistol only to the left with on body to the right.....	117
Figure 56: CWT of replica.44 revolver only to the left with on body to the right.....	118
Figure 57: CWT of camera only to the left with camera on body to the right.....	119
Figure 58: CWT of keys only to the left with on body to the right.....	120
Figure 59: Flowchart of wavelet based LTR algorithm.....	123
Figure 60: Replica .38 revolver in isolation to the left, Richardson-Lucy deconvolved signal to the right.....	124
Figure 61: Replica .38 Revolver on body to the left, Richardson-Lucy deconvolved to the right.....	125

Figure 62: Plot of all 9 target sets using CWT with value 1 as threat and value 0 as non-threat	127
Figure 63: ROC curve split dataset CWT binary classifier	128
Figure 64: CWT plot of all 9 target sets against their expected classification value ...	130
Figure 65: ROC curve nine individual targets classified individually, split dataset....	131
Figure 66: DTWT of body only, hands at side to the left and hands behind back to the right.....	137
Figure 67: DTWT of 6.5 cm needle in isolation to the left and 6.5 cm needle on body to the right.....	138
Figure 68: DTWT of 11 cm steel rod in isolation to the left and on body to the right	138
Figure 69: DTWT of kitchen knife in isolation to the left and on body to the right....	139
Figure 70: DTWT of replica .38 calibre revolver in isolation to the left and on body to the right.....	140
Figure 71: DTWT of gas powered target pistol in isolation to the left and on body to the right.....	141
Figure 72: DTWT of replica .44 calibre revolver in isolation to the left and on body to the right.....	142
Figure 73: DTWT of Fujifilm digital camera in isolation to the left and on body to the right.....	142
Figure 74: DTWT of keys and keyring in isolation to the left and on body to the right.....	143
Figure 75: DTWT results for all 9 targets, 1 represents a threat, 0 represents a non-threat	144
Figure 76: DTWT ROC curve, split dataset without PCA	145
Figure 77: DTWT ROC curve, split dataset with PCA	146
Figure 78: CCWT of body only, hands at side to the left, hands behind back to the right.....	148
Figure 79: CCWT of 6.5 cm needle in isolation on the left, 6.5 cm needle on body on the right.....	149
Figure 80: CCWT of 11 cm steel rod in isolation on the left, 11 cm steel rod on body to the right.....	150
Figure 81: CCWT of kitchen knife only to the left, on body to the right	151
Figure 82: CCWT of replica .38 revolver in isolation on the left, on body to the right.....	152
Figure 83: CCWT of GP target pistol only to the left, on body to the right	153
Figure 84: CCWT of replica .44 revolver only to the left, on body to the right	154
Figure 85: CCWT of camera in isolation to the left, on body to the right	155
Figure 86: CCWT of Keyring only to the left, on body to the right	156
Figure 87: CCWT plot of all 9 target sets with value 1 as threat and value 0 as non-threat	157
Figure 88: CCWT training ROC, binary classifier	158
Figure 89: CCWT generalised ROC, binary classifier.....	159

Figure 90: CCWT plot of all 9 target sets against their expected classification value 160

Figure 91: CCWT 9 object classifier, split dataset 161

Figure 92: CCWT Generalised 9 item classifier 162

Figure 93: Replica .44 calibre revolver..... 189

Figure 94: Gas powered target pistol 189

Figure 95: replica .38 calibre revolver 190

Figure 96: Keyring..... 190

Figure 97: Fujifilm camera 191

Figure 98: Kitchen knife 191

Figure 99: Steel rod..... 192

Figure 100: 6.5cm needle..... 192

LIST OF TABLES

Table 1: IEEE standard Electro-Magnetic frequency band designations	6
Table 2: Basic Restrictions for frequencies 100 kHz – 3 GHz [90]	28
Table 3: Pyramidal horn antennas used	28
Table 4: Fundamental Resonant Frequencies of Simulated and Practical targets	42
Table 5: Table of wavelet components with correlation values	71
Table 6: True positive rates for individual threat items analysed using the GPOF method with and without PCA	105
Table 7: False positive rates for individual non-threat items analysed using the GPOF method with and without PCA	105
Table 8: Table of Targets vs model order and resonant frequencies	108
Table 9: Table of basic wavelet properties	111
Table 10: Table of individual target true positive classification rates using CWT for the binary classifier.....	129
Table 11: Table of individual target true positive classification rates using CWT for 9 object classifier	132
Table 12: DTWT classification results with and without PCA	147

Abbreviations and Acronyms

ANN	Artificial Neural Network
CNR	Complex Natural Resonance
CTD/CWD	Concealed Threat Detection/ Concealed Weapon Detection
CWT	Continuous Wavelet Transform
DWT	Discrete Wavelet Transform
EM	Electro-Magnetic
FFT	Fast Fourier Transform
FMCW	Frequency Modulated Continuous Wave
GPM	Gaussian Processes for Machine learning
GPOF	Generalised Pencil-of-Function
GPR	Ground penetrating radar
IED	Improvised Explosive device
IFFT	Inverse Fast Fourier Transform
IR	Infra-red
LDA	Linear Discriminant Analysis
LTR	Late Time Response
MEM	Maximum Entropy Method
MFS	Multi-Frequency Synthesis
MMW	Millimetre wave
MPM	Matrix Pencil Method
MUSIC	Multiple Signal Classification
NN	Neural Network
PBIED	Person Borne Improvised Explosive Device
PCA	Principal Component Analysis
PSD	Power Spectral Density
PSF	Point Spread Function
RF	Radio Frequency
SEM	Singularity Expansion Method
SG	Savitsky-Golay
SNR	Signal to Noise Ratio
SVD	Singular Value Decomposition
UWB	Ultra-Wideband
VNA	Vector Network Analyser

Publications

This thesis contains material that has previously been included in the following list of publications:

- 1) Hutchinson, S. J. et al., 2013. *Investigation of LTR Analysis for Concealed Object Detection*. Manchester, Proceedings of the Manchester Metropolitan University Science and Engineering day [2].
- 2) Hutchinson, S. J. et al., 2013. *Investigation of Late Time Response analysis for detection of multiple concealed objects*. Dresden. Germany, Proc. SPIE 8897, Electro-optical remote sensing, photonic technologies and applications VII [1].
- 3) Taylor, C. T. et al., 2014. *Investigation of Radio Astronomy Image Processing Techniques for use in the Passive Millimetre-Wave Security Screening Environment*. Baltimore, Maryland, USA, SPIE 9078, Passive and Active Millimeter-Wave Imaging XVII. [3]
- 4) Hutchinson, S. J. et al., 2014. *Late Time Response Analysis for the Discrimination of Multiple Simulated Objects in concealed Threat Detection*. Manchester, UK, IEEE CSNDSP14. [4]
- 5) Hutchinson, S. J. et al., 2014. *Investigation of the CLEAN deconvolution method for use with Late Time Response analysis of multiple objects*. Amsterdam, Proc. SPIE 9252, Millimetre Wave and Terahertz Sensors and Technology VII. [5]
- 6) Hutchinson, S. J. et al., 2015. *A Morlet, Continuous Wavelet Based Late Time Response Classification Regime for use in Security Screening* to be submitted to IEEE Microwave Theory and Techniques. Paper written, currently under reviewed
- 7) Hutchinson, S. J. et al., 2015. *Continuous Versus Complex Wavelet Analysis, a study in Optimizing LTR Security Screening* to be submitted to PIERS

ACKNOWLEDGEMENTS

Firstly, I would like to express my sincere gratitude to my advisors, Dr. Michael Fernando and Dr. David Andrews for their continuous support during the course of my Ph.D. study, in particular for their patience, motivation, and boundless knowledge.

Further thanks go out to the rest of my supervisory team: Prof. Nicholas Bowring and Dr. Stuart Harmer. Your support, insight and questions have helped to drive this research forward.

My sincere thanks also goes to Dr. Christopher Johnson, Dr. Dean O'Reilly, Dr. Matthew Southgate, Dr. Nacer Rezgui, Dr. Neil Salmon and Dr. David Leonard, who provided me an opportunity to join their team, and supported access to the laboratory and research facilities. Without this precious support it would been challenging to conduct this research. Also I would like to thank Dr. Christopher Taylor from the University of Manchester's Jodrell bank group. The work on non-linear deconvolution algorithms performed collaboratively proved to be very enlightening.

I would like to thank my wife Clare for her great patience over the last three years. You have provided encouragement, support, stability and motivation when I most needed it. Last but not the least, I would like to thank my parents and my sister for supporting me during this time.

Chapter 1

Background and Introduction

Preview.

This chapter aims to provide an overview of the field of security screening, specifically with reference to current standoff techniques and technologies. Signal processing approaches are discussed with reference to the techniques presented in the work to follow along with a discussion of the current progress of Late Time Response (LTR) analysis covering publications and application. The aims and objectives of the research program are presented along with a discussion of the contribution and novelty of the work.

1.1. Literature Appraisal

Preview

The following literature appraisal will provide a comprehensive review of the current and historical fields of interest in the area of Concealed Threat Detection (CTD) with an emphasis towards Radio Detection and Ranging (RADAR) based techniques. Starting with an overview of the history of RADAR systems, the appraisal will consider the techniques and the hardware required to implement existing Concealed Threat Detection (CTD) systems then move on to the signal processing methods currently of interest. Finally the appraisal will consider the use of Complex Natural Resonances (CNR), Late Time Response (LTR) techniques, techniques for estimation of signal parameters and the classification techniques available.

1.1.1. Background

The origins of RADAR development begin with the publication of James Clerk Maxwell's (1831-1879) seminal 1865 paper "A dynamical theory of the electromagnetic field" [6] [7] [8] where he demonstrated that electrical and magnetic fields could propagate as waves through space moving at the speed of light. This work was followed up by

Heinrich Hertz's (1857-1894) experiment in 1887 which confirmed that radio waves could be generated experimentally and were reflected by metallic objects.

It took until the turn of the 20th century for these principles to be implemented in practice when Christian Hulsmeyer (1881-1957) [9] used them to build and patent a simple device for detecting and avoiding ships in fog. This was not a true RADAR in the terms of being able to both detect and determine the range of the target as it did not provide a range, though it is the first commercial system to use radio waves to detect the presence of an object.

In 1922, Guglielmo Marconi (1874-1937) published a paper [10] recounting a set of experiments and a speech he presented on the Salisbury plain in 1899. This intervention by a titan of industry in the form of Marconi sparked a wider interest in the development and applications of RADAR systems.

With the realization that war with Germany was a real possibility in the mid 1930's the British government set up a committee to look into the development of air defence systems. This committee founded a new establishment whose superintendent Sir Robert Watson-Watt (1892-1973) was to pioneer many significant developments in RADAR systems, including the 37MHz chain home air defence RADAR system which is credited with helping the RAF to emerge victorious from the battle of Britain.

Following the Second World War RADAR systems continued to develop for air defence applications. By the 1970's new techniques to improve the detection of fast moving targets using Moving Target Indication [11] had been developed. Also identification of RADAR targets was now a possibility due to the development of CNR detection techniques [12].

RADAR systems can be classified into four distinct types. These are monostatic, bistatic, synthetic aperture and array based systems. These types determine the footprint of the system and the processing required to obtain the data. A monostatic system is a RADAR where the transmitting and the receiving antenna are the same, with the antenna switching between transmit and receive modes. Figure 1 presents an example of a monostatic radar system.

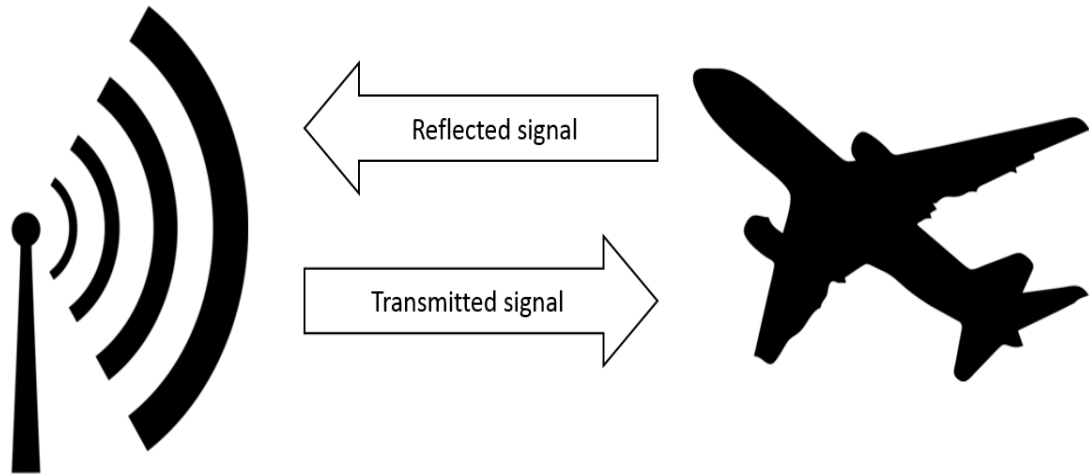


Figure 1: Example of a monostatic radar system

A bistatic RADAR is a RADAR where the transmitting and receiving antennas are separated by a distance roughly equivalent to that of the range to the target. Figure 2 presents an example of a bistatic RADAR system. Most early RADAR systems were of monostatic or bistatic design [13].

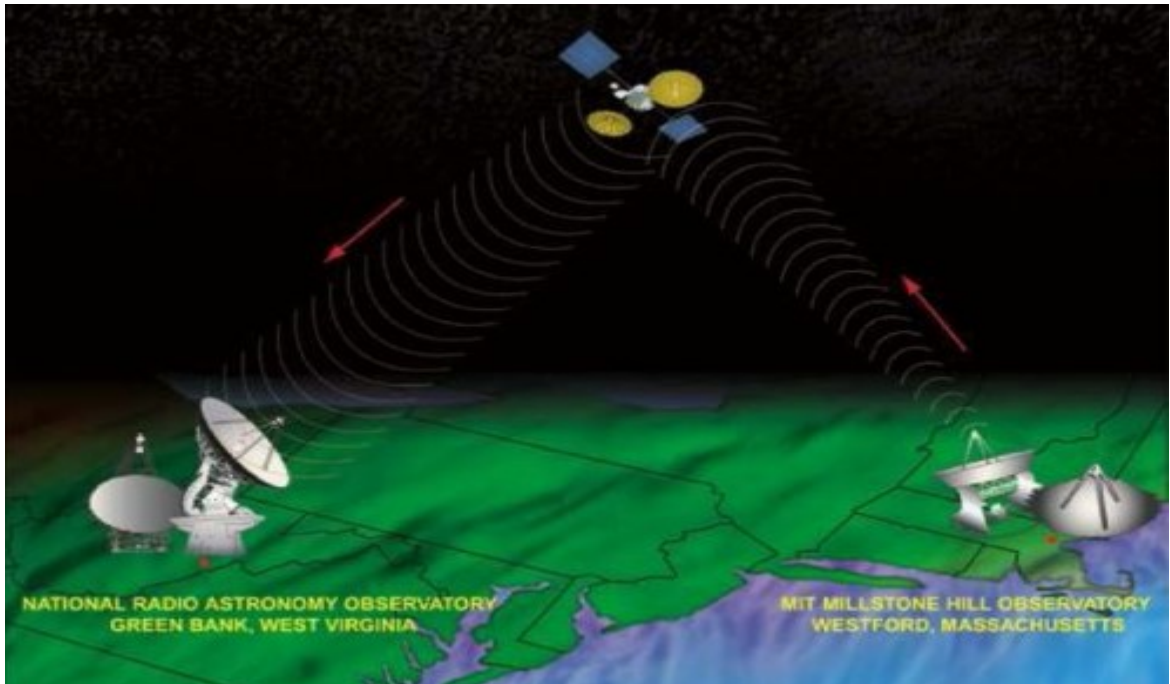


Figure 2: Example of a Bistatic radar system [14]

Synthetic Aperture RADAR is a more complex system that requires the use of a moving antenna to synthesize a larger aperture for the antenna than can be obtained using the static

antenna. Multiple RADAR scans are taken at multiple locations and signal processing is used to build a RADAR image from this data (see Figure 3). [15]. Applications of SAR RADAR systems include for military aircraft detection and planetary geosciences.

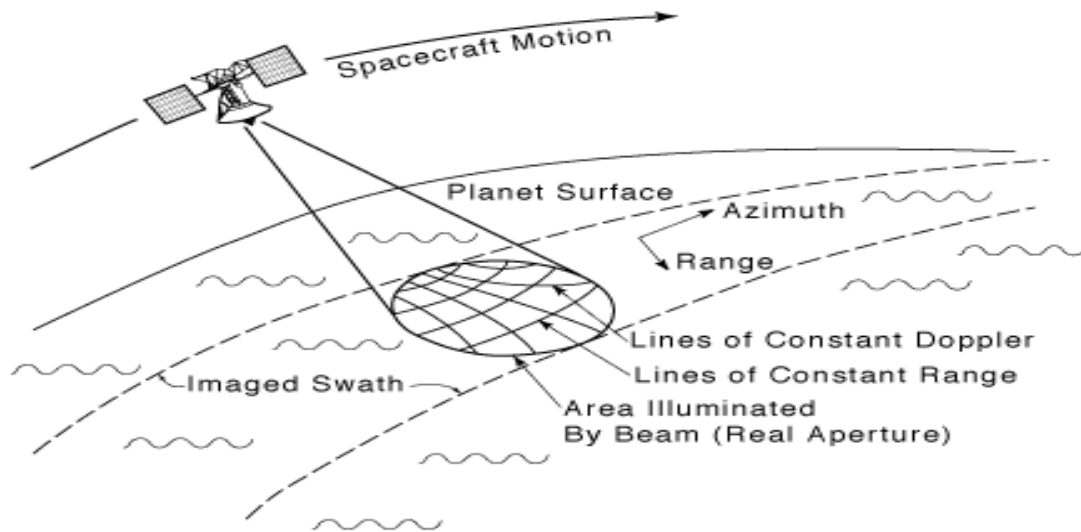


Figure 3: Example of a Synthetic Aperture Radar (SAR system) [16]

Array based RADAR systems involve the use of a larger number of transmitting and receiving antennas. These systems are commonly known as phased array systems as they use the phase difference (also known as the time difference) in the receipt of the RADAR signal at different receiving antennas to build the RADAR image. These systems can provide greater power in the RADAR beam but have a larger footprint and require greater signal processing. Many modern advanced RADAR systems, such as the Samson RADAR found on the Royal Navy's type 45 Daring class air defence destroyers along with the SPY RADAR found on US navy Ticonderoga class cruisers and Arleigh Burke class destroyers are phased arrays systems (see Figure 4).



Figure 4: Example of a phased array radar system [17]

Frequency bands were developed as a way to separate the electromagnetic spectrum. The bands of specific interest for the field of radar range from the Ultra High Frequency (UHF) band to the X band. Many frequencies bands exist above this range although the utility of these higher frequency bands in practical radar applications is only starting to be realised. Table 1 outlines the specific frequency ranges comparable to each bandwidth.

Table 1: IEEE standard Electro-Magnetic frequency band designations

Band designation	Frequency Range	Wavelength(λ) (m)
ELF	3 – 30 Hz	100000000 - 10000000
SLF	30 – 300 Hz	10000000 - 1000000
ULF	300Hz – 3 kHz	1000000 - 100000
VLF	3 – 30 kHz	100000 - 10000
LF	30 – 300 kHz	10000 - 1000
MF	300 kHz – 3 MHz	1000 - 100
HF	3 – 30 MHz	100 - 10
VHF	30 – 300 MHz	10 - 1
UHF	300 MHz – 1 GHz	1 – 0.3
L	1 – 2 GHz	0.3 – 0.15
S	2 – 4 GHz	0.15 – 0.075
C	4 – 8 GHz	0.075 – 0.0375
X	8 – 12 GHz	0.0375 – 0.0250
Ku	12 – 18 GHz	0.0250 – 0.0166
K	18 – 27 GHz	0.0166 – 0.0111
Ka	27 – 40 GHz	0.0111 – 0.0075
V	40 – 75 GHz	0.0075 – 0.0040
W	75 – 110 GHz	0.0040 – 0.00273
Millimetre	110 – 300 GHz	0.00273 – 0.0010
Terahertz	300 GHz+	$\lambda < 0.0010$

1.2. Existing Concealed Weapon Detection methods

1.2.1. Introduction

Since the turn of the millennium, world events have taken on an increasingly unstable and often violent nature. Due to this the development of new technology for detecting and classifying concealed threat objects to combat this threat has come to the forefront of security applications. In particular, high profile mass casualty terrorist attacks have led to an increase in the demand for effective methods to assist security personnel in screening for concealed weapons in high-risk environments. Among the many current screening methods found at transport hubs and secure sites such as airports and government installations there are some substantial limitations in their ability to detect and classify threat items.

Current technologies used for personnel screening at security points in airports and other secure installations include portal based metal detection systems and in some locations millimetre wave scanners. These methods suffer from limitations, for example, the metal detector has only limited capacity for differentiating between threat and non-threat items. It also has no capability to detect non-metallic items, while the millimetre wave scanners image the human body leading to privacy issues, both perceived and real.

A method that has shown promise in the detection and classification of concealed objects is the use of LTR analysis. Military units first exploited the LTR technique in order to allow the detection and classification of missiles and aircraft by ground and air based radar systems. Current systems that use LTR are large and incapable of detecting small-concealed objects within the urban environment and use power levels far too great to be safely applied in personnel screening. As a result, it would be desirable in the fields of policing and security to have a non-ionizing, non-imaging Concealed Threat Detection (CTD) technique. This research sets out to investigate the exploitation of LTR techniques for personnel screening in high-risk security environments.

1.2.2. Infra-red and Data Fusion based methods

Infra-red (IR) waves are electromagnetic waves that sit in a frequency bracket between 300 GHz and 400 THz with wavelengths ranging from 1 mm to 0.7 μm . Commonly IR technologies can be found in night vision goggles and other items of surveillance equipment. All objects emit IR radiation at different temperatures and its use as a surveillance technology is well established. Early research into possible applications of IR technologies was performed by military services, in particular the United States of America Department of Defense (DoD) for the purpose of early warning detection of ballistic missile launches, detection of chemical weapons in the atmosphere, precision guidance of smart weaponry systems and surveillance [19]. IR waves also have the capability to penetrate adverse weather conditions such as fog, which are opaque to the visible spectrum [20].

In 1995 the National Institute of Justice (NIJ) in the United States of America, working with the Air Force research laboratory funded a weapons detection program. The aim of this program was to develop and eventually deploy concealed weapon detectors capable of automatic detection and recognition [21]. Work has been progressed within the field of CTD using IR techniques as demonstrated in [22] looking into the capability of IR techniques to penetrate clothing in particular.

As with other detection technologies, achieving a viable standoff distance has presented a technical challenge. Hanton et al [23] investigate the effectiveness of the use of super resolution image reconstruction techniques as well as deconvolution methods in improving standoff infra-red images. The results of [23] conclude that a combination of super-resolution and resolution enhancement techniques show considerable improvement in the apparent image quality.

A number of signal decomposition methods have also been considered as methods for improving apparent image quality. The use of multi-resolution Wavelet decomposition with image fusion is discussed in [24] as a possible method for clutter reduction and increased detection rates while [25] look at a number of decomposition methods,

concluding that visual and IR signal fusion can be used for concealed object detection though there are limitations dependent on the method applied.

The prevalence of data fusion methods using IR signals and data from another sensor show that IR on its own, due in part to its difficulty in penetrating clothing and the poor discrimination between body and object when the temperature difference is small [26] show that IR sensing with data fusion may have promise. The limitations of IR sensing alone however means that a viable weapons detection system is unlikely.

1.2.3. Acoustic

Acoustic methods for Concealed Threat Detection (CTD) have shown some promise in the laboratory. The systems developed have focused on the use of ultrasound which sit in a frequency range between the upper limit of human hearing 20 kHz and 20 MHz [27], which is used by some medical ultrasound devices. In their work [28], DuChateau and Hinders tested four different frequencies of ultrasound to determine the optimal frequency at which ultrasound could penetrate fabric and return an acceptable resolution. The frequencies tested were 41 kHz, 50 kHz, 120 kHz and 200 kHz. They discovered that as a result of increased frequency, effective range decreases leading to a compromise between range and resolution, eventually settling on using 50 kHz for their experiment. The conclusions presented show that it is possible to detect concealed objects on the human body though identifying what has been detected presents a further challenge.

In their work [29], Achanta et al discussed the concept of using non-linear acoustic detection for CWD in order to improve the effectiveness of clothing penetration and reduce the number of false positive detections caused by specular reflections using standard ultrasound techniques. The system designed was tested for standoff detection at ranges up to ~5 m using a number of potential concealed weapons such as guns, knives and tools.

Vadakkal, in his thesis [30] discusses the development of a practical acoustic Concealed Threat Detection system. The areas identified as important for research and development are cost, ability to detect metallic threats, effectiveness of detecting non-metallic threats, standoff range and ease of manufacture. Resonant Acoustic Spectroscopy (RAS) [30] was

used to extract the signature of the targets detected and a neural network was used to classify the targets. An acoustic camera was also used alongside the resonant acoustic spectroscopy technique to generate images of the target in real time for the system operator.

Existing Acoustic wave CWD systems available today come in two forms, hand held close range detectors that trigger an alarm when a weapon is detected and the Luna innovations system discussed in [29] which identifies targets at greater range [30]. Vadakkal concludes that although there is a substantial amount of interest in electromagnetic detection methods, the representation of acoustic systems is insufficient in the body of research.

In summary, the acoustic systems currently available have shown capability to detect concealed weapons though reflection from clothing and atmospheric attenuation of the signal still present technical issues that will require solving for a viable commercial product to be produced.

1.2.4. Magnetic field

Metal detectors are a mature technology with the first known use of them dating back 200 years in China where a doorway made of a metal 'attractor' was constructed at the entrance to the emperor's chambers [31]. This system was to ensure that anyone carrying a ferrous object into the emperor's presence would find themselves impeded by the attraction of the metal object to the doorway. Modern day detection systems come in two forms, portal or portable [32] and can be found in high security areas of major transport hubs and secure facilities throughout the world [32].

Conventional metal detectors come in two forms. These are based around eddy current sensors or magnetic perturbation sensors but come at the cost of a high false positive detection rate and slow scan times. As with all portal based systems, these systems are considered to be slow as they require a person to pass through a portal or have a security officer physically scan them using a handheld device. The high false positive detection rate comes from the presence of ferrous metals in many different everyday items. An unfortunate consequence of these slow scan times is the creation of bottlenecks with large numbers of people crowded into a small space. This can make security checkpoints a

primary target for Person Born Improvised Explosive Devices (PBIED's). An attempt to improve upon scan times can be found in [32] with the development of the Wide Area Metal Detection System (WAMDS). This system is intended for use as a crowd pre-screening device, to highlight targets of interest for further checks. Attempts have also been made to resolve the high false alarm rate by use of advanced signal processing techniques and lower frequency metal detectors [30]. This allows for better resolutions of up to 1 inch and provides extra information to the system.

In their work [33], Kotter et al discuss the use of pattern recognition, neural networks and joint time frequency analysis to both increase detection rates while reducing false alarm rates. The impediments to a viable commercial system mentioned are the limited range available due to the passive nature of metal detection systems, although within the envelope of detection provided by the eddy current sensors discrimination of threat and non-threat using these signal processing techniques is shown to be possible.

The effectiveness of magnetic field based detection systems is heavily dependent on cooperation of the person to be scanned and the presence of ferrous metal in the threat item. Common knowledge of their use in security environments has led to attempts to circumvent these capabilities as shown by the advent of liquid based Improvised Explosive Devices (IED's) being smuggled onto aircraft. The need to be in proximity to the person being scanned is a risk for security personnel and the bottlenecks they create add a vulnerability which can be exploited by IED's. For mass screening these devices provide limited detection capabilities to security forces though additional support, in the form of pat down checks and alternative security scanners is required.

1.2.5. Portal and back scattering x-ray scanners

Portal scanners can include a number of the technologies discussed in this review such as eddy current detection, Millimetre wave and X-ray technologies. Newer generation portals have high detection and low false alarm rates [34]. Portals in development are able to analyse vapours and particles which will allow for increased explosive and drug detection capability [34]. These systems use techniques such as ion mobility spectrometry,

chemiluminescence and electron capture detection [34]. As discussed by Tillery in [35], design of portals can protect both the operator and those outside the chamber though the issue of bottlenecks still remain.

Current commercial portal scanners at security hubs are dominated by the L3 Provision millimetre wave body scanner [36] and the Smith's detection Enhanced Metal Detector for magnetic, non-magnetic and mixed alloy weapons detection.

Body scanners have featured in news articles with regards to potential privacy and perceived health issues [37] [38]. Back scattering X-ray transmission systems are used extensively for luggage screening in particular at airports. [39]. More recently human body scanning X-ray based systems have been developed. The issues presented by these systems focus mainly on cost, safety and privacy issues. X-ray based systems can cost many thousands of US dollars making it prohibitively expensive alongside which X-rays are ionizing radiation which can be harmful. Privacy is also an issue as the systems create an image of the human body showing distinct anatomical features which is viewed by an operator [40]. Other issues presented for X-ray systems are that they require close proximity to the subject being scanned [35] and that they may miss objects that are of low density where low density objects are considered to have low absorption coefficients [39]. X-ray systems are active systems [41] therefore do not suffer from the indoor contrast issues prevalent in passive systems.

The technologies developed by American Science and Engineering have led to three commercial X-ray based systems one of which, the body search system could have been found in trial usage at Manchester and London airports [30].

Scanners such as the L3 provision have considered the privacy issues by offering a number of privacy options to avoid the potential issues highlighted in the press, while scanners such as the Smiths Detection Enhanced Metal Detector do not image the body, providing an audio output when detection occurs and so do not have the same issue.

1.2.6. Millimetre wave and Microwave technology

Millimetre and Microwave technologies represent some of the most heavily researched areas of security scanning technologies in recent years. Millimetre waves have frequencies

form 30 GHz to 300 GHz and wavelengths from 10 mm to 1 mm while microwaves have frequencies from 0.3 GHz to 300 GHz with wavelengths of 1 mm to 1 m [42]. Studies have shown that some clothing materials can be considered completely transparent at millimetre wave frequencies [43] while metals and plastics will appear opaque. Non-imaging millimetre wave RADAR systems with the ability to probe for concealed objects through clothing do require a method for identifying the target that has been detected as no image is produced. Analysis of the scattered return of the RADAR signal and processing through machine learning techniques has shown itself to be sufficient to meet this requirement [44]. Millimetre wave technology, although seemingly highly suitable for CWD due to the characteristics of millimetre waves does have some hurdles to overcome. First among these is the issue with privacy that has become apparent with imaging based systems. As with the X-ray based systems millimetre wave systems reconstruct an image of the body showing distinct anatomical features which require user input to classify [45]. In an effort to overcome this, algorithms have been created [46] which replace the reconstructed image with a neutral silhouette of the human body. Another issue that is impeding progress in the millimetre wave arena is the high cost of equipment that can be used at these frequencies [47]. Korneev goes on to discuss issues of clutter caused by millimetre wave emissions from the human body and the long exposure time required to build an image. Further difficulties occur with imaging based systems when attempting to adapt the technique to standoff ranges. Due to the tight spatial resolution requirements required when constructing an image from a MMW based system, the standoff ranges achievable with an imaging based system are considerably shorter than those achievable with a non-imaging based system [44].

For security applications both active and passive systems at 35 GHz have been developed [48]. At higher frequencies such as the 'W' band from 75 GHz to 110 GHz prototype active systems with an effective range of 25 m that analyse the back scattered return of a W band signal have been developed [49]. These systems have shown the ability to detect thin layers of dielectric materials making them effective at detecting Person Borne Improvised Explosive Devices (PBIED's) as well as conventional concealed weapons such as guns and knives [50].

Passive systems analyse the thermal emissions of the target while active systems provide their own illumination [51]. Passive millimetre wave systems also suffer from poor contrast when used indoors. This can be solved by use of cooled detectors [52]. A short pulse active 30 GHz millimetre wave system is discussed in [53]. This system uses pyramidal horn antenna with a bandwidth of 26 GHz to 32 GHz as the active scanning element. Results for targets such as an absorber and metallic objects are presented and discussed. Consideration is also given to the results from an optimised hybrid micro-strip/horn antenna developed for this application.

1.2.7. Terahertz and Sub-millimetre wave technology

There has also been research into the sub-millimetre band which sits between the frequencies of 300 GHz and 3 THz. These signals produce wavelengths between 1 mm and 100 μm . This area of the EM spectrum has been subjected to only limited study and is known as the Terahertz gap [54]. Sub-millimetre wave signals have shown the potential to be able to identify materials such as explosives [48]. The current state of research into Terahertz spectroscopy as an explosive detection technique is reviewed in Gao et al [55], concluding that although a number of challenges still exist, over the 15 years prior to the publication the spectra of more than 20 explosives and compounds have been investigated demonstrating the potential of the technique for Concealed Threat Detection (CTD) . An example of a terahertz imaging RADAR for personnel screening can be found in [56]. This system operates in the atmospheric window that can be found at 675 GHz and they conclude that although this system works well under laboratory conditions, for real world applications a suite of sensors may be more suitable. Further active terahertz imaging schemes are presented in [57] and [58]. The scheme presented in [57] demonstrates a proposed design for a quick scanning fan beam based terahertz personnel screening system with the intention to create a 0.2 THz proof of concept system for rapid personnel screening. Arusi et al [58] discuss the design and development of a 0.33 THz based system for security applications using a synthesized linear FM signal within the X-band and with a bandwidth of 200 MHz multiplied up to the terahertz range concluding that the early experiments performed show promise for future security applications.

Further discussion of the area focuses on the need for standoff detection common to all security applications. As published in Appleby & Wallace [59], to have a good chance of surviving the blast from a non-shrapnel based typical PBIED one must be more than 5 m away. Appleby & Wallace [59] go on to state that if the device is shrapnel based, this survival range should be increased to as much as 100 m. Appleby then proceeds to consider the effects of atmospheric attenuation and the sky temperature on the attenuation of the system.

In his work [60], Kemp presents a wide ranging discussion on the practicality of implementing a terahertz based CTD system. It is stated that due to the high levels of attenuation present in the signal that become more significant as the frequency increases and the weak returns from the spectral features of the explosives, a viable detection system in this frequency range is unlikely.

1.3. Signal processing techniques

Signal processing plays a significant role in many applications within the field of CWD/CTD. These can range from filtering of the raw signal to classification of datasets. A number of the techniques relevant to data processing are summarised here in this section.

1.3.1. Continuous wavelet transform based methods

The Continuous Wavelet Transform (CWT) is a joint time-frequency signal analysis method that has found applications in the fields of CTD including LTR analysis [61]. A method developed in the 1980's [62] as a potential replacement to the Fourier transform, the wavelet transform offers better resolution in the time domain at lower frequencies while giving better resolution in frequency at higher frequencies [63]. This adaptability makes the wavelet a very useful tool in signal analysis.

A large number of wavelets have been developed for use with signal analysis including the Daubechies [64], Morlet/Gabor [65], Gaussian and Shannon wavelets. Each wavelet type is suitable for a different data set, the challenge being selecting the correct wavelet for the task at hand.

Wavelet analysis has found applications in a wide field of disciplines, the most appropriate of which to this work are landmine detection [66] [67] and specifically in the field of Concealed Object Detection.

Within the field of LTR analysis there has been research conducted into the application of the CWT to CTD. In his work [68], Atiah performed initial experiments presenting images of the CWT output for several targets.

1.3.2. The complex continuous wavelet transform

The first example of the Complex Continuous Wavelet Transform (CCWT) arose with the development of the real valued Morlet/Gabor wavelet in 1984 [62]. This wavelet was presented as a method to be used with seismology, optimizing the analysis of datasets in the field. Developed from the Gabor transform, a special case of the STFT [69], the Morlet/Gabor wavelet also offered the opportunity to perform complex data analysis on a given dataset. This complex version of the Morlet/Gabor wavelet is sometimes known as the Gabor wavelet.

Since the development of the Morlet/Gabor wavelet transform, a number of wavelets have been designed to allow for the optimized processing of complex data using the CWT. These families are too numerous to list, though a selection of the ones relevant to this work include the complex Gaussian, Shannon and Frequency B-Spline [70].

1.3.3. The dual tree wavelet transform

The Dual Tree Wavelet Transform (DTWT) arose from attempts to improve the capabilities of the DWT when processing complex datasets. A full description of the principles behind the DTWT can be found in [71]. With particular relevance in shift invariance and directional filters [72], the DTWT shows great promise as a computationally efficient approach to the analysis of complex datasets using wavelet analysis.

The DTWT works by using two separate DWT decompositions divided into two trees (tree A and tree B). These trees can have differently designed filters applied to them in order to allow the DWT performed on tree A to calculate the real valued result of the

transform and the DWT performed on tree B to calculate the imaginary result of the transform. This can be visualized as per the block diagram in Figure 5.

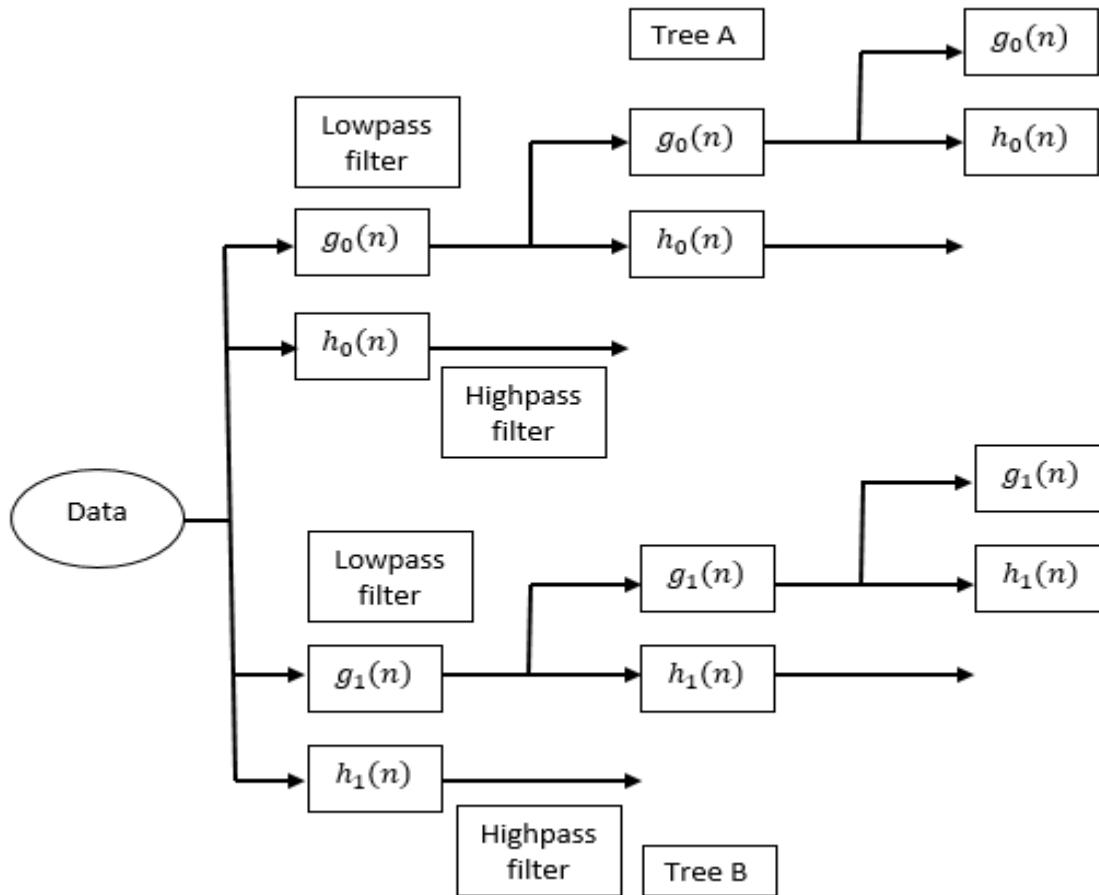


Figure 5: Dual Tree Wavelet Transform Filterbanks

There are many applications presented where the use of the DTWT can provide an improvement in the use of the discrete wavelet transform, for example in medical imaging [73]. Most importantly the introduction of the DTWT allows for the use of the DWT in feature extraction, an approach to which the real valued DWT alone is very limited [74] [75]. This use in facial feature extraction indicates that the DTWT may be a suitable method for decomposing a signal in security screening.

1.3.4. Empirical methods

Adaptive signal processing methods such as the Hilbert Huang Transform (HHT) [76] have been developed for improving the detection rates and the ability of signals to adapt to noisy environments. Comprising an amalgamation of the Empirical Mode Decomposition (EMD) and Hilbert Spectral Analysis (HSA) the HHT has found applications in areas that require nonlinear and non-stationary data analysis techniques [77]. An analysis of the benefits of the wavelet to that of the EMD can be found in the work of Grispino [78]. The greatest uptake of the EMD has been in combining the method with Independent Component Analysis (ICA) for biomedical signal processing applications [79]. These applications range from offering the ability to perform source separation of signals on single channel recordings to automatic detection of cardiac abnormalities [80].

EMD has also been studied in the field of communication security [81] where the EMD algorithm is used to separate the useful data in a signal from a dummy signal. EMD has also been considered for applications in SONAR [82] showing that the range of potential applications for this technique are large although within the field of CTD its usage so far has been very limited.

1.4. Use of late time response in concealed weapon detection

Another area of significant research in the area of CTD using microwave radiation is to use an ultra-wideband (UWB) RADAR pulse to attempt to excite the resonant frequencies of a concealed target. These Complex Natural Resonances (CNR) are unique to the target in question and as such can be used to identify the target [83], [84]. This technique has been used since the 1970s in the area of detection and identification of missiles and aircraft [12]. The effort to adapt these CNR extraction techniques to the area of on-body CTD is a more recent development though difficulties have been encountered when attempting to do so [84]. These difficulties arise mainly from the effect of the body, both in concealing the resonant frequencies and the complex residues of the threat by altering the dielectric environment surrounding the object [84].

The CNR pole extraction technique offers a number of benefits to the security researcher and there has been substantial research into overcoming the issues stated previously [85], [86], [87], [88]. When analysed the time resolved signal presents itself in the form of the Early Time Response (ETR) comprising the immediate return from the target and the induced Late Time Response which is a time delayed aspect independent property of an UWB RADAR pulse used to illuminate a conductive object [86]. The LTR takes the form of an exponentially damped sinusoidal waveform which comprises the unique signature of the target [89]. Figure 6 presents the LTR waveform of a 6.5 cm needle, with the ETR to the left of the dashed line and the LTR to the right.

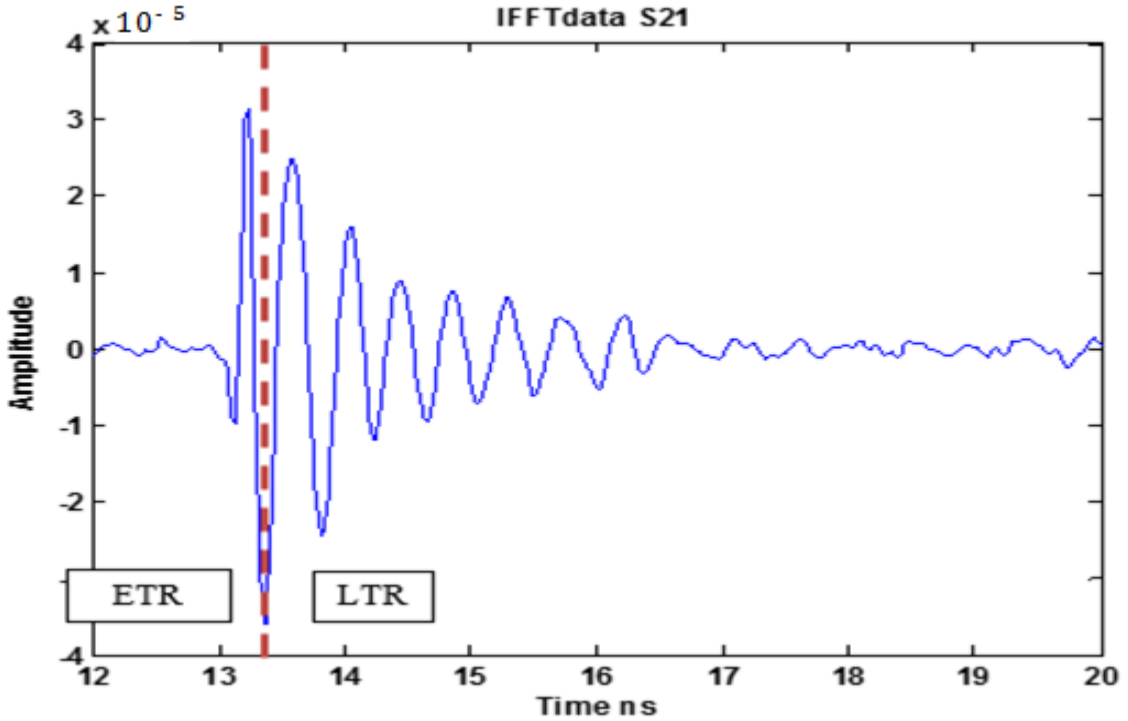


Figure 6: LTR waveform for a 6.5 cm needle

Its aspect independence gives this method an advantage over a number of the other methods presented in this review. A further advantage of the LTR technique is the low power levels required to excite the resonances of the target object. This will ensure that any commercial system is kept within recommended RF exposure safety levels [90].

The frequencies at which the resonances of the targets can be found can be approximated using the formula in Equation 1 [1]:

$$f_r = \frac{Ac}{2L} \quad \text{Equation 1}$$

Where f_r is the resonant frequency, c is the speed of light, L is the longest geometric length of the object and A is a dimensionless parameter based on the shape of the object. Due to the size of target objects such as pistols and knives, this leads to the bulk of targets of interest sitting in a frequency range below 2.5 GHz [87]. An example calculation for a 6.5 cm needle leads to:

$$f_r = \frac{0.85 \cdot c}{2 \cdot 0.065} \quad \text{Equation 2}$$

For the purposes of this calculation, variable A was determined experimentally to be 0.85. The value of this variable is affected by the geometric properties of the target being scanned. The values used for both c and L are in metres and metres/second. Rearranging Equation 2 indicates that in order for the frequency of the fundamental LTR pole to be above 2.5 GHz the object would need to be smaller than 5 cm in length.

The presence of the fundamental resonances in the low GHz region of the EM spectrum leads to a requirement to use large antenna, reducing the feasibility of creating a portable system [87].

Even with the substantial amount of research that has been performed into LTR analysis there are still gaps that need to be addressed. Reduction in the scale of the hardware required to operate a successful CTD system, improved signal deconvolution, improvements in signal processing methods and improved classification methods all need to be addressed. A recent paper presents the application of using the Total Least Squares Matrix Pencil Method (TLSMPM) [91] to improve clutter reduction in the signal. This has shown it is possible to separate the threat from the body.

Further work has been performed on the use of the Hankel Total Least Squares method coupled with Learning Vector Quantization neural networks by Vasalos et al [92]. The work presented includes a feasibility study on whether the frequencies of weapons overlap those of the human body and if a neural network can be used to classify targets including a grenade and S&W revolver. The Hankel total least squares algorithm is used to extract the LTR data. Vasalos et al [92] conclude it is possible with data presented to detect and classify the two targets. Learning Vector Quantization neural networks have been used which were a precursor to Self-Organising maps, both methods were developed by Teuvo Kohonen.

1.4.1. Estimating Signal parameters

Methods such as Prony's method [93], the E-pulse method [93] the Singularity Expansion Method (SEM) [94], and the Generalised Pencil of Function (GPOF) [95] have been applied to estimate the poles of the resonant signal. The SEM has been used

extensively on antenna characterization [96] and [97], though to a lesser extent in the field of security applications. The E-pulse method and Prony's method have found initial success in the area of analysis of UWB RADAR signals for security applications though the vulnerability of these methods to noise does pose challenges [98], [99] and [100].

Though these methods have proven to be reliable in extracting the required data, the GPOF method has been acknowledged as the least sensitive to noise in the signal [93], [101] and [96]. Due to this improved immunity to noise, the GPOF method is optimal for use in applications such as GPR [102] and detecting the CNR's of objects obscured by dielectric materials [103]. This indicates that the GPOF method is likely to be an effective method to apply to pole extraction methods in LTR analysis.

1.4.2. Other Applications of LTR

The applications available for use of CNR or LTR based techniques have become more numerous in current years. These applications are still theoretical in many cases, although a small number of the techniques described have found practical real world applications. In their work [104], Harmer et al consider the feasibility of using a radar based CNR approach to identify hostile fire in an urban campus/city environment. Harmer et al [104] present the results of LTR detection of projectiles in flight in order to identify the projectile and assist in locating the firing position of, for example a sniper. Harmer et al [104] go on to consider the bandwidth of the radar system that would be necessary to identify standard sizes of small arms projectiles in the range 5.56 mm to 13 mm. The effects of the motion of the projectiles are also considered.

Another of the available applications for LTR based systems is in the use of GPR. Chen et al [105] present LTR for identifying underground unexploded ordnance, in particular with a focus on the first few CNR's available in the signal. Chen et al [105] go on to discuss the requirement in GPR based systems not only for detection but also accurate identification of the detected target. An SVD based total least squares algorithm is used to process the datasets presented and consideration is given to Prony's and its use in improving the SNR of the received signal.

Kolba & Jouny [106] discuss the application of GPR to land mine detection. Though encountering many of the same problems as those discussed in [105], the approach of [106] is also to use Prony's method for optimising the SNR. Kolba and Jouny [106] then go on to discuss using comparisons of the CNR scans taken to a known database of objects for classification purposes with consideration given to detectors based at different distances.

The earliest examples of the application of LTR based systems is in the use of airborne radar and has been well covered in the literature [107] [108] [13] [15]. The use of these techniques to identify incoming aircraft and missiles is well documented and further potential applications have been discussed.

Several non-defence applications for LTR systems have been reviewed in the literature. One example of this type of application of LTR based systems is presented in [109]. This concept work presents the results of 26 GHz radar system using CNR to identify bolt plates from scattered EM return. This novel use for a CNR based system is intended to allow for automated recognition of mining infrastructure, such that an automated navigation system could be employed. This CNR based system would operate as an external reference to assist existing methods that are currently available. Hargrave et al [109] go on to present results of a simulation of the target identification process.

Another non-defence application for LTR systems is in the field of design of non-chip based RFID tags. In their work Rezaifarlak & Munteghi [110] present the use of CNR information derived from the structural parameters of the tag as a method of storing information on a non-chip based RFID tag. This allows for a low profile, high density storage RFID tag with the data encoded as CNR's associated with the devices structure to be developed. This novel approach to information storage has advantages in cost reduction due to removal of the microchip but does come at the cost of strict design parameters in order to ensure accurate presentation of the CNR's.

Another major field of application for LTR/CNR based systems is in medical applications. This is derived from the ability of the LTR/CNR based systems to detect dielectric objects as well as conductive objects. The challenges in this are great though, as due to the small RCS that is inherent with dielectric based returns to LTR systems and the requirement to keep power levels low for safe application to human targets, many obstacles

still remain to be overcome. Two of the major applications for these techniques in the medical field will be discussed. The first of these is the identification of cardiac arrhythmias using CNR's. As presented by Bani-Hasan et al [111] an ECG system using Prony's method to calculate the complex resonant frequencies is considered. The poles and frequencies developed are evaluated for 5 different types of arrhythmias and the results of these evaluations are discussed.

The second major application in the medical field for LTR/CNR based systems is in the detection of breast tumours. This is a very active field of research due to the import that has been given to breast cancer treatment in recent times.

Davis et al [112] discusses the feasibility of a 1-11 GHz based system to identify the features of a dielectric target. This work is performed with consideration given to identifying the size, shape and depth of potentially cancerous growths as a potential alternative to the existing methods used to characterize the architectural features of such growths.

Work on the use of LTR/CNR based techniques for breast cancer applications are presented in Hong [113]. In their dissertation [113] Hong gives consideration to the process by which illuminating a tumour at its resonant frequency would increase the coupling of the signal and therefore the rate of absorption of microwave energy resulting in a greater increase in temperature. A concept microwave based CNR system for screening is then considered.

Further work in this area presented by Bannis et al [114] takes a similar approach to that presented in [105] [106] [111] in using Prony's method to extract the CNR frequencies of the target object. Discussion is given to the effect of the tumour size, shape and depth on the CNR fields extracted, with the extracted CNR's used to identify the size shape and depth of the tumour. Of potentially greater implication is the possibility of using the method to identify a malignancy in a tumour. Current breast screening methods are painful and require a somewhat uncomfortable approach for the patient. The ability to identify breast tumours and potential malignancy using non-invasive LTR based methods would present a potential leap forward in breast screening.

1.5. Definition of Aims and Objectives

The aims and objectives of the research performed will now be discussed in greater detail. The aim of the research project was to develop a reliable algorithm for detecting concealed objects in security environments. The algorithm was required to be reliable with high successful detection rates as misclassifications would diminish confidence in the technique and in practical terms could have severe consequences. The security environments considered are locations such as transport hubs, stadia and secure sites. To meet this aim there are three distinct objectives involved.

The first objective involved development of a method for detecting the LTR of a target in isolation and a suitable algorithm for processing the data. This was necessary as in order to identify targets of interest on body, it is first required that the LTR characteristics of those targets without interference are known.

Once completed this led to the second objective of developing a method for detecting the LTR of multiple objects in the same scene. This is an important step in the development of a reliable algorithm as it is highly unlikely in a real world detection scenario that the person being scanned will have only a threat item on their person. The ability to discriminate between objects present in the same scene would allow for this to be taken into account.

Upon completion of the second objective it became possible to begin work on the third objective. This objective of determining the impact of the LTR method in detecting concealed objects in different environments, such as with a larger complex geometric object in the background led to the final result of this research program allowing for detection of concealed threat objectives secreted on the human body.

1.6. Summary

The literature appraisal presented above provides a review of the current state of CTD using IR, acoustic and microwave based techniques. These techniques have shown promise across a broad spectrum of capabilities though also come with limitations some of which are inherent to the technology, while others are issues of public perception and

implementation in a real world environment. The ever changing security threat shows the increasing necessity of the systems described above that, though limited can save lives. Improvements to these existing systems and development of new ones to improve on their capabilities is a global necessity that shows no sign of reducing severity in the foreseeable future. Although there are many systems available to detect a threat item there is a significant gap in the ability to determine what threat item has been detected. This presents a problem because if the detected threat item is a hand held weapon, such as a knife, security personnel may be able to approach with only limited risk to themselves and others. On the other hand if the detected item is a fragmentation based PBIED then approaching the individual carrying the item presents significant risk of harm to both security personnel and the wider public [59]. The ability of an LTR based security system to discriminate between objects and provide more information as to the potential threat detected is a viable approach to fill this gap and could provide both support to and replacement of many of the existing systems covered.

Discussion

In chapter 1, an introduction to the research project that has been performed has been presented. A literature survey discussing existing security scanning methods, signal processing applied to security scanning and the application of LTR to multiple scenarios has been presented. The aims and the objectives of the research has been outlined along with the contribution to knowledge as a result of this work. The following chapters will endeavor to present the techniques and results of work performed that meet the aims and objectives outlined.

Chapter 2 will present an overview of RF safety, LTR radar system and the experimental setup. Chapter 3 presents a discussion of clutter reduction, linear and non-linear deconvolution and classification techniques. Chapter 4 presents the results of LTR analysis using frequency analysis techniques. Chapters 5 and 6 present the results of LTR analysis using real and complex valued wavelets with chapter 7 presenting a final discussion and conclusions.

Chapter 2

LTR Experimental setup and Optimization

Preview.

This chapter provides an overview of the radar system and the experimental setup used for the work presented, covering both the practical setup of the experiments and some of the basic principles of LTR. The results of objects in isolation and a discussion of multiple objects present at the same range are presented.

2.1. RF emission safety

When using any transmitting Radio-Frequency (RF) device it is important to consider safe exposure levels. Although all life on earth has evolved to live in a low energy RF environment such as those transmitted by the sun, the biological effects of the introduction of man-made EM fields with much higher intensities in different parts of the RF spectrum are still not completely understood.

Radio-Frequencies sit in the range $10\text{ kHz} - 1\text{ THz}$ and are classified as nonionizing radiation because the frequency is too low for there to be sufficient energy in the photons to remove an electron from an atom as it passes through it thereby ionizing the atom [115] unlike ionizing radiation which has sufficient energy to do this. Nonetheless at sufficiently high intensities they can pose certain health risks due to RF induced heating of objects known as thermal effects. Also there is some evidence that at frequencies below those that induce thermal effects, magnetic fields can cause biological changes that are the focus of a considerable body of research. Ionizing radiation consists of alpha particles, beta particles, gamma rays and X rays while nonionizing radiation comprises low frequency radio waves, microwaves and visible light.

Safe exposure levels are determined by the incident power density on contact with the body. A number of attempts have been made to quantify a set level for this, for example with the IEEE standard on "Safety Levels with Respect to Human Exposure to Radio Frequency Electromagnetic Fields (300 kHz to 100 GHz)," [90] and the "ICNIRP Guidelines for Limiting Exposure to Time-Varying Electric, Magnetic and

Electromagnetic Fields (up to 300 GHz),” [116]. Table 2 shows the Basic Restrictions (BR) as outlined in the IEEE standard for frequencies from 100 kHz to 3 GHz. This Specific Absorption Rate (SAR) is measured in W/kg averaged over the entire body, see Table 2 for details. a

Table 2: Basic Restrictions for frequencies 100 kHz – 3 GHz [90]

		Action level ^a SAR ^b (W/kg)	Persons in controlled environments SAR ^c (W/kg)
Whole-body exposure	Whole-body average	0.08	0.4
Localized exposure	Localized (peak spatial average)	2 ^c	10 ^c
Localized exposure	Extremities ^d and pinnae	4 ^c	20 ^c
^a BR for the general public when an RF safety program is unavailable			
^b SAR is averaged over the appropriate averaging times			
^c Averaged over any 10g of tissue			
^d The extremities are the arms and legs distal from the elbows and knees respectively			

The appropriate averaging time for the frequencies covered is 6 minutes [90]. Below, Table 3 defines the pyramidal horn antennas used in these experiments as the gain of the horn must be factored in when calculating the power density.

Table 3: Pyramidal horn antennas used

Start Frequency(GHz)	Stop Frequency(GHz)	Gain (dB)	Description	Aperture dimensions (mm)
0.5	3	3.00	AtlanTec AS5749	430x260
1	18	3.73	AtlanTec Double ridged horn	240x138

The transmission power was set to -2 dBm. This value was determined experimentally to be effective at allowing for the detection of an LTR signal, while ensuring that power

levels are kept to a safe value. Given that the transmission power at the source was set to -2 dBm and that the shortest range to target used was 0.6 m we can use the radar equations to calculate the power density at the target. All values presented are to three significant figures.

First the power of -2 dBm in Watts must be determined as per Equation 3.

$$P_{tx} = 10^{\frac{(-2-30)}{10}} = 631 \times 10^{-6}W = 631 \mu W \quad \text{Equation 3}$$

Assuming an isotropic antenna (an antenna that radiates evenly in all directions) the power density at 1 metre range is shown in Equation 4:

$$P_{densityisotropic} = \frac{P_{tx}}{4\pi R^2} = \frac{0.000631}{4\pi(1)^2} = 50.21 \times 10^{-6} Wm^2 \quad \text{Equation 4}$$

Where P_{tx} is the transmitter power and R is the range to target. Taking into account the gain of the horn antenna as 3 dB the power density with gain P_{dg} , Equation 5 becomes:

$$(50.21 \times 10^{-6}Wm^2) \times 10^{3/10} = 1.00189 \times 10^{-4} Wm^2 \quad \text{Equation 5}$$

Given that the beam pattern from the transmitter measures approximately 90 cm tall by 60 cm wide at 1 metre range the power density assuming no losses would be as per Equation 6:

$$P_d = \frac{P_{dg}}{Area} = \frac{0.000100189}{0.6 \cdot 0.9} = 0.1855 \times 10^{-3} Wm^2 \quad \text{Equation 6}$$

The IEEE guidelines specify the maximum safe power limit for uncontrolled environments between 300 MHz and 3 GHz to be 2 mW/cm². Over 1 metre squared this limit is 20 W/m² and so this calculated figure of 0.1855 mW/m² is comfortably within the safety requirements.

2.2. The Radar System

2.2.1. Ultra-Wideband Radar

Ultra-Wideband (UWB) signals are signals defined as having a bandwidth greater than 500 MHz or 20% of the center frequency. The traditional applications for UWB radar have been in non-cooperative radar imaging and UWB radar is described in a number of books [117] [118]. It is particularly useful for LTR scanning as in order to induce a resonance on the target object it is necessary to illuminate it using a signal of the correct frequency. A multi gigahertz sweep will increase the chance of successfully transmitting the correct frequency and inducing the required surface current.

2.2.1.1. The Radar equation

The simple form of the radar equation relates the characteristics of the transmitter, receiver, target, antenna and environment to the range of the radar system. If we assume a lossless isotropic antenna (an antenna that radiates uniformly through 360°) is used to radiate the transmission power P_{tx} , the power density at range R (PDR) measured in W/m^2 will be equal to the radiated power divided by the surface area of a sphere of radius R presented in Equation 7 [15]:

$$PDR = \frac{P_{tx}}{4\pi R^2} \quad \text{Equation 7}$$

The gain of an antenna can be defined as the increased power density in a given direction provided by a directional antenna (PDU) when compared to the power density of an isotropic antenna given the same power input therefore Equation 8 [15]:

$$G = \frac{PDU}{PDR} \quad \text{Equation 8}$$

This leads to the power density of a transmitting directive antenna taking into account its gain via Equation 9 to be [15]:

$$PDU = \frac{P_{tx}G}{4\pi R^2} \quad \text{Equation 9}$$

The target will only couple to and re-radiate a percentage of the incident waveform illuminating it. This scattering effect is determined by the Radar Cross Section (RCS) of the target, denoted by σ , and as it is only the power re-radiated in the direction of the antenna that is useful the power at the receiver taking the RCS into account can be determined by Equation 10 [15]:

$$\text{Incident Power Density} = \frac{P_{tx}G}{4\pi R^2} \cdot \frac{\sigma}{4\pi R^2} \quad \text{Equation 10}$$

The power received by the radar in P_{rx} in watts is determined by the Incident Power Density (IPD) times the effective area of the antenna (A_{ef}). See Equation 11 where [15]:

$$A_{ef} = \rho_a A \quad \text{Equation 11}$$

And ρ_a is the aperture efficiency of the antenna. This allows the received signal power to be determined by Equation 12 to be [15]:

$$P_{rx} = \frac{P_{tx}G}{4\pi R^2} \cdot \frac{\sigma}{4\pi R^2} \cdot A_{ef} \quad \text{Equation 12}$$

This can be simplified, as per Equation 13 to [15]:

$$P_{rx} = \frac{P_{tx}GA_{ef}\sigma}{(4\pi)^2 R^4} \quad \text{Equation 13}$$

The maximum distance at which a target can be successfully detected (D_{max}) occurs when P_{rx} approaches the minimum detectable signal level (S_{min}). S_{min} is the point at which the SNR is sufficient to allow for the detection of useful information in the signal. To calculate this value use Equation 14 which represents the radar equation in its fundamental form [15]:

$$D_{max} = \left[\frac{P_{tx}GA_{ef}\sigma}{(4\pi)^2 S_{min}} \right]^{\frac{1}{4}} \quad \text{Equation 14}$$

2.2.1.2. Maximum unambiguous range for pulse radar systems

Using pulse based radar systems requires that once a signal has been transmitted, sufficient time must be given for the echoes of the signal to be detected before the next pulse is sent. This is to prevent the antenna in a monostatic (single antenna used for both transmission and receiving) system from switching to transmission mode before the

previously transmitted signal has been fully received. The maximum unambiguous range (R_{mur}) for a pulse radar is calculated using Equation 15 [119]:

$$R_{mur} = \frac{cT_p}{2} = \frac{c}{2f_p} \quad \text{Equation 15}$$

Where T_p is the pulse repetition period which is equal to $1/f_p$ and f_p is the pulse repetition frequency.

Standard Continuous Wave (CW) radar systems are not able to measure range in this method as there is no gap or pulsing of the signal. This leads to the requirement for the use of FMCW radar.

2.2.1.3. Frequency Modulated Continuous Wave radar

FMCW radar is similar to Continuous Wave radar in that the signal radiates at a continuous transmission power level. In contrast to the CW radar, FMCW radar can change its frequency mid-measurement allowing for frequency modulation of the signal. In this case to determine range requires that the waveform be marked in order to allow the propagation time to and from the target to be measured. The distance to the target object is determined by [15]:

$$R = \frac{c \cdot |\Delta t|}{2} = \frac{c \cdot |\Delta f|}{2 \cdot \left(\frac{df}{dt}\right)} \quad \text{Equation 16}$$

Where c is the speed of light, Δt is the delay time, Δf is the measured change in frequency, df/dt is the frequency shift per unit of time (the step size of the sweep) and R is the range to target.

2.2.1.4. Range resolution

Radar Range resolution is the ability of a radar system to distinguish between two objects located on the same bearing. This can be defined as the minimum separation between two objects required for a radar system to be able resolve them as separate objects. It is determined by the operating bandwidth of the transmitted signal. The equation for range resolution in terms of signal bandwidth is [119]:

$$RR = \frac{c}{2\Delta f} \quad \text{Equation 17}$$

Where RR is range resolution, c the speed of light and Δf is the effective bandwidth of the signal. For example at 1 GHz the range resolution would be 15 cm.

One potential issue that must be accounted for in the experiment is the potential for movement of the target within the beam. The maximum allowable movement can be controlled by adjusting the sweep time per point. The maximum movement distance allowable before the signal loses resolution can be determined by comparing the sweep time to the period of time the signal will cover. For example if the time resolution is determined to be 0.5 ns and the sweep time is 25 ms the maximum allowable movement before the movement will affect the signal is 75 mm [13].

2.2.2. VNA based LTR and scattering parameters

A Network Analyser (NA) is an advanced item of laboratory test equipment designed to measure the network parameters of electrical networks. Commonly NA's measure complex S-parameters which represent the elements of a scattering matrix describing the characteristics of electrical networks when excited by electrical signals. Two types of NA are commonly available. These are:

- The Scalar Network Analyser (SNA) – This is capable of measuring the amplitude properties of a network.
- The Vector Network Analyser – This is capable of measuring both the amplitude and phase properties of a given electrical network.

The ability of the VNA to measure electrical properties of a network is very useful, even more so as when an antenna is attached to the VNA it becomes a very versatile, broadband capable radar system. The flowchart representing the structure of a VNA based radar system can be found in 'Fundamentals of Vector Network Analysis' [120].

As the signal transmitted by a VNA propagates towards a target and then reflects from it, two major components of the waveform can be determined. These are the incident wave, which is the transmitted signal and the reflected wave, which is the waveform reflected and travelling in the opposite direction to the incident wave. The VNA separates these at the

test port with one being fed to the measurement channel and the other the reference channel. These are known as wave quantities [120] and S-parameters can be determined as the ratio between the transmitted incident and received reflected waveforms. The parameter S₂₁ is the S-parameter collected and used for this work. S-parameters for S₁₁ and S₂₁ can be determined by Equation 18 [120]:

$$S_{11} = \frac{b_1}{a_1} \rightarrow_{a_2=0}; S_{21} = \frac{b_2}{a_1} \rightarrow_{a_2=0} \quad \text{Equation 18}$$

Where the transmitted incident power is $|a|^2$ and the received reflected power is $|b|^2$, a_1 is the transmitted incident power on port 1, a_2 is the transmitted incident power on port 2, b_1 is the received reflected power on port 1 and b_2 is the received reflected power on port 2. S₁₂ and S₂₂ can then be determined using [120]:

$$S_{12} = \frac{b_1}{a_2} \rightarrow_{a_1=0}; S_{22} = \frac{b_2}{a_2} \rightarrow_{a_1=0} \quad \text{Equation 19}$$

The scattering matrix can then be represented by using the scattering parameters and the wave quantities as:

$$\begin{bmatrix} b_1 \\ b_2 \end{bmatrix} = \begin{bmatrix} S_{11} & S_{12} \\ S_{21} & S_{22} \end{bmatrix} \begin{bmatrix} a_1 \\ a_2 \end{bmatrix} \quad \text{Equation 20}$$

Therefore the amplitude of the S-parameter is determined by the amplitude ratio of the wave quantities while the phase of the S-parameter is determined by the phase difference between the two wave quantities.

The work presented will include elements of both time and frequency domain analysis. If a dataset is represented on a graph with the signal plotted against an X axis measuring time then this is considered to be time domain analysis. Conversely if the given signal is comprised of the amplitude of extracted sinusoids from the signal and plotted against an X axis measuring frequency then this is frequency domain analysis.

2.3. Experimental Algorithm

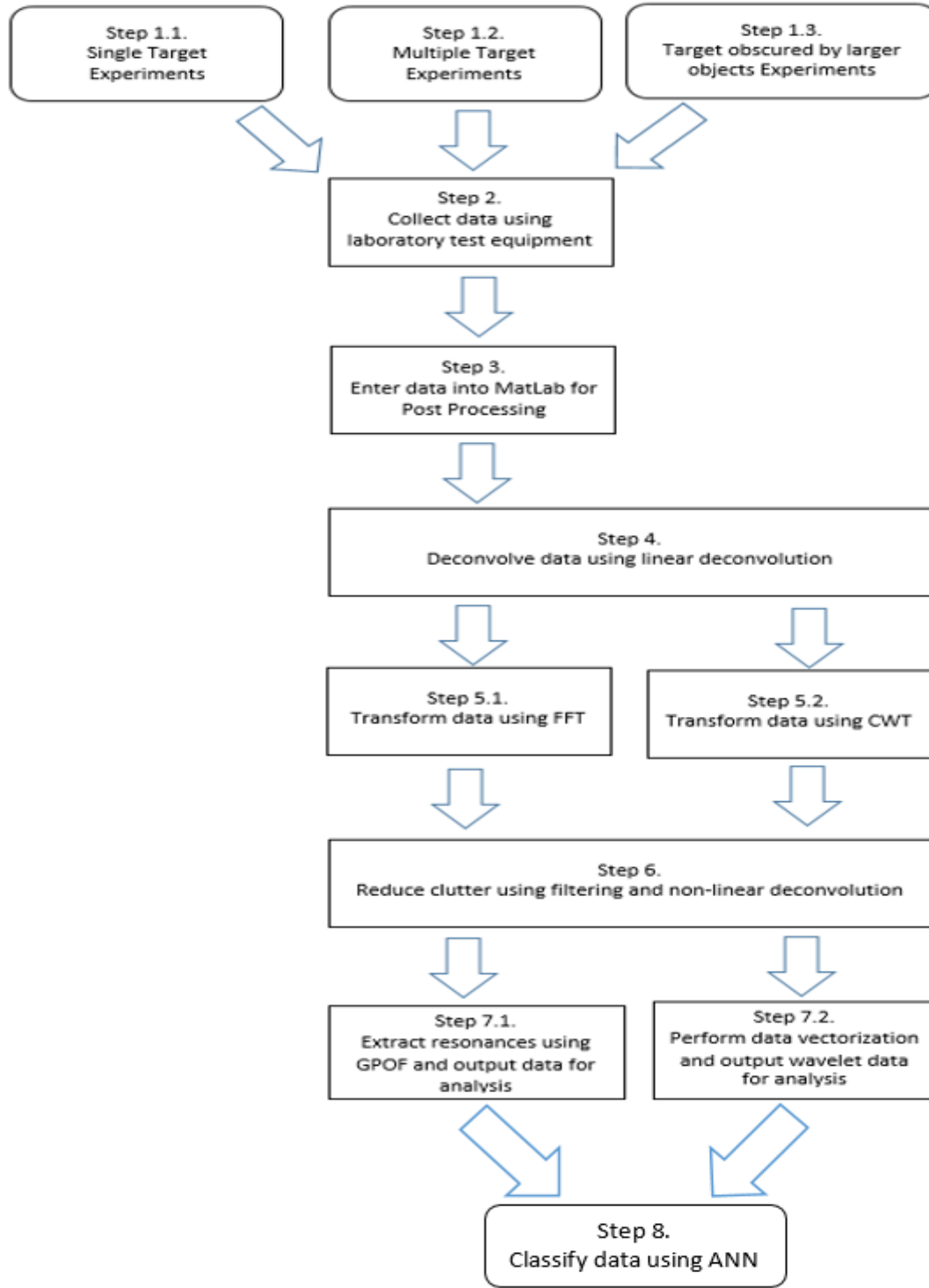


Figure 7. Block diagram outlining data flow

The block diagram in Figure 7 presents the data flow for the work performed. This includes the laboratory setup to take the data, transformation of the raw data into a dataset that can be processed and then decomposition of the data for further analysis. The data output from this process is further processed to be used in classification. For step 2 see Figure 8, Figure 9 and Figure 10 for a diagram of the experiment.

2.3.1. Setting up the experiment

When using a VNA to perform wideband radar experiments a number of settings must be considered. These are:

- The transmitted power level. This must be determined in advance in order to satisfy both RF safety requirements and be sufficient to successfully illuminate the targets presented. For all the work that has presented the power level at the source has been set to -2 dBm which is $6.3 \times 10^{-4} \text{W}$. Experiments have been successfully performed using a range of power levels from a maximum of 2 dBm down to a minimum of -4 dBm with no noticeable effects up to the maximum test range of 3 m.
- The IF bandwidth. This Intermediate Frequency (IF) is a frequency to which a carrier frequency is shifted during transmission or reception. It is mixed with a local oscillator signal in order to create what is known as a heterodyne signal. This allows for the frequency of the signal to be down converted to a more manageable level. This is useful because at very high frequencies, signal processing circuitry is not as effective and can perform badly. By reducing the frequency of the signal, devices such as transistors which suffer from very low gain at high frequencies can perform more effectively thereby favourably increasing the Signal to Noise Ratio (SNR). This also has the added advantage of reducing the cost of the components required to capture a signal. Limiting the size of the bandwidth of the IF frequency also improves the SNR. For all the work presented the IF bandwidth was set to 8 kHz in order to give the best compromise between scan speed and SNR. This leads to a total sweep time of 256 ms.

- Sampling Criteria. This includes both the number of points and the sweep. As discussed above the total sweep time for 2048 data points is 256 ms. This equates to 125 μ S per data point. The number of data points chosen can affect the unambiguous range of the system. Controlling this can reduce clutter/noise present in the signal. This is discussed further in the following point.
- Maximum unambiguous range of the system. This is an important consideration as the range at which the system is set to scan will help determine the power settings required in order to successfully illuminate the target as well as having an effect on the SNR. For example this can be calculated using a bandwidth of 2.5 GHz and 1023 sample points in Equation 21:

$$Range = \frac{C}{(2 * Bandwidth)} \cdot number\ of\ points = \frac{3 \times 10^8}{5 \times 10^9} \cdot 1023 = 61.38 \quad \text{Equation 21}$$

This range is far greater than that required for the experiments performed and as such can be controlled by either increasing the bandwidth of the frequency sweep or reducing the number of points/samples taken. It is preferable to increase the bandwidth of the sweep as a reduction in the number of points/samples taken could lead to loss of useful information. For example if the bandwidth were increased to the maximum available sweep range the VNA would allow of 39.5 GHz then the maximum unambiguous range would become 3.88m. This is more appropriate to the range over which the scans are being conducted, though it does introduce problems during signal deconvolution as the bandwidth of the sweep would be greater than the antenna is capable of providing, thereby deconvolution would in places be essentially dividing by zero. This issue and a solution are discussed further section 3.1.1.

2.3.2. Single and multiple target detection in isolation

2.3.2.1. Methodology

For each experiment the antenna were placed in a pseudo-monostatic arrangement with the VNA behind them. The VNA was connected to a PC running MatLab via a General

Purpose Interface Bus (GPIB) cable. Ten sweeps were performed on each target. The number of points taken varied depending on the experimental requirements. For experiments that require improved signal to noise ratio (SNR) a larger number of points were used but this comes at the cost of an increased sweep time. The data was filtered to reduce clutter, deconvolved to remove the transmission signal, decomposed to reduce the effect of the ETR and run through the GPOF method in post processing to extract the LTR poles.

Sweep time is determined by a balance between IF bandwidth and the noise floor. The lower the IF bandwidth, the slower the sweep time will become allowing for an improved noise floor. For the purposes of the experiments performed in this work an IF bandwidth of 8 kHz has been chosen [121].

Optimally the antenna gain would be flat across the measurement bandwidth. In practical terms this is very hard to achieve as most antennas resonate at a particular frequency themselves. Double ridged horn antennas in two frequency bands have been used. These bands are 0.5 GHz – 3 GHz and 1 GHz – 18 GHz. As is apparent, the smaller geometry horns in the 1 - 18 GHz range are not capable of seeing some of the larger objects due to their fundamental LTR frequency being lower than 1 GHz. For example the poles of a 12 cm steel rod, the results of which will be discussed in the results section, are located around the 0.8 GHz mark and so these horns would miss it. On the other hand, the larger dimension horns with the 0.5 – 3 GHz bandwidth would be able to detect this item but suffer from the drawbacks of excessive size and a smaller available bandwidth.

2.3.2.2. Single object detection

The experimental setup involved the use of a VNA to transmit a wideband Frequency Modulated Continuous Wave (FMCW) [13] radar pulse through a horn antenna with a frequency range of 500 MHz to 3 GHz. The objects presented from practical testing include a 12cm steel rod and a 6.5 cm needle. The target was placed 1.5 m from the transmitting and receiving antenna, suspended in free space using a non-reflective string. A block diagram of the experimental setup is shown in Figure 8.

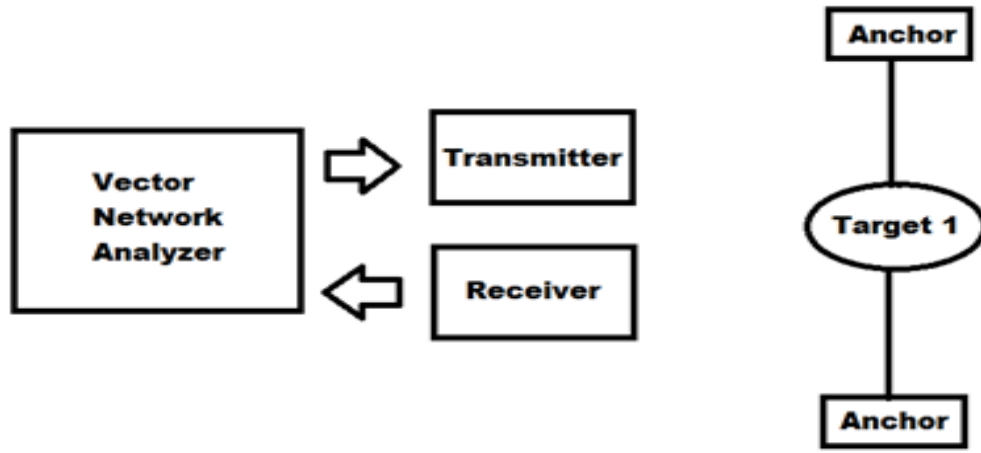


Figure 8. Block diagram for the single object in isolation experiment

2.3.2.3. Multiple object detection

The objects used for practical testing include two 12 cm steel rods, a 6 cm steel rod with an 11 cm steel rod, a kitchen knife with the replica Olympic starting pistol, the 13 cm kitchen knife with the replica .44 caliber magnum revolver and a replica Olympic starting pistol with the replica semi-automatic pistol.

The experimental setup involved the use of a VNA to generate and transmit a wideband FMCW radar [120] pulse through a horn antenna with a frequency range of 500 MHz to 3 GHz. The antennas were arranged as with the single object experiment and the range kept the same. The targets were suspended in free space using a non-reflective rope. The targets were separated from each other in increments to determine the separation required at which both targets could be resolved [1]. A block diagram of the experimental setup for the range resolution experiment is shown to the left in Figure 9 while the multiple objects at the same range is shown to the right in Figure 9.

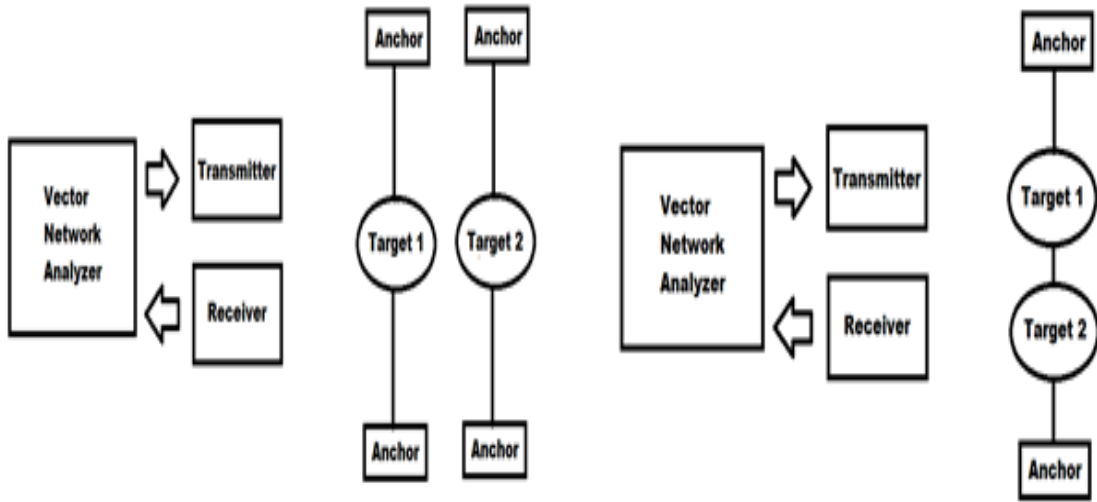


Figure 9. Block diagram for the range resolution and discrimination of two objects at the same range experiment

2.3.4. Detection of targets attached to larger objects

These experiments involved the use of a 70 cm water butt filled with saline as the larger object upon which a number of targets were attached. These targets included the 11 cm rod, the 13 cm kitchen knife, the replica Olympic starting pistol, the replica .44 caliber magnum revolver and the replica semi-automatic pistol.

The experimental setup is shown in Figure 10 below with a water butt placed behind and in contact with the target. As before these experiments used the VNA to produce a FMCW radar pulse with an increased frequency range of 500 MHz to 40 GHz giving a bandwidth of 39.5 GHz. The increased bandwidth allowed for greater control of the maximum unambiguous range as discussed in section 2.2.1.2. Maximum unambiguous range for pulse radar systems. For these experiments a maximum range to target of 3 m was chosen allowing for the maximum unambiguous range of the system to be calculated using [122]

$$Range = \frac{c}{(2 * Bandwidth)} \cdot number\ of\ points \quad \text{Equation 22}$$

For this experiment the maximum unambiguous range is

$$\frac{3 \times 10^8}{(2 \cdot (39.5^9))} \cdot 750 = 2.85m$$

Equation 23

This allows for greater control of the extent of the beam pattern and reduces the clutter detected. It is important to note that a frequency sweep of 39.5 GHz is greater than the available sweep range presented by the antenna. This can lead to problems of its own such as leading to the signal being divided by 0, as discussed in section 3.1.1. Signal deconvolution. The calculation in Equation 22 can be rearranged determine the number of points required. The number of points was selected to be 750 as this gives a range close to the 3 m required and allows for sufficient detail to be extracted.

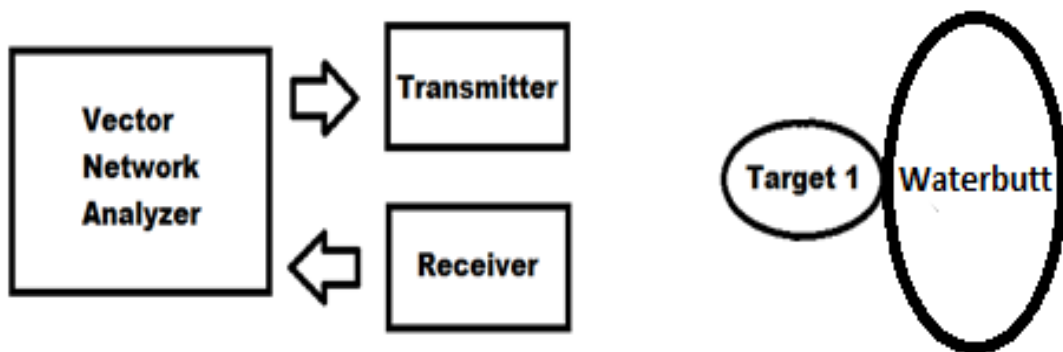


Figure 10. Block diagram for detection of objects attached to larger objects experiment

The results of the work presented with the threat object placed on the water butt showed the potential for a threat object to be isolated from the larger geometric object on which it was placed. This allowed for further work on CTD to continue.

2.4. Simulation procedures

Simulations of targets in isolation have been performed to ensure that the theoretically calculated expected resonant frequency of an object matches that of the simulation and the practically tested object. The formula for the theoretical calculation of the fundamental resonant frequency can be found in Equation 1. A list of targets versus theoretical, simulated and practical resonant frequencies is presented in Table 4:

Table 4: Fundamental Resonant Frequencies of Simulated and Practical targets

Target	Theoretical resonant frequency (GHz)	Simulated resonant frequency (GHz)	Practical resonant frequency (GPOF result) (GHz)
6.5 cm needle	1.961	1.89	1.92
Steel rod	1.1	0.96	1
Replica .38 revolver	0.76	0.742	0.75
Kitchen knife	0.98	1.04	1.35

In Table 4, the theoretical result is obtained using Equation 1, the simulated result was obtained by using computer based Finite Element Analysis and the practical result was obtained experimentally.

The results presented in Table 4 match well for theoretical, simulated and practical results of the first three objects. The knife is the exception, with the simulated result showing a considerable difference between itself and the other two results. This is likely due to the blade of the knife extending into the handle by an undetermined distance. The estimate of this distance used must be greater than that practically. Therefore the practical test observes a smaller distance over which the surface currents are generated and so shows as a higher resonant frequency.

All simulations for single and multiple object detection were performed with a uniform set of parameters to allow for accurate comparison of the results. The software used is the Finite Element Analysis (FEA) package COMSOL. The workspace in which the simulation

was performed was a volume of air in which the targets were located surrounded by a Perfectly Matched Layer (PML). A PML is a domain within the simulation which simulates a waveform propagating off to infinity and does not reflect any signal. Illumination was provided by a plane wave orientated in the X-axis and propagating in the direction of the negative Y-axis. The reflection from the target then returns along the positive Y-axis. The result of this is then divided with the background electric field in order to create a simulated S parameter for comparison with the data taken practically using a VNA. This was then recorded for the vertical polarization (co-polar) and the horizontal polarization (cross-polar) to compare with the practical results S11 and S21. Post processing in MatLab has been used to extract the pole data.

The simulation comprised a finite element analysis of the meshed target object and surrounding volume. A tetrahedral based mesh shown in Figure 11 was used to map the volume.

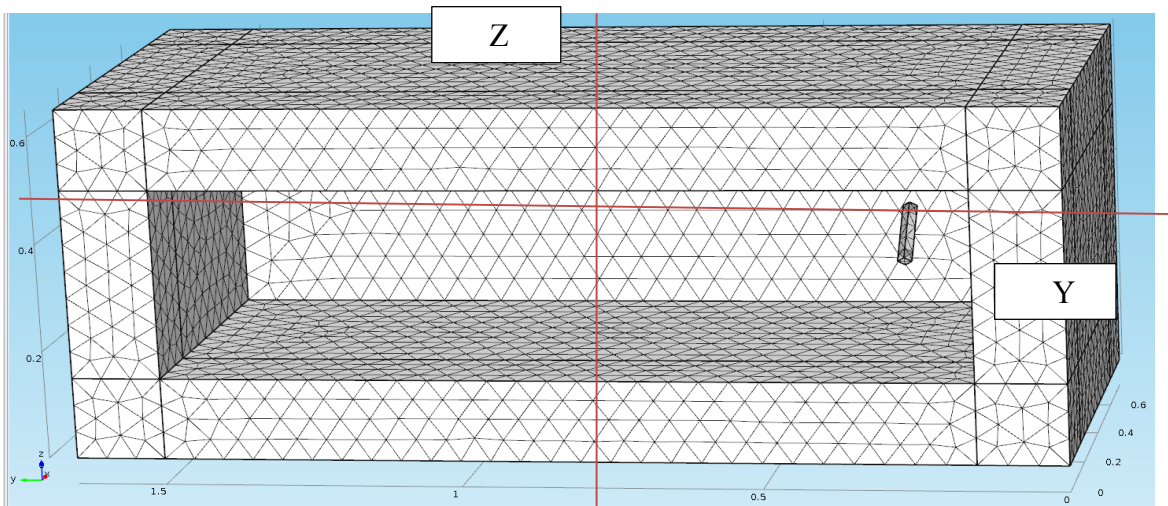


Figure 11. Meshed volume for simulation of a 11 cm length, 1.2 cm diameter steel rod

The number of elements involved in this simulation created by the use of meshing was ~ 100000 . The bandwidth of the sweep covered 500 MHz to 2 GHz with measurements taken every 10 MHz totaling 150 points of measurement. The number of points was chosen to be adequate for an accurate solution to the problem, though it is not the same as the practical measurements taken with 1001 points with an approximate bandwidth of 200 Hz between points. Due to the limitations in the processing power available for the simulation,

producing a full simulation of 1001 points is computationally prohibitive for reasons of solving the much more detailed mesh at higher frequencies. The alternative method used is to perform a simulation of 150 points correct for the difference by using Time-gating in post processing.

As is shown in Figure 12 below the scattered electric field strength of the steel rod illuminated by a plane wave drops off rapidly over distance. The volume of air within the perfectly matched layer measures 1.5 m in the Y axis by 0.6 m in the X and Z axis.

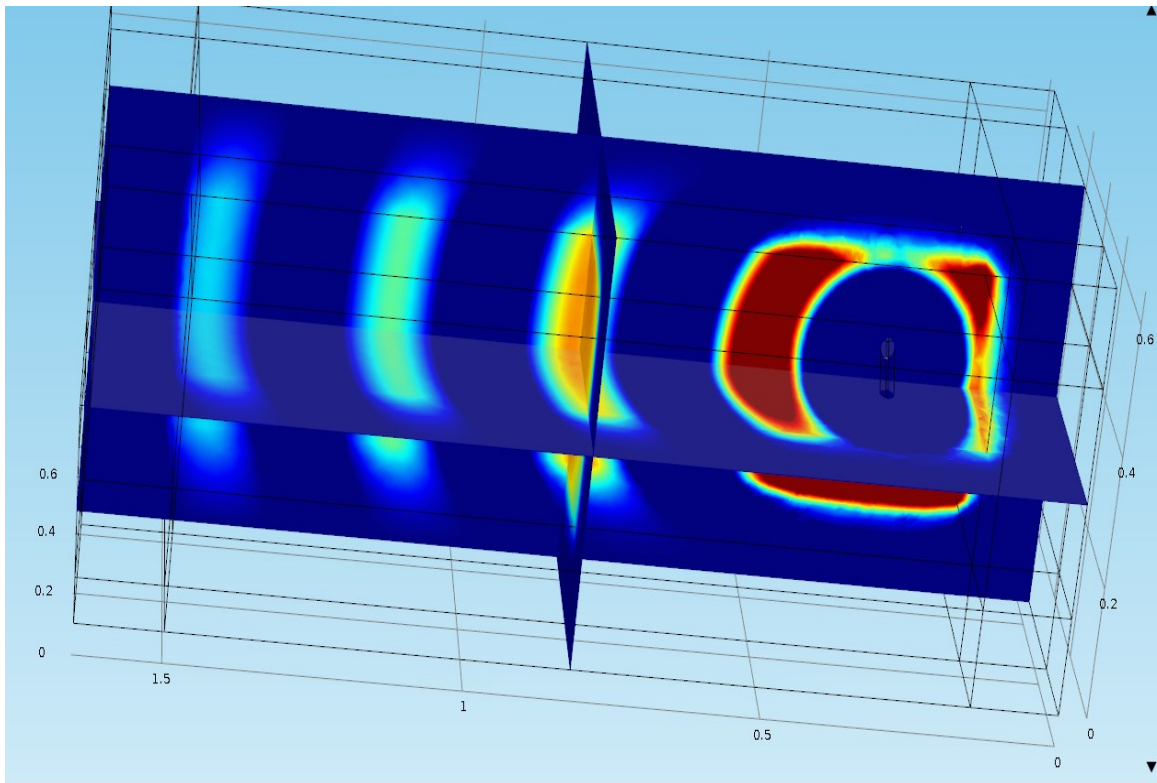


Figure 12. Simulated relative electric field results for an 11 cm length, 1.2 cm diameter steel rod at 960 MHz

Simulations of the individual targets in isolation have been completed with acceptable results as shown by the comparison of theoretical, simulated and practical results in Table 4. Objects on body are a more complex issue as the required meshing would be so dense as to render a simulation on the hardware available impossible. Consideration was given to the creation of a Debye model of the complex dielectric response of the human body in order to reduce the computational complexity of the mesh. This was unsuccessful as the mesh was still far too dense to be solved successfully. 2.5. EM propagation and scattering

Electromagnetic waveforms and their interaction with the physical world are governed by Maxwell's equations [6]. The propagating EM waveform presented in Figure 12 is a FEA example of this. The received signal then becomes dependent on the RCS of the target being illuminated. The size of the RCS of the target relative to the wavelength of the EM waveform illuminating will determine the scattering properties of the signal. This process allows for a direct analogy with the Rayleigh scattering regime. At higher frequencies, $\sim 0.5\text{-}1$ GHz, where free-space wavelengths (60-30 cm) are commensurate with the size of metal objects such as handguns and knives, the radar cross section of these objects display an oscillatory character analogous to the Mie scattering regime. This well understood process is also known as the resonant regime and therefore can be used to represent the scattering properties of LTR signals.

Discussion

The preceding chapter has presented an overview of RF emission safety with reference to IEEE standards and discussion of how that applies to this work. The experimental setup has been considered along with different target configurations. Finally the simulation procedures used have been presented. This experimental setup is standardized throughout the results presented. The data extracted from the experiments and simulations is in a raw format and needs to be processed to extract the useful LTR data. Techniques to facilitate this are discussed in the following chapter.

Chapter 3

Clutter Reduction, Deconvolution and Classification Techniques

Preview.

This chapter will discuss clutter reduction using three types of filter alongside linear and non-linear deconvolution techniques. Clutter reduction in RADAR systems is necessary as most scenes will have unwanted objects present within them. The filters to be discussed will be the discrete and continuous wavelet filter, the Savitsky-Golay smoothing filter and the Time-Gating technique. A brief introduction to both the CLEAN non-linear deconvolution algorithm and the wavelet transform have also been provided.

3.1. Signal Deconvolution

3.1.1. Signal deconvolution

One of the major problems encountered with RADAR signal processing is the convolution of the antenna response with the useful data. Convolution is a mathematical operation on two functions, producing a third function that is a modified version of the first function as presented in section 3.1.2. Linear deconvolution. This is a problem particularly in LTR analysis as the received power level of the useful LTR data is of considerably smaller magnitude than the Antenna Response. One solution to this is to perform a signal deconvolution. Signal deconvolution can be considered to be analogous to division of the two signals in the frequency domain as presented in [87]. This solution works in the case where the absolute value of the complex number \hat{g} is not equal to zero. In the case of signal deconvolution, \hat{g} can be considered to be the unwanted clutter that has been convolved with the valuable signal. In some cases, such as when the frequency sweep used is of greater bandwidth than that of the horns used to improve frequency resolution, this could approach zero.

To resolve the issue of when the absolute value of \hat{g} approaches zero a selection of non-linear deconvolution techniques have been developed, particularly in the area of radio astronomical imagery. These include the CLEAN algorithm [123] and the Burg algorithm,

more commonly known as the Maximum Entropy Method (MEM) [124]. The CLEAN algorithm is the most commonly used non-linear deconvolution method with a number of alternative versions such as the Clark CLEAN algorithm [125] being developed for imaging purposes. More recently, the possibility of applying the CLEAN algorithm to non-imaging RADAR systems has been considered as an alternative to the matched and Wiener filters [13] [126]. Algorithms such as coherent CLEAN, sequence CLEAN and lean CLEAN have been implemented and tested on standard RADAR based systems.

The process of developing the CLEAN algorithm suitable for radar systems started with the coherent CLEAN method published in Tsao and Steinberg 'Reduction of sidelobe and speckle artefacts in microwave imaging: The CLEAN technique' [127] concluding that the CLEAN technique allows for the improvement of both image contrast and dynamic range. This built on the work published by Clark [125] which used the Fast Fourier Transform (FFT) to reduce the computational intensity required to complete the CLEAN algorithm.

In 2002 Bose developed the sequence CLEAN algorithm as an improvement to the coherent CLEAN algorithm [128]. In over 100 different cases the sequence CLEAN algorithm provided equal to or better performance than that of the coherent CLEAN algorithm. Bose's sequence CLEAN algorithm has also been applied to Inverse Synthetic Aperture Radar (ISAR) images of aircraft with promising results. Further work investigating the application of CLEAN to radar systems can be found in the work of Martorella [129] where a Gaussianity test (GT) was performed and a probability of false alarm determined to improve the performance of the CLEAN algorithm.

To address some of the performance issues identified in the CLEAN deconvolution algorithms the lean CLEAN algorithm was introduced by Bose [130]. This version of the CLEAN algorithm detects and discards any spurious peaks within the signal and so corrects for some of the problems with coherent CLEAN. This led to the development of the active CLEAN algorithm [131] to improve the detection of closely spaced targets.

The CLEAN algorithms application to security scanning systems is a current area of research. Techniques such as multi-frequency synthesis, the CLEAN algorithm and the Maximum Entropy Method, also known as the Burg algorithm for the application of vehicle scanning at ports of entry have been considered with an aim to reducing the cost of

large antenna arrays [132]. This work was followed up with a measure of the level of improvement provided by these techniques [3].

3.1.2. Linear deconvolution

Signal convolution of the antenna response with the useful data presents one of the major problems encountered with radar signal processing. The convolution theorem in the time domain is shown in Equation 24 below:

$$\hat{h} = \hat{f} * \hat{g} \quad \text{Equation 24}$$

Where \hat{h} is the experimentally obtained signal, \hat{f} is the useful signal to be recovered and \hat{g} is the signal with which \hat{f} has been convolved.

This is a problem particularly in LTR analysis as the useful LTR data is of considerably smaller magnitude than the frequency variation of the antenna response. One solution to this is to perform a linear signal deconvolution. As stated previously, in its simplest form, linear signal deconvolution is equivalent to division of the two signals in the frequency domain for example:

$$\hat{f} = \hat{h}/\hat{g} \quad \text{Equation 25}$$

This solution only works in the case where the absolute value of the complex number \hat{g} is not equal to zero. To account for the potential for the transmission signal values to approach zero, an offset determined as a percentage of the maximum magnitude of the transmission signal has been added to the transmission signal in order to ensure that the value cannot reduce to zero. This results in the deconvolution equation becoming:

$$\hat{f} = \hat{h}/(\hat{g} + (g_{max} * g_0)) \quad \text{Equation 26}$$

Where g_0 is the fixed offset which can have a value between 0 and 1. The reference signal g is obtained experimentally by measuring the output of the horn antenna with the transmitting and receiving antenna aimed towards each other and free space in between.

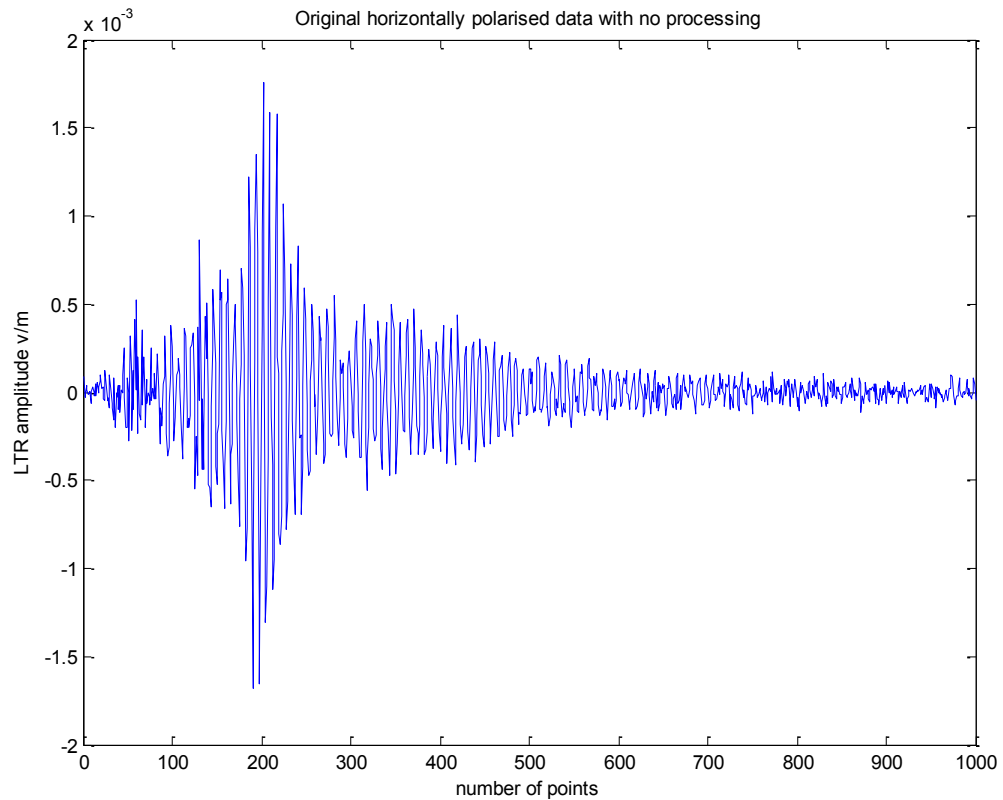


Figure 13: 6.5 cm needle original data grabbed by VNA, no signal processing, frequency domain, real part shown

Figure 13 above presents the data in the form of the horizontally polarised S21 scattering parameter (S parameter) grabbed by the VNA, with the greatest magnitude peak corresponding to the LTR. These S parameters represent the elements of a scattering matrix for a target object illuminated by a propagating planar EM waveform and contain information on both the magnitude and phase properties of the received signal. This information is presented in the complex frequency domain in Figure 14.

The 6.5 cm needle is used as a representative target for this as its resonant frequency sits close to 1.9 GHz and it provides a relatively high resonant response. This means that in LTR terms the signal decays over several nanoseconds, making for an object that is comparatively simple to detect. The smooth damped sinusoid produced by the needle is also very close to the ideal representation of an LTR waveform and presents a good example of the type of data that can be expected to be extracted.

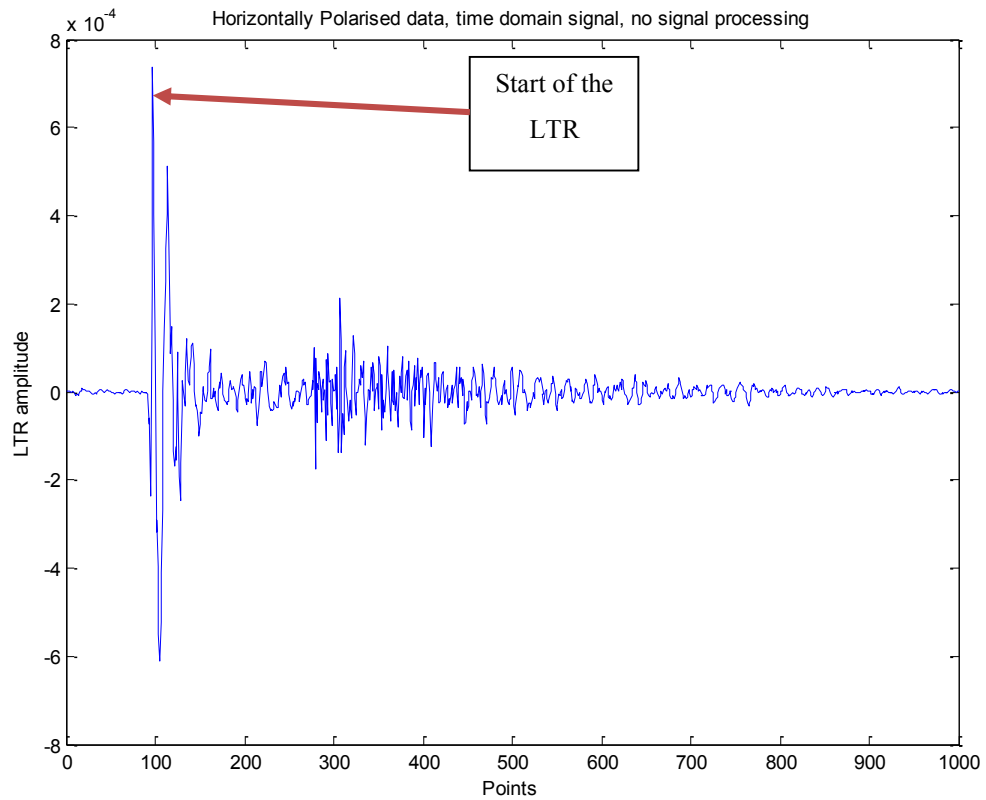


Figure 14: 6.5 cm needle original data grabbed by VNA, no signal processing, time domain, real part shown

Figure 14 represents the same 6.5 cm needle after the signal has been transformed into the time domain using the inverse FFT. At this point no further signal processing has been performed. The relative magnitude of the largest peak in the plot compared to the transmission signal of 0 dBm is approaching 8×10^{-4} and is located just after point 100. Further peaks of lesser magnitude can be found between points 300 and 400. This shows the antenna response saturating the signal and potentially masking the useful information that LTR can provide. This level of transmission characteristics contained within the signal mean that without further processing the data would be unsuitable for the work to be performed. Therefore, deconvolution of the signal is a necessity and is the next stage of processing to be performed.

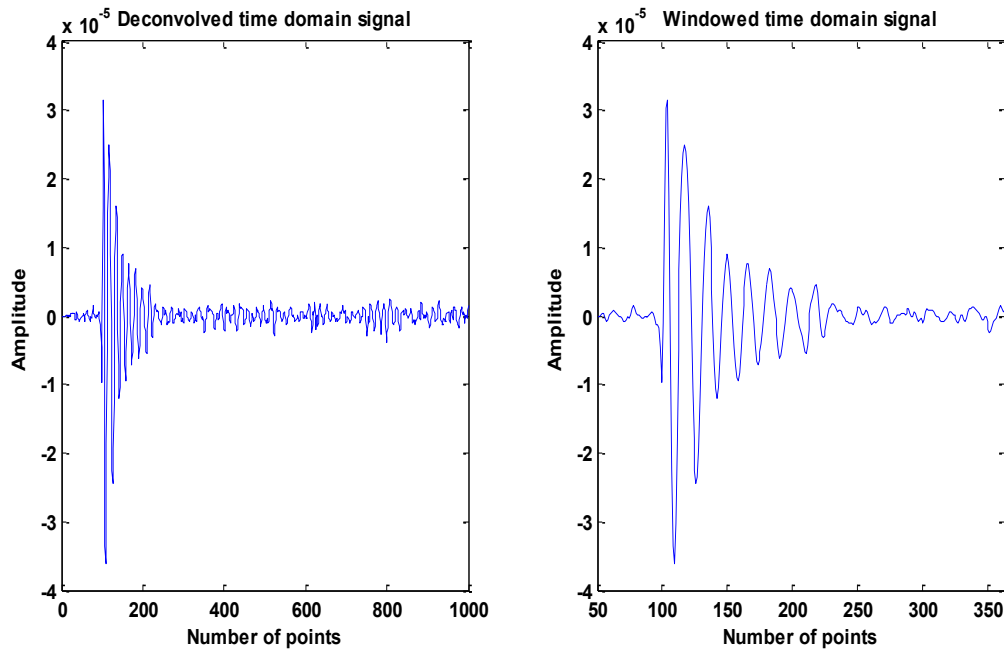


Figure 15: 6.5 cm needle data grabbed by VNA, deconvolved, time domain, real part shown

Figure 15 presents two plots of the deconvolved signal from the 6.5 cm needle. The plot to the left provides a representation of the deconvolved signal over the same axis as those in Figure 13 and Figure 14. For ease of analysis the plot to the right in Figure 15 shows the same dataset zoomed on the features of interest. In the left plot the signal shows a sharp decay with a smaller tail, while when zoomed in it is apparent that the signal has a more damped sinusoidal appearance. The first point of note is that the maximum relative magnitude of the deconvolved signal is now 3×10^{-4} of the transmitted 0 dBm signal in this case. This magnitude of this signal is dependent in the antenna gain as well as attenuation of the signal caused by range to target. This occurs at \sim point 130 which when compared to figure 8 shows itself to be within the high magnitude antenna response. This indicates that as this feature is of smaller magnitude than the antenna response at this point, without the application of signal deconvolution the feature may be missed. This presents a good example of one of the major issues that presents itself when attempting LTR analysis. In effect if the deconvolution of the signal is unsuccessful/not possible then the ability to use the LTR method to obtain useful target information in general terms is essentially zero.

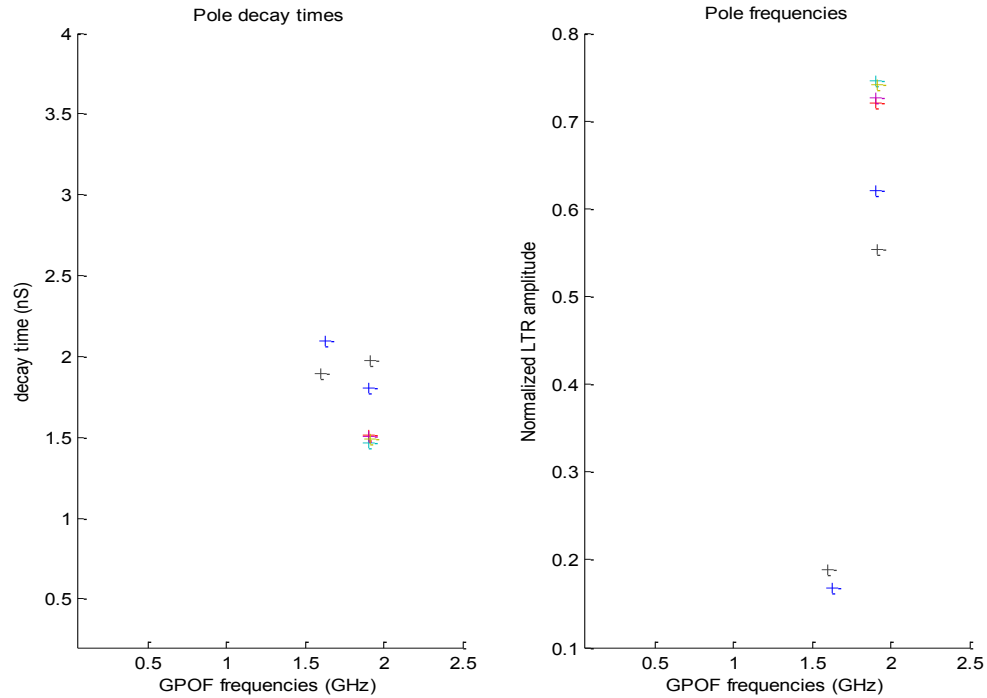


Figure 16: Pole plot results for 6.5 cm needle only with signal deconvolution

The extracted pole values using the standard Generalised Pencil Of Function (GPOF) method for the same 6.5 cm needle are presented in Figure 16. The GPOF method will be discussed in detail in section 3.1.3. GPOF and Singular Variable Decomposition. As mentioned previously the frequency of the fundamental poles for the needle can be expected to occur at values approaching 1.9 GHz. The plot to the left in Figure 16 shows the signal decay time against the frequency of the poles while the plot to the right presents the energy of the pole against frequency. The spurious poles located at ~ 1.6 GHz have much lower energy than those at ~ 1.9 GHz and so can be safely discounted. Without deconvolution the results can be a little different. The 6.5 cm needle was chosen for this test as it is the only object tested that presents frequencies close to that of the deconvolved signal with no deconvolution. It is apparent that these frequencies are still different though, therefore for classification purposes the needle data without deconvolution is useless.

3.1.3. GPOF and Singular Variable Decomposition

The Generalised Pencil of Function is used as a reliable method for estimating the parameters of a signal. It is used to find a set of complex coefficients when given a set of discrete data. The method requires the solution of a generalised Eigenvalue problem in order to find the poles. When compared to Prony's method and other Pencil-of-functions which obtain the information in two steps, the GPOF method is less sensitive to noise and computationally more efficient. A full discussion and derivation of the GPOF method can be found in Hua and Sarkar's seminal 1989 paper [95].

The first step of the GPOF algorithm used for this work involves determination of a pencil parameter from the dataset for use in estimating the data. This requested model order is then checked against this parameter to ensure that the model order does not exceed the size of the pencil parameter. For this work the pencil parameter has been set to half the length of the data set.

This algorithm presented in [95] allows the extraction of frequency, decay time and amplitude pole data. This data is then used to reconstruct the original signal to allow the standard error between the input data and the processed data at various model orders to be calculated.

Use of this extracted standard error data allows for the determination of the correct model order. Once this has been determined, the algorithm can be run again with the correct model order.

Singular Variable Decomposition (SVD) is a method used for transforming correlated variables into a set of uncorrelated ones that better demonstrate the relationships between the data points while identifying and ordering the dimensions of the data along which there is the most variation.

The SVD is based on the fundamental theorem of linear algebra as presented by [133] that states a matrix can be broken down into three matrices - orthogonal matrix U , diagonal matrix S and transpose matrix V as shown in Equation 27 [133].

$$A_{mn} = U_{mm}S_{mn}V_{nn}^T \quad \text{Equation 27}$$

It is necessary to perform SVD on the data to obtain the three components stated in Equation 27. These components are used to solve the eigenvalue problem used by the GPOF method in order to extract the poles of the data.

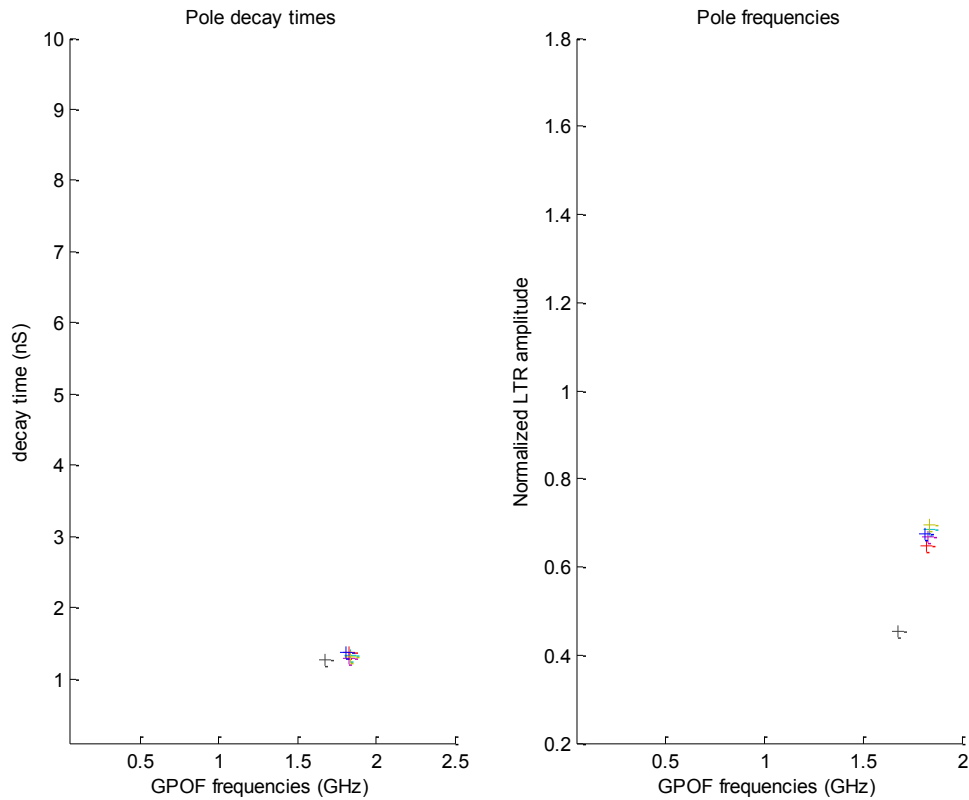


Figure 17: Pole plot results for 6.5 cm needle only without signal deconvolution

The differences between the results for the 6.5 cm needle with and without deconvolution presented in Figure 16 and Figure 17 are quite small although still significant enough to cause errors in classification. For example where the deconvolved signal finds the resonant frequency of the needle to be 1.9 GHz and decay time to be ~ 2 ns, the non-deconvolved signal gives ~ 1.8 GHz and ~ 1.3 ns. The energy levels present in the useful poles are also lower, while the spurious poles are stronger. Due to its highly resonant nature the 6.5 cm needle is capable of providing a response even without signal deconvolution, although not a particularly accurate one. For objects of a less resonant

nature it becomes progressively more difficult to extract any usable information without application of signal deconvolution.

The results presented in this section show the value of linear deconvolution techniques to a radar based LTR security system. As mentioned this approach is not without its limitations therefore alternative methods of signal deconvolution, in particular non-linear deconvolution techniques have been explored as a method to support or even potentially replace linear deconvolution.

3.2. Non-Linear deconvolution: The CLEAN approach

Non-Linear deconvolution techniques are an approach that has been applied in the field of radio astronomy to improve the fidelity of images obtained using interferometric antenna arrays [123]. As with radar systems, radio astronomers discovered that the presence of unmeasured regions in the Fourier plane resulted in an undefined result for that particular pixel, therefore rendering standard linear deconvolution techniques inadequate to the task. Non-linear deconvolution, in particular the CLEAN algorithm first presented in [123] presented a potential solution to this. Variants of the CLEAN algorithm include the original Hogbom, Clarke and Cotton-Schwab algorithms.

Outside of the radio astronomy community the CLEAN algorithm has found applications in a number of areas due to the feature extraction capabilities of the technique. A number of applications in radar signal processing have been attempted ranging from imaging and Linear Frequency Modulated Continuous Wave (LFMCW) radar systems to improving detection of helicopters [128] [130] [131] [134] [135] [136].

3.2.1. 1D signal analysis: The CLEAN algorithm

The CLEAN algorithm requires two major components to function. The first of these is known as the dirty map. This is the dataset that the CLEAN algorithm is intended to improve, in this case the horizontally polarised S21 data. The second component required is the Point Spread Function (PSF) of the signal. In the case of a 1 dimensional non-imaging radar system this can be considered to be the Impulse Response Function (IRF) of that

system and is estimated by computing the IFFT of the signal and centering the result at the origin.

The operation of the CLEAN algorithm determines the location of assumed point sources within the dirty map. In the case of a 1 dimensional LTR signal these point sources can be assumed to be the major peaks within the signal. The algorithm then determines the point of maximum correlation within the dataset, the PSF is shifted to match and then subtracted from the image. This subtracted data is used to create a delta function with peak intensity and location equal to that of the subtracted data. This is then saved to a separate dataset and is known as a CLEAN component. An example of this process is shown in Figure 18. The process is then repeated until a predetermined threshold is reached.

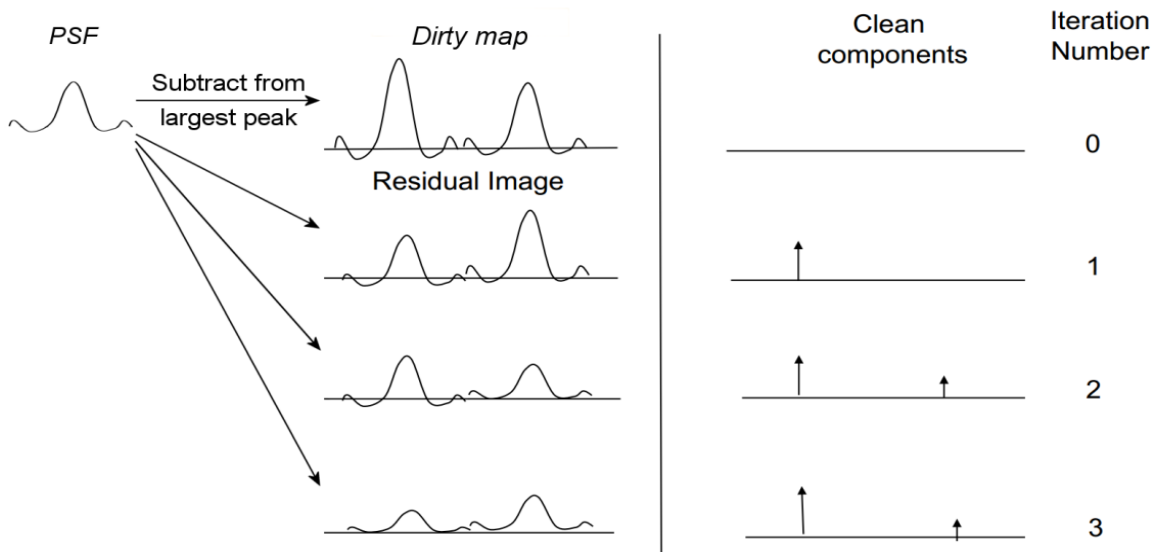


Figure 18: The CLEAN deconvolution technique applied to a 1D signal for creating the CLEAN components [3]

The iterative approach to this method builds up a set of CLEAN components in the separate dataset created whose peak intensity and location equate to the location of the point sources within the dirty map. Once the stopping criteria has been met, the CLEAN components are then convolved with the CLEAN PSF. This CLEAN PSF is an ideal Gaussian function fitted to the central maximum of the PSF. The residual dataset left over from the iterative subtraction is then added to this to create the final CLEAN image.

The benefits to the use of the CLEAN algorithm in this application are in its ability to separate out the peaks within a given signal. This allows for smaller peaks that may have

been suppressed within the original data to be brought into focus and their effect on the dataset to be analysed. When used in support of the linear deconvolution approach the CLEAN algorithm allows for improved detection of poles with the downside that in order for it to be performed correctly the threshold must be very accurately determined a priori.

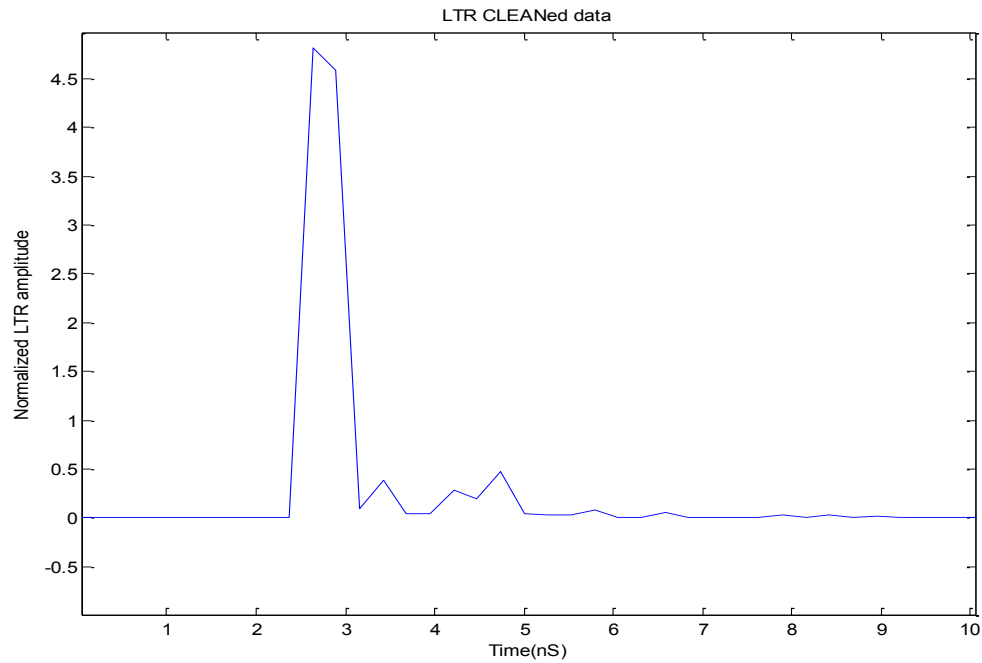


Figure 19: CLEANed LTR signal for 6.5 cm needle

The CLEANed LTR signal is presented in Figure 19. This represents itself as a peak occurring 2.4 ns into the signal, followed by several much smaller peaks spread over the following ~2 ns. This data is then processed using the GPOF and the pole plots are presented in Figure 20.

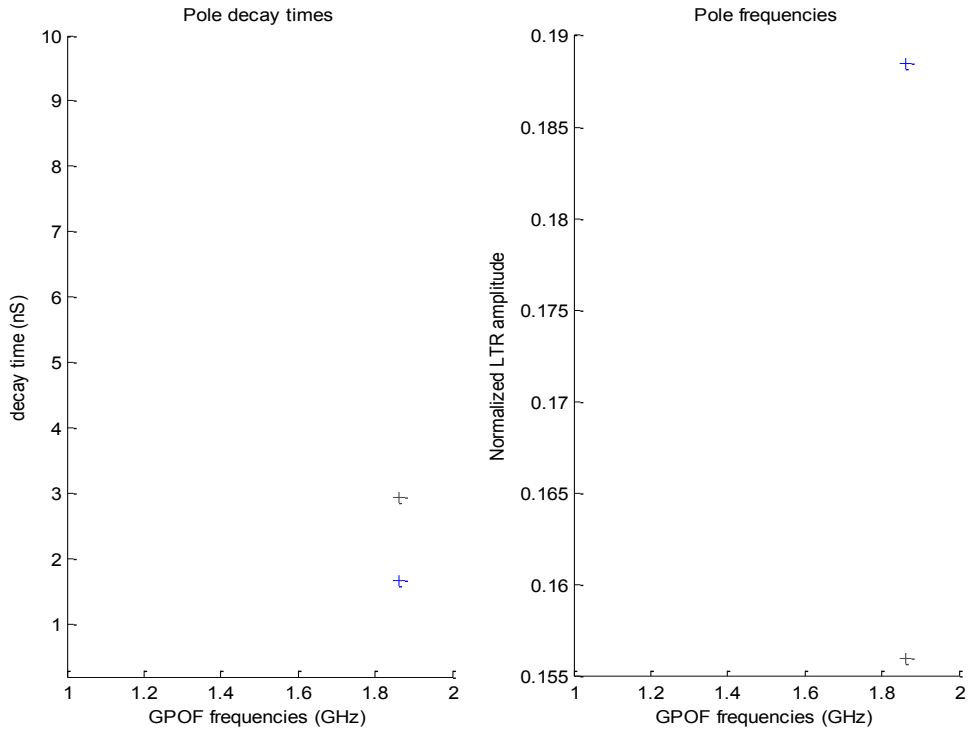


Figure 20: Pole plots for CLEANed 6.5 cm needle only

As the poles for the 6.5cm needle have been calculated to occur at 1.961 GHz, it is apparent when Figure 20 is compared to Figure 16 that the CLEAN algorithm has removed the unwanted poles that occurred at 1.6 GHz using the original FFT and GPOF approach. This has come with the cost that some of the useful poles to be found around 1.9 GHz have also been removed from the signal.

The modified CLEAN algorithm used in this work comprises the following steps:

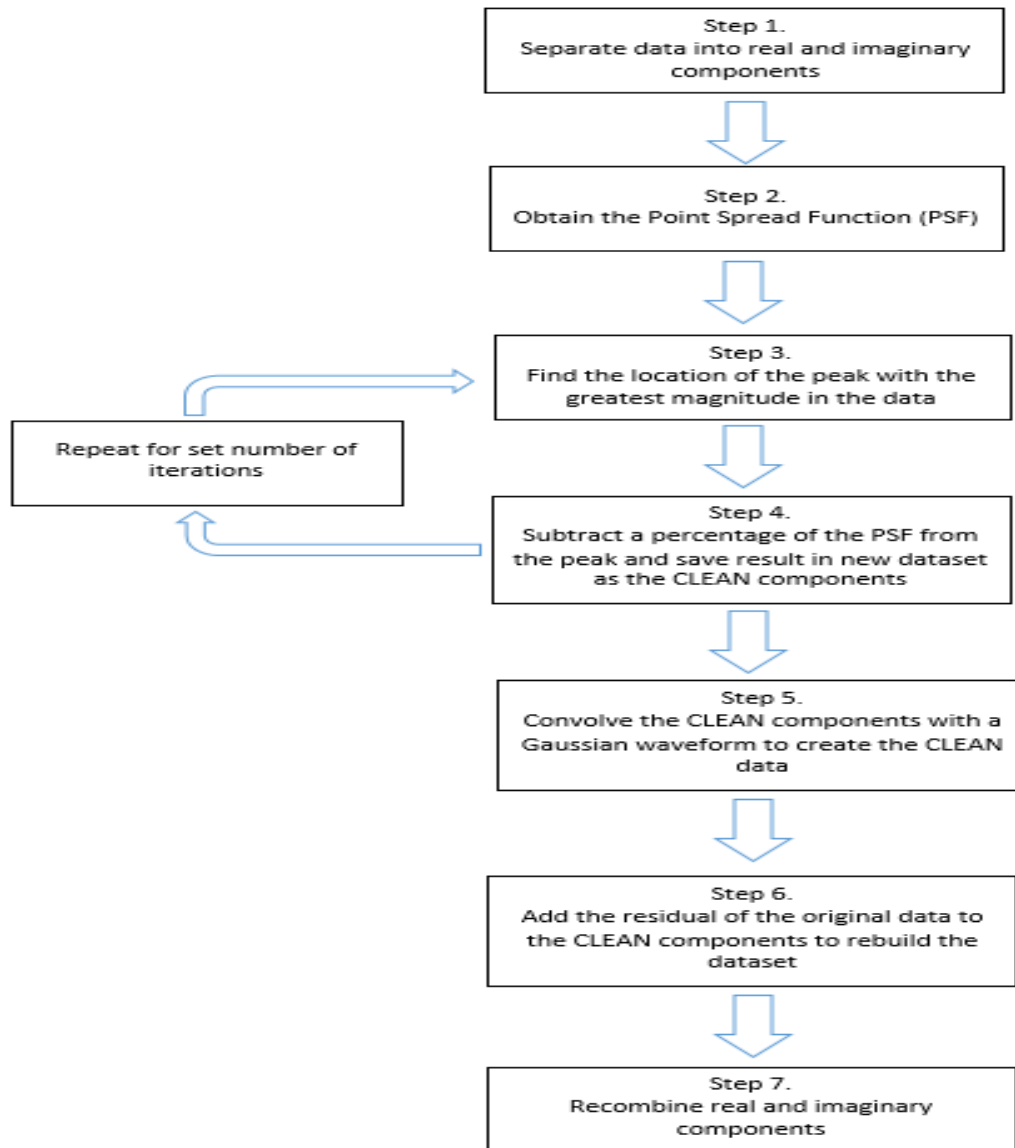


Figure 21: Flowchart of CLEAN non-linear deconvolution process

This method allows for the lesser magnitude components of a signal to be separated from their larger cousins, potentially reducing the effect of the Early Time Response (ETR) on the signal.

3.3. Filtering and Clutter reduction

Filtering and clutter reduction techniques are an important part of any signal processing approach. High frequency noise and unwanted features in a signal are commonplace and can provide significant disruption to a signal. Three types of filtering/clutter reduction have been applied to the datasets to improve Signal to Noise Ratio (SNR).

3.3.1. Introduction to wavelets and the wavelet transform

The wavelet analysis approach is used to decompose a given signal, be it sound, image or radar return, into components of varying durations which are known as wavelets. These components or wavelets contain localized features of the analysed signal over dilated and translated wavelets and can be used for a broad range of signal processing tasks. One of the tasks that can be performed using wavelet analysis is noise/clutter reduction of the signal. Wavelets can also be used to perform accurate signal compression and it is by applying this capability for compression that filtering of the signal using wavelets can be performed.

A wavelet is a function that satisfies at least the two following criteria [137];

1. The integral of the function $\psi(x)$ over all x is 0.

$$\int_{-\infty}^{\infty} \psi(x) dx = 0 \quad \text{Equation 28}$$

2. The square of $\psi(x)$ has integral 1.

$$\int_{-\infty}^{\infty} \psi^2(x) dx = 1 \quad \text{Equation 29}$$

To meet the first criterion the wavelet must have an equal area above and below the X axis. The second criterion requires that as the function approaches towards positive and negative infinity that the function decays to zero. As this means the function will decay as it moves away from the origin as opposed to infinite sinusoidal waveforms, the signal duration is finite and is therefore a wavelet as opposed to a wave.

The first and simplest of the wavelet transforms made available is based around the Haar wavelet which was used for analysis of discrete signals. A representation of the Haar wavelet can be found in Figure 22 [137];

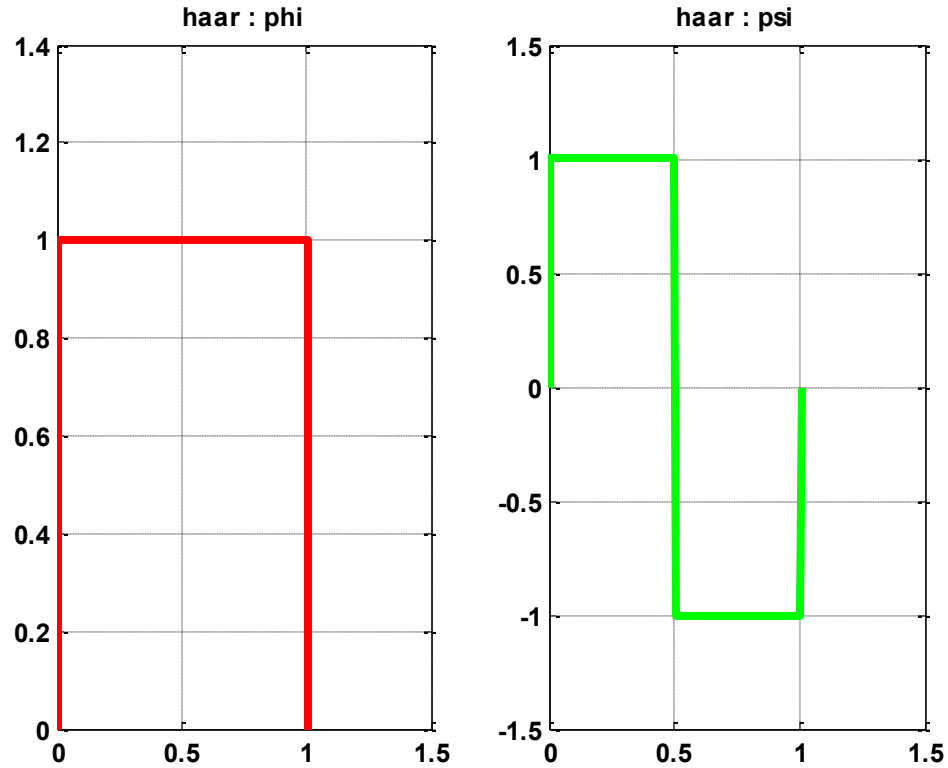


Figure 22: The Haar wavelet with the scaling function (phi) and the mother wavelet (psi) which uses this scaling function [138]

As this transform can only be applied to discrete signals, it is necessary to define what a discrete signal is. Therefore a discrete signal can be defined as a function of time with values occurring at discrete intervals. We shall express discrete signals in the form:

$$df = df_1, df_2, \dots, df_n \quad \text{Equation 30}$$

Where n is a positive even integer which equates to the length of 'df'. If n has an odd value a zero must be appended to the end of the signal to make the length of 'df' even. The values of 'df' are the measured values of a given signal 'g' measured at different points in time 't_n' therefore the values of s are:

$$df_1 = g(t_1), df_2 = g(t_2), \dots, df_{3n} = g(t_n) \quad \text{Equation 31}$$

The Haar transform as with all wavelet transforms decomposes the signal presented to it. This decomposition results in two subsignals, half the length of the original being generated. These subsignals are known as the trend (a running average) and the fluctuation

(a running difference). The trend is calculated by averaging pairs of values through the signal, for example;

$$A_1 = \frac{df_1+df_2}{2}, A_2 = \frac{df_3+df_4}{2}, \dots, A_n = \frac{df_m+df_{m+1}}{2} \quad \text{Equation 32}$$

Where m is an integer value. The fluctuation is then calculated using:

$$D_1 = \frac{df_1 - df_2}{\sqrt{2}}, D_2 = \frac{df_3 - df_4}{\sqrt{2}}, \dots, D_n = \frac{df_m - df_{m+1}}{\sqrt{2}} \quad \text{Equation 33}$$

Therefore the first level Haar transform will be:

$$df \xrightarrow{H_1} (A^1 | D^1) \quad \text{Equation 34}$$

To decompose the discrete signal 'df' into its trend (A^1) and fluctuation (D^1) components. This process can be reversed, allowing for the original signal to be retrieved from the two components of the transformed signal using Equation 35:

$$f = \left(\frac{A_1 + D_1}{\sqrt{2}}, \frac{A_1 - D_1}{\sqrt{2}}, \dots, \frac{A_N + D_N}{\sqrt{2}}, \frac{A_N - D_N}{\sqrt{2}} \right) \quad \text{Equation 35}$$

The major advantage of this particular form of transform is shown by the result of the trend and fluctuation subsignals. The trend subsignal will be similar in form to the original signal, although with increased magnitude while the fluctuation subsignal will normally have a large number of values around zero. The small fluctuations feature of the Haar transform lends itself to signal compression which in turn is very valuable for noise reduction in the signal.

The CWT is also capable of performing compression and filtering of a signal. To define the CWT we use the analyzing function $\psi(x)$, the definition of which is shown in Equation 36 [137];

$$\psi(x) = 2\pi w^{\frac{-1}{2}} \left[1 - 2\pi \left(\frac{x}{w} \right)^2 \right] e^{-\pi \left(\frac{x}{w} \right)^2}, w = \frac{1}{n} \quad \text{Equation 36}$$

This is the well-known Mexican hat representation which is a 2nd order Gaussian wavelet with width parameter 'w', shown in Figure 23 below:

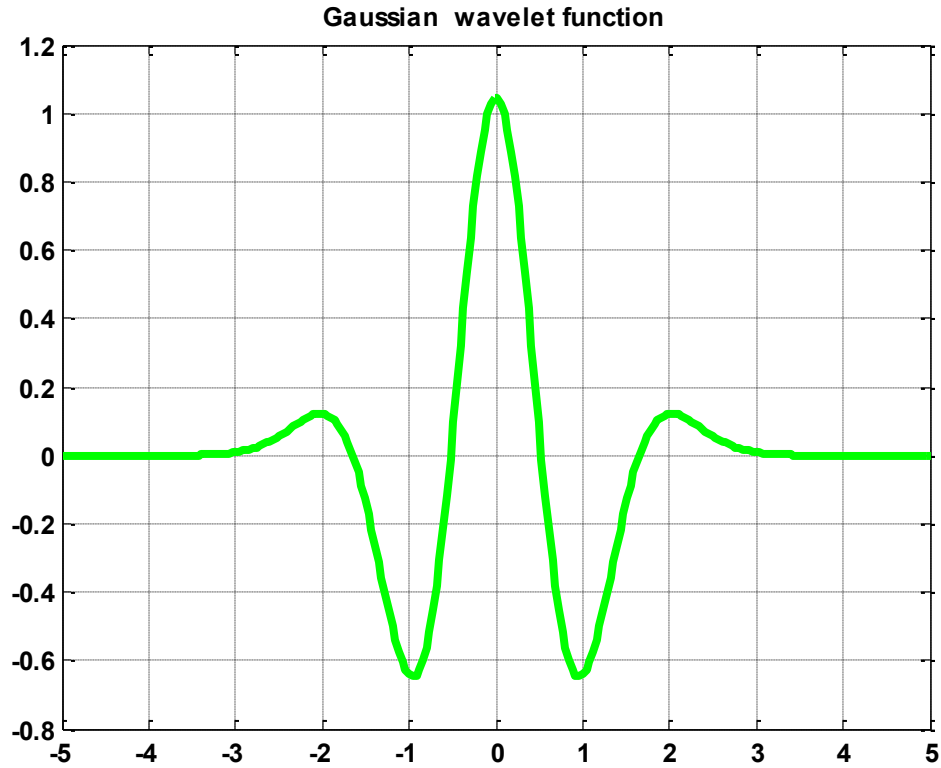


Figure 23: Gaussian4 / Mexican hat wavelet

By altering parameter ‘w’ it is possible to dilate or constrict the wavelet for use in analysis. For example the smaller the value of ‘w’ the more of the energy contained within the wavelet is contained over a smaller spread of the x axis and vice versa.

Once an analyzing wavelet has been determined, the CWT of discrete signal ‘f’ is determined by calculating the correlations of the signal with discrete samplings of function $\psi_s(x)$ as determined by:

$$\psi_s(x) = \frac{1}{\sqrt{s}} \psi\left(\frac{x}{s}\right), \quad s > 0 \quad \text{Equation 37}$$

where the s parameter is the scale parameter. When the signal is sampled at discrete time values t_1, t_2, \dots, t_n , where n is the length of signal ‘f’ then the discrete signal g_s will be generated:

$$g_s = (\psi_s(t_1), \psi_s(t_2), \dots, \psi_s(t_n)) \quad \text{Equation 38}$$

The results for the CWT are now a collection of discrete correlations. By making careful choices as to the width and scale parameters it becomes possible to perform a very finely detailed time-frequency analysis on the signal presented. Results of the application of the CWT can be found in section 5.1. Real valued wavelet analysis. The same method is used to calculate the complex CCWT with one difference, when calculating the correlations of the imaginary component the CWT reuses the real valued wavelet while the CCWT uses the imaginary component of the complex wavelet.

Walker [137], presents an example of how to calculate the wavelet coefficients effectively. For example in order to calculate the coefficients for the CWT a mother wavelet is selected. This is then constricted or dilated in order to create a windowed mother wavelet for use in calculating the correlations.

In order to successfully complete this process the range of scales required must be known, along with choice of a mother wavelet that matches as closely as possible to the waveform being analysed.

Choosing the correct wavelet is very important when approaching wavelet analysis. Two of the fundamental types of wavelet that have been tested in this work are the Morlet/Gabor wavelet as shown in Figure 24 and the Gaussian/Mexican hat wavelet presented in Figure 23.

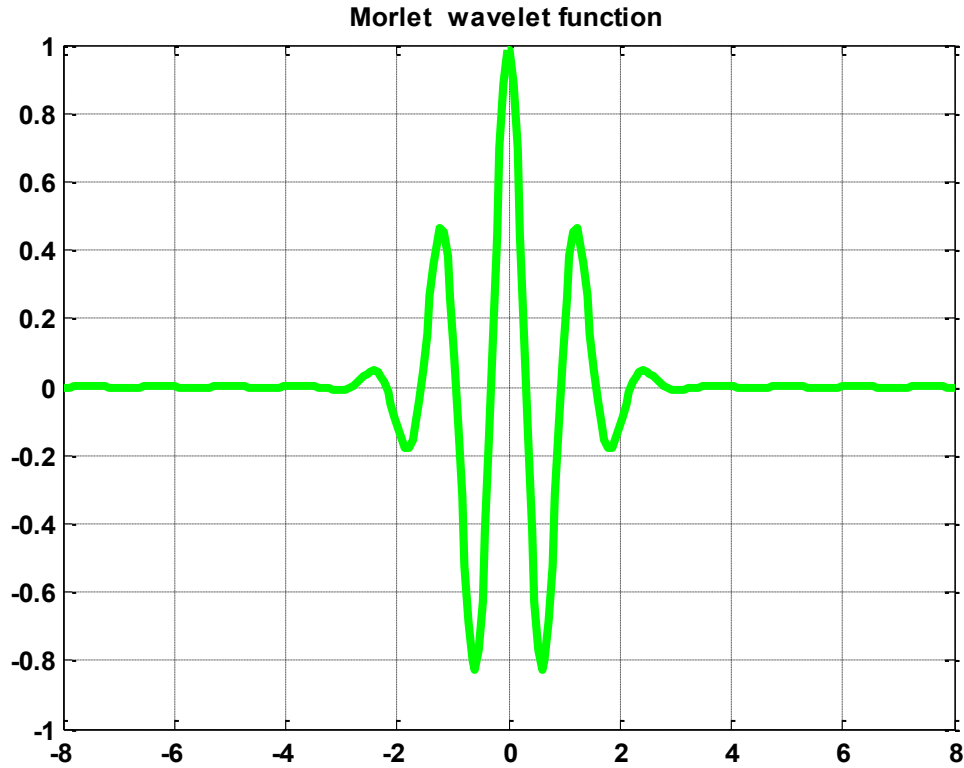


Figure 24: Morlet wavelet

The equation representing the analyzing Complex Gabor wavelet is [137]:

$$\psi(x) = \frac{1}{w} e^{-\pi \left(\frac{x}{w}\right)^2} e^{i \frac{2\pi v x}{w}} \quad \text{Equation 39}$$

Where 'v' represents the frequency/scale parameter and 'w' is the width parameter. As this wavelet is complex valued the real component is known as the Morlet wavelet and is represented by:

$$\psi_R(x) = \frac{1}{w} e^{-\pi \left(\frac{x}{w}\right)^2} \cos\left(\frac{2\pi v x}{w}\right) \quad \text{Equation 40}$$

The imaginary component is:

$$\psi_I(x) = \frac{1}{w} e^{-\pi \left(\frac{x}{w}\right)^2} \sin\left(\frac{2\pi v x}{w}\right) \quad \text{Equation 41}$$

3.3.2. Threshold filtering with the wavelet transform

For the wavelet transform approach to LTR scanning the wavelet based threshold filter was selected to perform the next stage of filtering. The use of wavelet threshold filtering in audio signals analysis is a well-known practice [137]. This can be performed using either the discrete or continuous wavelet transforms. As with the wavelet transform, the first wavelet filter to be produced was based around the Haar wavelet for discrete signal filtering. With the progression of wavelet analysis to the continuous form, continuous wavelet filters based initially around the Daubechies wavelet family [64] became available.

The steps required to perform wavelet filtering of a signal are as follows. Firstly, a CWT is performed on the signal using a specified wavelet. Next a threshold value must be chosen for which any values below this threshold can be removed and any points within the transformed signal below this value are set to zero. Finally an inverse CWT is performed ideally leaving behind a perfect representation of the original signal with clutter removed from it. An example of this will now be presented.

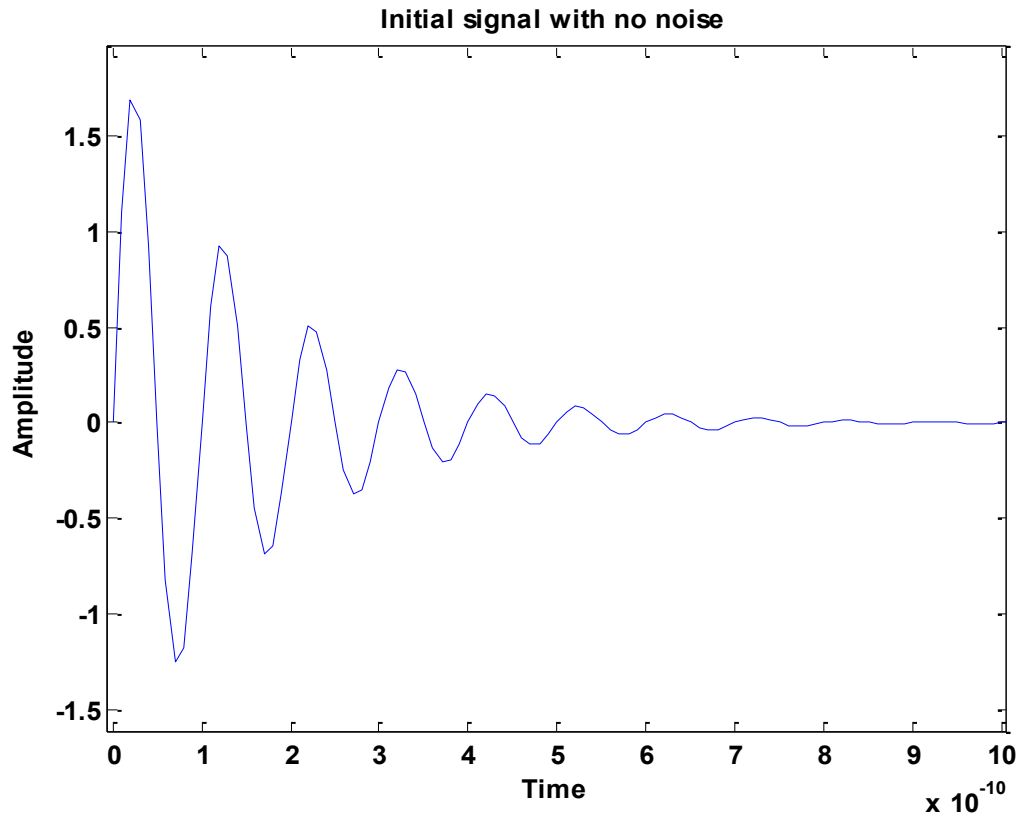


Figure 25: Initial 10 GHz signal with no noise

The signal generated and presented in Figure 25 was a damped sinusoidal waveform with a maximum amplitude of 2 and a frequency of 10 GHz. The signal was designed to last for a total of one nanosecond and attenuates down to approach zero in 0.6 nanoseconds. This signal is without noise and makes for a good example of the sort of idealized signal that would be expected with an LTR response, albeit in practice LTR signals will have a considerably higher frequency. For example a highly resonant object, such as the 6.5 cm needle that has been tested has a similar form of response with a frequency of approximately 1.9 GHz.

To statistically analyse the advantage of using the filtering methods the correlation between the input and the outputs has been calculated using linear regression. Correlation is a statistical measure that measures the relationship between two different signals with respect to each other. If the value of correlation is 1, the relationship between the two datasets is known as a perfect correlation, i.e. when variable X goes up, variable Y also

goes up in a perfectly linear fashion. If the value of correlation is -1 the relationship between the two variables is a perfect anti-correlation, i.e. when variable X goes up, variable Y goes down in a perfectly linear fashion. If the value of the correlation is approaching zero there is no relationship between the variables.

3.3.2.1. Linear Regression using least squares

Linear regression is a powerful tool in statistical analysis. It allows for the modelling of the relationships between a dependent and one or more independent variables. The least squares method is considered the standard mathematical approach to solving a linear regression problem. This involves creation of a least squares regression line which minimizes the sum of the squared residuals of the data points from the regression line with the goal to find the equation of a straight line which would best fit the data points. The regression coefficient 'r' can then be used to calculate the correlation between the two datasets and is found using Equation 42:

$$r = \frac{\sum_{j=1}^k (x_j - \bar{x})(y_j - \bar{y})}{\sqrt{\sum_{j=1}^k (x_j - \bar{x})^2 \sum_{j=1}^k (y_j - \bar{y})^2}} \quad \text{Equation 42}$$

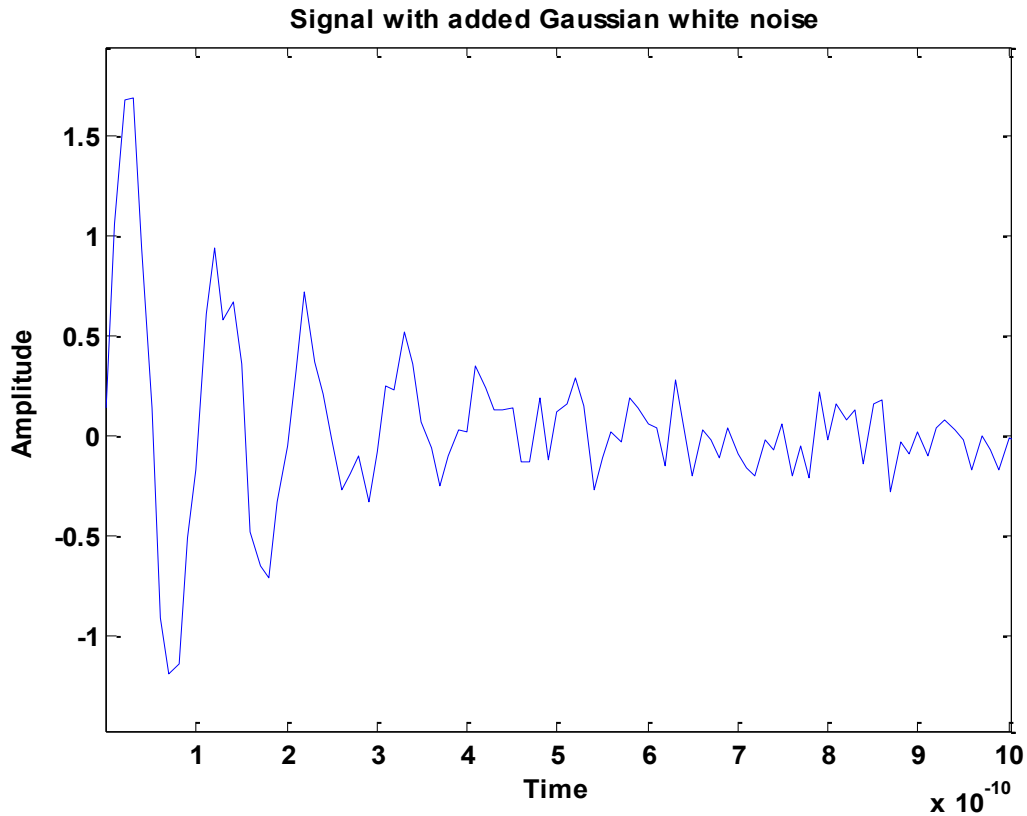


Figure 26: Signal with added Gaussian white noise

Figure 26 presents the same artificially generated 10 GHz signal in the presence of additive Gaussian white noise. This noise was generated using MatLab's built in AWGN (Add White Gaussian Noise) function. Signal processing considers additive Gaussian white noise to be a signal with uniform power across the frequency bands, with a normal distribution in the time domain that averages to zero. It is known as additive as it can be added to a given signal to mimic the effect of natural processes on the signal. The noise added to the signal in this case has a Signal to Noise Ratio (SNR) of 10 dB.

In the case of the signal with added Gaussian white noise the cross-correlation between the original and noise added signals is 0.8175.

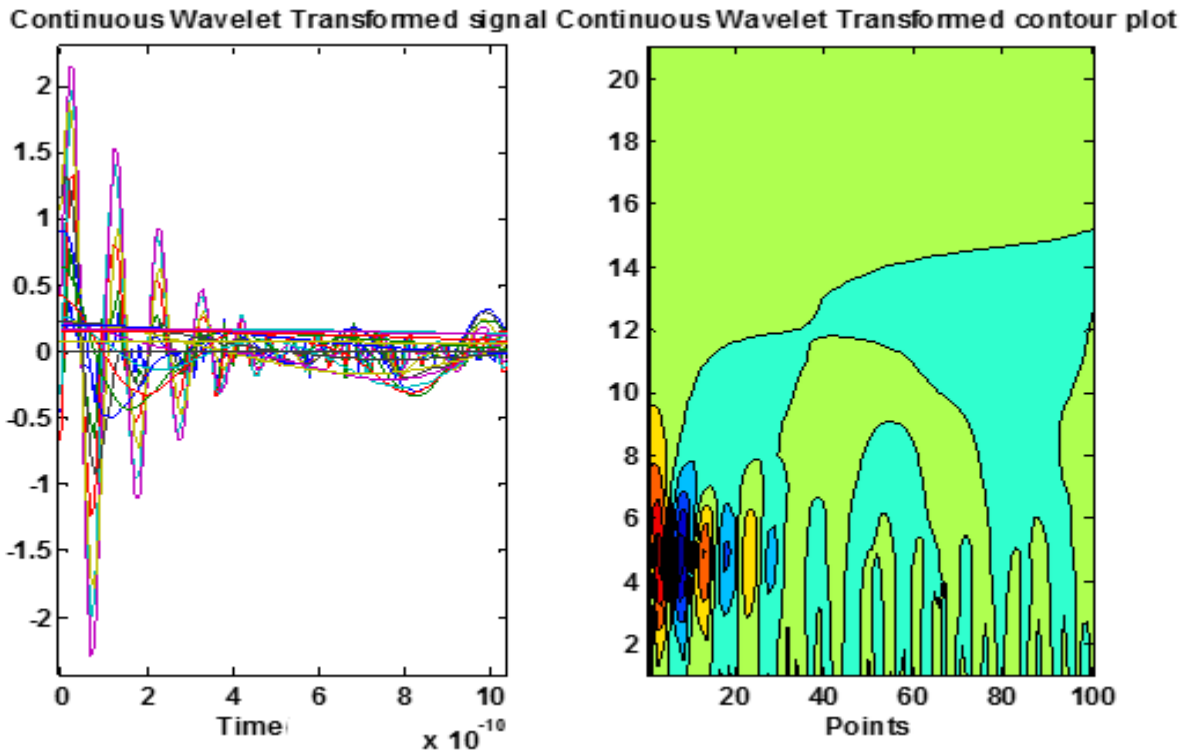


Figure 27: CWT of noisy signal

The intermediate step of converting the signal using the CWT is presented in Figure 27. The two plots presented in Figure 27 show this data in two different formats. To the left the plot shows each of the results of the analysis at different scales as an individual waveform. In this particular example, the CWT has been performed over 14 scale points. Even with such a limited number of scale points the plot has become very difficult to read therefore an alternative method of presenting the data is necessary. The plot on the right is an example of a suitable alternative. This plot is a filled contour map of the complex data created by the CWT. Thresholding is then applied to the dataset and an inverse CWT is performed. The threshold level was determined by calculating the standard deviation of a section of the signal known to contain only noise, then multiplying this by two to ensure that any noise components in the signal are eliminated as per [137].

Table 5: Table of wavelet components with correlation values

Scale Component number	Original signal to wavelet correlation	Noisy signal to wavelet correlation	Recovered signal to wavelet correlation
1	0.5388	0.5239	0.5463
2	0.7962	0.6516	0.8097
3	0.9018	0.6847	0.9170
4	0.9387	0.6927	0.9527
5	0.9452	0.6879	0.9672
6	0.9107	0.6552	0.9205
7	0.7193	0.5090	0.7259
8	0.3604	0.2572	0.3752
9	0.2148	0.1733	0.2544
10	0.1558	0.1528	0.2243

Table 5 shows the correlation of the first 10 wavelet components against the original clean signal, the original signal with additive noise and the recovered signal. The correlation between the wavelet components and the original/recovered signals is greatest around a scale factor of 5 in this case. As the scale factor increases beyond 5 the correlation begins to drop off, with a particularly large decrease between scale factors 6, 7 and 8. The correlation between the original signal with no noise and the recovered signal after filtering is very high at 0.9726.

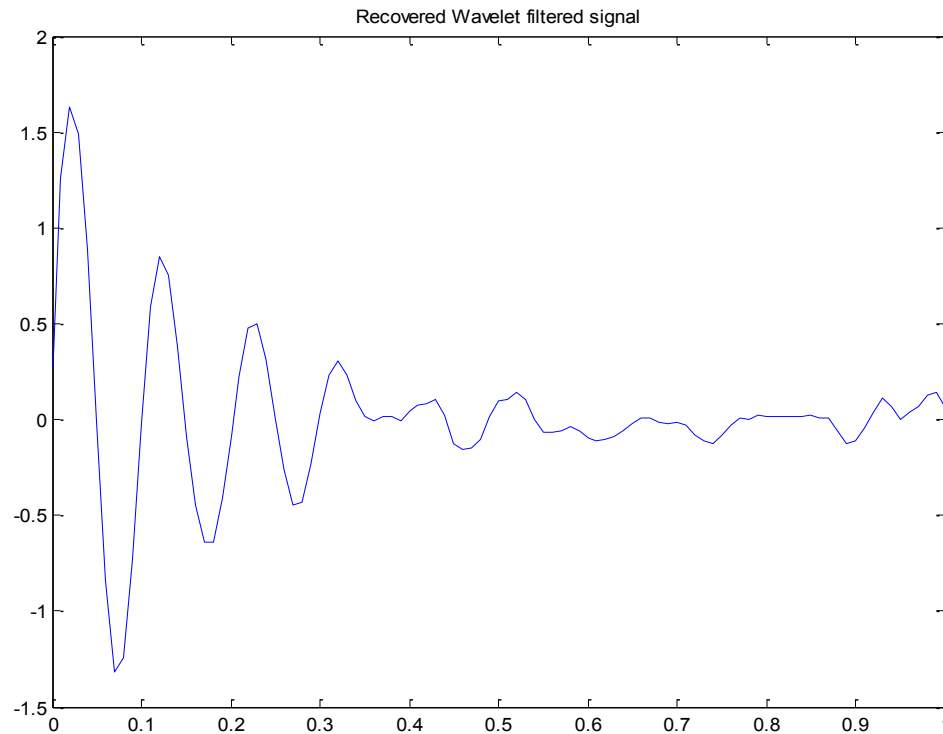


Figure 28: Reconstructed signal after wavelet filtering

This process leads to the filtered signal presented in Figure 28 after the application of a Savitzky-Golay (SG) filter. SG filters are explained in detail in the next section. With the application of this filter type to the wavelet filtered data the cross-correlation between the original signal and the filtered data was measured at 0.9813 while without the application of the SG filter this value becomes 0.9170. This shows that the wavelet filter is of value when applied to a signal on its own, although improvements can be achieved by merging this with other techniques.

3.3.3. Savitzky-Golay Filters

The SG filter, first proposed in 1964, is a digital filtering technique that uses Linear Least Squares (LLS) polynomial approximation to remove high frequency noise from a given signal. It has the effect of smoothing the data provided to it therefore increasing the SNR while limiting the amount of distortion that the method introduces into the signal. The

method was first publicized in [139] and since then has become one of the most influential publications in the Journal of Analytical Chemistry, lending some credence to the statement "it can be argued that the dawn of the computer-controlled analytical instrument can be traced to this article" [140].

In their seminal work, Savitzky and Golay showed that by fitting a polynomial to a set of inputs, the result evaluated at a single point is equivalent to a discrete convolution of the two discrete time signals with a fixed response to an impulse input.

The SG filter acts on a vector of input samples $x(k)$ to produce a smoothed signal $y(k)$. This is done by selecting a window of $2M + 1$ samples from the $x(k)$ dataset. A best least squares fit of a polynomial vector $p(-M), \dots, p(M)$ with an even order 'N' is then applied to the data. The output $y(0)$ is equal to the value $p(0)$ at the centre of the window. The window is then shifted by k time steps and the same process applied for $x(k - M), \dots, x(k + M)$.

If the vector of input samples is defined as:

$$x = (x(-M), \dots, x(-1), x(0), x(1), \dots, x(m))^T \quad \text{Equation 43}$$

and the value of the polynomial coefficients 'a' can be represented as:

$$a = [a_0, a_1, \dots, a_N]^T \quad \text{Equation 44}$$

This gives:

$$Ba = A^T Aa = A^T x \quad \text{Equation 45}$$

The solution of the polynomial coefficients C_n for use in the application of the filter are then determined by:

$$C_n = (A^T A)^{-1} A^T x, \quad \text{Equation 46}$$

Where $A = \alpha_{n,i}$, $\alpha_{n,i} = n^i$, $-M \leq n \leq M$ and $i = 0, 1, 2, \dots, N$, the inverse of A, $A^T = \alpha_{i,n}$, and the product matrix $B = A^T A$. Derivations of how to obtain the equation shown in Equation 46 above along with example code can be found in [141]. Together with the wavelet filter, the Savitzky-Golay filter is applied to wavelet based LTR methods to allow for signal processing to be successfully performed.

3.3.4. Background subtraction

The first stage in filtering of the signal collected by the VNA is a background subtraction. This method involves using the VNA, sweeping through the same frequency bandwidth that is intended for use during scanning of targets, to take scans of a known environment in which the system is to be placed and then subtracting this result from future scans taken. This is a very valuable technique in reduction of clutter in signals as it allows for a known environment to be removed from the signal and considerably reduces potential clutter. This does not come without a potential drawback though which is that if the background/environment within which the system is placed were to change in some manner, for example a piece of furniture were to be moved, the background subtraction would become invalid and could present spurious signals to the operator. In the event that something such as this were to occur a new background scan would need to be taken therefore operators of the system would need to be trained in order to do this. To avoid this situation the system should be placed in a controlled or known environment in order to function optimally.

3.3.5. Windowing of the signal

In many cases it is important to know the range at which the initial return from a radar target occurs and ends. If this is known then it is possible to screen out all clutter that occurs outside the area of interest within the signal. This is done with a time-gating filter in the time domain. Time domain signals are signals which vary over a period of time, in the case of the measurements taken here, these signals are time vs amplitude. An example time domain signal with additive Gaussian noise is shown in Figure 29:

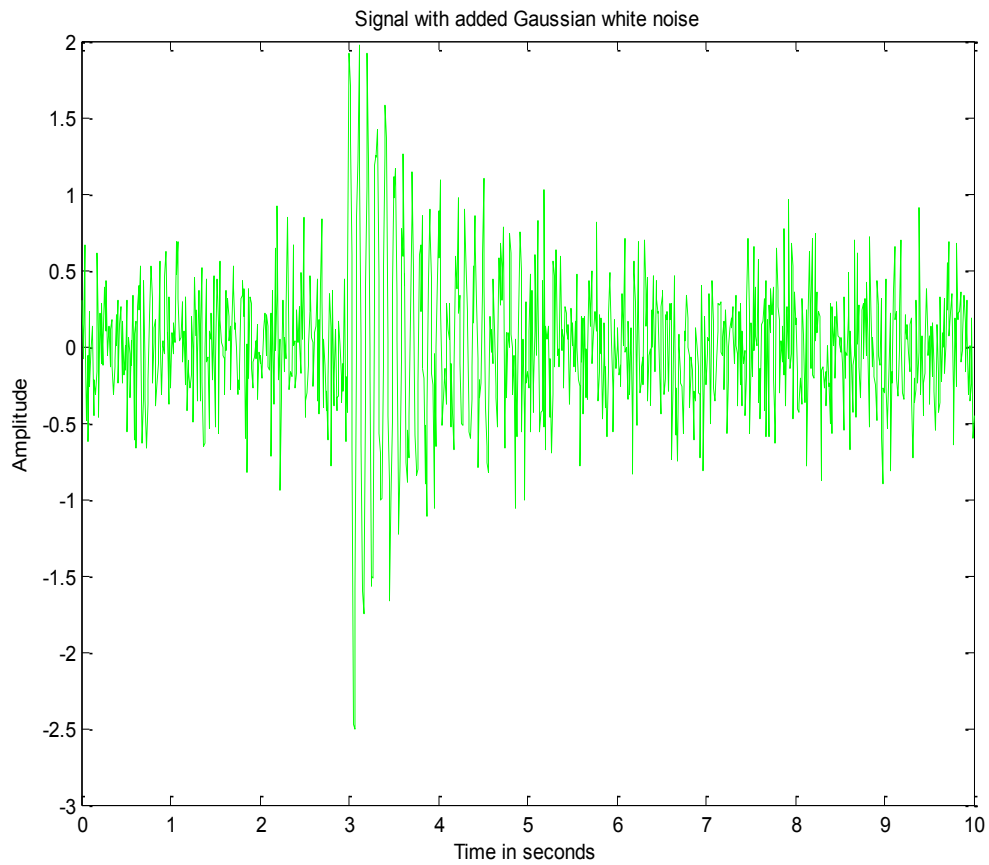


Figure 29: Time domain 10 Hz signal with additive Gaussian noise

Figure 29 shows that although it is possible to locate the start of the useful part of the signal with peak finding or by inspection, locating the end of the signal presents a significantly greater challenge. Time-gating the signal is a solution for this as by locating the initial peak of the useful component of the signal, then estimating how long the signal will last large segments of the clutter are removed. This is presented in Figure 30:

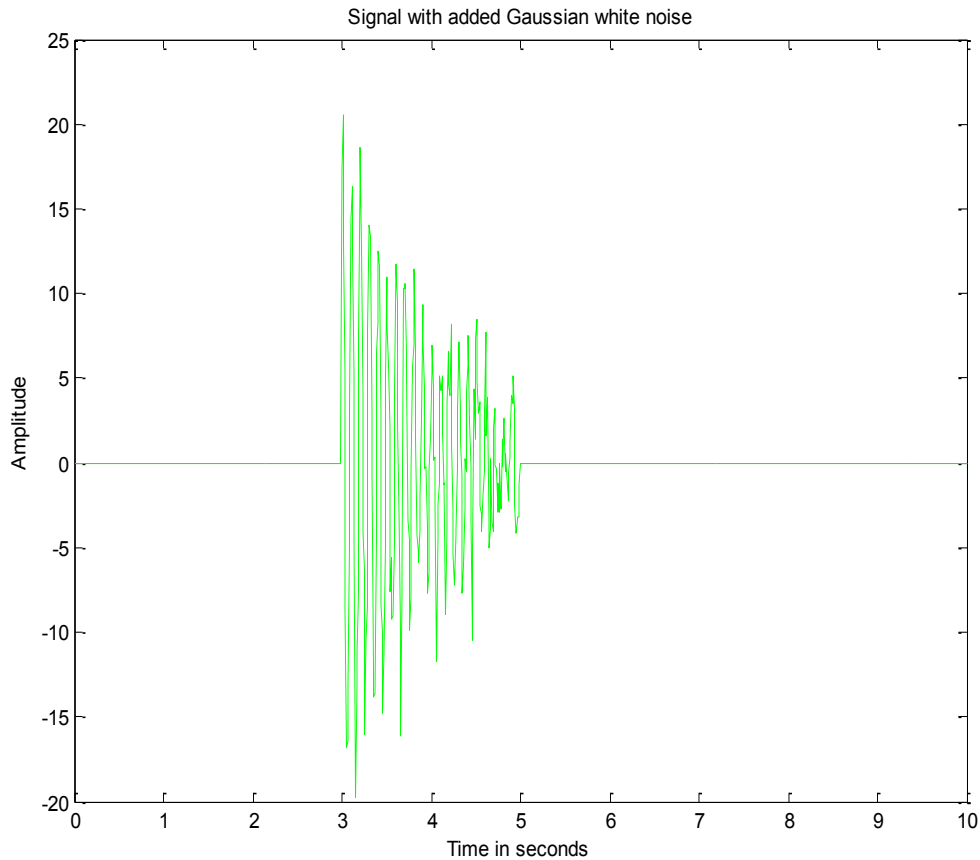


Figure 30: 10 Hz noisy signal with Time-gating applied

Figure 30 shows that this is a very effective method for eliminating clutter outside of the range of interest. When coupled with the Savitsky-Golay filter for the removal of high frequency noise within the range of interest this filtering regime is very effective and allows for the GPOF method to function effectively, as without knowing a priori the useful part of the signal the GPOF method will not function.

3.3.5.1. Locating the start of LTR

Locating the start of the LTR signal is of great importance in particular for the GPOF method as mentioned previously. Two methods have been applied to attempt to successfully locate the start of the LTR signal. The first of these methods is to use peak finding after the signal has been deconvolved. This involves searching through the time

domain signal after it has been deconvolved to locate the peak with the greatest magnitude within a specified region of the signal defined by a minimum and maximum range. This should be the ETR of the target object that is being scanned for. Once this short lived signal has been located, a small time delay is added and the LTR is measured from that point. This is an effective approach, although it does suffer from the downsides that if the estimated time delay after the LTR is set to too great a length, some of the LTR may be missed as well.

The second approach is to use the spectral norm of the impulse response data matrix, also known as the Hankel matrix to locate the start of the LTR signal [142]. The method presented requires the use of the Matrix Pencil Method (MPM) [143] in order to function. This method was compared directly to the previous peak finding method with a delay and found to have minimal benefit for the extra computational time required. Using the example of the 6.5 cm needle, at a range of 1 metre the peak finding method calculated a start for the LTR to occur at 506 points into the signal which is 13.29 ns after commencement of the scan. The Hankel method calculated that the LTR started earlier, 457 points into the signal which corresponds to a time of 12 ns after the commencement of the signal. Although this difference in time equates to more than a nanosecond, or a distance of 33.19 cm travelled by the propagating wave the resulting extracted frequencies are very similar, although the decay times are different due to the different windows used to measure the energy in the signal. See Figure 31 for the plots of the extracted poles from the two methods.

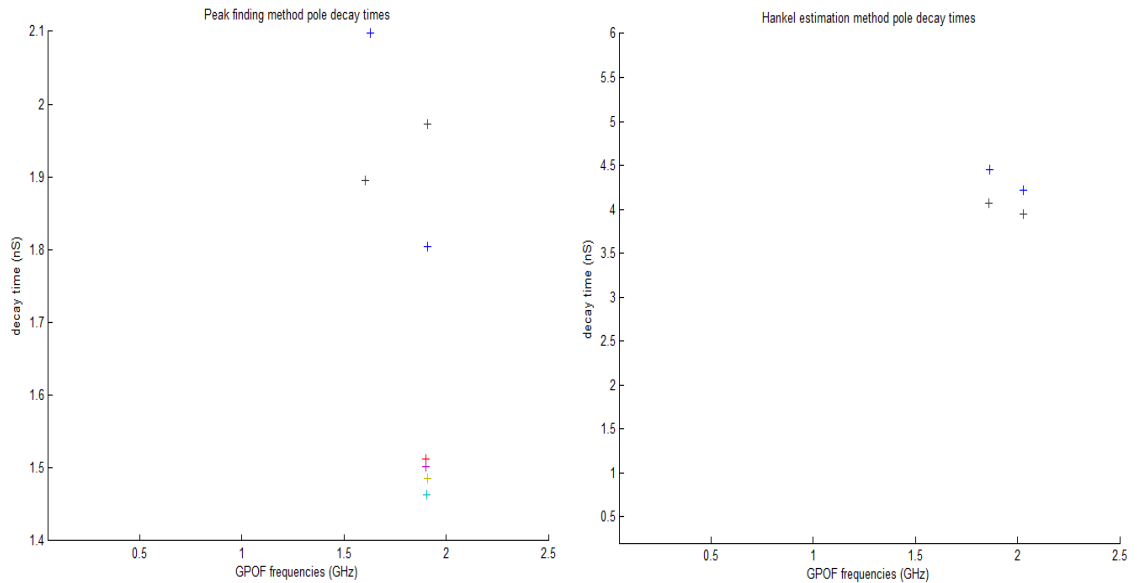


Figure 31: Results of GPOF analysis on the 6.5 cm needle using the two presented methods for locating the star of the LTR with the 1-18G Hz horns. Decay time against frequency is on the left and amplitude against frequency on the right

For the expected decay times the original extracted waveform which when plotted against time, will indicate the more accurate of the two plots. Figure 32 represents this data.

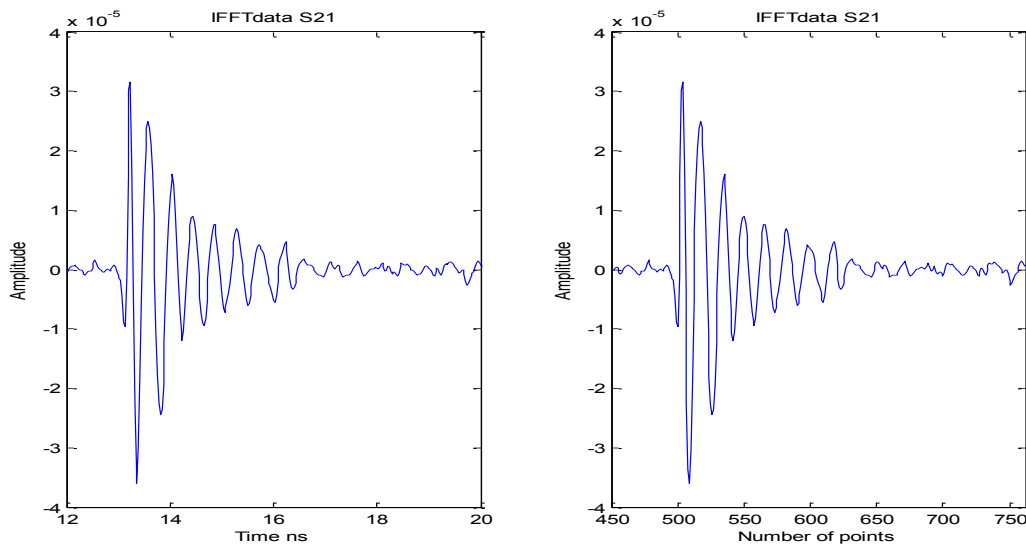


Figure 32: Waveform of the grabbed data for the 6.5 cm needle against both time and number of points axis

Figure 32 above represents the needle waveform plotted against both a time and points axis, it can be observed that the damped sinusoidal signal lasts for a total of 98 points which is approximately 2.5 nS. This shows that the peak finding method has slightly

underestimated the decay time, approximately by 16% while the Hankel method has considerably overestimated this by approximately 68%. This shows that both of the methods are not without flaws, although in balance the peak finding method can be considered to be the more accurate of the two.

3.3.6. Supervised artificial neural networks

There are two main types of Artificial Neural Network (ANN) that have been used in this work. These are supervised and unsupervised networks. Unsupervised learning based neural networks, in this case the SOM attempts to organize an input dataset into a map where nearby locations on the map represent inputs with similar characteristics. This is useful for both data vectorization and feature identification in large, unlabeled datasets. The supervised ANN, in this case the feedforward, backpropagation neural network works differently, as it is given a labeled training set informing it what should be considered a target and what should not. This network then attempts to extrapolate this learned data onto new datasets presented to it. The result of the use of both of these methods is a significant reduction in data size while maintaining the characteristic features of the dataset which can then be classified as per the training set. The three training functions analysed for this application are:

The first method attempted was the Levenberg-Marquardt. This algorithm is capable of learning to classify the data provided but training is very slow compared to the other methods used and it does become trapped by local minima. Due to this slow training speed an alternative was required.

The second method attempted was the variable learning rate approach. This is where an adaptive learning rate is applied to the training method by calculating new weights at biases at each new epoch. This allows for an increase in the learning rate but is limited by the stability of the algorithm. If the learning rate is increased too much it can cause the algorithm to oscillate and lead to a neural network that will not train correctly.

The third method the conjugate gradient descent training algorithms come in four different types. These are the Fletcher-Reeves update, Polak-Ribiere update, scaled

conjugate gradient and Powell-Beale restarts. All of the algorithms follow the same steps for the start of the process which is [144]:

- Search in the steepest descent direction on the first iteration.

$$P_0 = -g_0 \quad \text{Equation 47}$$

- Perform a line search to determine the optimal distance to move along the current search direction:

$$x_{k+1} = x_k + \alpha_k P_k \quad \text{Equation 48}$$

- Determined the next search direction that is conjugate to previous search directions.

$$P_k = -g_k + \beta_k P_{k-1} \quad \text{Equation 49}$$

This is the point at which the algorithms begin to differ defined by the method in which β_k is calculated. In particular for the Powell-Beale reset version the value is calculated using:

$$\beta_k = \frac{\Delta g_{k-1}^T g_k}{g_{k-1}^T g_k} \quad \text{Equation 50}$$

This is the same method by which the Polak-Ribiere algorithm is calculated, the benefit in the Powell-Beale restart algorithm comes with how it resets. Like all conjugate gradient methods the search direction is periodically reset to the negative direction the difference with the Powell-Beale algorithm being that it will reset the weight values when a predetermined gradient value is reached. This is what allows it to avoid becoming trapped by a local minima.

Discussion

Successful deconvolution of the horizontally polarised S21 data is critical in order to allow the LTR method to function. The linear deconvolution approach of measuring the antenna response and bitwise dividing this from the signal is an effective technique with some limitations. These limitations come from imperfect measurement of the antenna response and the potential for certain points within the signal to approach zero. One of these can be overcome by using an adaptive offset in the transmission signal calculated as a percentage of the magnitude of the transmission signal to prevent the signal from

approaching zero. The imperfect measured antenna response presents a greater challenge. Optimised experimental setup would be the ideal solution, though as this is not always possible non-linear deconvolution can be used to deconstruct and rebuild the signal while preserving the features that the LTR technique relies on. 1D CLEAN algorithms have shown that it is possible to do this, though determining the required threshold a priori presents a significant challenge and impediment to any operational LTR security system.

The clutter reduction and filtering techniques presented are used to condition the signal to allow for further processing of the LTR data after deconvolution. Clutter reduction using background subtraction, the wavelet and SG filters is of critical importance as any spurious signal located within the return could mask a significant component of the LTR contribution. These methods do not come without drawbacks such as the SG filters need for an accurately sized window over which to process the signal, though properly used the benefits outweigh the downsides. Time-gating is also a very valuable technique, though the need to calculate the start of the LTR without knowledge of the target beforehand can pose a challenge. Both of the two techniques for locating the start of the LTR presented have shown themselves to be valid in detecting the LTR and its frequencies, though due to its lesser computational complexity and slightly better accuracy in determining the signal decay times the post deconvolution peak finding method was selected as the appropriate method to apply.

Chapter 4

Frequency Analysis techniques

Preview.

This chapter will discuss Fourier transform based techniques for LTR analysis. First the Fourier transform itself will be presented, followed by the application of the Generalized Pencil-Of-Function for signal decomposition and feature extraction. In order to perform classification on this decomposed data, Principal Component Analysis is necessary and so will be discussed.

4.1. Signal decomposition

4.1.1. Fourier

An inverse Fourier transform is used to convert frequency based data to time based data and vice versa. The Discrete Fourier Transform is commonly used for data sampled at discrete times or frequencies. The formula for the DFT is [145] [146]:

$$f_n = \sum_{k=0}^{N-1} F_k e^{\frac{-2\pi jkn}{N}}, k = 0, 1, \dots, N - 1 \quad \text{Equation 51}$$

Where F_n is the transformed output signal required, F_k is the input signal to be transformed

While the formula for the inverse DFT is [145] [146]:

$$F_k = \frac{1}{N} \sum_{n=0}^{N-1} f_n e^{\frac{2\pi jkn}{N}}, n = 0, 1, \dots, N - 1 \quad \text{Equation 52}$$

Where F_k is the transformed output signal required and f_n is the input signal to be transformed.

The Fast Fourier Transform is an algorithm that is commonly used to accurately compute the DFT and its inverse. The FFT performs this task more rapidly, as its name implies by factorizing the DFT matrix into a product of sparse factors, thereby decreasing the complexity of the required method for solution. The FFT is given by [147]:

$$X(k) = \sum_{j=1}^N x(j) \omega_N^{(j-1)(k-1)}, j = 1, 2, \dots, \quad \text{Equation 53}$$

Where $X(k)$ is the required output signal, $x(j)$ is the input signal to be transformed and $\omega_N = e^{\frac{(-2\pi i)}{N}}$.

The Inverse Fast Fourier Transform (IFFT), used in this work to convert frequency domain S parameters taken by the VNA to time domain signals is derived from the FFT and given by [147]:

$$x(j) = \frac{1}{N} \sum_{k=1}^N X(k) \omega_N^{-(j-1)(k-1)}, k = 1, 2, \dots, \quad \text{Equation 54}$$

Where $X(j)$ is the required output signal, $x(k)$ is input signal to be transformed and $\omega_N = e^{\frac{(-2\pi i)}{N}}$.

The Fourier transform and its cousins are critical to the ability to use the GPOF method on a set of data taken by a VNA. This is because the VNA records S parameters, which are strictly frequency domain measurements. In order to be able to process the data through the GPOF method the information must be in the time domain, therefore the IFFT's ability to rapidly convert a data set from the frequency to the time domain is useful. Below is an example of the Fourier transforms capabilities. The signal below contains three components at 1500, 3000 and 4500 Hz with amplitudes of 0.4, 1 and 0.6 respectively. These signals have been corrupted by additive noise as shown in Figure 33.

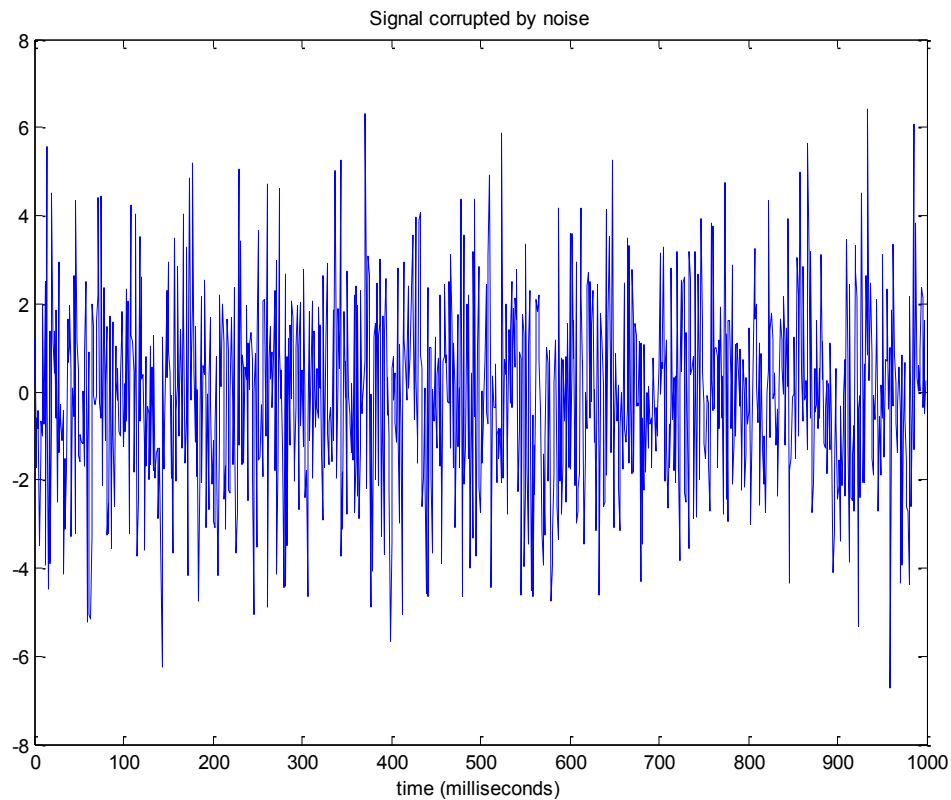


Figure 33: Signal containing 3 components at 2000, 3000 and 4500 Hz corrupted by noise

It is apparent that when the signals have been corrupted by noise it is very difficult to discern the individual components in the time domain. Although the three frequency components are still present in the signal they have become hopelessly lost in the additive noise. Once again without further processing of the signal, it would be virtually impossible to retrieve any useful data from the waveform. Conversion to the frequency domain via the Fourier transform presents the same data but with the components visible in the signal as shown in Figure 34.

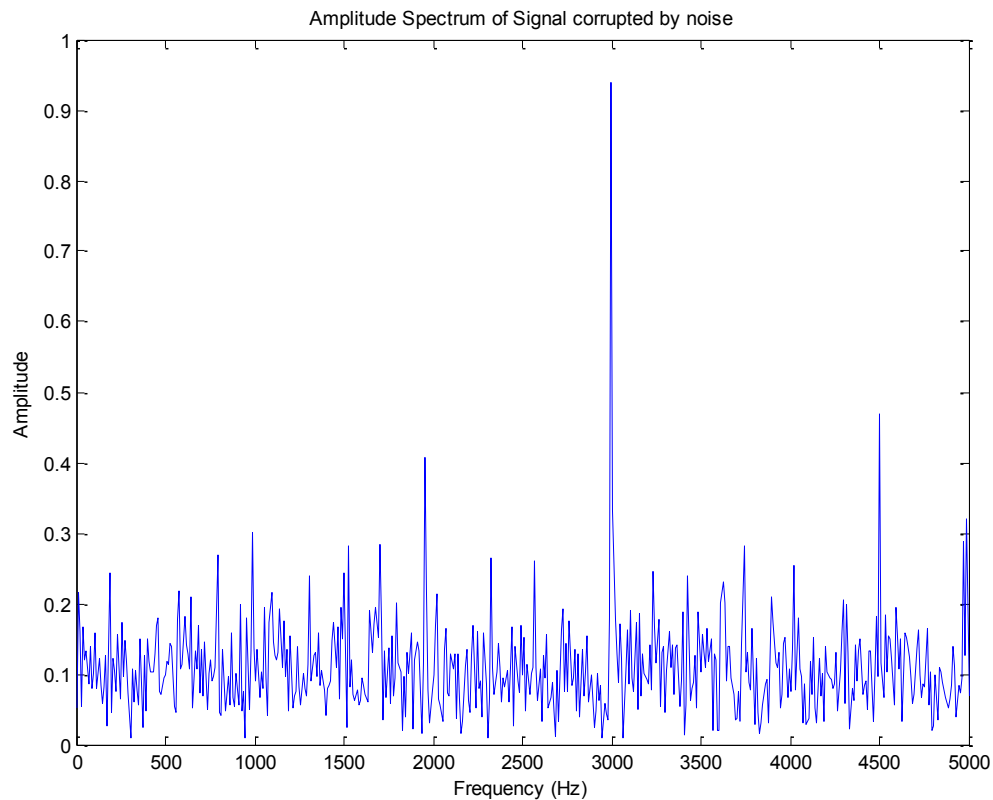


Figure 34: Fourier domain representation of the signal corrupted by noise

The three major peaks present at the correct frequencies show the ability of the Fourier transform to extract frequency data from the signal. Unfortunately due to the inherent assumption that all waves will continue on to infinity, small signals such as the damped sinusoidal waveforms that make up an LTR signal can be missed. More advanced techniques such as the Windowed STFT, GPOF, Continuous wavelet and Empirical Mode Decomposition must be considered for these types of signals [145] [76] [63].

4.1.2. Complex natural resonances and the late time response

The transient late time response of a conducting object that has been illuminated by a wideband radar signal contains aspect independent poles that depend on the object geometry and its surroundings [148] [103]. The singularity expansion method can be used

to show that the LTR can be expressed as a sum of damped sinusoids [83]. The time domain data can then be represented by [87],

$$S[n] = \frac{1}{2} \sum_{m=1}^M (C_m \exp(Z_m n \Delta t) + C_m^* \exp(Z_m^* n \Delta t)) + N[n] \quad \text{Equation 55}$$

when the signal is sampled at discrete intervals Δt using a VNA to measure the returned scattered electromagnetic field. In Equation 55, M represents the model order and is the number of poles present in the signal, N is the noise corrupting the signal, C_m is the complex amplitudes of the signal and $Z_m = -\alpha_m + j2\pi v_m$ where α_m is the damping factor and v_m is the frequency of the aspect independent poles.

Through practical experimentation it has been determined that only the first few CNR's have sufficient amplitude to be observable. This coupled with the tendency of the higher order resonances to decay more rapidly means that to approximate the LTR signal, only the lower order modes make a significant contribution to the signal and need be taken into account.

The noise N comprises contributions to the LTR from a number of sources not involving the re-radiation from the induced surface currents on the target. These noise sources such as electronic background clutter, can have a severe effect on the GPOF methods accuracy when extracting the signal poles [95].

The complex amplitudes of the signal are dependent on the orientation of the illuminating pulse but the re-radiated frequencies and their inverse lifetimes are independent of aspect and the illuminating waveform. The usefulness of the aspect independence of the poles has been displayed in the widespread use of this method with airborne radar to identify airborne targets such as aircraft or missiles [86].

For the purposes of this work the FFT has been used to convert the frequency data to time domain and then the CWT has been taken. The GPOF method has been chosen to extract the poles of the time domain signal. This mathematical algorithm for extracting the complex poles for an object with unknown model order is an area of interest within electromagnetic problems [95] [149].

4.1.3. Model order

The model order is of critical importance when performing LTR processing using the GPOF method. This is because if the model order is over estimated then the GPOF method will produce extra poles that do not correspond to the target in question while if the model order is underestimated then useful information for classification may be missed.

The ability to determine the model order of a non-cooperative target presents quite a challenge. In this work the method used to overcome this lack of a priori knowledge is to test the target using a model order far greater than would normally be found, in this case 10. An iterative approach is used with a reconstruction of the signal being performed at each model order up to 10 and the standard error between this and the signal is calculated. The point at which the standard error reaches its minimum and stabilises is then selected as the model order and the algorithm is rerun using this assumed model order.

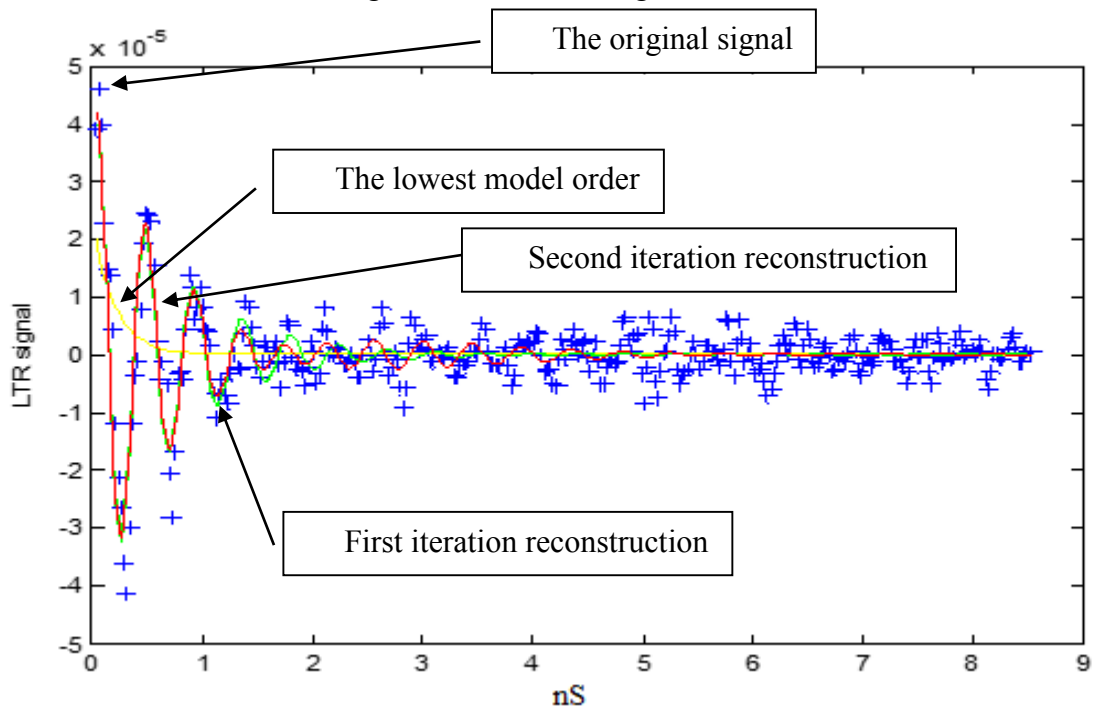


Figure 35: Plot of 6.5 cm waveform with reconstructions at different model orders

Figure 35 shows the initial plot of the extracted LTR with blue crosses. The yellow line represents the lowest model order comprising one pole with zero frequency, the green line

represents the reconstructed signal from the first iteration of poles while the red line represents the reconstruction from the second iteration.

4.1.4. Principal Component Analysis

Principal Component Analysis (PCA) was first introduced by Karl Pearson in 1901 [150] and further developed by Harold Hotelling in 1933 [151], who is also responsible for naming the technique. PCA is a technique that as stated in the name, finds the principal components of a given dataset. It goes by a number of names in different fields of study such as the Karhunen-Loeve transform in signal processing and many others. The method uses an orthogonal transformation to convert a set of potentially correlated data variables into a set of linearly uncorrelated data variables. These principal components are the points which best explain the variance in the data and represent the underlying structure of that data. The value of PCA lies in its ability to be used as a dimensionality reduction technique in order to take a highly dimensional dataset and transform it into a smaller dimensional space. This is very often done in preparation to running machine learning algorithms on data such as clustering techniques and ANN. The benefits of using PCA are:

1. Data reduction. PCA allows for the removal of data that does not meet a predetermined threshold for the value of its contribution to the dataset. This leads to a reduction in computational intensity ensuring that algorithms will run more efficiently, reducing the need for computer time.
2. Data ordering. PCA orders the data by its contribution to the dataset allowing for the most significant principal components to be easily identified.
3. Simplification of the dataset. Very complex datasets may overwhelm the capabilities of machine learning when attempting to process data. PCA improves the likelihood that the data will be processed correctly thereby reducing the probability of over or under classification.

Conversely it must be noted that PCA does suffer from some weaknesses. These include:

1. PCA looks for linear combinations of the original features. If the dataset is non-linear then the eigenvectors used may not describe the features as accurately as a non-linear approach could.
2. PCA is a purely descriptive technique therefore it is not capable of predicting what future datasets may look like
3. PCA gives uncorrelated components which are not necessarily independent components.

PCA works by transforming the data presented to it into a new coordinate system where the first axis will correspond to the first principal component representing the data with the largest variance, the second axis will correspond to the second principal component representing the data with the second largest variance and so on. Each successive principal component is constrained by the rule that it must be orthogonal (uncorrelated) with the component that came before it.

4.1.4.1. Eigenvalue decomposition

An eigenvalue decomposition performed on the covariance matrix of the data can be used to mathematically calculate the principal components of a dataset. As covariance is defined as the measure of how much two variables change with relation to each other, a covariance matrix is a matrix whose element at the M, P position is the covariance between the Mth and Pth elements of the vector thereby measuring how the two matrices change with relation to each other.

A covariance matrix can be calculated using Equation 56:

$$Covariance(M, N) = \sum_{i=1}^N \frac{(M_i - \bar{M})(P_i - \bar{P})}{(N - 1)} \quad \text{Equation 56}$$

Where N represents the number of scores in each dataset, \bar{M} is the mean of the N scores in the second dataset, M_i is the ith score in the set, \bar{P} is the mean of the N scores in the first dataset and P_i is the ith score in this set.

In matrix form for a 3 dimensional dataset using M, P and R to represent the dimensions a covariance matrix would appear as follows in Equation 57

$$C = \begin{pmatrix} cov(M, M) & cov(M, P) & cov(M, R) \\ cov(P, M) & cov(P, P) & cov(P, R) \\ cov(R, M) & cov(R, P) & cov(R, R) \end{pmatrix} \quad \text{Equation 57}$$

It is necessary to define eigenvectors and an eigenvalues. An eigenvector is a characteristic vector of a square matrix, in this case 'K' and is represented by Equation 58:

$$(Ku = \lambda u) \rightarrow (K - \lambda I)u = 0 \quad \text{Equation 58}$$

Where u is the eigenvector of matrix K and λ is the associated eigenvalue. For example for the matrix K:

$$K = \begin{pmatrix} 5 & 7 \\ 5 & 3 \end{pmatrix} \quad \text{Equation 59}$$

The normalized eigenvectors are:

$$eigenvectors = \begin{pmatrix} 0.8137 & -0.7071 \\ 0.5812 & 0.7071 \end{pmatrix} \quad \text{Equation 60}$$

The corresponding eigenvalues are:

$$eigenvalues = \begin{matrix} \lambda_1 = 10 \\ \lambda_2 = -2 \end{matrix} \quad \text{Equation 61}$$

The eigenvectors can then be stored in matrix U in which the columns of U represent the individual eigenvectors and the eigenvalues are placed in diagonal matrix Λ where the diagonal elements of the matrix are the Eigenvalues and the rest of the elements are zero.

A summary of the PCA algorithm is as follows [152]:

1. Take the whole dataset containing S dimensional samples.
2. Calculate the mean for all dimensions in the dataset.
3. Calculate the covariance matrix of the entire dataset.
4. Calculate the Eigenvectors ($U_1, U_2, U_3, \dots, U_n$) and the Eigenvalues ($\lambda_1, \lambda_2, \lambda_3, \dots, \lambda_n$ corresponding to these vectors).
5. Sort the Eigenvectors by Eigenvalue. This should be done in order of decreasing magnitude of the Eigenvalue. Select the number of components required and take this number of the Eigenvectors starting with those with the largest eigenvalue. This is used to build the $S \times T$ matrix, R where each column of the matrix represents one Eigenvector.
6. Transform the processed data onto a new subspace using Equation 62

$$PCA_{nss} = R^T \cdot X \quad \text{Equation 62}$$

Where PCA_{nss} is the transformed sample in the new subspace and X is a $S \cdot 1$ dimensional vector of a single sample.

4.1.5. GPOF Results and Classification

A total of eight targets have been used in these experiments. These targets include both threat and non-threat items. Additionally the human body has been scanned in two postures to allow for the effect of the posture on the signal to be taken into account. The threat items used were a 6.5 cm needle, an 11 cm cylindrical steel rod with a diameter of 1.5 cm, a 13 cm kitchen knife, a replica .38 caliber revolver, a wooden handled replica air pistol and a replica .44 magnum revolver. These items should present a range of frequencies from as low as 500 MHz to almost 2 GHz as per Table 8. The non-threat items were, a Fujifilm digital camera and a key ring with car, bike and house keys. Finally the two body postures used were the body with hands behind the back and the body with the hands at the side. The GPOF plots to follow will present the return from these targets individually and on the body. The boundaries for these datasets are 0.1 – 2.5 GHz frequency and 0 to 4 nS decay time. Any data outside this range is discarded. For a target with model order of 2 a total of 6 poles will be presented. For a target of model order 4, a total of 14 poles will be present. This is due to each iteration of the model order plotting all of those that come before it as well.

Figure 36 to Figure 44 all have the same structure. There are four plots in each figure with the two left hand plots representing one target scenario and the two right hand plots representing a second target scenario. The leftmost plot of each target scenario represents pole decay times in nanoseconds on the Y-axis and frequency in GHz on the X-axis. The second plot in each scenario represents normalized pole amplitudes on the Y-axis and frequency in GHz on the X-axis.

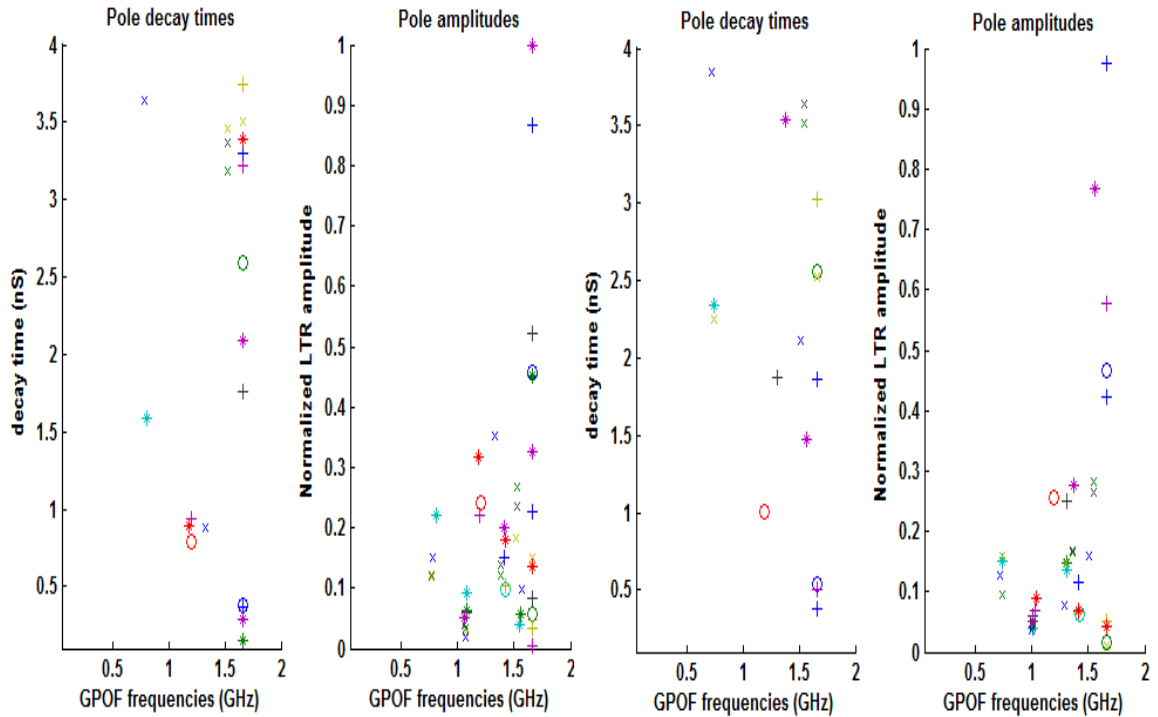


Figure 36: GPOF plots including model orders up to 4 with the body with hands at side to left and hands behind back to right

The frequencies present for the body in two different postures can be found in Figure 36 above. The body with hands at the side presents frequencies between 0.7 GHz and 1.6 GHz with the bulk of them to be found between 1.5 and 1.6 GHz. These are the dominant component in the cross polar return, while another less dominant cluster can be found around 1.2 GHz. When compared to the body with the hands behind the back it is apparent that there is a greater cross polar return when the arms and hands are in the signal due to the return from the body with hands behind the back having a less clustered return. The frequencies across which data can be found are the same though, 0.7 GHz to 1.6 GHz.

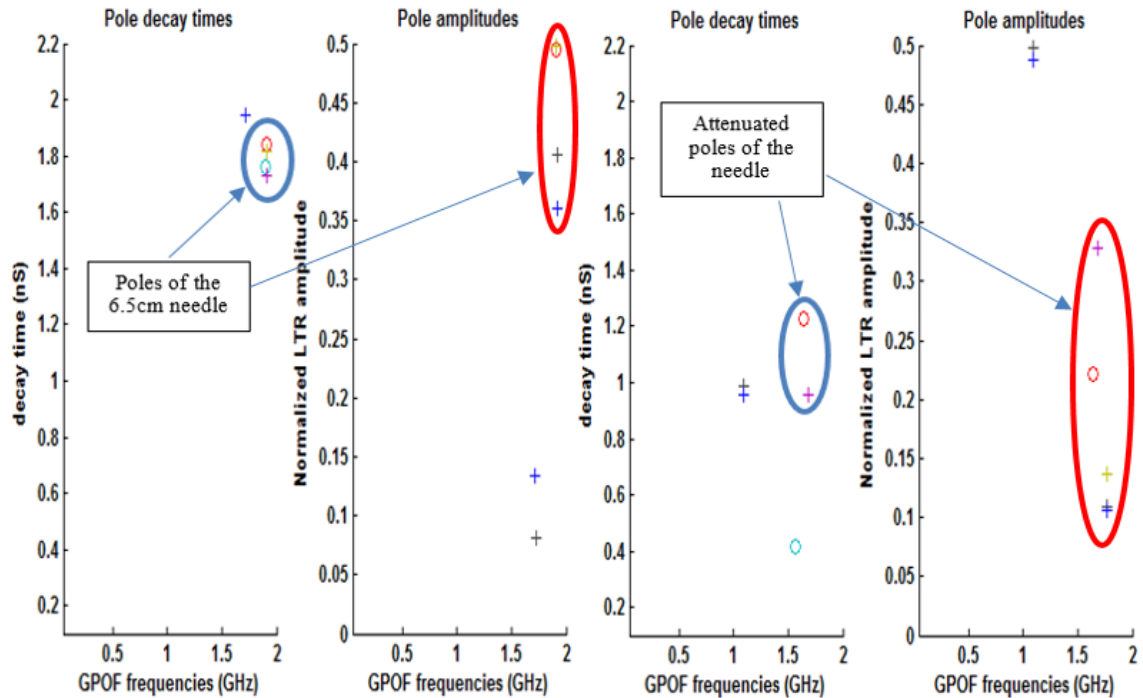


Figure 37: GPOF plots including model orders up to 2 with the 6.5 cm needle only to the left and the 6.5 cm needle on body to the right

The 6.5 cm needle presents a very interesting target to work with when performing LTR analysis. This is mainly due to its highly resonant nature which presents as a damped sinusoidal signal decaying over ~ 2 ns. When in isolation this object is very easy to detect but when another object is present its small radar cross section makes it very challenging to see. The plots of the needle in isolation shown to the left in Figure 37 present the frequencies of the needle at ~ 2 GHz while the plots to the right present the needle on the body. These frequencies are still present when the needle is placed on the body although both the amplitude of the poles at 2 GHz have been attenuated and have shifted slightly. A decrease in the decay time is also seen though this can be potentially be attributed to the very small window used to detect the needle as well as interference from the body.

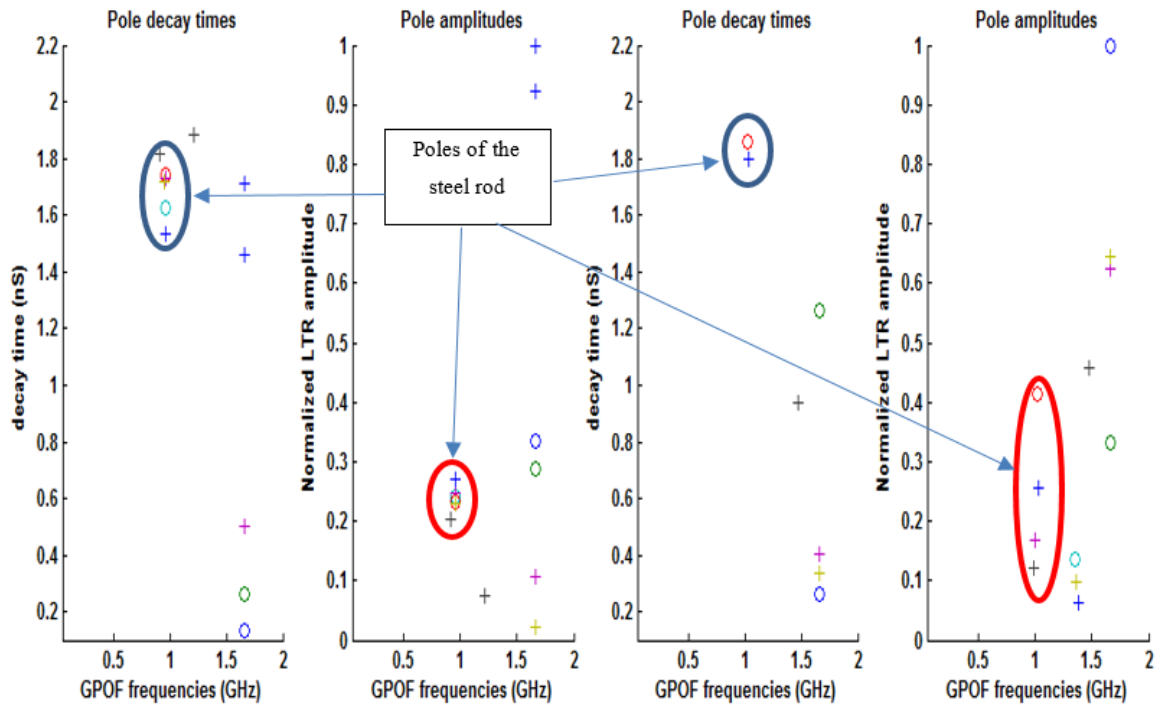


Figure 38: GPOF plots including model orders up to 4 with the steel rod only to left and the steel rod on body to right

The steel rod is another of the simple objects used to test the LTR system although unlike the needle in the case of most security environments a steel rod could be considered to be a threat. The useful poles for this target can be found around a frequency of 1 GHz as shown by the plot of the target in isolation in Figure 38. This can also be seen in the plot of the steel rod present on the body, though it must be noted that several of the poles located around this point can no longer be seen when the body is introduced to the scan. Of interest is the presence of poles located at ~ 1.6 GHz in both the object in isolation and the object on body. The poles with decay times below 0.5 ns at this frequency can be attributed to a portion of the body response remaining in the signal.

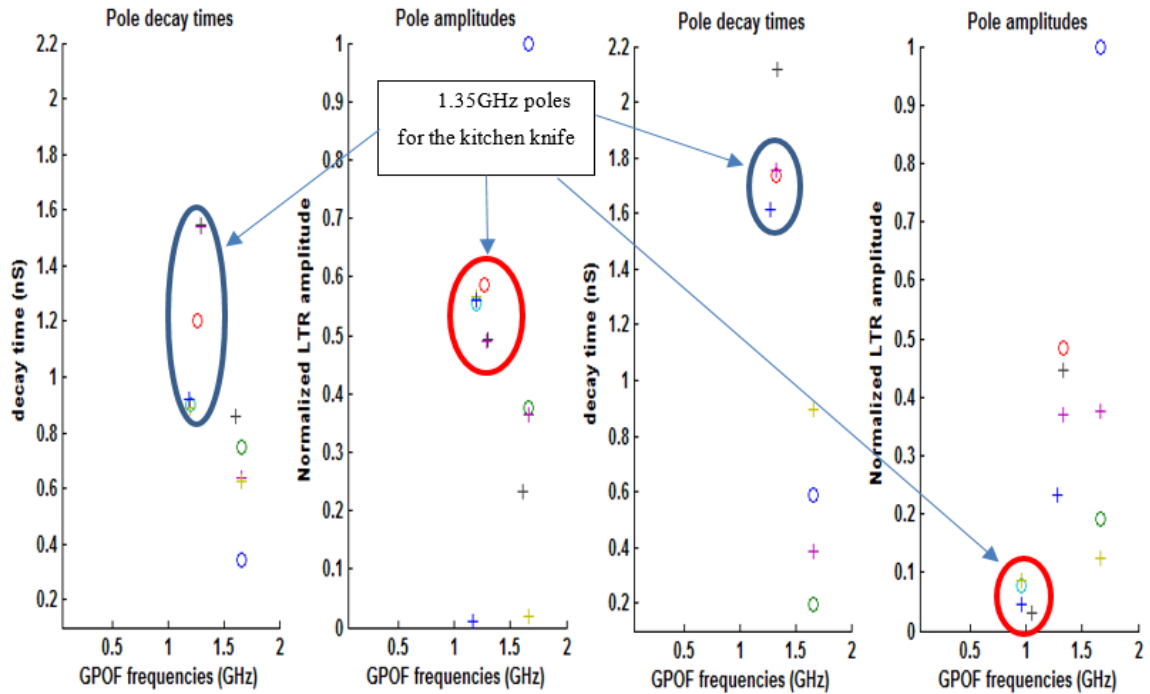


Figure 39: GPOF plots including model orders up to 4 with the kitchen knife only to left and the kitchen knife on body to right

The frequencies presented by the small kitchen knife used as a threat object can be found in Figure 39. The useful, dominant poles in the signal can be found located around 1.35 GHz. As the kitchen knife is a relatively simple object its model order is low, therefore not as many frequencies can be associated with it. When this is then applied to the presence of the target on body the same frequencies of approximately 1.35 GHz can be found. Interestingly the decay times for the target placed on the body are greater than those of the target in isolation. This could potentially be caused by a number of factors first among which is coupling of the signal to the knife. As the knife presents a large RCS when the flat of the blade is presented to the radar and a very small RCS when the edge of the blade is presented the orientation of the target is important for this target. Although LTR techniques are considered to be aspect independent in frequency, this only applies if the waveform can successfully induce a surface current on the object, therefore this part of the process is orientation dependent. A second possibility for the increased decay time is the introduction of multipath signals reflecting between the knife and the body. This would

have the effect of smearing the LTR return, making it appear to last for a greater period of time than is actually the case.

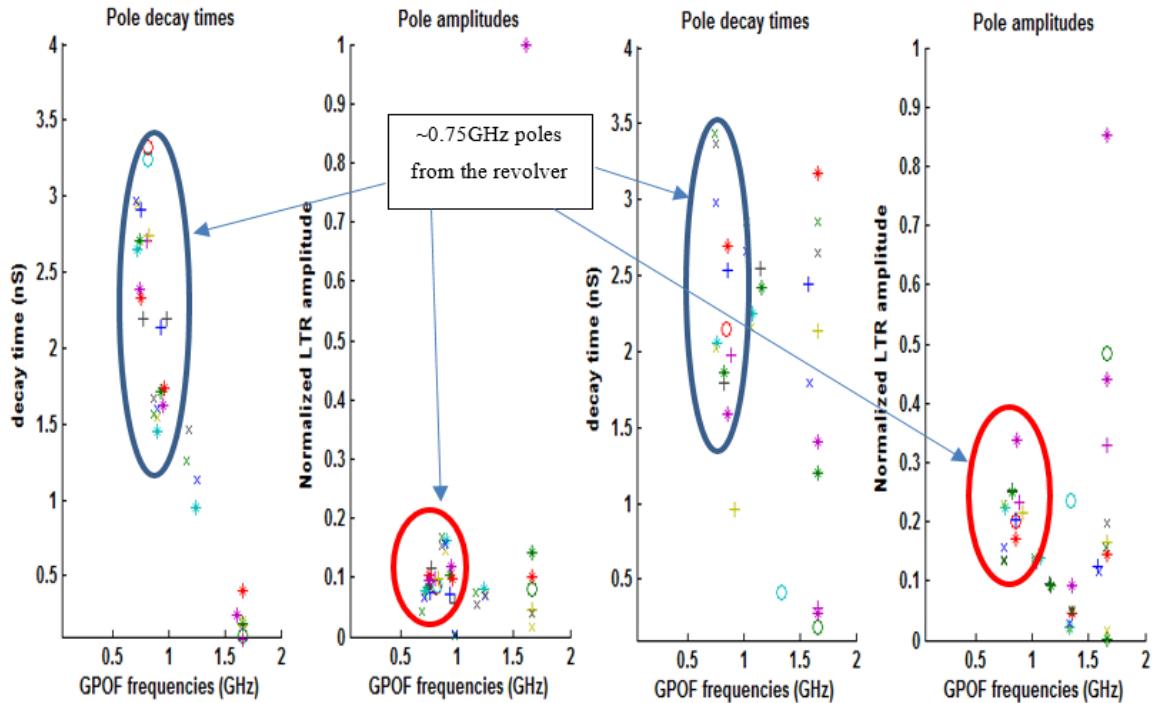


Figure 40: GPOF plots including model orders up to 4 with the replica .38 calibre revolver only to left and the replica .38 calibre revolver on body to the right

The GPOF results for the replica .38 calibre revolver can be found in Figure 40 above. Along with semi-automatic pistols, this target is one of the most significant threats that can be carried through a security environment as it is both very compact and allows for multiple shots to be fired in a short space of time. The majority of the frequencies of the target can be found at ~ 0.75 GHz. The short decay poles around 1.6 GHz are also present in this signal as previously, lending credence to these being the result of the characteristics of the system/hardware rather than the target itself. Once the body has been added into the signal as shown on the two plots to the right in Figure 40 further poles located around 1.6 GHz in frequency are present though these are much more significant due to their longer decay times.

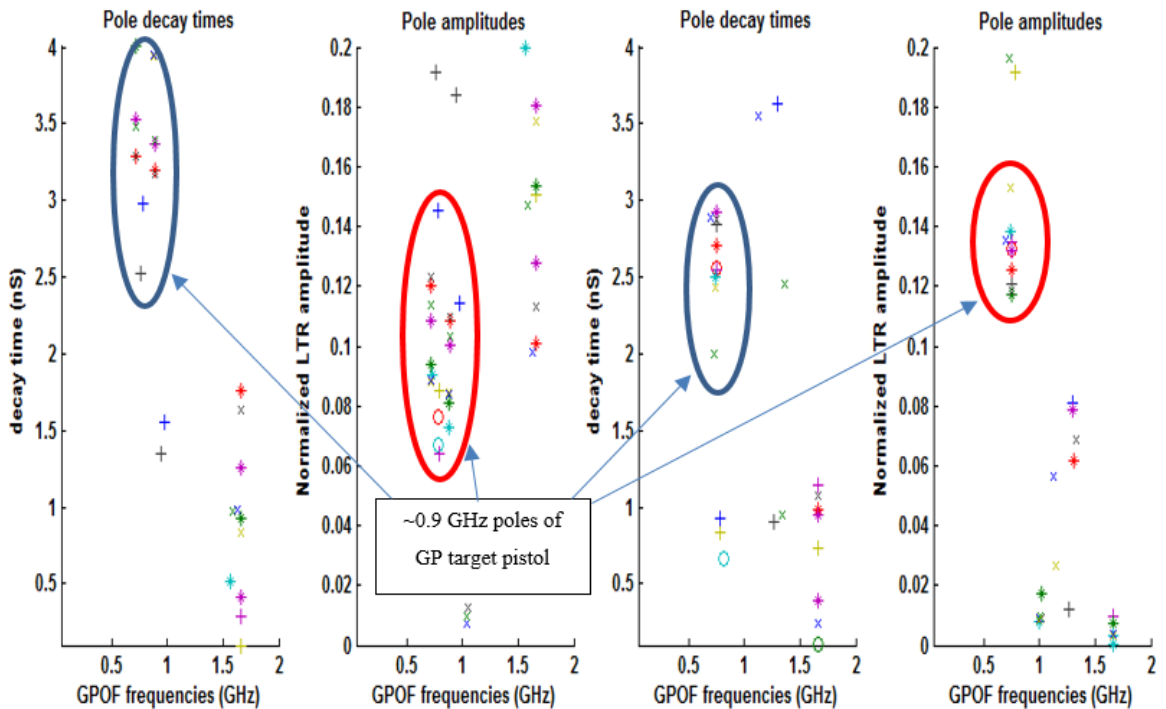


Figure 41: GPOF plots including model orders up to 4 with the gas powered target pistol only to the left and the gas powered target on body to the right

The resulting frequencies from the gas powered target pistol are presented in Figure 41. This is a larger target than the replica .38 revolver but simpler as it has less components and a wooden handle. Therefore the bulk of the resonances that will be detected emanate from the barrel which is a cylinder of the same diameter as the steel rod but slightly longer in length. This is evidenced by the presence of the dominant detected resonances located between 0.85 GHz and 0.95 GHz as opposed to those located around 1 GHz for the steel rod. Some information is located around 1.6 GHz though as there is a resonance of the horn located at this point, this information must be carefully considered before it can be used. When compared to the target on body the resonances are occurring in a similar range between 0.85GHz and 0.95 GHz. Additional data is also located around 1.3 GHz. This is most likely due to the interaction of the target with the body causing multipath signals and so these poles are of no use for classification purposes.

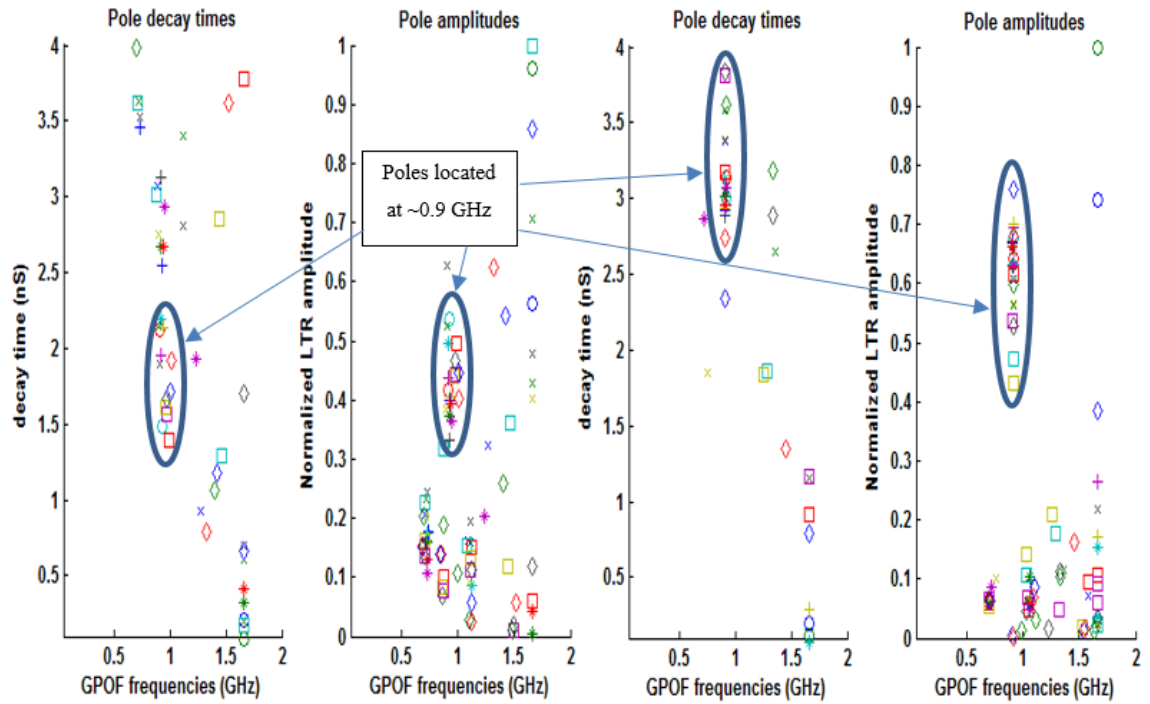


Figure 42: GPOF plots including model orders up to 6 with the replica .44 calibre revolver only to left and the replica .44 calibre revolver on body to right

The result of the largest of the threat items tested, the replica .44 calibre revolver can be found in

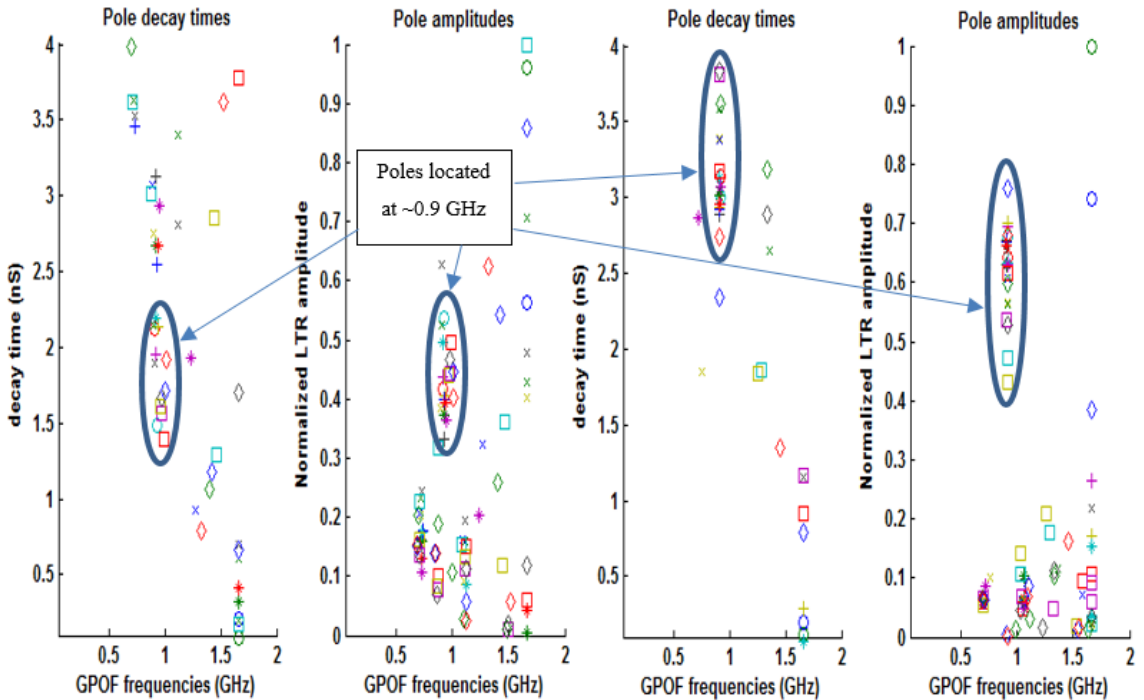


Figure 42. This revolver stands at the limit of what could be potentially concealed on a person as its size is so great. This also presents a challenge when it comes to detecting this object as its extreme length means the expected frequency that it will resonate at is very low, approaching the minimum threshold of the antennas available. The dominant poles for this target can be found at ~ 0.65 GHz with a large number of resonance found at ~ 0.9 GHz. When looking at the target located on the body the poles at ~ 0.9 GHz are still clearly present with the poles at 0.65 GHz having been attenuated and reduced in number. A number of poles are also located around 1.25 GHz for this target although they are few in number.

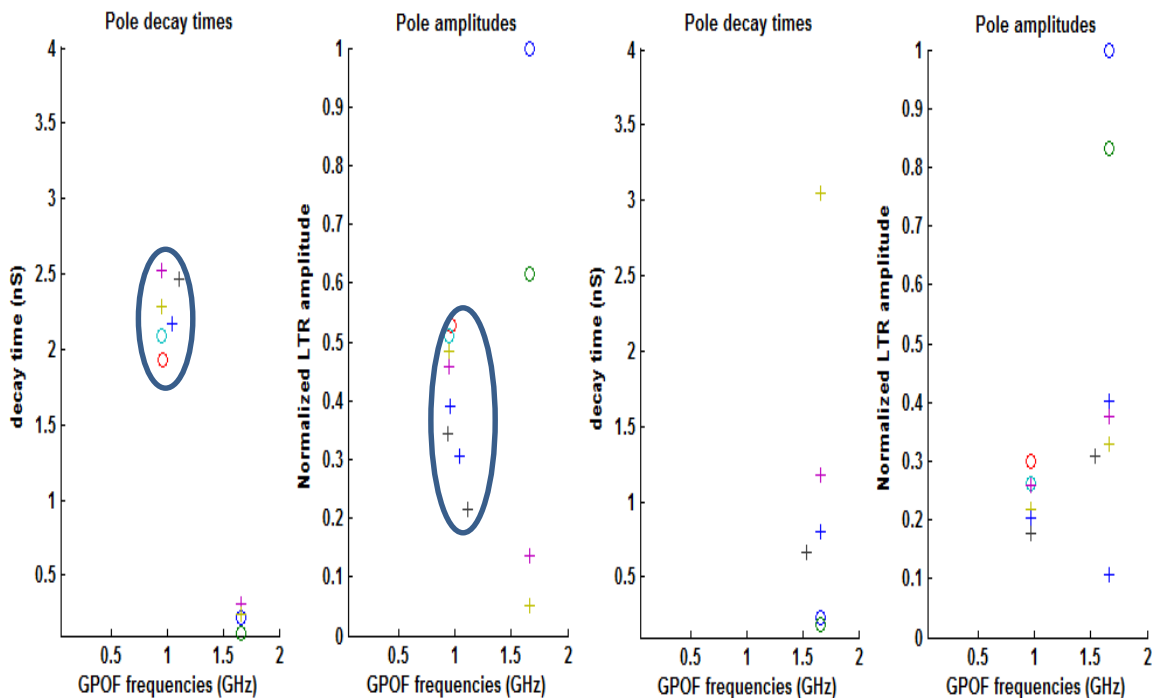


Figure 43: GPOF plots including model orders up to 2 with the camera only to the left and the camera on body to the right

The first of the non-threat items tested, a Fujifilm digital camera is presented in Figure 43. A fairly simple object with a small number of resonant frequencies located from 0.95 GHz to 1.35 GHz that can be seen when the object is in isolation. When the target is present on body only a small number of these poles are still present which can pose a problem when it comes to classification of the target.

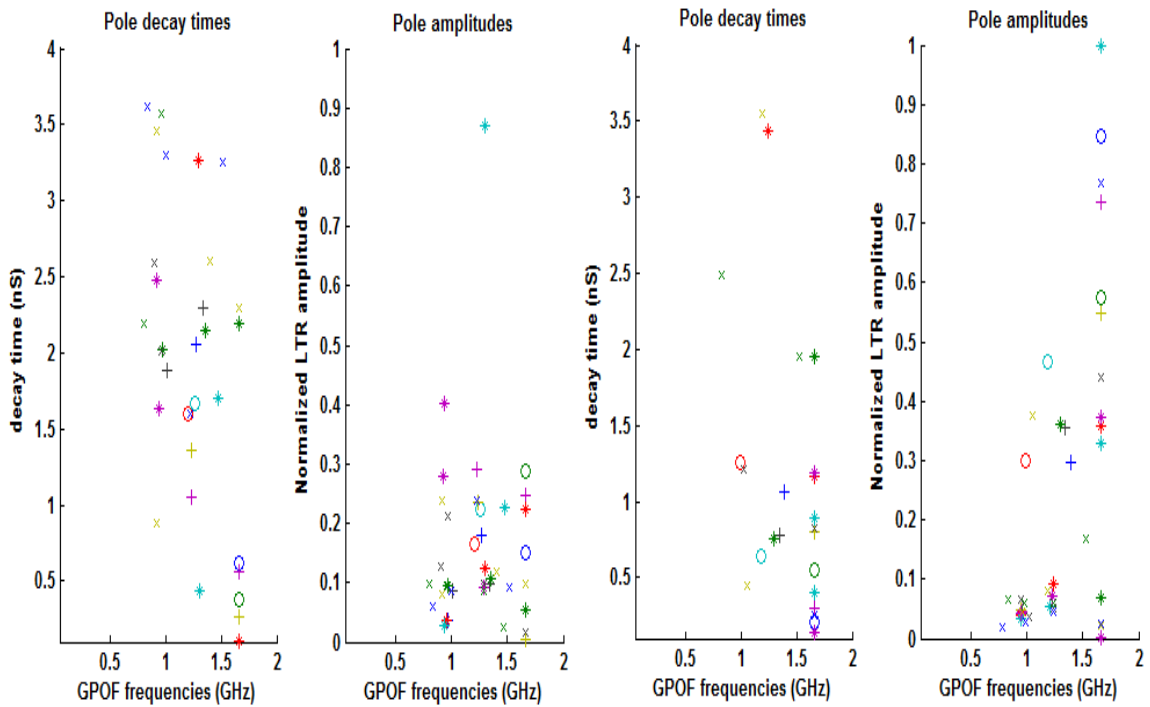


Figure 44: GPOF plots including model orders up to 4 with the keys only to the left and the keys on body to the right

The final target tested was a key ring with a number of keys on it. The results of this are presented in Figure 44. This is a more complex target to deal with as shown on the target in isolation as it may change its RCS due to the location of the keys and keyrings with relation to each other therefore there is a large spread of resonant frequencies in the signal stretching from 0.6 GHz to 1.7 GHz. This is emulated in the return from the target on body with no real clustering of the poles being present.

4.2. GPOF classification results using Artificial Neural Networks

The following section discusses the use of a trained neural network to classify the targets presented to it. The data fed into the ANN for training is the result of using GPOF based signal processing on experimental datasets comprising both threat and non-threat items.

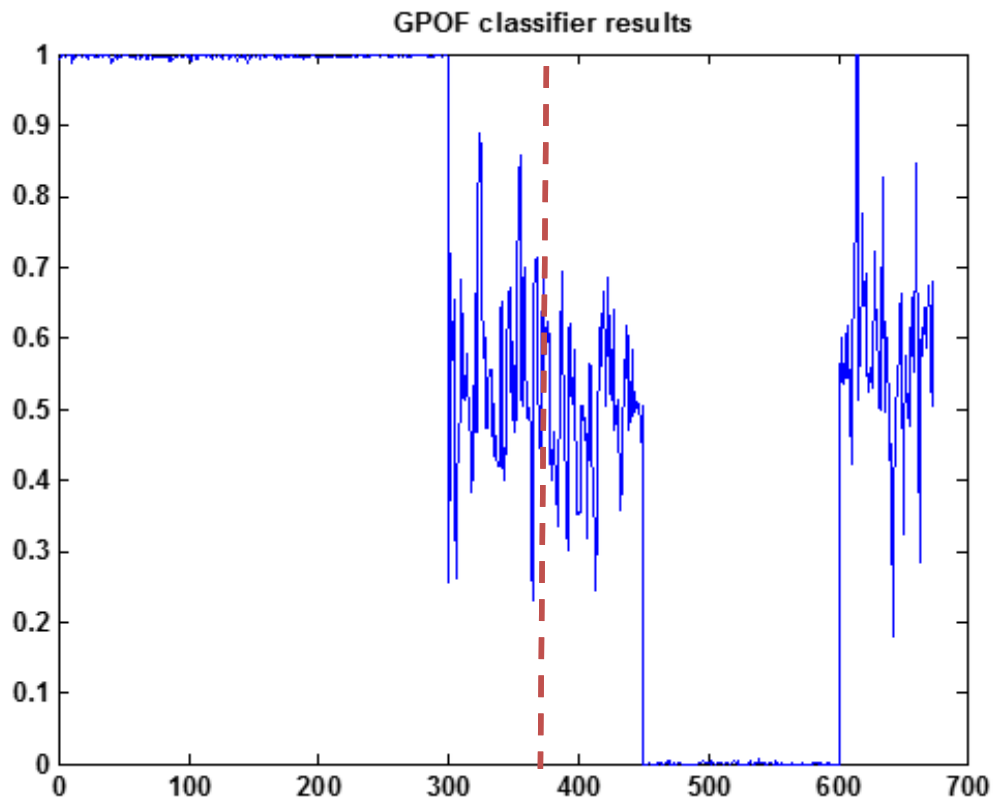


Figure 45: GPOF output data for binary threat/non-threat classifier

The plot presented in Figure 45 is the result of the network processing a target dataset. The 375 targets to the left of the dashed line are threat items and should therefore present a result of 1. The 300 targets to the right of the dashed line are non-threat items and should therefore return a zero. The Y-axis presents the result of the classification between 0 and one while the X-axis lists the number of target sets. A list of the targets used in order is presented in Table 8 although the 6.5 cm needle has not been used in this case.

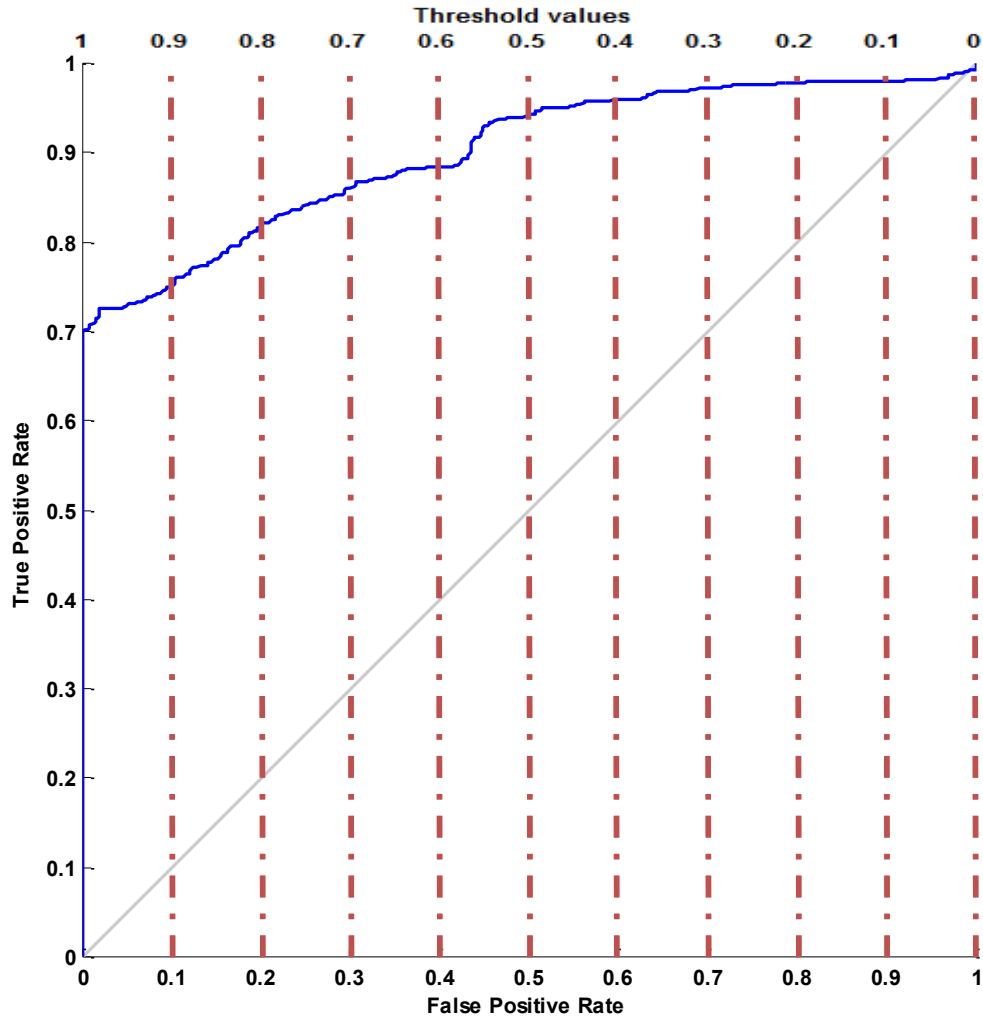


Figure 46: GPOF classification for a binary threat/non-threat classifier

Figure 46 presents the Receiver Operating Characteristic (ROC) curve for the probability of the true positive and false positive rates with the detection of concealed targets using the neural network method. In all ROC curves presented in this work the Y-axis gives the true positive rate, the X-axis gives the false positive rate and the threshold value is given by the top axis. In Figure 46 the data has been fed directly from the GPOF method into the neural network and the classification rates presented. As labelled the X axis represents the probability of a false positive while the Y axis represents the probability of a true positive. The blue line represents the actual result of testing the dataset against thresholds ranging from a value of zero on the right of the X axis to 1 on the left of the X axis. The gray line represents a 50-50 guess therefore anything approaching the top left corner of the plot can be considered to be a valid classification technique while anything

to the right of the line would indicate the algorithm is not viable for use at that threshold. The closer the blue line approaches the top left corner of the chart, the better the performance of the classifier.

The result presented in Figure 46 shows the technique of using the GPOF method to extract the poles of the data to be a valid technique for classification. Given the most challenging threshold available of one, the network is capable of providing a true positive classification rate of 70% without presenting any false positives. Keeping the false positive rate as low as possible is very valuable as false positives can degrade peoples trust in the utility of a security system and potentially in some cases could lead to severe consequences if an innocent individual was misidentified as a threat.

Although 70% is not ideal for a successful classification rate, the ability to scan a potential target multiple times in under a second as the system is capable of taking data at greater than 4 Hz, can account for the deficit. It would therefore be ideal to scan a potential target at least three times in order to minimize the possibility of the system missing a threat.

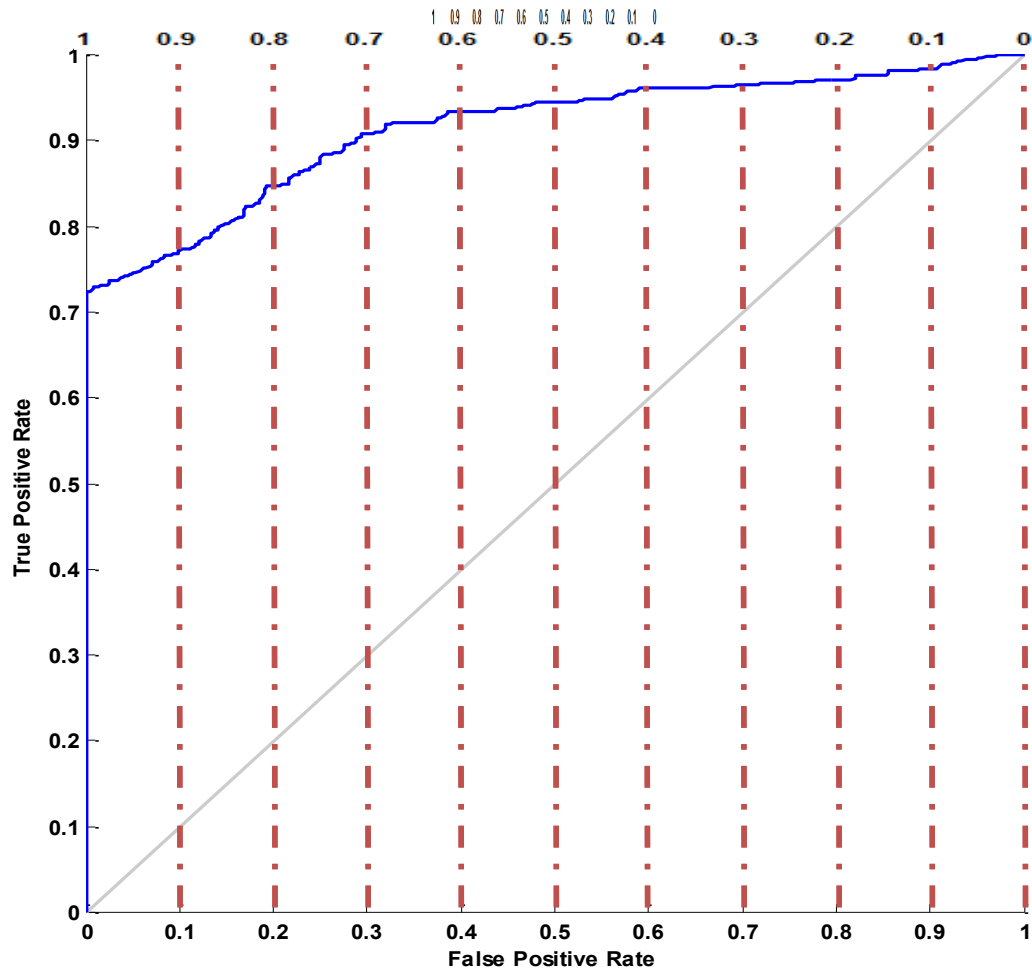


Figure 47: GPOF PCA ROC curve results for a binary threat/non-threat classifier

A small improvement on the true positive classification rate for the GPOF based algorithm has been presented in the ROC [153] curve in Figure 47. For this particular technique the optimal true positive classification rate at which the false positive rate is 0% presents as 73%. This improvement has been achieved by processing the data using PCA before running it through the trained ANN. This has allowed for data that does not significantly contribute to the dataset to be removed and then be reordered in the form of its principal components first. Another effect of using this method is additional smoothing of the curve, with the large jump located at a false positive rate of 0.45 in Figure 46 being removed from the data. This small increase in true positive classification rate is not significant enough to remove the need for the use of multiple scans of a target to improve the likelihood of detection but will help improve the overall accuracy of any system based

on the GPOF method. Table 6 presents the true positive classification rates for the individual targets when the false positive rate is zero while Table 7 represents the false positive rate for non-threat items.

Table 6: True positive rates for individual threat items analysed using the GPOF method with and without PCA

Target	True positive rate without PCA%	True positive rate with PCA%
Steel rod	37.3	42.6
Kitchen knife	56.3	65.3
Replica .38 calibre revolver	64.7	72
Gas powered Target pistol	82.6	84
Replica .44 calibre revolver	77.3	78.6

Table 7: False positive rates for individual non-threat items analysed using the GPOF method with and without PCA

Target	False positive rate without PCA%	False positive rate with PCA%
Camera	0	0
Keyring	3.9	0
Body, hands at side	1.3	1.3
Body, Hands behind back	1.3	0

4.2.1. Operating conditions and Data structure

The data extracted from the GPOF method included three columns representing the frequency, amplitude and time data for the target. This data was normalized before being

passed across to the ANN for classification. The large 0.3 – 3 GHz horn antennas were used for all results presented in chapter 4. A model order of 6 was chosen to be used for all targets as it encompassed the model orders of all targets presented and allowed for a consistently sized dataset to train the neural network with. Hidden layers of 8 neurons were used for the binary threat non-threat classifier as this provided the best result through experimentation. As with the other sections a 9 object classifier was attempted with 60 neurons in the hidden layer although in this case it was unsuccessful in classifying the data presented.

The operating conditions required to perform GPOF LTR analysis experimentally are as follows:

- The parameter to be extracted is the horizontally polarised S21 parameter.
- The number of points required is by default 1001, although this can be adjusted to meet a required unambiguous range.
- 10 scans of the target added together to form one sweep.
- The frequency sweep must cover a range of 500 MHz to 2 GHz in order to extract useful target information. A lower start frequency than this should be used if antennas are available in order to perform this.
- The total sweep time should be below 256 ms.
- The range to target should be between 1 and 3 m.
- The power level at the VNA used should be between 2 dBm and -4 dBm.
- The antennas should be directional, with a gain of 3 dB or greater.

4.3. Overview of Algorithm 1: LTR using the GPOF method

The final LTR algorithm based around the GPOF method is structured as follows in Figure 48:

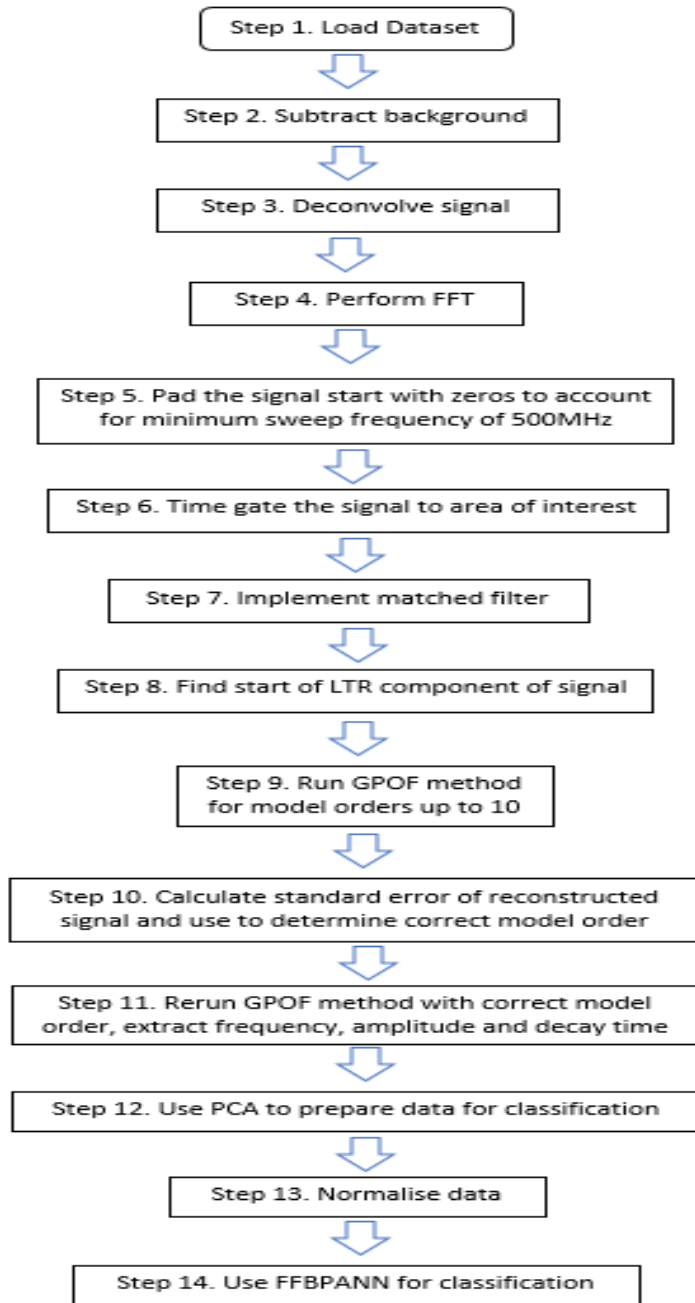


Figure 48: Flowchart of FFT GPOF based LTR algorithm

Discussion

The preceding chapter has presented an initial solution to the problem of LTR security scanning using PCA and the GPOF method. From a discussion of the Fourier transform and the complex natural resonances, to a discussion of how to obtain the model order of a non-cooperative target and the GPOF method this chapter covers the algorithm developed in detail. The individual targets used have been presented with their pole plots. Table 8 shows the targets with their known model orders and expected fundamental resonant frequencies.

Table 8: Table of Targets vs model order and resonant frequencies

Object	Expected Classification value	Model order	Fundamental Frequency
6.5 cm needle	n/a	2	2 GHz
11 cm steel rod	1	2	1 GHz
13.5 cm kitchen knife	2	2	1.35 GHz
Replica .38 revolver	3	4	0.75 GHz
Gas powered Target pistol	4	4	0.85 GHz
Replica .44 revolver	5	6	0.65 GHz
Body with hands at side	6	n/a	n/a
Body with hands behind back	7	n/a	n/a
Fujifilm camera	8	2	0.95 – 1.35 GHz
Keyring	9	Configuration dependent 2 - 6	0.7 – 1.6 GHz

Some of the targets used present more of a challenge to an LTR security system than others. For example the very large revolver is very easy to detect due to the size of its RCS as the available wavelengths in the propagating EM used to excite the LTR range from 0.1 – 0.6m. This places the revolvers relationship with the wavelength in the Mie [154] or resonant range and therefore should allow for a strongly resonant return from the target. The knife is more of a problem as depending on its orientation, the blades edge may be facing the propagating signal, causing a large proportion of the waveform to miss the object and not necessarily illuminate the knife with enough energy to induce a useful surface current. Finally the value of PCA to classification of this data has been covered.

This PCA GPOF method provides good true positive classification rates of greater than 70% while not presenting any false positives. For any viable LTR security scanning system keeping false positives as low as possible is a critical requirement to ensure trust in the robustness of the system. The results presented above are of use in development of an LTR system, though as the Fourier and GPOF methods only work on time or frequency data individually it is important to consider a method that can look at both of these domains at the same time. This will be covered in the following chapter.

Chapter 5

Real Valued Joint Time Frequency Wavelet Analysis techniques

Preview.

This chapter will discuss wavelet based techniques for LTR security analysis. Real valued continuous wavelet techniques will be analysed and their value in classification of security data discussed. Application of the non-linear Richardson-Lucy deconvolution technique for clutter reduction and improvement of the Neural Network classification rates will also be considered.

5.1. Real valued wavelet analysis

5.1.1. Wavelet Families

There are many different wavelet families available for use in processing datasets. The wavelets applied to this work come in to distinct categories, the real valued wavelets include the Morlet wavelet [62], which is the original wavelet used for continuous wavelet analysis. Its functionality allowed the field of continuous wavelet analysis to develop. The second real valued wavelet used is the Gaussian wavelet. Its 2nd order component, commonly known as the Mexican hat wavelet is one of the most easily recognised and commonly used wavelets. A discussion of the CWT can be found in section 3.3.1. Introduction to wavelets and the wavelet transform. Full details on the wavelets used can be found in the Matlab wavelet toolbox users guide [138] [137]. The following plots in section 5.1.1.1. The continuous real valued wavelet transform (CWT) all use the Gaussian ‘4’ wavelet as the mother wavelet [137]. This wavelet is a derivative of a complex Gaussian function and takes the form [138]:

$$\Psi_G(t) = C_N \frac{d^{(N)} e^{-\mu} e^{-t^2}}{dt^N} \quad \text{Equation 63}$$

Where N is the model order and in this case is 4. This value denotes the initial shape and scale over which the mother wavelet occurs. If the value of N is even, then the wavelet will be symmetrical around the Y axis. If the value of N is odd then the wavelet will not be

symmetrical around the Y axis. Both the Morlet and Gaussian wavelet families have been tested with real valued wavelet analysis with the best result being provided by the Gaussian wavelet. The application of the CWT to 1 dimensional data is covered in section 3.3.1. Introduction to wavelets and the wavelet transform. Some basic properties of the wavelets used can be found in Table 9.

Table 9: Table of basic wavelet properties

Wavelet type	Complex (Y/N)	Symmetrical (Y/N)	Length of mother wavelet
Morlet	N	Y	256 points
Gaussian 4	N	Y	256 points
Complex Morlet/Gabor	Y	Y	256 points
Complex Gaussian 4	Y	Y	256 points

5.1.2. Real valued wavelet Transforms

Figure 49 to Figure 57 all represent data in the same fashion. There are two plots in each figure with the left hand plot representing one target scenario and the right hand plot representing a second target scenario. The two plots share the same axis. The X-axis presents time in nanoseconds, the Y-axis presents wavelet scale and the Z-axis presents amplitude.

5.1.1.1. The continuous real valued wavelet transform (CWT)

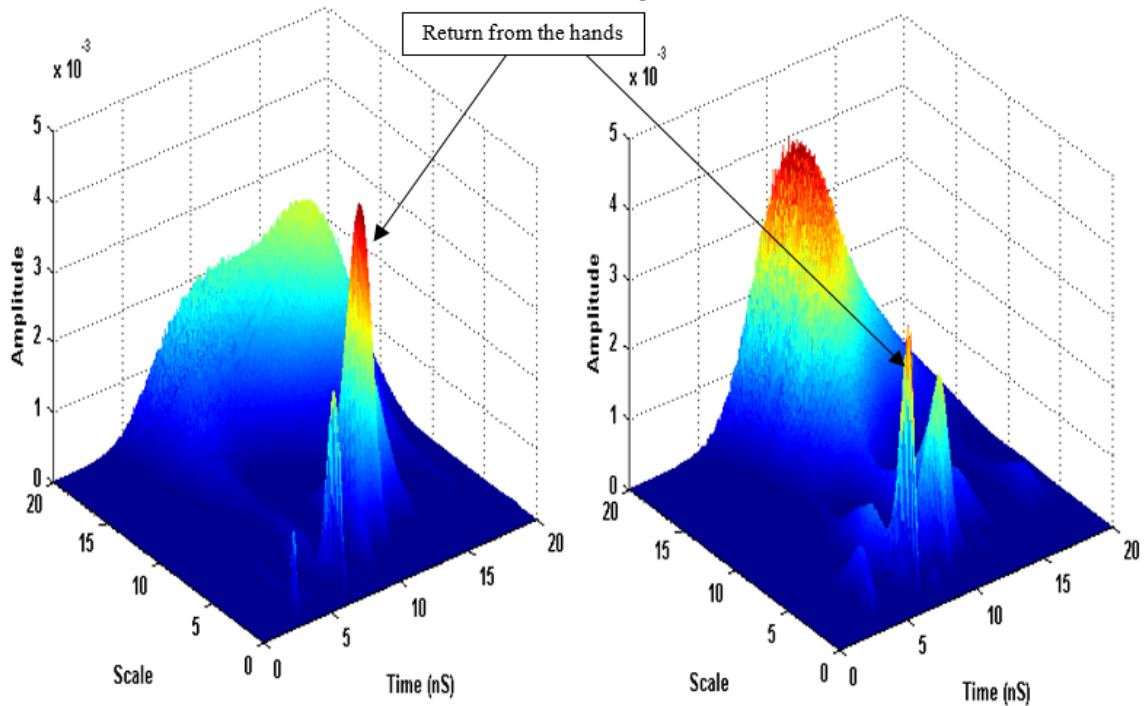


Figure 49: CWT of body hands at side to the left with body hands behind back to the right

To locate the start of the LTR the same method of peak finding has been applied as that presented in section 3.3.5.1. Locating the start of LTR. Once located, zeroes have been added in front of the peak to allow for ease of readability in the surface plots. The surface plots presented in Figure 49 represent the radar return from the human body in two postures after the CWT has been applied. The plot to the left is representative of the human body with hands by the side while the plot to the right is the same body with hands behind the back. A broad spectrum of frequencies are covered by the return from the body, particularly towards the higher end of the scales. In the plot with the hands at the side the highest intensity of the signal occurs at approximately 10 nanoseconds. This peak sits at a similar frequency range to that where many of the threat objects could be located and is most likely a result of the interaction of the signal with the arms and hands as when compared with the plot with hands behind the back the peak intensity is located at a different scale. For this particular plot the peak intensity is located at a much higher scale, ergo a lower frequency, which lasts for a longer period of time. This is due to the return from the initial propagating wave as it makes contact with the contours of the body.

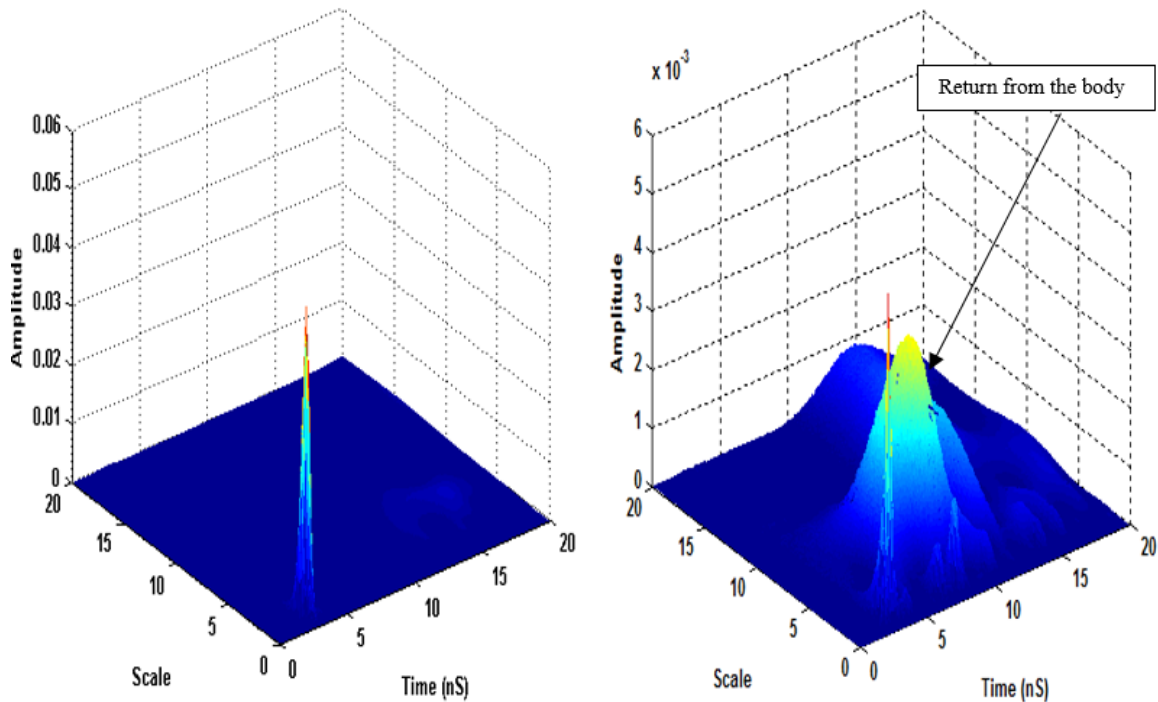


Figure 50: CWT of 6.5 cm needle only to the left with on body to the right

Figure 50 presents the return from the 6.5 cm needle target using the CWT to process the data. The plot to the left shows the needle in isolation as a very sharply defined peak, representing the low model order of the needle. The needle return occurs at scale range 0.8 - 1.7 at approximately 4 ns on the time axis. As shown in the GPOF data the needle can be expected to return a very narrow band of frequencies and the sharpness of this peak would lend credence to that. Looking towards the right hand plot which represents the needle on body it is still possible to visually locate the presence of the return from the needle in this plot, although the return from the body is approaching the same level of intensity and as a result may interfere with successfully extracting the needles resonances. This effect has shown itself to occur with a number of needles of varying sizes and so is most likely an effect of the very small RCS presented by objects of this type. The minimal coupling of the waveform to the target due to the RCS does not present the opportunity for the return from the target to dominate the signal in the way the return from some of the following targets does.

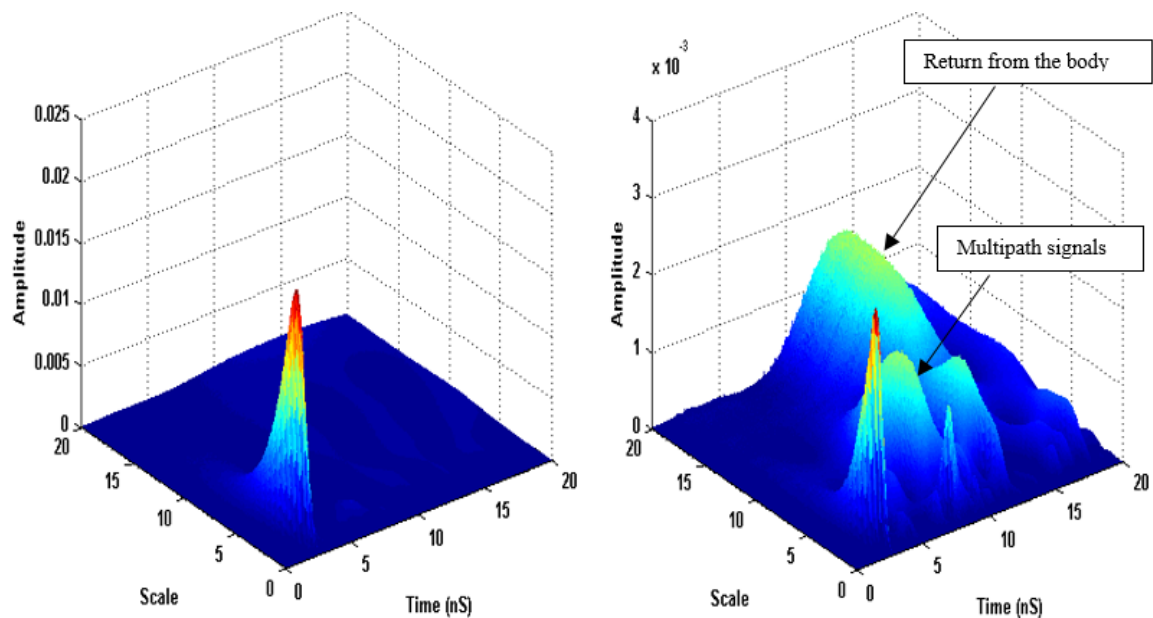


Figure 51: CWT of steel rod only to the left with on body to the right

The next target, presented in Figure 51 is the 11 cm steel rod. This is a simple target as with the needle due to a low model order which allows a sharp peak to appear in the plot representing the target in isolation. The scale range for the steel rod is between 2 and 5.6 at approximately 4 ns on the time axis. This is to be expected as during the experiments the range to target has been maintained as closely as possible. Looking towards the plot with the steel rod on body we can see that a similar effect to that of the needle has occurred, with the peaks from the body approaching the same intensity of that of the rod, although not quite to the same degree. Fortunately the highest intensity of the return from the body in this case is well separated from the return of the steel rod in scale and so it is simpler to discriminate between the two parts of the signal in the case of this target object. This separation in scale will be a result of the increased geometric dimensions of the rod and the return from the body is of a lower intensity due to the rods presence in this signal.

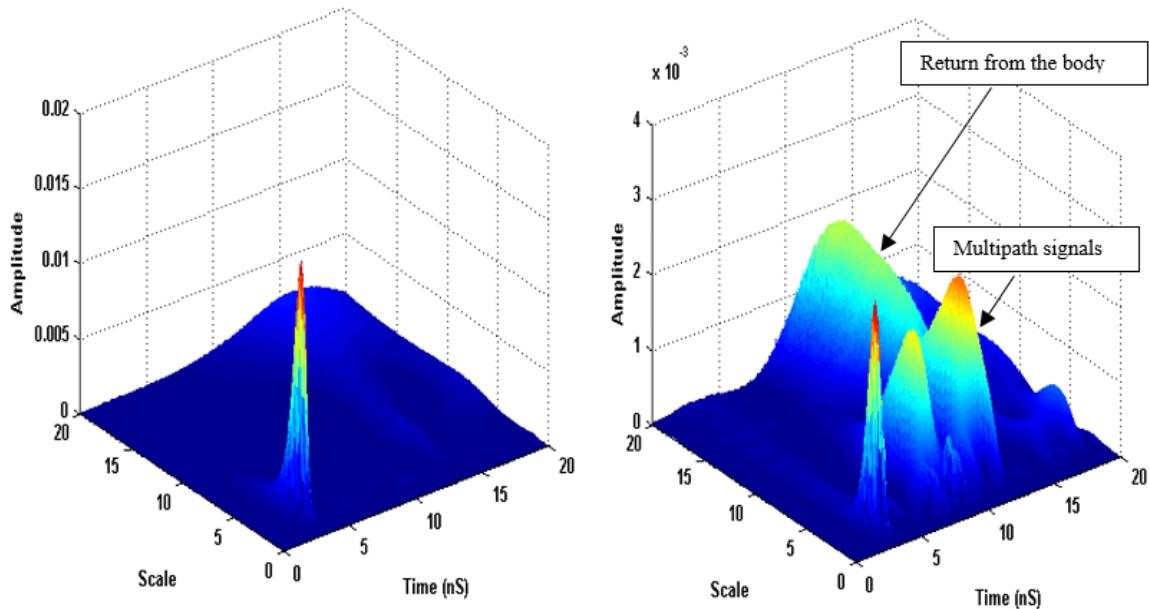


Figure 52: CWT of kitchen knife only to the left with on body to the right

The kitchen knife, presented in Figure 52, is the last of the simple threat objects used to test the CWT based LTR algorithm. Like the needle and slightly more so than the steel rod this item presents as a sharply defined peak after processing by the CWT. Once again this is due to the items low model order. The greatest magnitude return from the knife occurs between scales 1.6 and 3.4 at approximately 4 ns on the time axis. Once the body is added into this scenario as shown in the plot on the right of Figure 52, it becomes less clear. The peak representing the knife is still present, though at very similar scale ranges are two more peaks separated in time. This is potentially a result of the interaction between the knife and the body as the planar structure of the knife blade would have the effect of causing the signal to bounce between the knife and the body. This shows that the knife could potentially be a problematic target to detect in some scenarios as if the range to target is not calculated accurately, one of these peaks approaching similar intensity values could cause confusion within the classification algorithm.

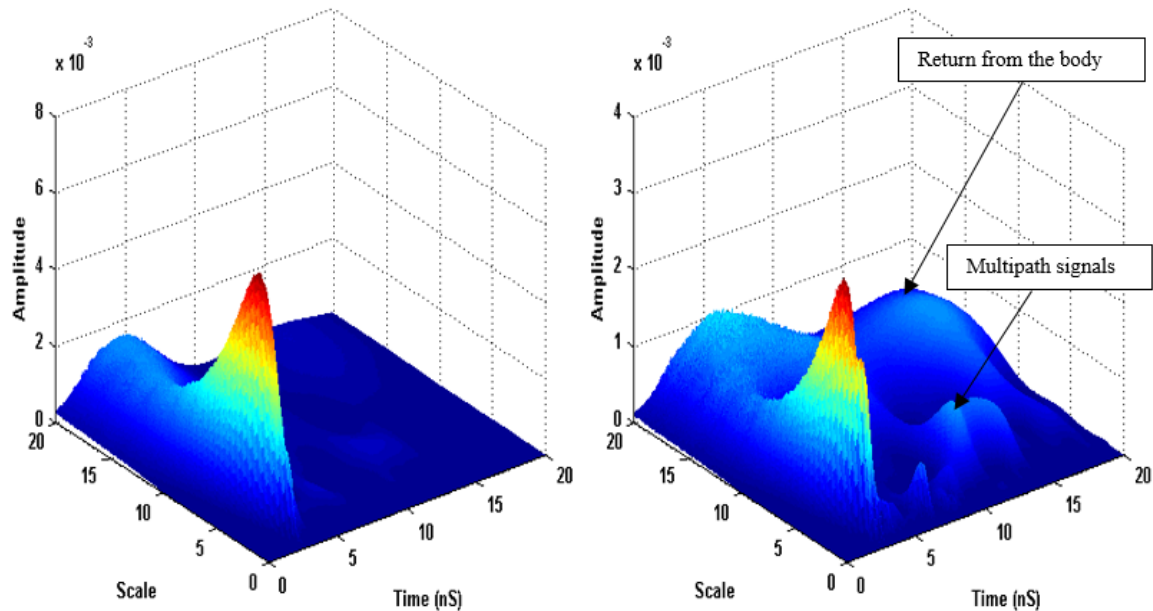


Figure 53: CWT of replica .38 revolver only to the left with on body to the right

The more complex replica .38 revolver is presented in Figure 53. This target is a good example of a potential concealed threat due to its diminutive dimensions and simple, reliable operation. As can be seen in the plot of the object in isolation, the revolver has a greater spread over the scale range, thereby indicating a greater number of frequencies present in the signal and a higher model order as shown in Figure 40. This range of scales is 5.3 to 11.7 at approximately 4 nS on the time axis. This is interesting as this broader peak still maintains a very strong intensity in terms of LTR signals and also spreads into the range of frequencies that would be expected to be generated by the body. As a result of this it would be reasonable to assume that the body would interfere with and disrupt the return from the revolver. This though is not the case as presented in the right hand plot in Figure 53. When compared with the plot of the body only in Figure 49 it can be seen that small peaks are still occurring at locations where the return from the body should be located but the power levels of these components are so small as to potentially be insignificant. This indicates that the revolver is very effective at gathering and reradiating the transmitted signal to such a degree it masks large components of the body in the returned signal.

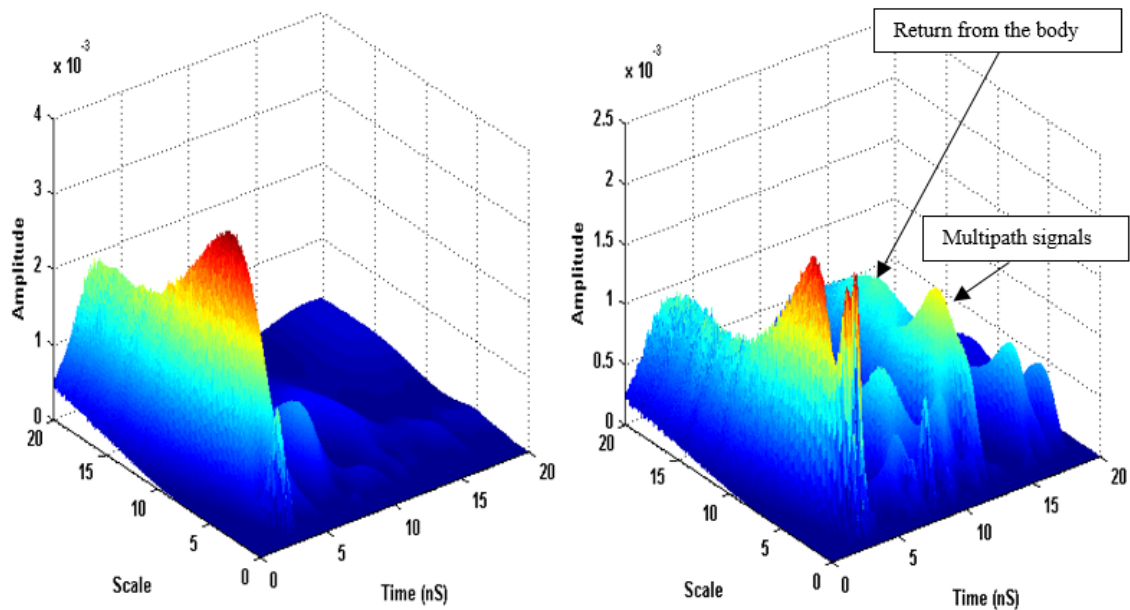


Figure 54: CWT of gas powered target pistol only to the left with on body to the right

The gas powered target pistol presented in Figure 54 also shows a broad range of scales over which the return can be found. The return from this is mainly dominated by the barrel which as a cylinder with approximately the same length as the steel rod presents a challenge for any classification regime. When in isolation it is easily apparent as to the nature of the object, its distributed peak covering a large portion of the available scales with high intensity is similar to the revolver but when looking at the target presented on body an interesting characteristic emerges. This is the presence of a double peak in the signal, one of which is quite sharp while the other is more spread out over the scale range, occurring at the same point in time but with a different spread of scales for each peak. The scale range of the major peak is between 8 and 15.8 at approximately 4 ns on the time axis. It becomes apparent that the body is capable of having more effect on the return with the GP target pistol as well, due to one of the peaks for the region of the body having a significant intensity close to that of the threat and in the same scale range.

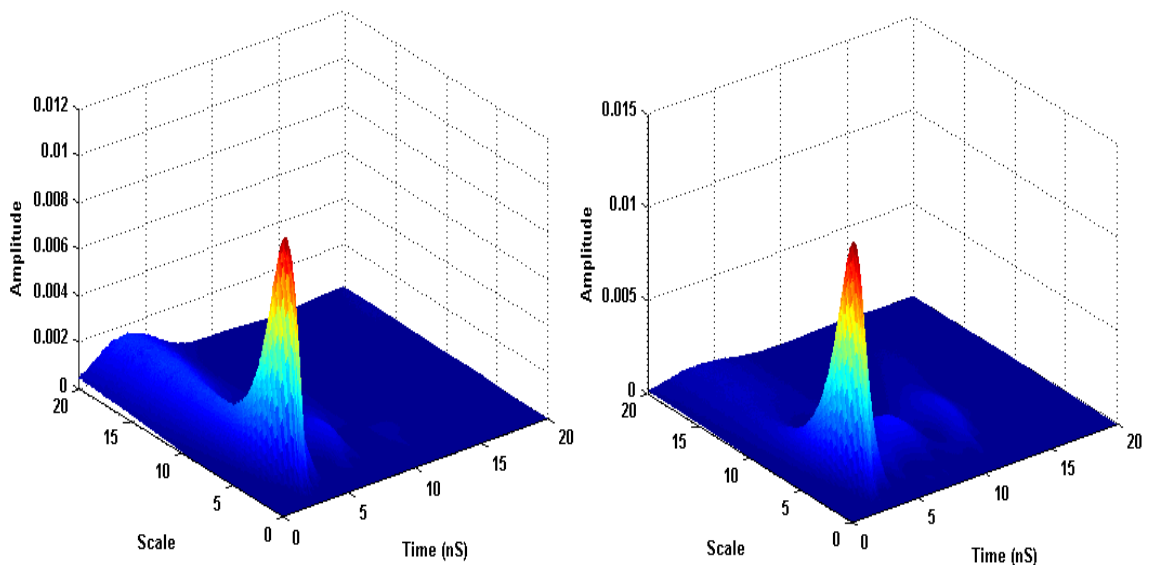


Figure 55: CWT of replica.44 revolver only to the left with on body to the right

The large replica .44 caliber revolver is presented in Figure 55. Although this particular target has a high model order, the range over the scale axis in which these resonances occur is fairly small as shown in the left hand plot for the revolver in isolation in Figure 55. This shows that the individual characteristics of the target geometry will have a direct effect on the detected return, for example in the case of the large revolver many of its features dimensions are quite substantial but similar in length, indicating that the expected resonances should occur in a similar scale range to each other with the greatest magnitude being in the range 3.5 to 6.6 at approximately 4 ns on the time axis. When the target is then placed on the body it is still very prominent. As with the replica .38 revolver presented in Figure 53, the return from the revolver dominates the signal and suppresses the return from the body. In the case of the replica .44 revolver this effect is even greater than that of the replica .38 revolver, suppressing the return from the body to such a degree that it is nearly completely removed from the signal. For classification purposes this is very useful as there is only a very limited amount of detectable change in the signal between the threat item only and the threat item on body. This makes the large revolver a very easy object to detect. It is important to note that the size of this object ensures that the fundamental resonance is

right on the edge of the horn antennas lower sweep range and as a result, smaller features than the barrel such as the cylinder can become very important in identifying the target.

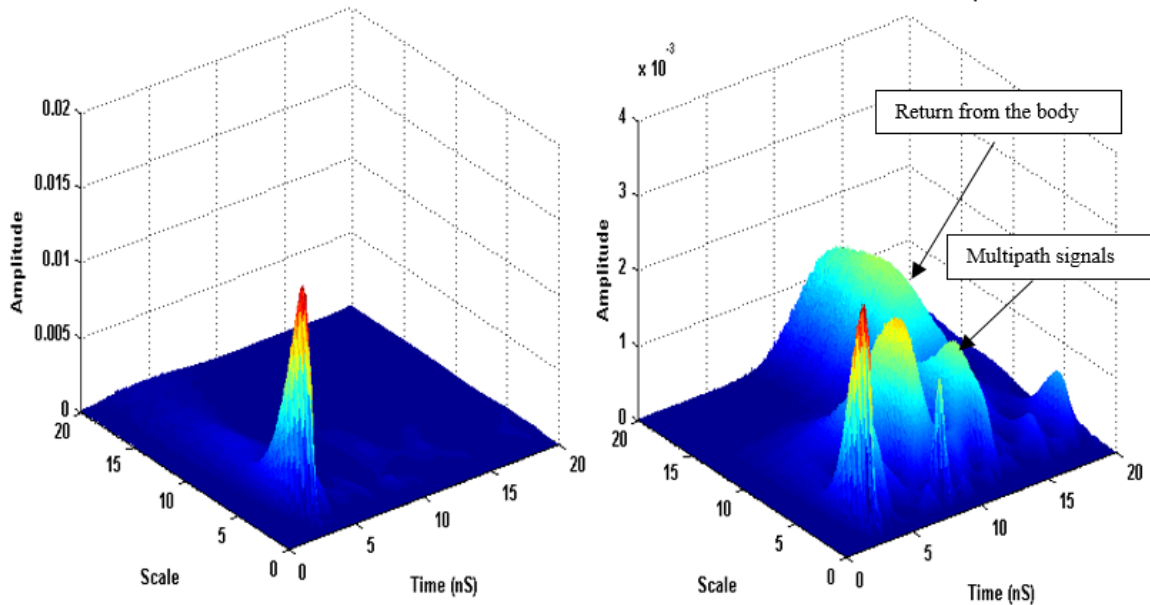


Figure 56: CWT of camera only to the left with camera on body to the right

The Fujifilm camera used as a non-threat object in Figure 56 is a representative example of the type of small digital camera that has become common in recent years. It can also be considered that its small dimensions and plastic casing would allow it to be representative of a number of smaller, commonly carried objects such as personal data assistants and some of the older, thicker mobile phones. When presented in isolation as in the plot to the left of Figure 56 it is apparent that the return from this particular camera has a small range of available scales, between 2.3 and 4.4 in which it can be found at approximately 4 ns on the time axis. As a relatively simple target with planar surfaces for the most part and very little metal to speak of, its return is not very resonant though when it is placed on the body an effect similar to that of the kitchen knife occurs where some secondary peaks in similar scale ranges with intensities approaching that of the useful data are present. The return from the body is also much more visible in the camera scenario than for the revolvers presented in Figure 53 where the body is partly suppressed and Figure 55 where the body is completely suppressed.

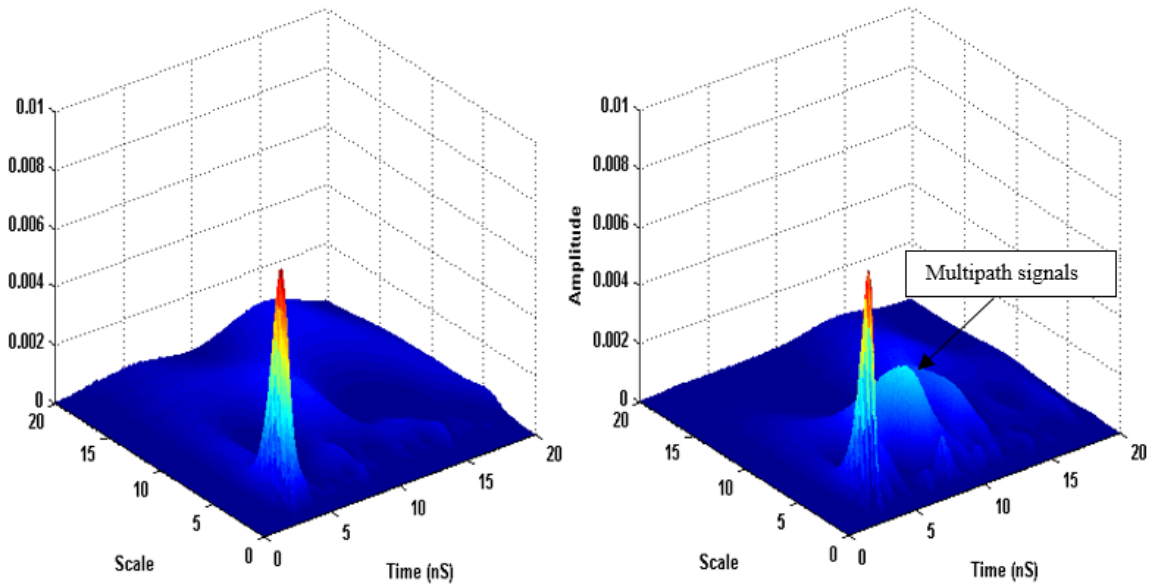


Figure 57: CWT of keys only to the left with on body to the right

A keyring with a number of keys and various pieces connected to it is presented in Figure 57. As is shown in the plot to the left of the keyring in isolation, a very small number of frequencies are present in the signal. This is unexpected as the keys in the signal have varying lengths and geometries therefore it could be expected that they would present a broad range of resonances when illuminated. As this is not the case, it must be considered that the objects extremely close proximity to each other is causing the keys and the keyring to resonate as one very complex object in a scale range between 2.65 and 4 at approximately 4 nS on the time axis. This presents a potential limitation of the radar system as its wavelength is such that it will struggle to discriminate between metallic objects in close proximity. When on the body this particular target presents similar characteristics to the revolvers in that it suppresses the return from the body considerably. This indicates that great care must be taken to ensure that these particular characteristics do not lead to misclassifications in the algorithm as this would increase the false positive rate of the system. The features observed in Figure 49 to Figure 57 are used to train the ANN based classifier, though the volume of data produced by use of the CWT can overwhelm the ANN. Therefore it is necessary to find a way of reducing the size of the dataset while

maintaining the useful features in order to allow for successful processing. This led to the use of the Self Organising Map (SOM).

5.2. Self Organising Feature Maps

Self Organising Maps are a form of ANN that uses unsupervised competitive learning techniques to produce a lower dimensional dataset from an input dataset. This method was developed by Professor Teuvo Kohonen [155] to allow for visualization of complicated highly dimensional datasets in a simpler form. The history of the models used in these networks can be traced back to early morphogenesis models introduced by Alan Turing [156].

There are a number of very useful features available with SOM along with its ability to present highly dimensional data in a lower 1 or 2 dimensional space. This includes that the technique ensures that any topological relationship information is maintained and that regions within the data containing similar properties will be found adjacent to each other. More specifically to the LTR problem, using the SOM reduces the sensitivity of the signal to locating the start position of the LTR, thereby ensuring that only those features useful to the following analysis are extracted.

The networks hidden layer is created from a 2 dimensional lattice of nodes each of which is connected to the input layer. Each of the nodes has a specific XY position and will contain its own weight vector. It is important to note that although all the nodes are connected to the input layer, there are no connections between the nodes themselves. These XY positions are used to create a grid that is overlaid on the dataset. The neighbourhood connections in the grid can be of any form from a square grid to the hexagonal grid used in this work.

Unlike a feedforward backpropagation ANN, the SOM does not need to have a target vector presented to it in order to change. Instead where a node's weights match those of the input vector the area of the grid at that point is optimized to more closely resemble the data. As it is an iterative process that starts with randomized weights, this can require a large number of iterations before the map becomes a collection of stable zones. Each of these zones can be considered to be identifying a feature of the input dataset.

The training process requires the following steps:

1. Initialize the node weights for all nodes
2. Select the initial value for the radius of the node region of influence. This is typically much larger than the actual result.
3. Present a random vector from the training set to the grid. This is the input vector.
4. All node weights are analyzed. The Euclidean distance between each node weight and the input vector is calculated. The node with the weights closest to the input vector by this definition is chosen and defined as the Best Matching Node (BMN)
5. Calculate the radius of the region of influence for the BMN. This value should reduce with each time step until it reaches a stable level.
6. Each of the nodes within the BMN region of influence then has its weights adjusted to more closely resemble the BMN.

$$W(t + 1) = W(t) + \Phi(t)L(t)(V(t) - W(t)) \quad \text{Equation 64}$$

The closer the node to the BMN, the more its weights will be altered.

7. Return to step 3 and repeat.

The Euclidean distance between two vectors can be calculated using:

$$E_{dist} = \sqrt{\sum_{i=0}^{i=n} (v_i - w_i)^2} \quad \text{Equation 65}$$

Where v is the training vector and w is the weight vector at the corresponding node. As the effect of the node distance from the BMN effects the amount of training applied to the nodes within its locality, ϕ has been selected to denote this and is calculated using:

$$\Phi(t) = \exp\left[-\frac{distance^2}{2\sigma^2(t)}\right] \quad t = 1,2,3 \quad \text{Equation 66}$$

Where distance is the distance a node is from the BMN and sigma is the width of the region of influence. The ability of the SOM to determine these regions of influence and then shrink them in size allows for the function to be used to reduce the size of the intensity maps that are provided by continuous wavelet based LTR techniques. In effect it allows for the BMN to be used as a centroid, identifying the feature with the most valuable

information. This location of these centroids can then be fed into a supervised neural network to allow for individual target classification.

5.3. Algorithm 2: LTR using the wavelet method

The final LTR algorithm formulated around the wavelet based methods is structured as follows in Figure 58:

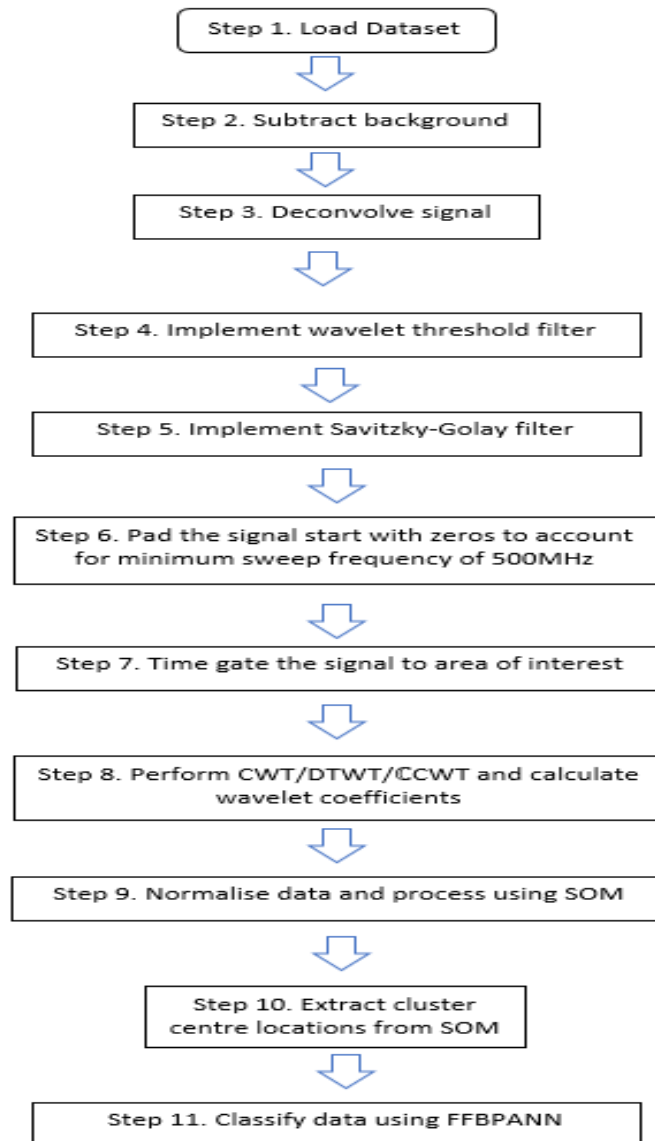


Figure 58: Flowchart of wavelet based LTR algorithm

5.4. Non-linear Deconvolved Wavelet Results

5.4.1. Non-Linear Deconvolution: The Richardson-Lucy approach

A second approach to non-linear deconvolution was considered for use with the real valued wavelet transforms, the Richardson-Lucy algorithm [157] [158]. The aim of using this method was to sharpen the edges of the extracted features, in order to provide a sharper representation of the scale range over which the features exist. This iterative process, developed for recovering better defined detail from blurred images is best known for its use on correcting for faults in the optics of the Hubble space telescope. When applied to the intensity maps generated by a CWT it presents the opportunity to further remove clutter and redundant information from the datasets before classification is performed. An example of the effect of Richardson-Lucy deconvolution on the targets used will now be presented. Figure 59 and Figure 60 have the same axis as Figure 49 to Figure 57.

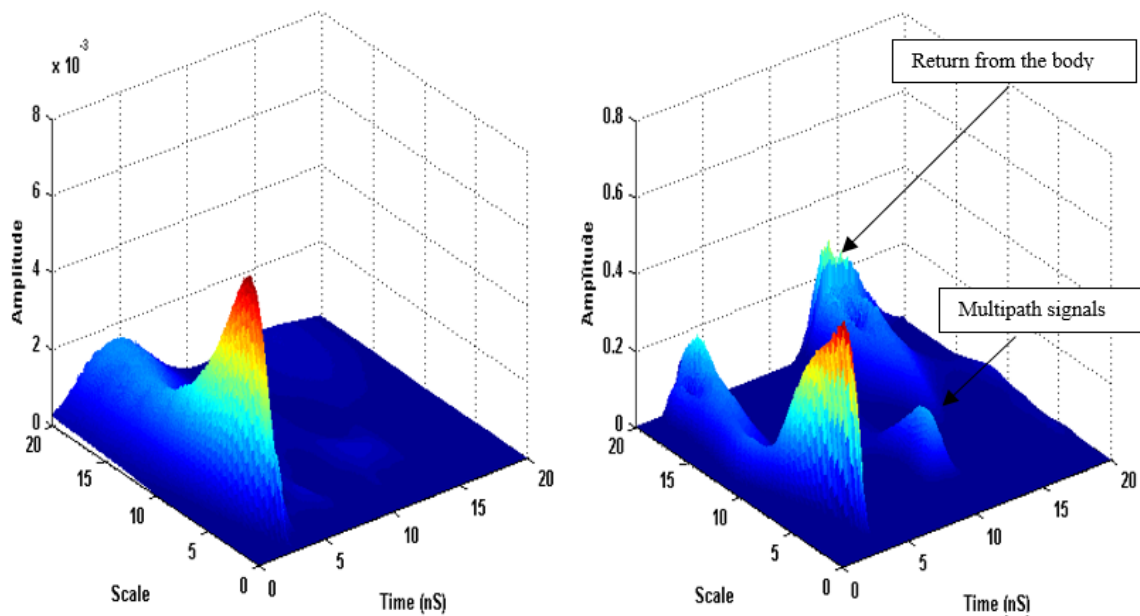


Figure 59: Replica .38 revolver in isolation to the left, Richardson-Lucy deconvolved signal to the right

Figure 59 above presents the results of the replica .38 calibre revolver in isolation. To the left we have the result of the standard CWT with the result of the CWT combined with the non-linear Richardson-Lucy deconvolution algorithm applied presented on the right.

The target in isolation with no non-linear deconvolution has a scale range of 5.3 to 11.7 while with non-linear deconvolution applied it has a range of 5.6 to 9.8. The target return occurs as expected at ~ 4 ns on the time axis. It is apparent that when applied to a target of this nature in isolation the Richardson Lucy deconvolution algorithm is of limited value. The peak of the signal occurs at both the same time and scale range over both of the surface plots presented as expected. It is with the amplitude where some changes can be seen. If the maximum amplitude of the major peak of the two signals is compared directly it can be seen that the result presented by the Richardson-Lucy algorithm is of considerably greater magnitude than that of the CWT alone. Indeed the amplitude of the non-linear deconvolved signal is in the order of 100 times greater than that of the CWT alone. This potentially could be due to the data normalization process that is part of the Richardson-Lucy algorithm. For detection purposes this is very useful though it does not come without drawbacks. Along with in effect amplifying the return from the target, certain sections of the clutter remaining have also been amplified as shown by the data beyond ~ 10 ns.

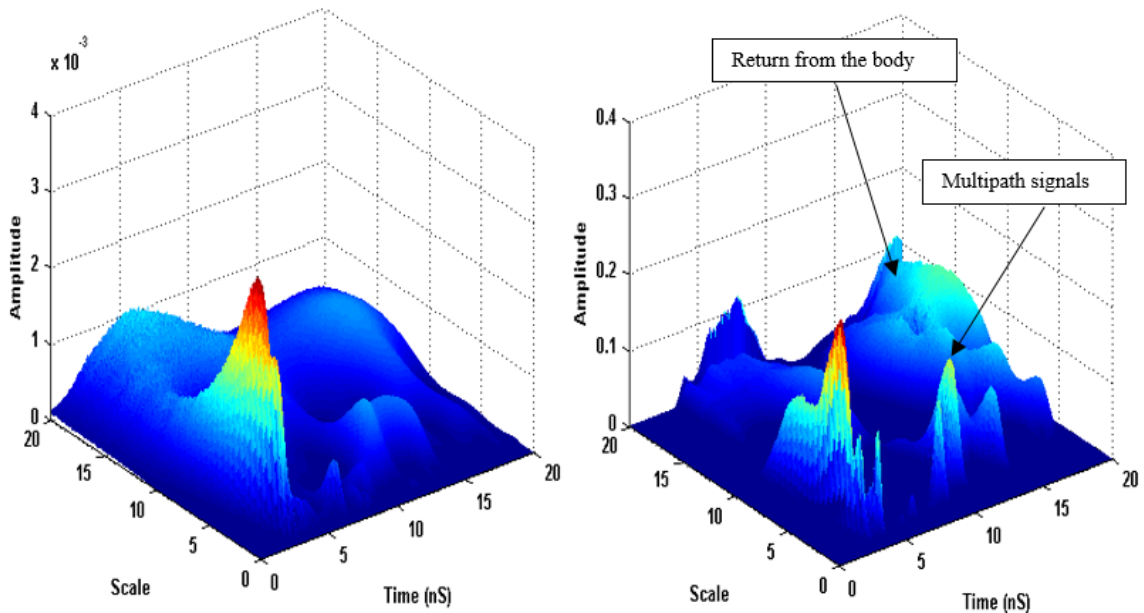


Figure 60: Replica .38 Revolver on body to the left, Richardson-Lucy deconvolved to the right

A similar effect to that discussed in Figure 59 can also be seen in Figure 60 above. This is the revolver presented on the body with the CWT alone in the plot to the left and the non-linear deconvolved signal in the plot to the right. Once again the time remains the

same, though the scale range has shrunken slightly leaving a more defined peak. In particular it is of note that a substantial percentage of the lower power return from the revolver on body, in the scale range 10+ has effectively been removed from the signal. This would make identifying the fundamental frequency simpler for classification purposes. Conversely the effect of the deconvolution method in increasing in power some sections of the return from the body could present issues for any system that is not able to completely remove them via filtering or training effectively to counter this.

The Richardson-Lucy deconvolution algorithm has shown itself to be effective at removing some segments of the signal that are of no interest and of amplifying others, although for LTR purposes it has also removed some of the useful frequency information. Unfortunately due the above mentioned drawback and to the very close proximity of the target object and the body, coupled with the fact that the return from the body is substantial in intensity and the number of iterations required would need to be calculated a priori, it is impractical to use this algorithm in a viable LTR security system.

5.5. CWT classification results using Neural Networks

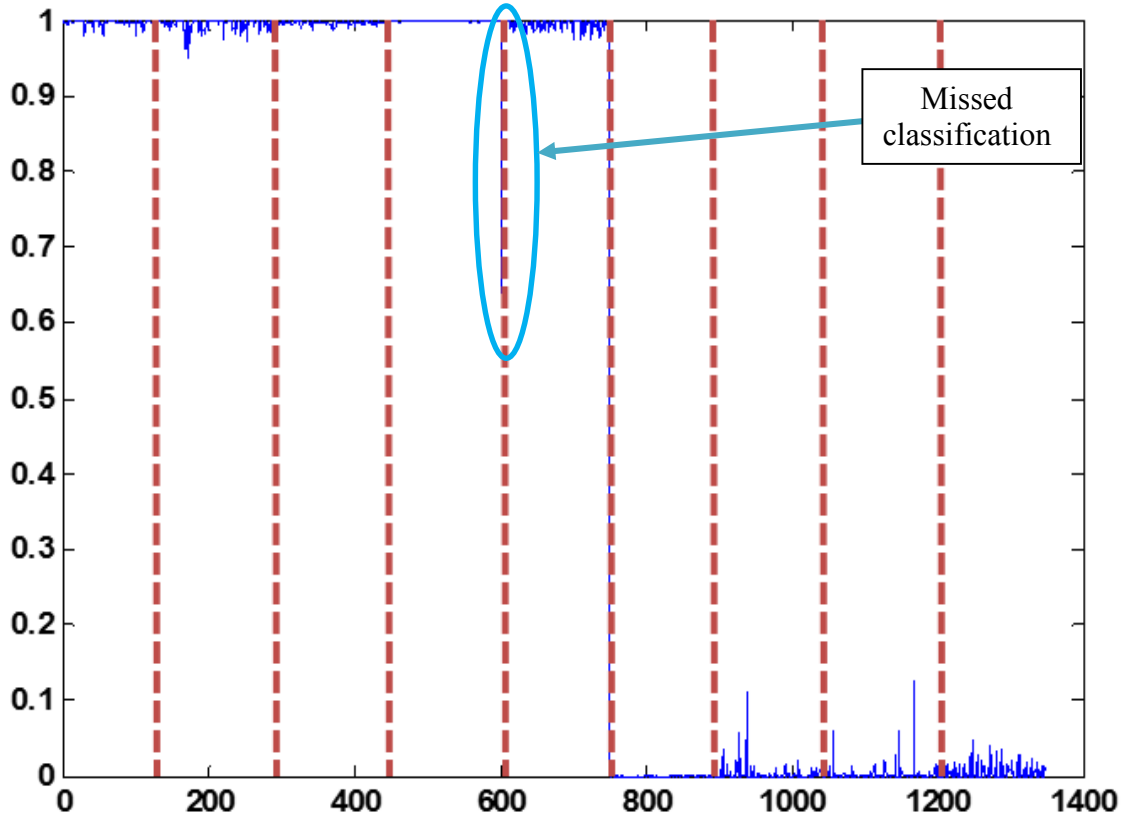


Figure 61: Plot of all 9 target sets using CWT with value 1 as threat and value 0 as non-threat

Figure 61 presents the results of a binary threat non-threat classifier using the CWT to process the dataset. All threat objects are expected to have a result of 1, while all non-threat objects are expected to have a value of zero. The targets are arranged as per Table 8 although the 6.5 cm needle has not been included. In Figure 61, all points up to 750 on the X axis were threat objects and as such should present with a value of 1. All points above 750 on the X axis are non-threat objects and as such should present with a value of 0. A total of 1350 sweeps are presented with the true positive classification rate for this particular classifier in Figure 62. The threshold value selected in order to allow a target to be successfully identified was ± 0.3 around the target value.

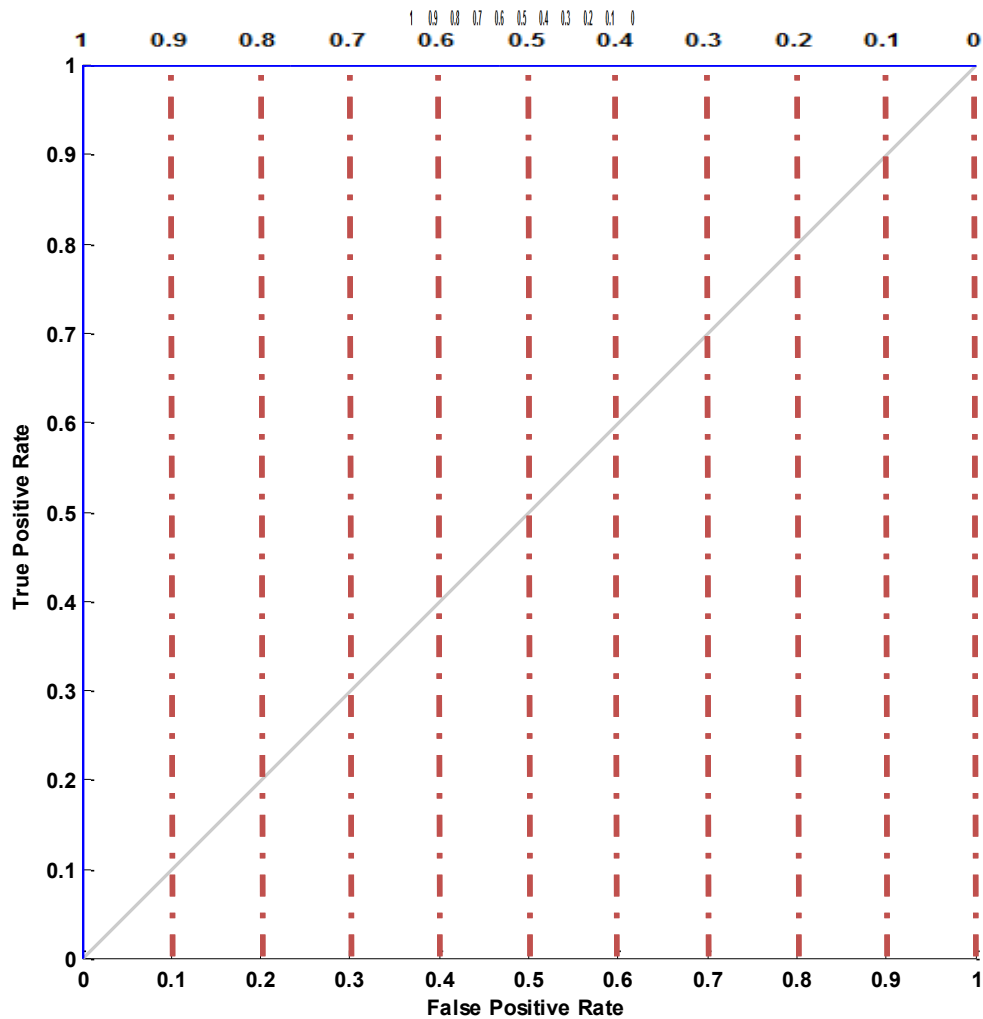


Figure 62: ROC curve split dataset CWT binary classifier

The ROC curve in Figure 62 represents the results of a binary classification threat/non-threat CWT based LTR algorithm. This curve was created by using one half of a given dataset to train the neural network and the other half of the dataset to test it. The blue line on the graph represents the probabilities of a true or false positive at a given threshold and this curve is a result for the test set. Figure 62 shows that in these circumstances the true positive classification rate at the highest threshold of 1 is very high, approaching 100% while the false positive rate can be seen to be 0%. This would be ideal for any real world system though this result would be close to impossible to recreate in a real world system. As before the gray line represents the point at which the system can be considered to be

working with points to the left of the gray line showing a successful classifier while those close to the gray line or to the right of it showing a classifier that is not viable for use. The ANN used to create this ROC curve had 1 hidden layer and a total of $n-1$ neurons or 8 in this case. Table 10 presents the classification rates for each of the targets taken individually.

Table 10: Table of individual target true positive classification rates using CWT for the binary classifier

Target	Correct classification rate (%)
11 cm steel rod	100
Kitchen Knife	100
Replica .33 calibre revolver	100
Gas Powered Target pistol	100
Replica .44 calibre revolver	99.33
Body, hands at side	100
Body, hands behind back	100
Fujifilm Camera	100
Keyring	100

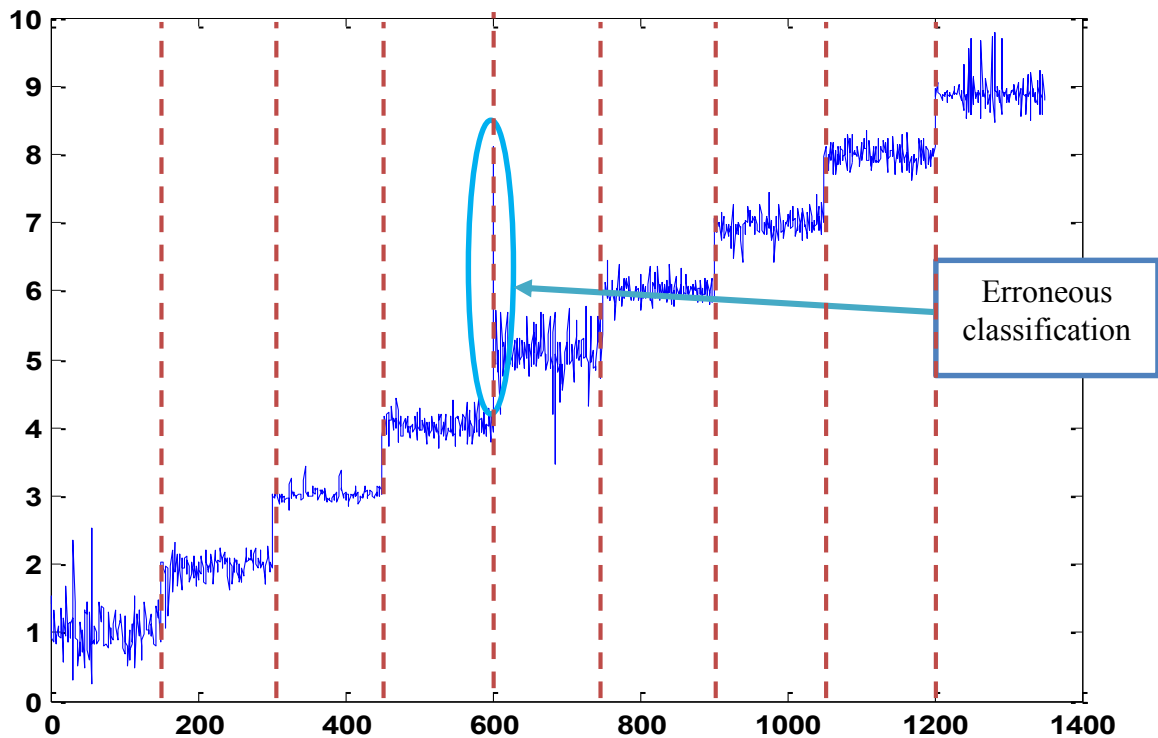


Figure 63: CWT plot of all 9 target sets against their expected classification value

Figure 63 presents the results of the 9 object group classifier. Each of the targets was assigned an individual value as per those specified in Table 8 with the needle not being used. The threshold value around the specified values was maintained at ± 0.3 . The misclassification at point 600 has been highlighted as this is a particularly serious error where the neural network has identified a threat in the form of a revolver as a camera. Each of the targets is represented with 150 sweeps and all targets have been given a positive integer value between 1 and 9, therefore any values found outside this range can be considered to be failed classifications.

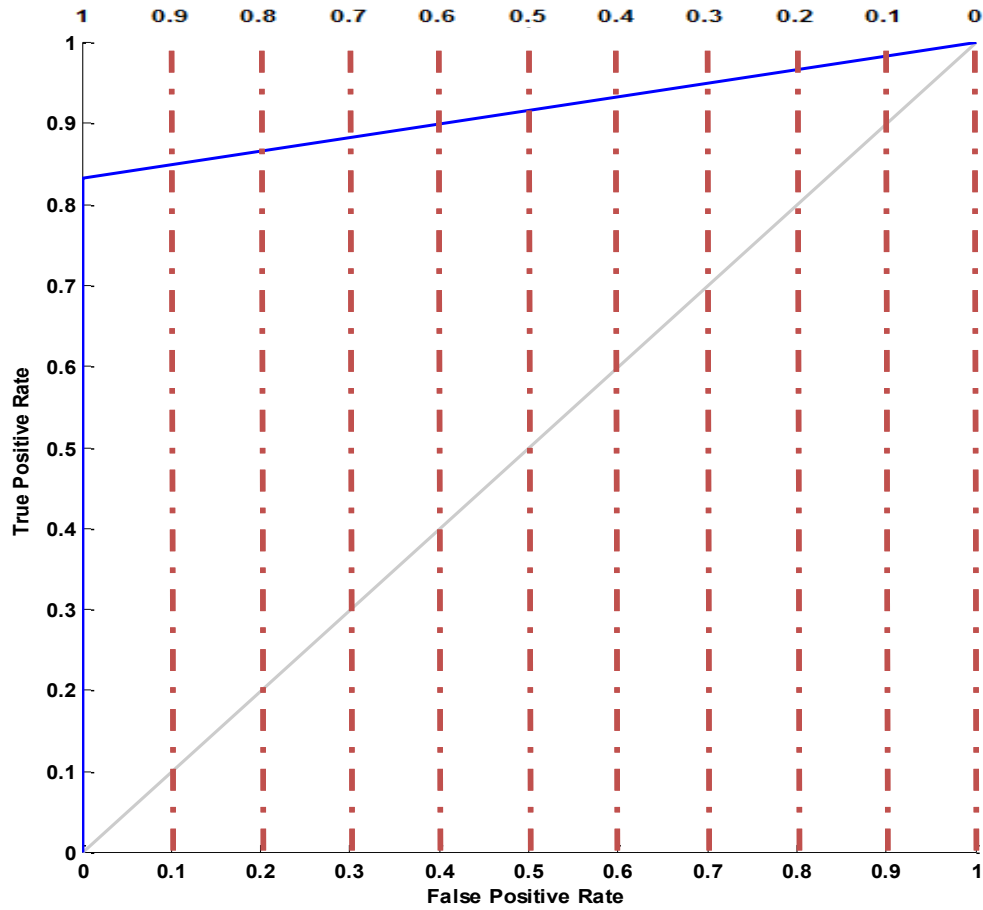


Figure 64: ROC curve nine individual targets classified individually, split dataset

The ROC curve in Figure 64 presents the classification results for a multiple object classifier using the CWT based LTR algorithm. This is a much more complex problem for the ANN to classify as it is now being asked to tell the user of the algorithm what of 9 objects has been detected. As before the data used was a test set taken from splitting a large dataset in half and using one half to train the network, the other half to test the network. The true positive rate at a threshold of 1 in this case is still high at 83% for no false positives although when compared to Figure 62 it can be seen that this rate has fallen. The increase in the complexity of the problem required that a larger neural network be used to classify, in this case the network still has 1 hidden layer but that layer now consists of a total of 60 neurons. Table 11 presents the results for each of the targets tested individually.

Table 11: Table of individual target true positive classification rates using CWT for 9 object classifier

Target	Correct classification rate (%)
11 cm steel rod	75.31
Kitchen Knife	94
Replica .33 calibre revolver	98.67
Gas Powered Target pistol	96
Replica .44 calibre revolver	69.32
Body, hands at side	86.71
Body, hands behind back	86.71
Fujifilm Camera	88.7110
Keyring	85.33

5.6. Some classical problems with real valued wavelets

The real valued wavelet transform has shown itself to be a powerful tool in analysing LTR datasets though it does have certain classical drawbacks that are not present when using the Fourier transform. These drawbacks are [71]:

1. Time Variance: This is an occurrence when a small time shift of the signal will cause considerable disturbance in the wavelet coefficient patterns around singularities leading to the response of the signal being dependent on the time at which an event occurs
2. Oscillations: The presence of oscillation in the signal around events considerably complicates the process of signal modelling and analysis using real valued wavelet based transforms. As a direct result of these oscillations it is possible for a wavelet overlapping an event to have coefficients approaching or equal to zero. This therefore would yield no useful information at these points.
3. Aliasing: As with many signal processing approaches, real valued wavelet based analysis can find itself subject to aliasing. This can be caused by overly wide spacing of the wavelet coefficient samples or introduced via signal processing operations applied to the signal such as wavelet threshold filtering. This can result in the appearance of artefacts in the signal some of which may be substantial in magnitude and could lead to confusion over the validity of a target.
4. A lack of directionality: The pattern produced by wavelets, unlike higher dimensional Fourier sinusoids which correspond to directional plane waves, is largely omni-directional. This lack of directivity causes issues when processing the edges of features in a given signal.

Discussion

The preceding chapter has presented real valued wavelet analysis as a potential solution to the LTR security scanning problem. From a brief discussion of the wavelet families relevant to this process through the results of the real valued wavelet transforms and then on to the application of non-linear deconvolution and potential problems with the approach, this chapter has attempted to give an overview of this novel approach to security scanning.

The results of the classification on the data presented in the surface plots show that a viable LTR system could be constructed using the CWT base method although certain technical issues specific to this method would need to be overcome. This is mainly the issue that the processing per sweep currently takes more than 30 seconds, this would mean that for example in an airport bottlenecks would be caused as people queued to be scanned. The Self-Organising feature map has been introduced and its utility in processing wavelet based LTR datasets considered. Finally potential problems with the real valued wavelet transform at a fundamental level have been specified. These problems can be overcome or reduced by changing to complex wavelets as described in the following chapters.

Chapter 6

Complex Joint Time Frequency Analysis Wavelet techniques, a more accurate approach to LTR security screening

Preview.

This chapter will discuss complex wavelet based methods for LTR security scanning. Covering both the DTWT and the CCWT approaches, the relative benefits of using discrete or continuous wavelet methods for classification in both binary and multiple object classifiers is discussed. Finally the SOM for data clustering is considered and the benefits of differing numbers of neurons weighed. The complex valued wavelets considered for processing include the Gabor wavelet, which is the complex equivalent of the Morlet, The complex Gaussian wavelet, the Shannon wavelet and the Frequency B-spline wavelet. Full details on these wavelets can be found in the Matlab wavelet toolbox user's guide [138] [137].

6.1. The Discrete Dual Tree Wavelet transform

6.1.1. Overview

The DTWT represents a discrete approach to complex wavelet analysis [71]. Developed to overcome four of the problems of real wavelets outlined in section 5.3, the DTWT is also intended to reduce the computational requirements over the CCWT. The DTWT functions by employing two real DWT's, the first DWT provides the real component of the transform and the second DWT provides the imaginary component. Two sets of filters are used, one set for each of the DWT's performed, and are designed to meet the conditions for a perfect reconstruction filter for that particular signal as outlined in [71]. The DTWT is invertible, therefore allowing the original signal to be retrieved after processing if necessary. When performed on a real signal, the result of the DTWT is a complex data set with real and imaginary components. When performed on a complex signal the result of the DTWT is two complex variables, one of which represents the result of the real transform and the other the result of the imaginary transform. Therefore the output vector

of the DTWT will always have twice as much data as the input vector. All of the following experimental results show only the first 3 levels of data handling of the signal performed by the DTWT. At each ascending level, the data is compressed by half so if the original signal had 2048 points, at level 1 it will have 1024, at level 2 it will have 512 points, at level 3 it will have 256 points and so on while the DWT attempts to maintain the features of the signal. The advantages of this are that the dataset generated is smaller than that generated by the CWT (see section 5.1.1.1. The continuous real valued wavelet transform (CWT)), allowing for easier processing and no need for the SOM. Conversely the disadvantage to this is that there is a finite limit on the number of the output levels and as the compression reaches greater and greater numbers of levels, some of the information can be lost. The following plots present the time domain response as processed by the DTWT with three levels of compression applied to the signal. The figures presented from Figure 65 to Figure 73 contain six separate plots covering two target scenarios. The three left hand plots present the level 1, 2 and 3 DTWT decompositions for the first target scenario with the three right hand plots presenting the same information for the second target scenario. The Y-axis on all plots is normalized amplitude and the X-axis is time in nanoseconds.

6.1.2. DTWT Results and Classification

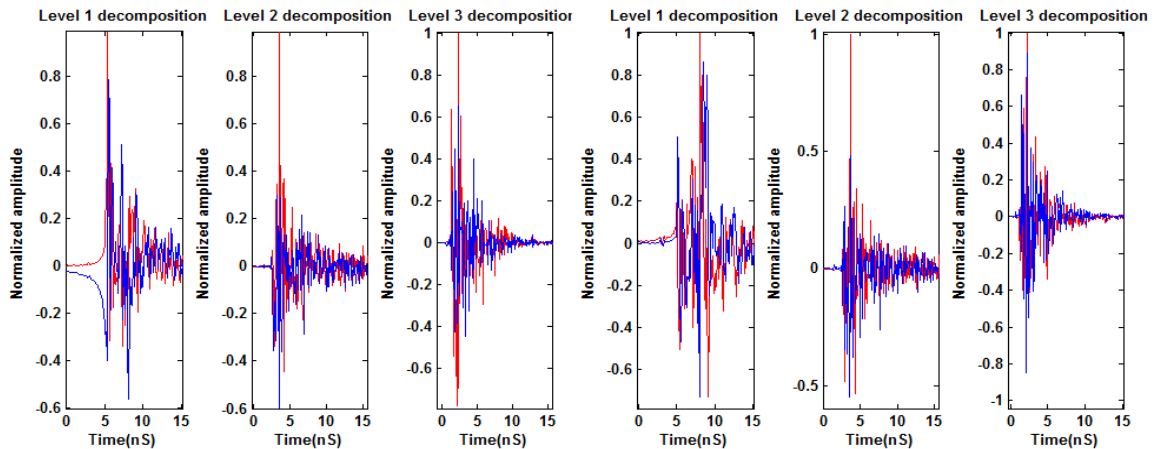


Figure 65: DTWT of body only, hands at side to the left and hands behind back to the right

The body only is presented in the same two postures as previously discussed in Figure 65. In the case of the DTWT of the body the three levels of compression of the signal by the wavelet transform show some similar characteristics. For example if the level 1 compression of the signal is considered, multiple peaks are present indicating multiple features within the signal. This signal at level 1 compression will reduce the original signal length by half from 2048 to 1024 points although the step size between the individual points will be twice as large as in the original signal. Conversely the level 2 compression shows a damped sinusoid which is of a much more idealized representation of the nature of an LTR signal. This is particularly apparent with the body with hands behind the back indicating that the presence of the arms is returning a strong cross polar signal when the arms are placed at the sides of the body. This signal is reduced in length by half again to 512 points. The level 3 compression of the signal is quite similar in both cases, therefore it will be difficult to identify individual features and tell one body posture from the other. This final signal is reduced in size to 256 points.

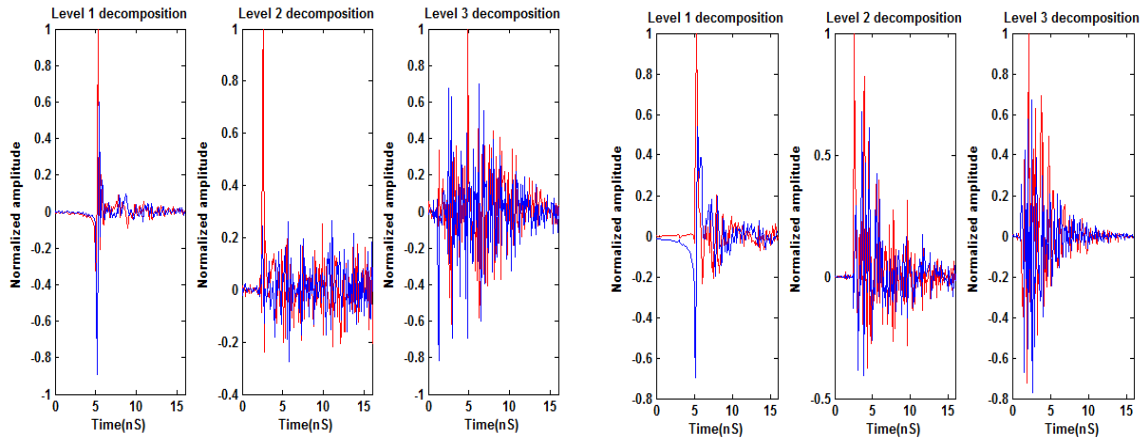


Figure 66: DTWT of 6.5 cm needle in isolation to the left and 6.5 cm needle on body to the right

The first target that will be considered is the 6.5 cm needle. Given that this target is a very simple object, when in isolation as presented on the left in Figure 66 its features are clearly present in the first two levels of compression of the signal. When on the body as presented to the right in Figure 66, the presence of the body has begun to mask some of the return from the needle and although it can still be seen in the level 1 compression and the level 2 compression, the peak representing the start of the return from the needle is not as clear. In the level 3 compression a number of the peaks from the body are approaching the level of the peak from the needle. As a result unless the signal is windowed with a high level of accuracy, it would be very difficult to discern one from the other.

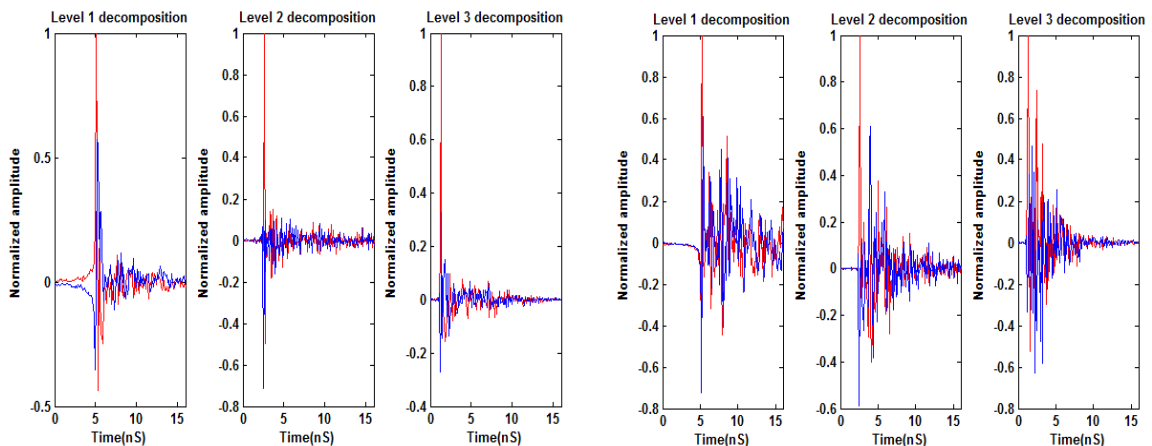


Figure 67: DTWT of 11 cm steel rod in isolation to the left and on body to the right

The 11 cm steel rod is very similar to the needle in a lot of respects. As can be seen in the plots to the left of Figure 67 there is a very clear peak present when the response from

the rod is introduced to the signal. This is consistent across all three levels of compression provided by the DTWT. When the body is introduced to the signal, as shown in the three plots presented on the right of Figure 67, this peak is still very clearly present in levels 1 and 2. In level 3 as with the needle the peaks from the body are beginning to approach the same magnitude as those from the target, though in the case of the rod this is not as severe as with the needle.

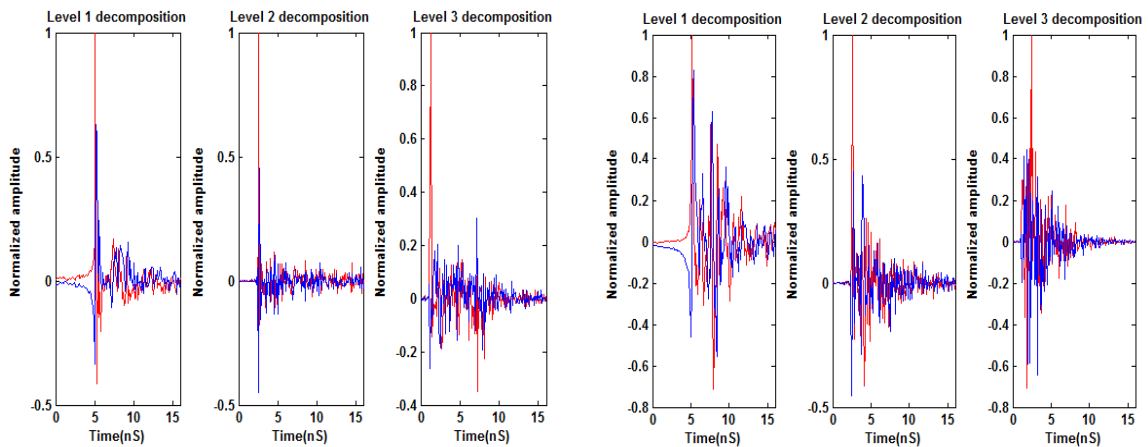


Figure 68: DTWT of kitchen knife in isolation to the left and on body to the right

The kitchen knife, results of which are presented in Figure 68, is an excellent target for this particular LTR scanning method. When the knife is presented in isolation, as in the three plots on the left of Figure 68, the peak caused by its presence in the signal is very clear in all three levels of compression. It is important to note there is some clutter still present in the level 3 compression, although this signal is approximately a third of the size of the threat objects and so does not have too much effect. When the body is introduced into the signal though, there are a few things to note. Firstly there is a distinct double peak present in the first 2 levels of the signal. In the level 1 compression this secondary peak is 60% of the primary and so must be taken into account when processing. Moving on to level 2, this secondary peak drops to approximately 45% of the primary which is still significant, though its effect on the signal is reducing. When the signal reaches its level 3 compression, this secondary peak is reduced even further and becomes much harder to discern within the signal.

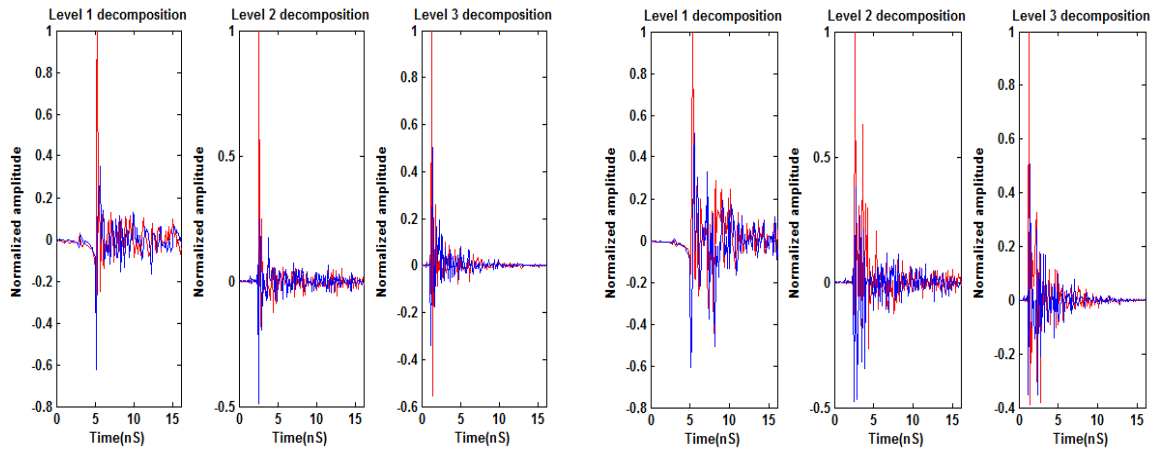


Figure 69: DTWT of replica .38 calibre revolver in isolation to the left and on body to the right

As with previous methods, the result of the replica .38 revolver presented in Figure 69 is very distinctive. When in isolation at all 3 levels of compression used the revolver presents an excellent target, with the peak at the start of its return clearly visible and more than 4 times greater in magnitude than any other section of the signal. When the replica revolver is moved onto the body this characteristic continues, although it must be noted that the difference in magnitude between the signals has reduced a little. In the level 1 and level 3 compressions, the magnitude from the target is still at least 3 times greater than that of the body. The level 2 compression bucks this trend though, as the secondary peak representing the body is approaching 55% of that of the revolver. As long as care is taken when dealing with the secondary peak in the level 2 compression of the signal this target should present one of the best opportunities for successful on body classification.

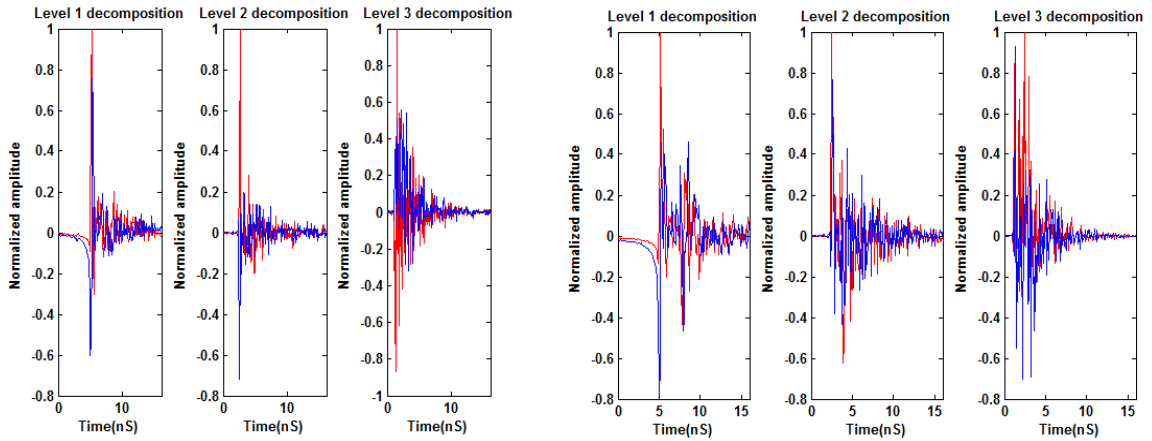


Figure 70: DTWT of gas powered target pistol in isolation to the left and on body to the right

The gas powered target pistol is a very large target compared to most of the dataset used. The results presented in Figure 70 show that in isolation, as with the replica .38 revolver the fundamental peak from the weapon is very large compared to the background with the primary peak being approximately 4 times that of the rest of the signal in the first 2 levels of compression.. Particularly at level 3 there is a nicely oscillating damped sinusoid which would be characteristic of the LTR from this target. When moved onto the body this pattern continues with the peak from the weapon being clearly present in the first two levels of compression, although the secondary peaks have increased in magnitude compared to targets in isolation and at level 3 the peak has become lost in the clutter presented by the body and so care would have to be taken using this for classification.

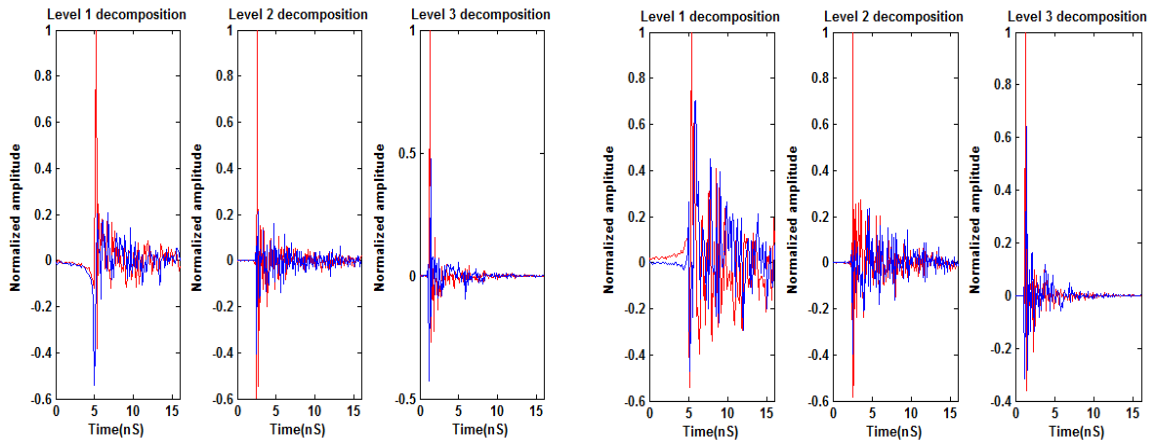


Figure 71: DTWT of replica .44 calibre revolver in isolation to the left and on body to the right

As with the replica .38 revolver, the replica .44 calibre revolver presented in Figure 71 is an excellent target for ease of detection. Its large geometric dimensions ensures that the waveform couples to the target efficiently and reradiates back to the antenna with a considerable intensity. In isolation as shown in the three plots to the left in Figure 71, the return from the main peak of the replica .44 revolver is even stronger than that of the replica .38 revolver. Moving the target onto the body has minimal effect, with the main peak of the signal from the revolver clearly present in all three levels of compression. This should ensure the target is both very easy to detect and presents sufficient features that the target should present only a limited challenge to any classification regime.

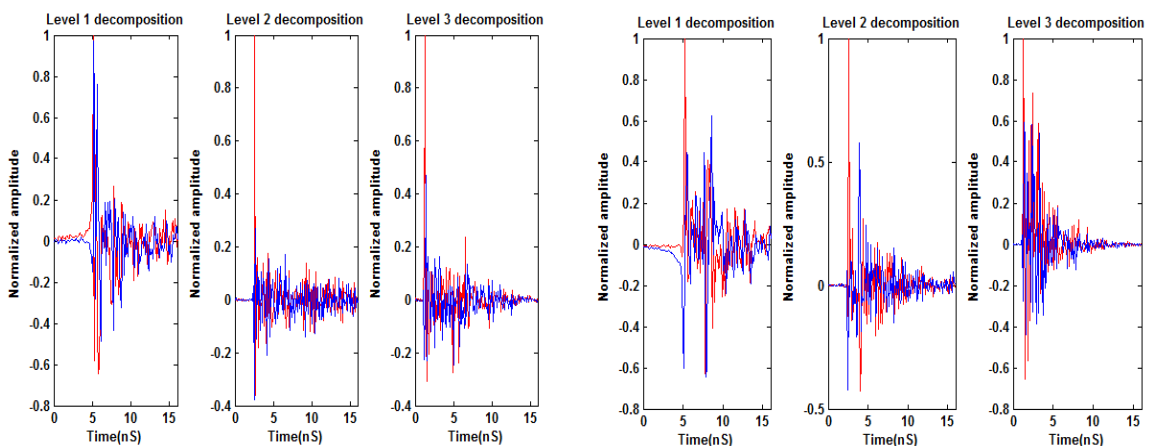


Figure 72: DTWT of Fujifilm digital camera in isolation to the left and on body to the right

The Fujifilm camera used as a non-threat item that may be found on the body is presented in Figure 72. The effectively planar surface that it presents to the radar system

when in isolation ensures a large peak at the point where the signal from the camera begins. When it is moved onto the body this large peak is still present, though the return from the addition of the body into the signal is almost half that of the return from the camera in the first 2 levels of compression. The strength of the secondary peak is even greater in the third level of compression reaching more than 75% of that of the return from the camera. The strength of this secondary peak in such close proximity to the primary peak could present significant issues for a classification regime. There is also a third major peak reaching 60% of the initial which could present an issue.

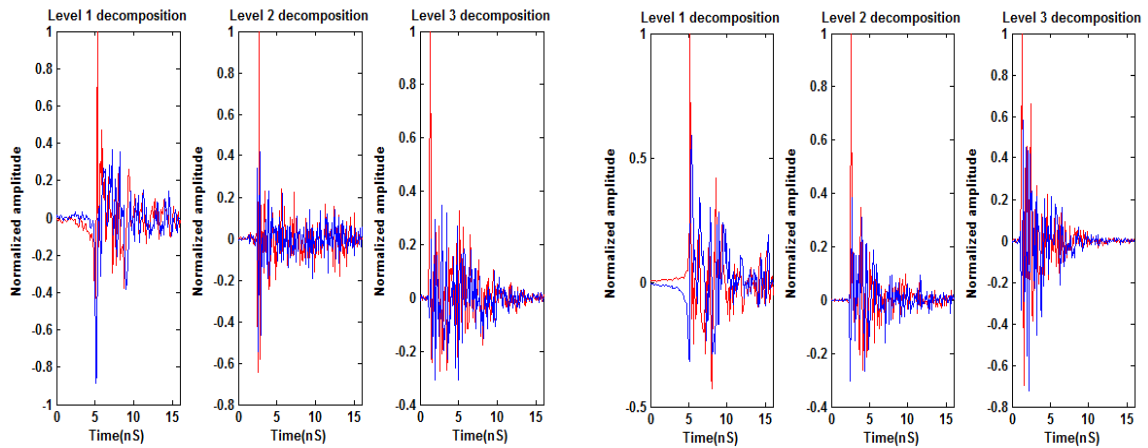


Figure 73: DTWT of keys and keyring in isolation to the left and on body to the right

The second non threat object, the keyring results of which can be found in Figure 73 presents a distinctive return which should make for simple classification. The major peak is clear in all three levels of compression for the object in isolation while when placed on the body, the secondary peaks introduced by the presence of the body in the signal are only limited in comparison for the first 2 levels of compression. Once the signal reaches the third level the secondary peak begins to become more substantial and could potentially present issues during classification.

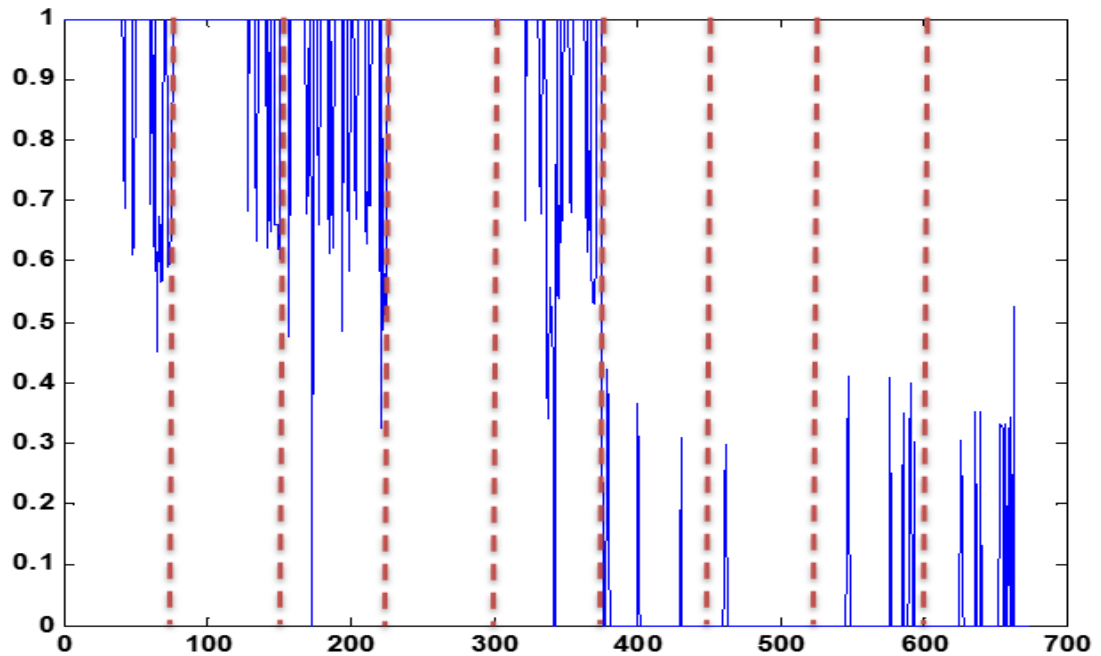


Figure 74: DTWT results for all 9 targets, 1 represents a threat, 0 represents a non-threat

The data presented in Figure 74 represents the entire target dataset classified either as 1 for a threat or 0 for a non-threat item. The objects are arranged as per Table 8. The data sent to the classifier is in the form of a matrix of three columns, with each column containing normalised results for one of the three levels of waveform presented. The first 5 targets, representing the first 375 points on the X axis are the threat items and so should all present as a value of 1. This is not the case therefore it can be inferred that the network is not perfect from this figure. The following 300 points represent the non-threat items. These should all present a value of 0 and as this is not the case therefore there will be some misclassifications in the network. The objects used are as per the order in Table 8: Table of Targets vs model order and resonant frequencies.

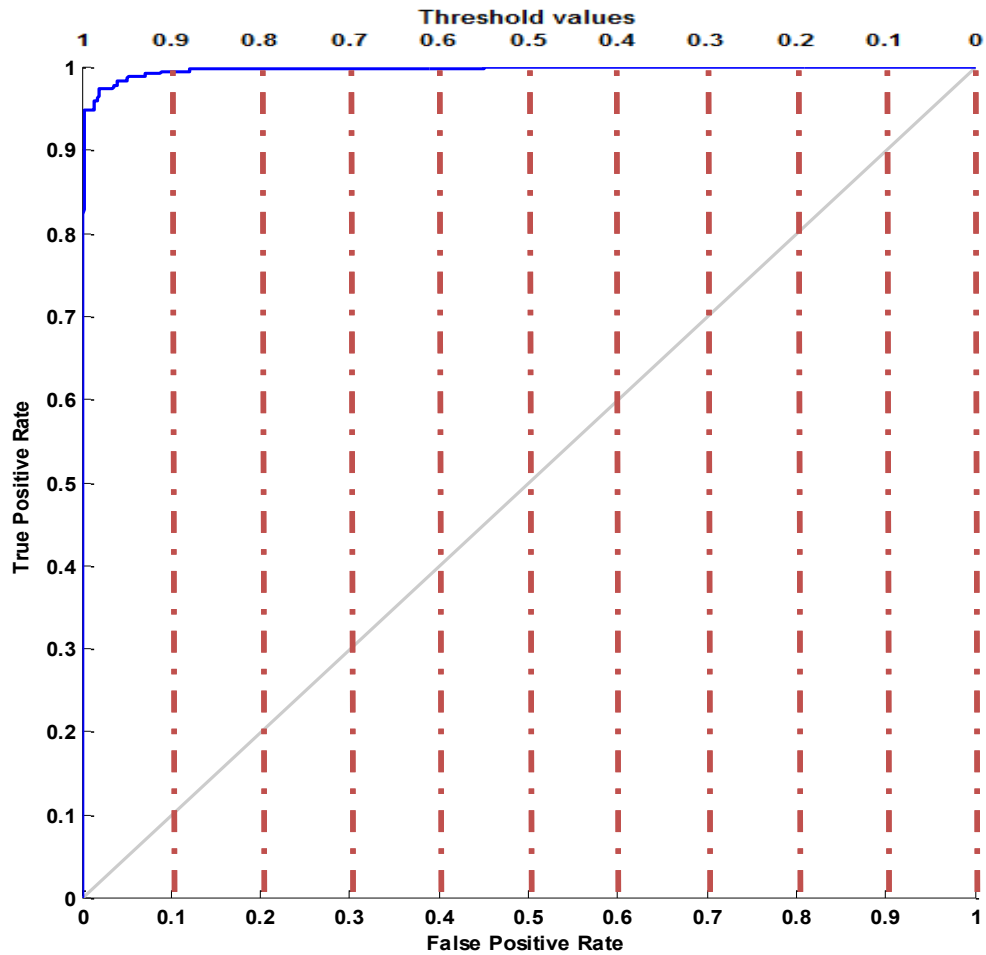


Figure 75: DTWT ROC curve, split dataset without PCA

Figure 75 presents the results of classification by an ANN for the DTWT dataset. The blue line on the figure represents the classification result at a given threshold value ranging from 0 to 1. The gray line represents the results of a 50-50 guess therefore a result appearing to the left of the gray line is of value while a result appearing close to or to the right of the gray line indicates a non-viable classification regime. This result was generated by taking a dataset, splitting it in two, training the network on one half of the dataset and then using the other half as a test set. Figure 75 shows data from the test set only without PCA applied. Figure 76 presents the same dataset with PCA applied. The application of PCA has given a small improvement in classification rates from 94% to 98%.

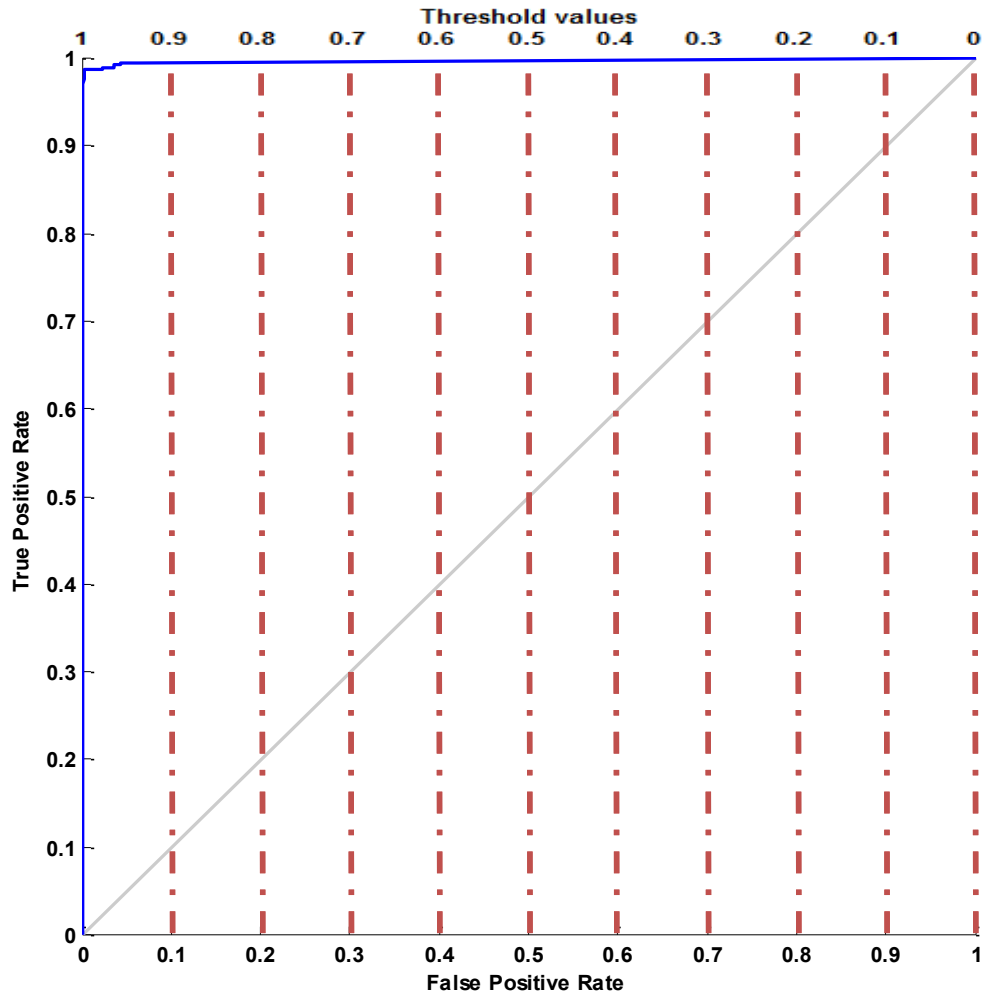


Figure 76: DTWT ROC curve, split dataset with PCA

In circumstances such as this very high true positive classification rates are possible with the rate without PCA reaching 94% and with PCA approaching 98% whilst still maintaining a zero false positive rate. A real world classifier that functioned as well as this would be ideal for security classification in high security environments. It must be noted that the DTWT has no capability to classify objects individually as the classification of an object dataset yielded no usable result.

Table 12: DTWT classification results with and without PCA

Target	Correct classification rate with PCA (%)	Correct classification rate without PCA (%)
11 cm steel rod	100	98.67
Kitchen Knife	95.76	95.76
Replica .33 calibre revolver	97.33	96
Gas Powered Target pistol	100	98.67
Replica .44 calibre revolver	94.66	89.11
Body, hands at side	95.76	95.76
Body, hands behind back	98.42	97.09
Fujifilm Camera	95.76	95.76
Keyring	98.42	95.76

6.2. The continuous complex wavelet transform

6.2.1. Overview

The CCWT is the preferred solution to wavelet based analysis of LTR security applications. It contains all of the benefits of both the continuous wavelet transform as well as complex wavelets without the reduced classification rate introduced by the DTWT. It is very simple to implement, using the same method as the real valued CWT, but as opposed to applying a real valued wavelet to both parts of a complex dataset, it applies a complex valued wavelet using the real values of the wavelet to transform the real component of the signal and the imaginary values of the wavelet to transform the imaginary component of the signal. Please refer to section 3.2.1 for a discussion of how the continuous wavelet transform works.

A number of different wavelets are available for use when performing complex continuous wavelet analysis. Of the many different types considered, the four that have shown to have value are discussed in section 5.1.1. The following section presents the results of the use of the complex Gaussian wavelet as it can be compared directly to the real valued Gaussian wavelet results presented in chapter 5 as opposed to the Shannon or Frequency B-spline wavelets which have no real valued equivalent. The same target set

used in the previous sections has been used for these experiments and so a direct comparison between the techniques is possible.

6.2.2. CCWT Results and Classification

The following plots, Figure 77 to Figure 85 follow the same structure as those presented in Figure 49 to Figure 57.

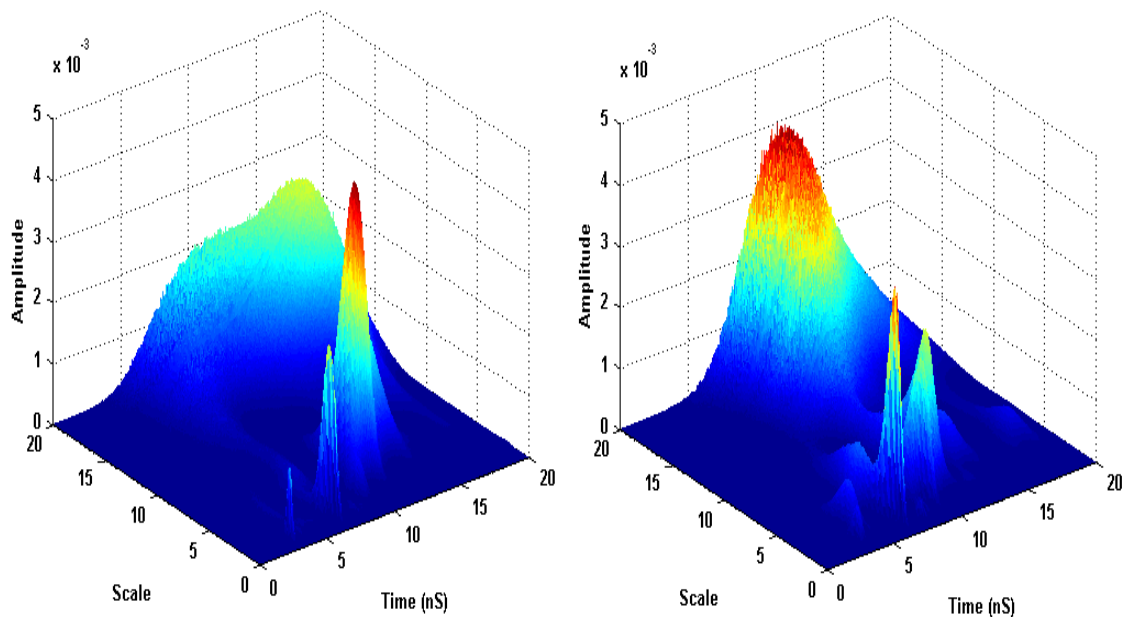


Figure 77: CCWT of body only, hands at side to the left, hands behind back to the right

Figure 77 shows the body in the two postures mentioned previously. As you can see the results are very similar to those presented by the real valued CWT in Figure 49. In fact for all intents and purposes the two returns are indistinguishable. This is useful as it shows that the return from the body is very consistent meaning that accounting for the effects of the body on the signal should be simpler. Once again it is important to note the intensities of the return from the body, these values sit in the range of 10^{-3} with a number of peaks varying in intensity over a large scale range. The presence of the arms in the signal as shown in the plot of the body with hands by the side returns a strong cross polar signal at a lower scale, while when the arms are removed from the signal the torso at a higher scale range has more influence on the signal. It is important to note that the intensity of the targets on body is reduced from that of the targets in isolation. This is due to the additional

processing required in order to distinguish the target when on body as opposed to in isolation and is consistent with the same effect found in section 5.1.1.1. The continuous real valued wavelet transform (CWT).

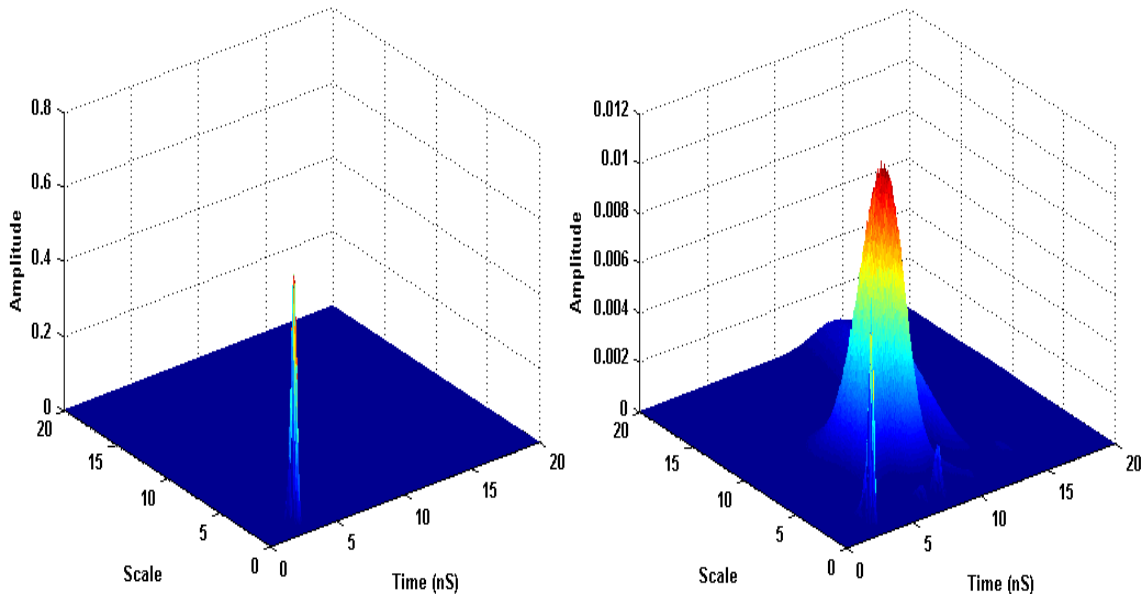


Figure 78: CCWT of 6.5 cm needle in isolation on the left, 6.5 cm needle on body on the right

The CCWT result of the 6.5 cm needle on body in Figure 78 is similar in scale range to that found in Figure 50 of the same object using the CWT. As with previously presented figures it produces a sharp peak when in isolation though in this case the peak retains more energy after the transformation. It is interesting to note that using this method for the target placed on the body, the ratio of energy in the target signal versus that of the return has changed, showing that contrary to expectations in this case the CCWT actually makes it more difficult to successfully detect and classify a needle on the body. The needle return can be found at ~ 4 ns on the time axis with a scale range of 0.8 to 1.7. The intensity of the peak from the needle has also been considerably attenuated. This attenuation could potentially be caused by the position of the needle on the body being physically masked by a part of the body therefore completely blocking a percentage of the return signal.

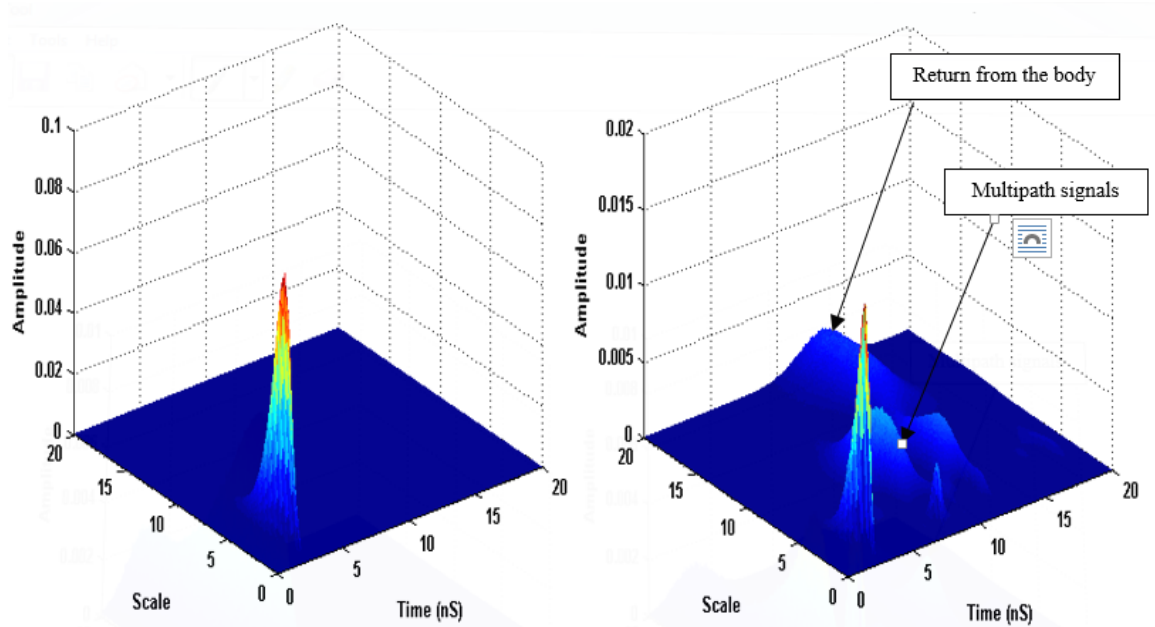


Figure 79: CCWT of 11 cm steel rod in isolation on the left, 11 cm steel rod on body to the right

Fortunately, the effect of the body increasing in magnitude does not consistently alter the returns using the CCWT. In the case of the 11 cm steel rod, presented in Figure 79 it is apparent that the target in isolation is still a well-defined peak with a small spread over the scale range. When comparing to the CWT result in Figure 51 the similarities are apparent. Moving the target onto the body and processing using the CCWT does present some differences to that shown in Figure 51, as the effect of the body in the signal is minimal, while the peak from the rod is still clearly apparent. The return from the target is located around ~ 4 nS with a scale range of 2.3 to 5.4. It is important to note that the intensity of the peak presented by the steel rod has been somewhat attenuated though not as significantly as the 6.5 cm needle.

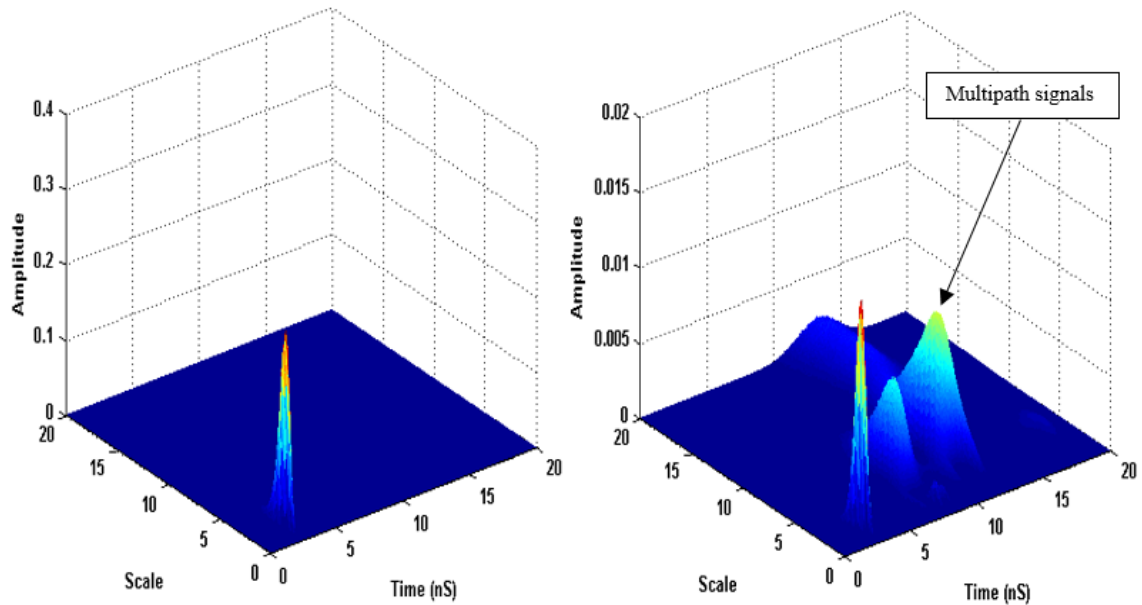


Figure 80: CCWT of kitchen knife only to the left, on body to the right

For the small kitchen knife, results of which are presented in Figure 80 the return from the knife in isolation is still represented by a well-defined peak with a small spread over the scale range. Figure 52 which presents the results of the CWT of the same target shows there to be a small amount of clutter towards the higher scale ranges, in the case of the CCWT this is not present. The scale range at which the return from the knife can be found peaks between 2.1 and 2.9 at ~ 4 ns on the time axis. When the target is moved onto the body it is still clear that the return from the needle is present in the signal, although it must be noted that there are some secondary peaks caused by the interaction of the signal with the body that are potentially of high enough intensity to cause problems in classification.

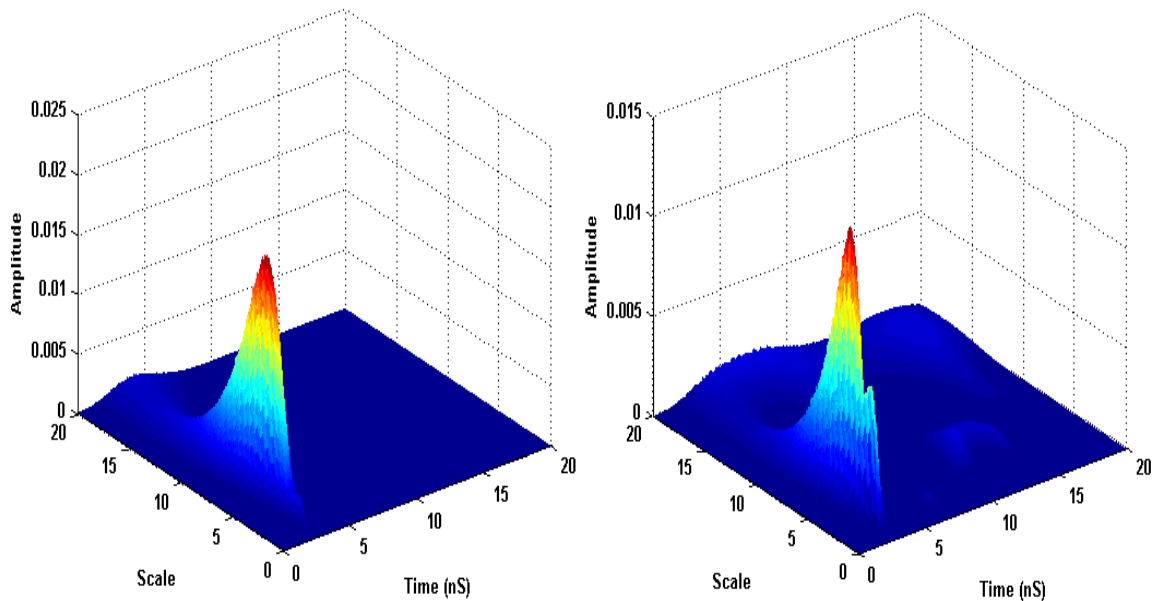


Figure 81: CCWT of replica .38 revolver in isolation on the left, on body to the right

The CCWT result for the replica .38 revolver presented in Figure 81 shows similar characteristics to that of the CWT for the same target presented in Figure 53. When the target is presented to the algorithm in isolation, a strong peak with a reasonable spread over the scale range is apparent though this scale range is concentrated between scale 5 and 10. A low intensity component of the signal can be found in the scale ranges from 10 upwards. When the target is moved onto the body, once again the revolver proves itself to be a very simple target to detect as the return from the target masks that of the body. The scale range at which the revolver can be found is between 5.4 and 11.7 at ~ 4 ns on the time axis. In the case of the CCWT dataset there is very little of the return from the body that can be discerned. It must be noted that some attenuation of the signal does occur, though not to the same level as with previous targets and that the peak from the revolver has deformed towards the lower end of the scale range available.

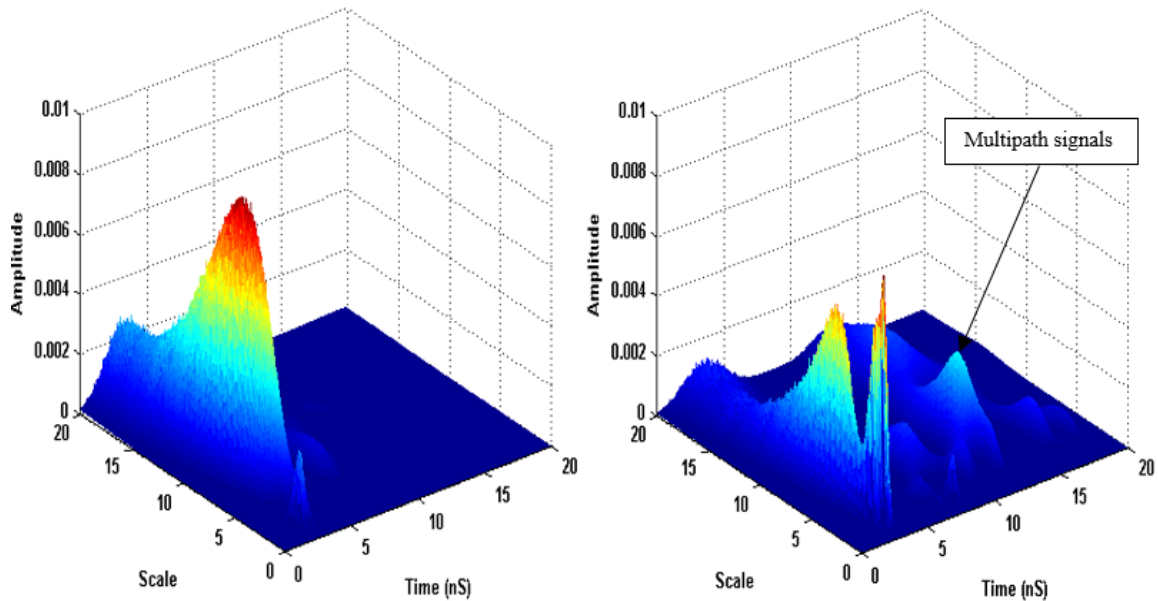


Figure 82: CWT of GP target pistol only to the left, on body to the right

The result of the experiment using the gas powered target pistol with the CWT processing technique is displayed in Figure 82. As previously demonstrated in figure 52 by the same target with the CWT applied, this target presents a very broad range of scales when presented in isolation. The scale range at which this target can be found is between 8 and 24 at ~ 4 ns on the time axis. When moved on to the body there is a similar effect, though it is interesting to note that the deformation of the peak at lower scales presented by the revolver in Figure 81 has also occurred with this target only to such a degree that two distinct peaks at different scale ranges are visible. The return from the signal interaction with the body is heavily suppressed such that it should have minimal to no effect on classification algorithms.

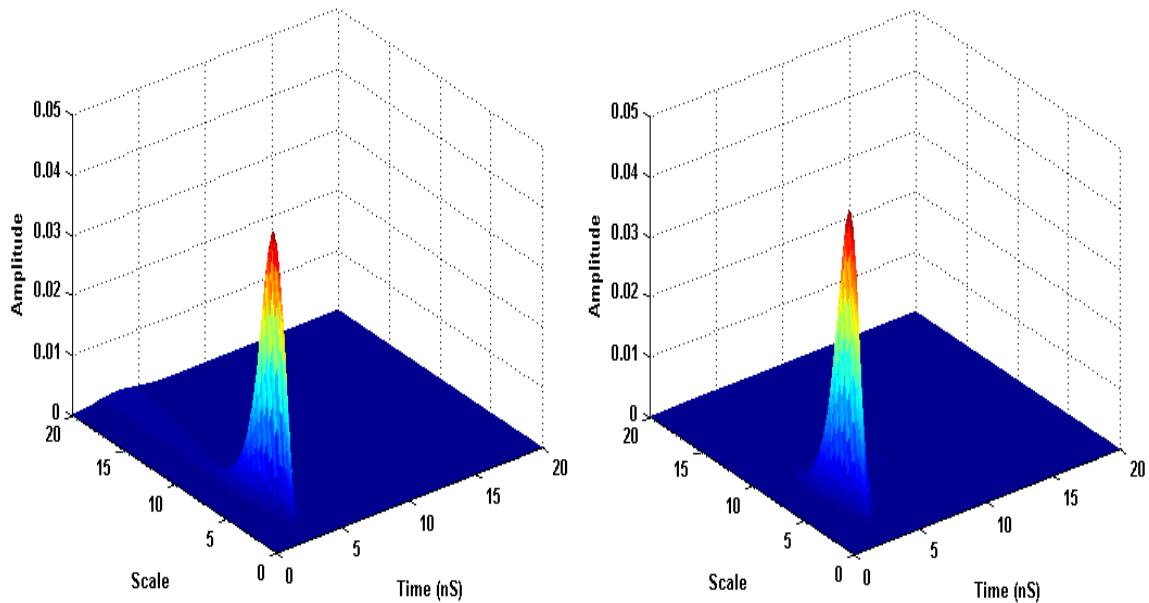


Figure 83: CCWT of replica .44 revolver only to the left, on body to the right

The large replica .44 calibre revolver has also been tested using the CCWT based method. The results of this presented in Figure 83 are quite unique amongst the target sets used in this work. The target in isolation presents as a well-defined peak with a small spread of scales as with the result of the CWT for the same target in Figure 55. The scale range between which this target can be located is 3.5 and 6.5 at ~ 4 ns on the time axis. The target on body also presents as a single well defined peak with a small spread of scales and the return from the signals interaction with the body has been completely suppressed. This indicates that the replica .44 revolver is an ideal target for classification as its characteristics are such that the presence of a larger geometric but nonmetallic object such as the body is not able to interfere with its return.

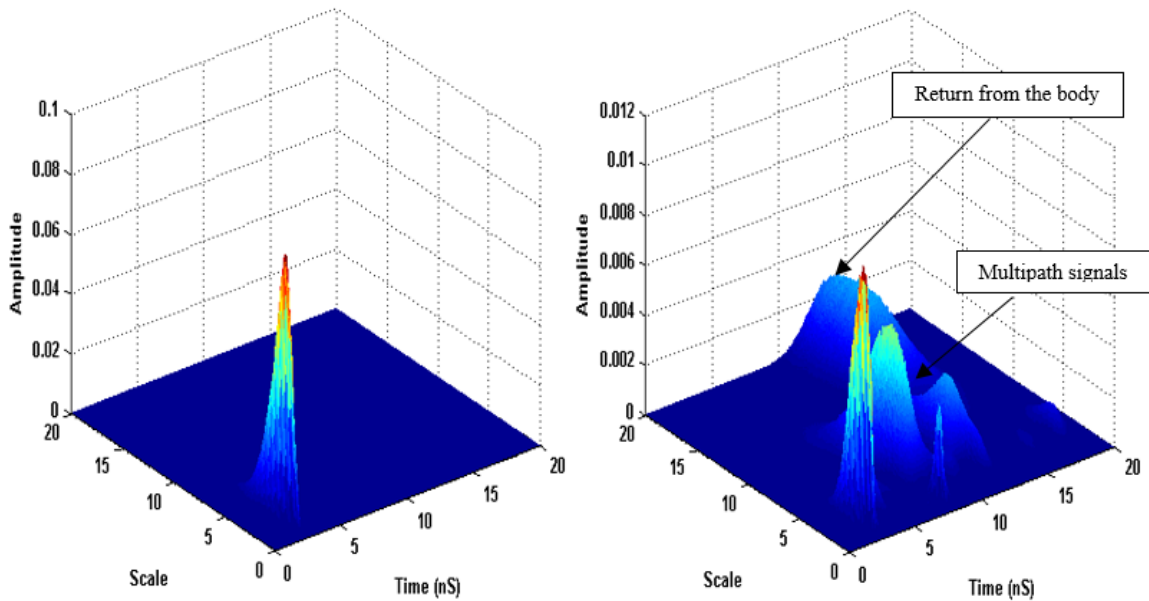


Figure 84: CWT of camera in isolation to the left, on body to the right

The Fujifilm camera presented in Figure 84 shows some useful characteristics. In isolation its single well defined peak allows for ease of identification of the needles characteristics while when it is moved on to the body, this peak is still clearly present. The scale range at which the camera can be located is between 2.4 and 4.4 at ~ 4 ns on the time axis. It must be noted that the peak has been heavily attenuated and so is now in a similar range to the return from the signals interaction with the body. Indeed the peaks representing the clutter introduced by the body in the signal are approaching 60% of the value of the return from the camera.

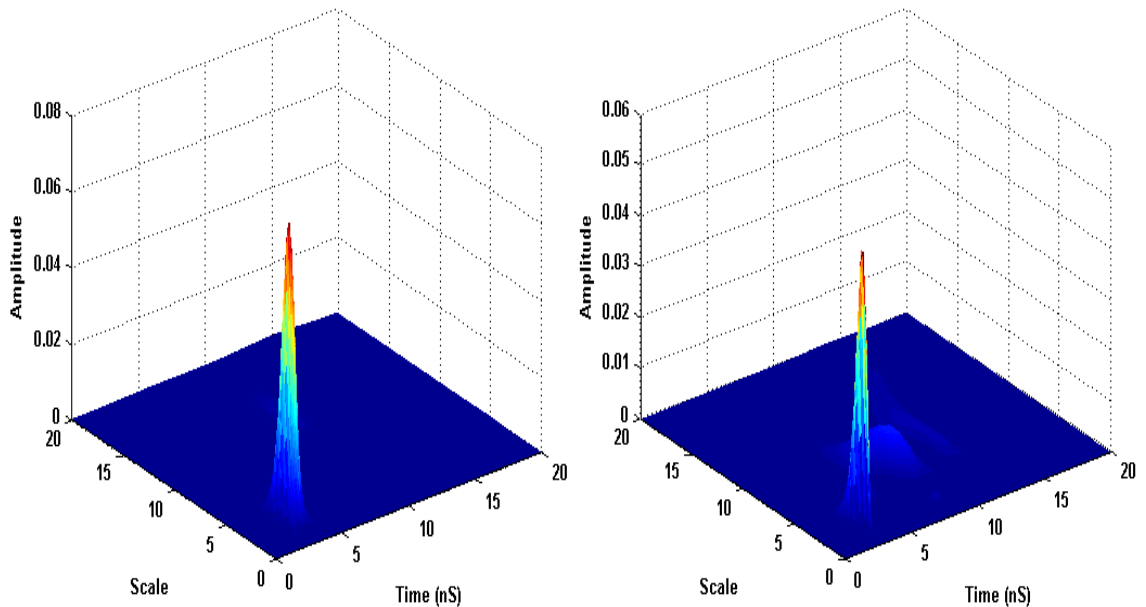


Figure 85: CWT of Keyring only to the left, on body to the right

The second non threat object presented is the keyring. Figure 85 demonstrates the result of applying the CWT based technique to this particular target. As before it is apparent that this target offers a very LTR signal and as such is very easy to detect. It also has a very similar effect to the revolvers presented previously in that when the body is introduced to the signal, this target is capable of suppressing the signal from it. The scale range at which the keys can be located in this instance is between 2.6 and 4 at ~ 4 ns on the time axis. As there is a large quantity of metal present and all are of a complex geometric nature, in all the targets that are capable of having this effect it must be considered as to whether the quantity of metal present can be used to determine a threat object and if any successful method could be used to eliminate non threat items such as keyrings from detection.

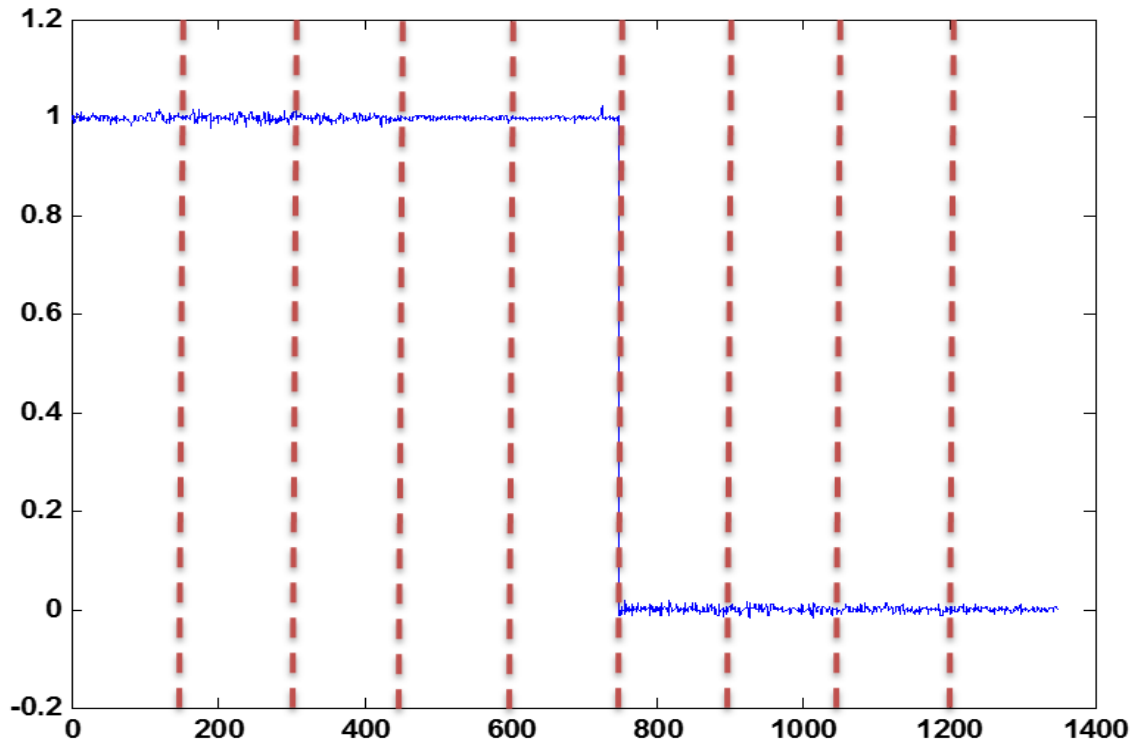


Figure 86: CCWT plot of all 9 target sets with value 1 as threat and value 0 as non-threat

Figure 86 shows the result of the binary threat/non-threat classifier using the CCWT. All 9 targets are presented as per Table 8 with 150 sweeps for each target and can be compared with Figure 61. It is known that the first 5 targets are threat items on the body therefore the plot in Figure 86 should show a value of 1 as far as 650 points in. This is the case as the blue line representing the result has stayed high to this point. It then drops down to 0 as would be expected for the remaining 600 sweeps. This is an excellent result as it has successfully trained and classified on the dataset. All objects are presented in the order laid out in Table 8: Table of Targets vs model order and resonant frequencies.

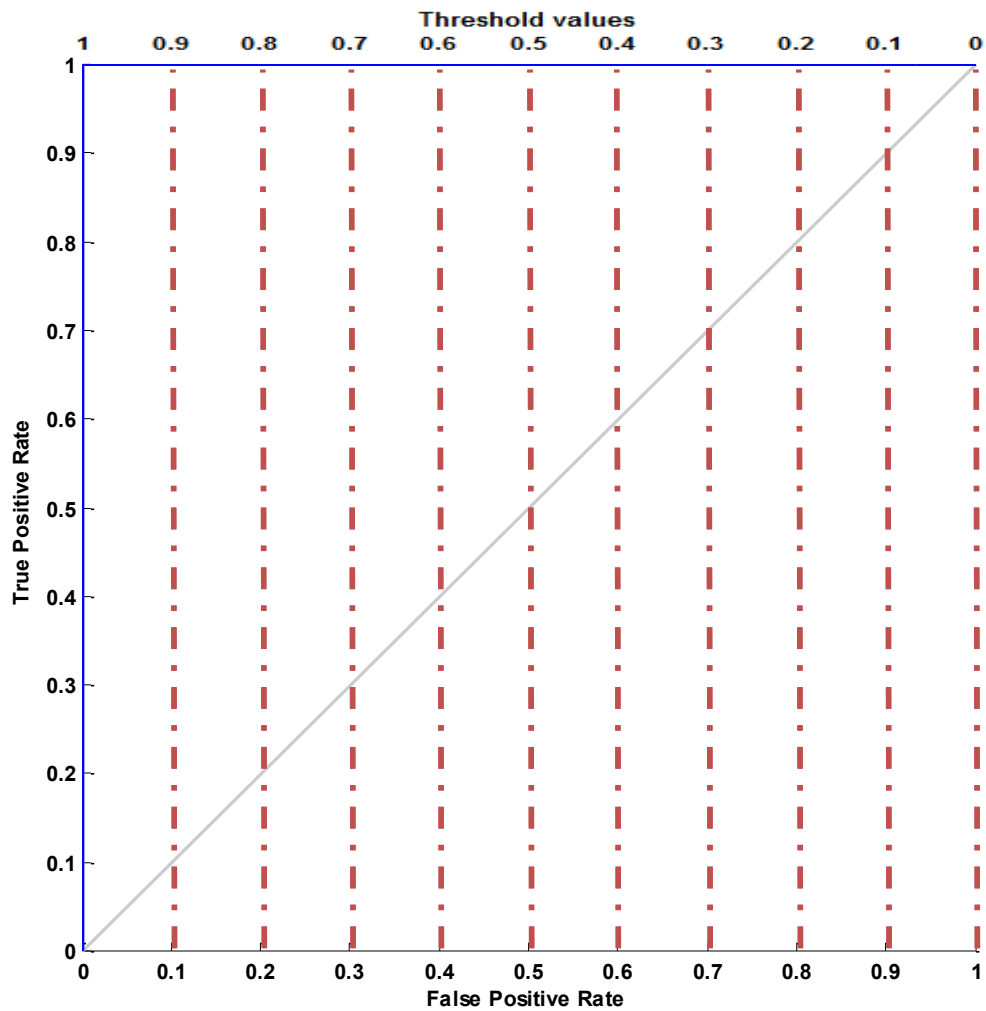


Figure 87: CCWT training ROC, binary classifier

Figure 87 is a ROC curve representing the same dataset as that shown in Figure 86. As the result in Figure 86 was close to a perfect result, the blue line in Figure 87 would be expected to stay very close to the Y axis until it reaches a value of 1. As this is the case, it can be seen that for any threshold value, with this particular test set the classifier is very effective. It is important to see if this result can be generalised to different datasets.

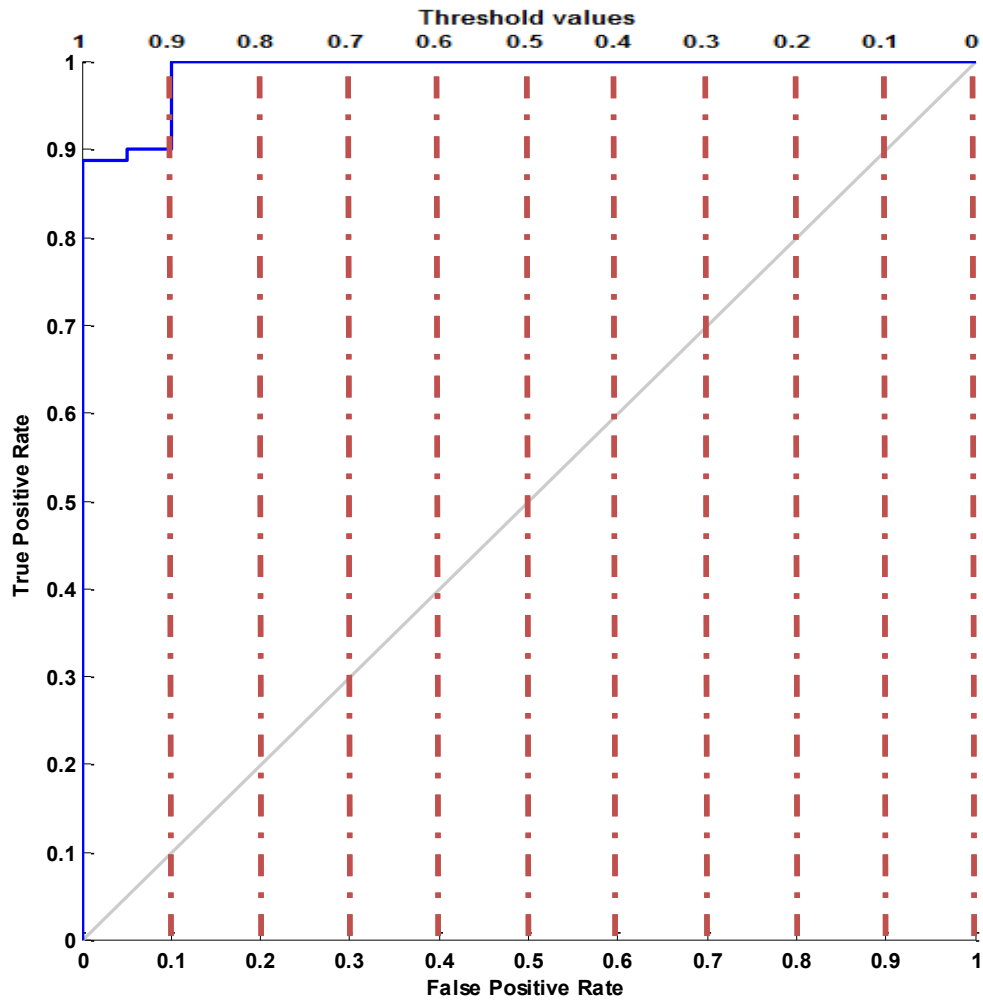


Figure 88: CCWT generalised ROC, binary classifier

Figure 88 is a ROC curve representation of the trained neural network used in Figure 86 and Figure 87 on a generalised data set. To test the sensitivity of the network to target type, a further set of data was taken using similar weapons and benign objects at different target range with a differing number of points. This generalised data set was processed using the same method as applied to the CCWT test set. It was important to test the effect of range as it could potentially have had a significant effect on the classifiers performance due to changes in received power levels. The number of points taken was altered to test whether this could cause loss of resolution sufficient to increase errors in the classification algorithm. The classification algorithm has proven to be robust as it has maintained a very

high true positive classification rate, although it must be noted that the value of the true positive classification rate where false positives will be 0% has dropped from 100% to 88%. This means that in order to successfully detect all targets passing the systems field of view, it would be necessary to set the threshold value to 0.9. This would incur a penalty of a 10% false positive rate which is very high for a potential practical system. It would be more useful to set the threshold to 1, thereby only having a successful true positive rate of 88% and sweeping targets multiple times.

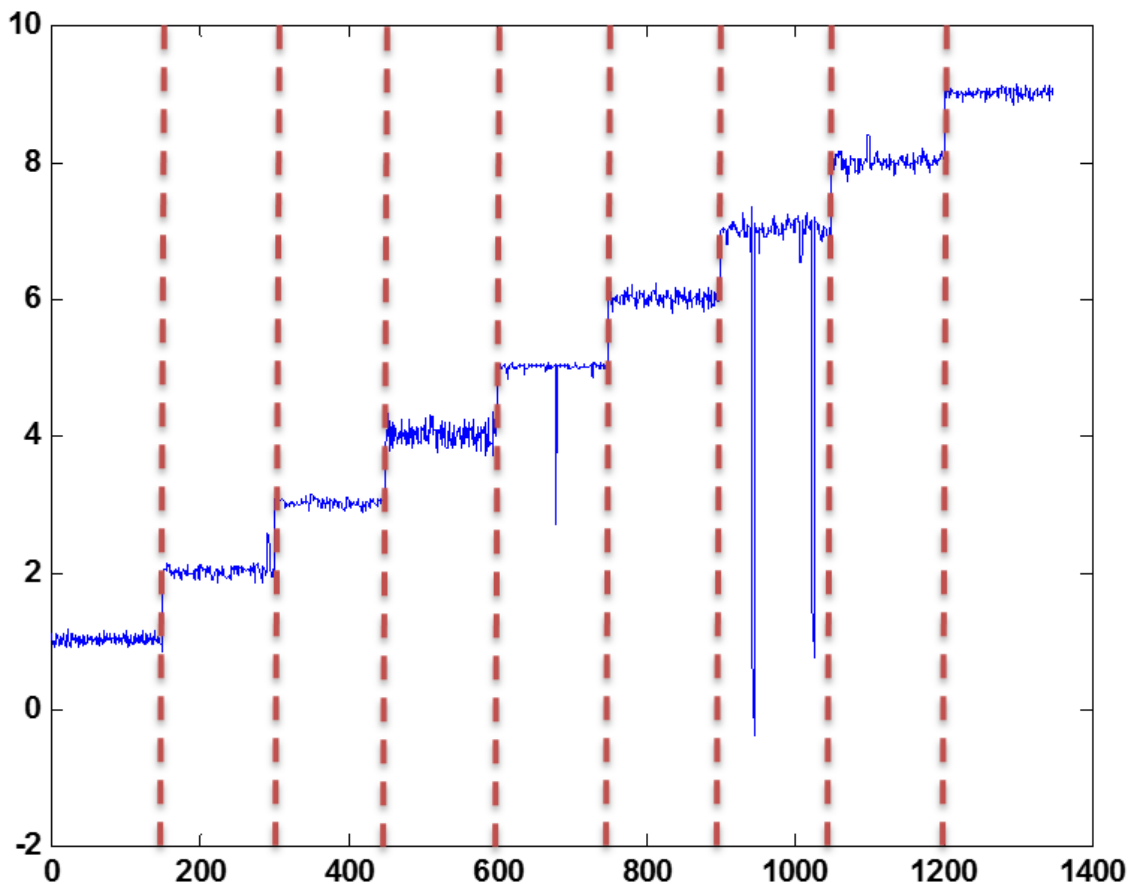


Figure 89: CCWT plot of all 9 target sets against their expected classification value

The additional complexity of attempting to classify 9 different objects on body provides for a complex representation on the plot in Figure 89 and can be compared with the data shown in Figure 63. The expected value for each target can be found in Table 8. The data presented is from the test set and presents a good result for classification with only a few misclassifications. The result of applying a threshold of ± 0.3 to the dataset can be found

in the following ROC curve. This threshold value of ± 0.3 was chosen as it allowed for some small variation in target response due to movement etc. while presenting the best result for true positive classifications of the targets given and keeping false positives to a minimum.

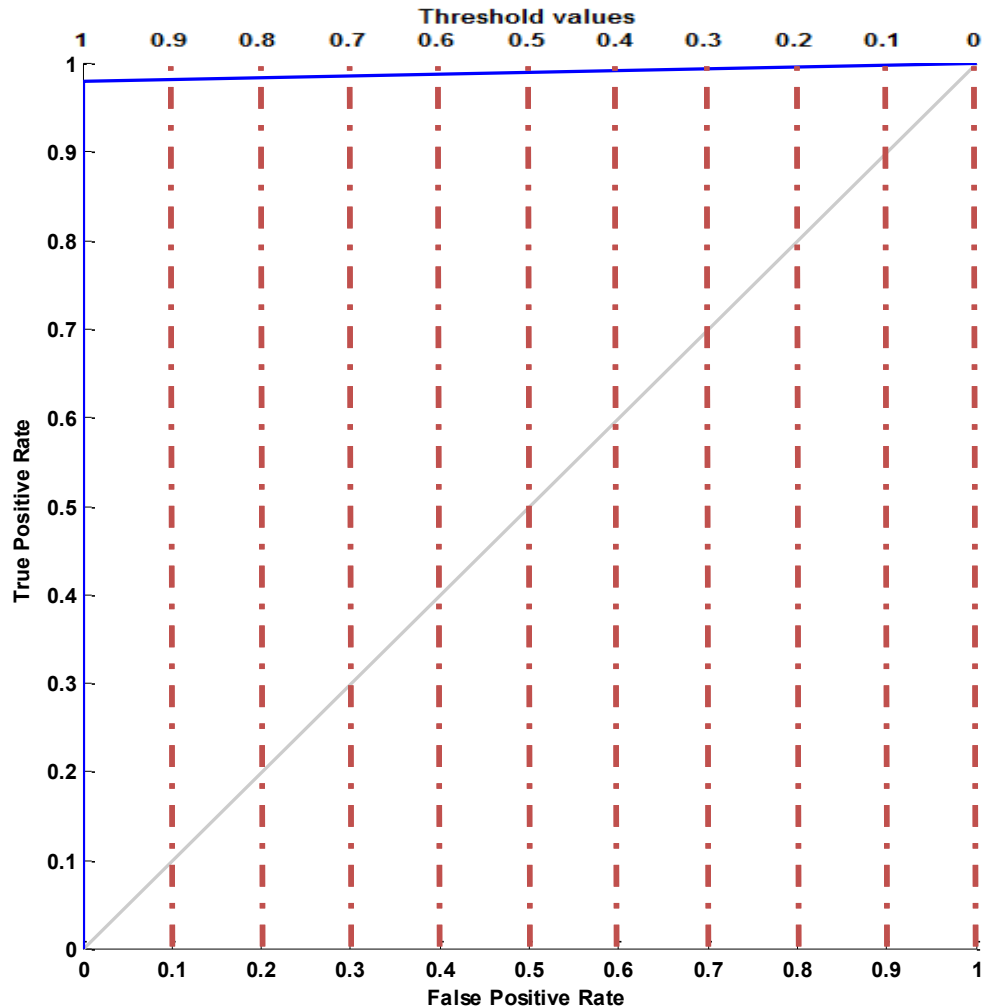


Figure 90: CCWT 9 object classifier, split dataset

Figure 90 is the ROC curve representing the trained neural network used to produce Figure 89. As can be seen the true positive classification rate remains very high for this dataset, approaching 97% while keeping false positives to a minimum. When compared to

Figure 64 representing the CWT result for the same target set where the true positive classification rate is 83%, a marked increase in performance can be noted.

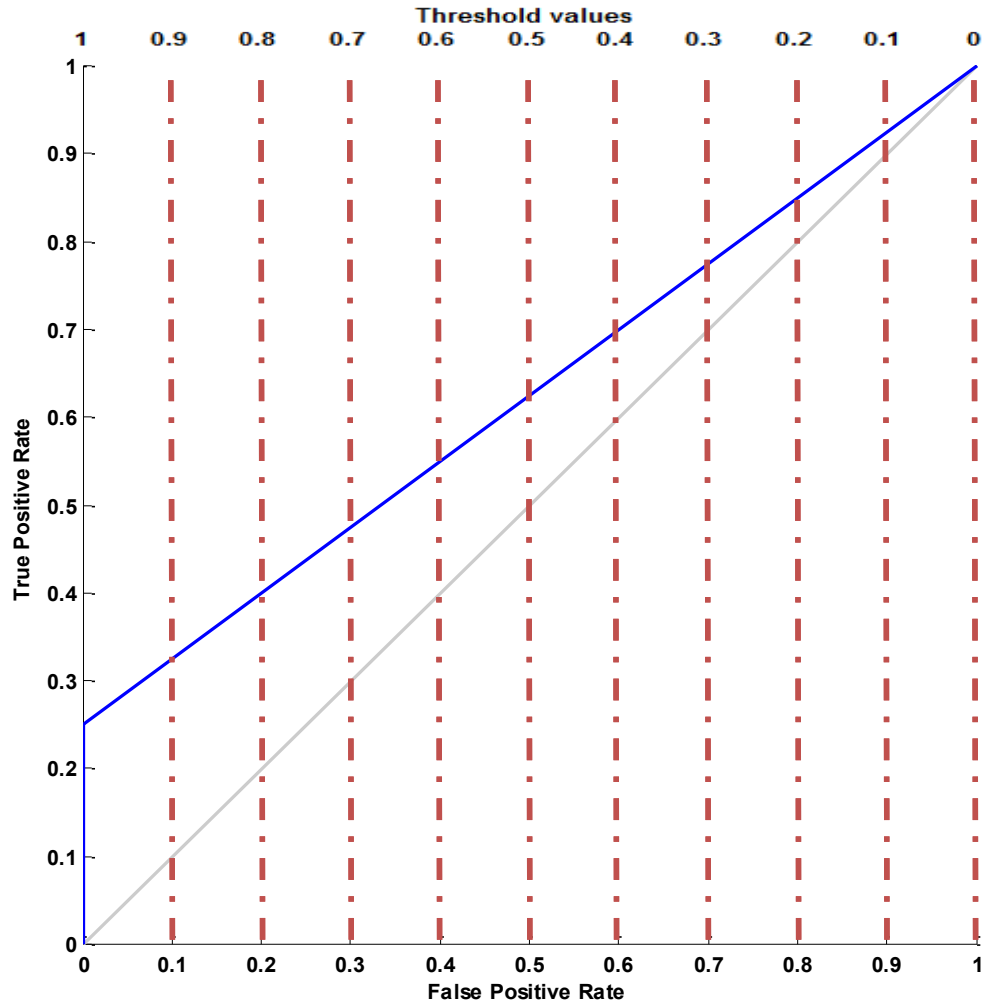


Figure 91: CCWT Generalised 9 item classifier

Finally the generalised result for the 9 object classifier is presented in Figure 91. This result differs from that shown in Figure 90 as it uses a generalised dataset on which the classifier was not trained. The true positive classification rate is located around the 25% mark, very low when compared to other datasets though it must be noted that this is greater than the result of the CWT, the result of which is the same as the gray line on Figure 91. It is notable that this is the only method that showed a greater than 50-50 guess result for the generalised 9 item classifier. The results for the 9 object classifier using the CWT, DTWT

and GPOF methods have not been included as they show no better performance than a 50-50 guess.

Discussion

This chapter has presented the results for tests performed using both the DTWT and CCWT for LTR security applications. It has been determined that the DTWT is able to perform binary threat/non-threat classification though it has no capacity to be able to classify different items specifically. The CCWT has shown itself to be the most capable of all the algorithms tested, with high classification rates in binary threat/non-threat classification and some capability to classify individual though these classification rates are considerably lower than those presented in binary classification.

Chapter 7

Discussion and conclusions

Preview.

This chapter presents a discussion of the work performed in the previous chapters. This discussion will focus on potential scenarios in which an LTR system may be deployed and how the results may be applied to a practical weapons detection system. The discussion will also cover the issues discovered with the different techniques and the mitigating actions that should be taken to allow for a creation of a viable LTR system and the appropriate algorithms to be used.

7.1. Summary of work done

A laboratory evaluation of the LTR has been carried out and involved the use of a VNA to provide the source for an UWB radar system which illuminated targets to excite and extract CNR's. The VNA itself provided a sweep of 500 MHz to 3 GHz has been used. The additional higher frequencies available with the VNA could be used to detect smaller objects via the LTR method in other scenarios although it is important to note that for this, some technical hurdles will need to be overcome.

The experimental work performed was supplemented by computer simulations performed on objects in isolation and have helped to confirm the expected locations of the fundamental resonant frequencies for a selection of the targets used. This has backed up the theory and provided additional confidence in the practical results obtained. A complete simulation of objects and a human body has proved to be impossible as due to the density of the mesh required, the limitations of the computer memory available mean that any mesh created is not sufficiently dense and so cannot provide an accurate result.

The data analysis techniques used have proven themselves critical to the LTR method that has been developed. The application of the matched filter and wavelet filters with time gating to reduce noise in the signal and windowing the area of interest within the signal have allowed the required processing volume to be reduced. Also adjustment of parameters applied to the SOM has shown the capability of reducing processing time further, without

sacrificing much with regard to accuracy. For certain of the methods tested, PCA has also shown itself to be of value in reducing false positives.

7.2. Assessment of how project objectives were addressed

The three main objectives for this research program are outlined in section Aims and Objectives of the Research Program. Each of these represented a step along the road to creating a suitable algorithm for threat classification in the real world. Objective 1 was to develop a reliable method of detecting a target in isolation and develop a suitable algorithm for processing the data using the GPOF method. The results of this can be found in the plots from Figure 36 through to Figure 44. A discussion of the approach taken in the development of this algorithm can be found in Chapter 2 and further details can be found in Chapter 4. This objective required that a number of techniques already believed necessary be verified and improved upon. The successful completion of this allowed for progression on to objective 2.

Objective 2 required that an investigation into multiple objects present in the same radar beam at the same range be undertaken. Details of this can be found in section 2.3.2. Single and multiple target detection in isolation and in [1]. This investigation showed that it was possible to detect two objects of similar dimensions when both objects were at the same range using LTR based methods. This required much more accurate windowing of the signal and detection of the first two major peaks with windows placed around both. The confirmation of this allowed further progression on to objective 3.

Objective 3 involved determining the impact of the LTR based method in detecting objects in different environments, in particular environments where the LTR of the object in question may be obscured by the return from a larger, complex geometric object. This objective represents the bulk of the results presented in this thesis in Chapter 4, Chapter 5 and Chapter 6. These results clearly show that it is possible to detect the LTR of an object of interest when it is in close proximity to a much larger complex geometric object. Once this had been determined it was then necessary to increase the scope of the research and determine if it was possible to use machine learning to identify these objects. This required the introduction of a number of statistical signal processing and filtering techniques in order

to allow for machine learning algorithms to process the data. These techniques have proven successful allowing for true positive classification rates on test datasets of between 70% and 100% for binary threat/non-threat classifiers. The GPOF and DTWT classifiers represent the most computationally efficient algorithms, although they also have lower true positive classification rates than the continuous wavelet based methods. Application of these methods in a security environment would require a target to be scanned multiple times to ensure successful detection. The higher classification rates made available by the continuous wavelet based methods would require fewer scans be taken though this comes with the drawback that the greater computational intensity of these algorithms would require either longer processing times or more capable/expensive computer hardware.

When applied to generalised datasets the binary true positive classification results approached 88% for the CCWT and 25% for the individual object classifier. With more complex problems such as identifying individual objects only the continuous wavelet based methods were able to process this with lower true positive classification rates at between 84% and 97% for the test set using these methods.

The overall aim of this research project as outlined in the aims and objectives, to investigate the application of Late Time Response based techniques to develop an algorithm that will robustly detect concealed threat objects in security environments, has been met and exceeded. Four potential classification algorithms that could be used are described in chapters 4, 5 and 6. The benefits and downsides in the use of each of these algorithms has been outlined and a determination made that the algorithm that best meets the requirements of a potential LTR security system is the CCWT. A discussion as to the best type of wavelet for use with this transform has been presented with the Gaussian wavelet showing itself to be the most effective. A discussion of the benefits and downsides of each of the four algorithms developed has been presented at the end of chapters 4, 5 and 6 with a conclusion as to the best choice for overall performance being made.

7.3. Discussion

7.3.1. Signal smearing

A viable LTR security system has a number of potential deployment opportunities. The physical requirements of the experimental LTR system used here will allow for either a fixed installation system or a system that could be installed in a vehicle. Unfortunately due to the low frequencies at which the fundamental resonances for most objects of interest are found, the antennas required are large making a man portable system highly unlikely. It is envisaged that a deployed fixed installation LTR system using the algorithm developed could involve the use of a planar array of concurrently fed patch antennas [159], allowing for the creation of a wideband RF sweep and control of the beam while reducing the form factor of the system. This system could then be deployed on the walls in secure areas, allowing for scanning individuals as they walk by.

This does lead some to potential problems, preeminent among which would be the effect of moving targets. This causes a change in the return time from an observer moving relative to the signal source during the time taken to complete the frequency sweep, which in turn could cause the LTR returns from target objects to become confused, rendering the classifier as trained ineffective. Therefore the design must be robust enough to handle a certain level of motion before smearing in the signal will become an issue. As a human being can walk approaching speeds of 1.4 m/s, the sweep time of the system must be set to accommodate this. The sweep time is currently limited by the VNA setup to 256 ms. Use of discrete hardware could improve this. For example at a frequency of 1 GHz, time smearing should be kept to less than 0.5 ns to avoid smearing. Therefore the maximum allowable motion within the beam can be calculated using Equation 67:

$$\Delta L = \left(\frac{0.5 \times 10^{-9}}{2} \right) \cdot 3 \times 10^8 = 75 \text{ mm} \quad \text{Equation 67}$$

With ΔL the maximum allowable motion in the beam before smearing occurs. This requires that the frequency sweep be completed within 25 ms, which could be achieved using customized hardware. The ability to scan targets in motion has a fundamental

advantage over many portal based systems currently in production, in that it could reduce the issue of bottlenecks at security checkpoints.

7.3.2. Attenuation

Another consideration is the sensitivity of the system to the microwave power employed. The power levels used range from 2 dBm to -4 dBm with little variation in performance found. This is important because the strength of the return signal can be affected by target distance and by attenuation due to clothing. Rahim et al [160] discuss the effect of four different textiles on path attenuation of a signal in line of sight and non-line of sight scenarios at frequencies between 2 GHz and 3 GHz. Another potential problem is the attenuation caused by the materials used to make the clothes themselves. Rahim et al [160] conclude that of the materials tested, polyester produces the most attenuation of the signal, approaching a loss of 13.9% with the major contributing factor being the dielectric constant of the material. When compared to results at higher frequencies as demonstrated in [59] these low frequency losses are of lesser magnitude. The power values used have been successfully tested out to ranges of 3 m with similar results for each demonstrating the robustness of the algorithm in handling attenuation and indicating that lower frequencies suffer less attenuation by clothing.

7.3.3. Filtering and SNR

There are two different filtering approaches applied in the work presented, one for the GPOF based approach and the other for the wavelet based approach.

The first step in filtering applied to the GPOF was to average 10 sweeps of the target together to reduce noise. This was followed by time-gating the signal, an approach which removes information outside the region of interest. This was followed by a matched filter, used to maximize the SNR before processing with the GPOF.

The filtering for the wavelet based algorithms involved time-gating of the signal as only a single sweep was processed each time for this. The next step comprised a wavelet based

threshold filter using a Gaussian mother wavelet followed by a SG filter for high frequency noise.

The goal of the filtering methods applied is maximizing the SNR of the signal while minimizing any changes caused by filtering the signal. The GPOF filtering approach of using a matched filter requires some knowledge of the signal a priori and the averaging of the 10 sweeps together introduces longer scan times. This led to the introduction of the single processed sweep to reduce scan times and the SG filter to remove high frequency noise. The matched filter was replaced by the wavelet filter when using wavelets as it does not require a priori knowledge of the signal and can therefore be applied simply.

Deconvolution of the transmission characteristics from the signal is a necessary component of the algorithm if any successful LTR signal is to be extracted. This has been analysed in two ways, firstly linear deconvolution which performs a division in the frequency domain of the known transmission signal from the target scans and secondly with non-linear deconvolution, which comprises either the CLEAN or Richardson-Lucy deconvolution methods. The linear deconvolution method is very effective in its ability to remove transmission characteristics from the signal, although in cases where the signal sweep is broader than the available frequency range of the horns an offset must be added into the transmission in order to prevent a case where the signal may be divided by zero. The non-linear deconvolution methods have shown they are able to help with frequency extraction in some circumstances, though the additional computational complexity introduced by these algorithms and the requirement for a priori knowledge in order to apply them effectively does limit their utility.

7.3.4. Feature extraction and classification

Intelligent learning processes such as artificial neural networks are a growing area of research in security applications. The ability of feedforward backpropagation neural networks to classify unknown targets after presentation of a set of training data is very useful when attempting to identify these items. These networks are very adaptable with performance depending on the size of each layer of neurons and transfer function that is

chosen [161]. The hidden layer of the FFBP networks used comprised 8 neurons and used tangent-sigmoid transfer functions while the output layer of 1 neuron uses a linear transfer function allowing for an output value ranging between any set ranges of the designers choice. For the 9 object classifiers used the hidden layer comprises 60 neurons. An alternative to this would be to have an output layer comprising as many neurons as targets that the network is trained for. This would make the network larger and more complex to train, though it would allow for the use of a tan-sigmoid transfer function on the output layer which would constrain the values between 0 and 1, potentially improving classification rates for larger target sets. For the current approach the ANN's used have proven to be very effective and robust. Faster training networks such as cascade feedforward networks [144], which operate by including a connection from the input layer and every previous layer to the following layers have been considered. Although there is an improvement in training time, it does not present a sufficient improvement to justify the extra complexity of the network therefore the FFBP network was selected as the classifier of choice.

The training functions available to teach the neural network to classify the targets presented to it are numerous. A common method uses Levenberg-Marquardt optimization. This is effective though it has two drawbacks in that training using this method is slower when compared to other methods and it can potentially find a local minima while training rather than the global minimum, leading to suboptimal network operation. Use of the gradient descent with momentum and adaptive learning rate backpropagation training functions greatly accelerated the training speed of the algorithm but did not address the algorithm potentially resolving to a local minima. The solution that allowed for both drawbacks to be resolved was to use conjugate gradient backpropagation with the Powell-Beale restarts training function [144]. This approach has both improved training speed and ensures the network will resolve to a global minima.

The utility of PCA in dimensionality reduction of datasets is well known. The method's ability to determine the most useful components of a dataset and eliminate those that don't contribute sufficiently to the overall picture provides an excellent capability to any application to which it lends itself. Of the many statistical methods available, PCA was

chosen because it allows for rapid processing of datasets while maintaining the characteristics of the original data. When coupled with a method such as an ANN, PCA is able to improve performance of the network while actually reducing the computational effort required to train the network.

Theoretically the GPOF method lends itself well to LTR signal processing with certain caveats. Firstly, the windowing of the signal must be very accurate in order to ensure that the presence of clutter does not present spurious poles at frequencies not applicable to the target. Secondly, the model order of the target must be obtained in order to ensure that only those poles relevant to the target are presented. The algorithm created allows for automatic location of the start of the LTR signal which has shown itself to have a good level of accuracy, though accurate prediction of the end of the LTR window is a challenge that has yet to be overcome. The algorithm developed ensures that the whole of the LTR signal is obtained by taking 7.5 nS of data which is greater than any of the expected LTR lengths though this does come at the cost of potentially adding in unnecessary clutter to the data. The approach that has been used to determine the model order is computationally intensive as it requires all possible useful model orders to be run, the standard error calculated at these points for a signal reconstructed from the poles produced and then the algorithm be run again for the correct model order.

The GPOF method developed has shown itself to be capable of performing binary threat/non-threat classification of targets successfully. With true positive classification rates of 70% with 0% false positives as shown in Figure 46, a viable security system using this method could be developed. With the application of PCA to the dataset, this increases the true positive classification rate to 73% while maintaining 0% false positives as shown in Figure 47. There has only been very limited success in classification of individual objects.

The groundwork for the application of the real valued CWT to LTR analysis can be found in [68]. The intensity maps presented in this publication indicated that it may be possible to use the CWT for LTR security screening purposes. The work presented used the Morlet wavelet to analyze the horizontally polarised returns from a number of targets, the processed images of which showed distinct objects at different scale points. Progressing

onwards from this point, so that the images could be individually analysed presented quite a challenge. Due to the scale and complexity of the data it was not possible to obtain a classification result directly from the intensity plots, further intermediate steps were required. These steps including improving on the filtering regime and data vectorization using unsupervised ANN techniques allowed for a classifier to successfully learn from the data.

Competitive learning functions [144] are an alternative training method that allows for the creation of unsupervised ANN's. Known as unsupervised random order weight/bias training, these algorithms attempt to train the network with weight and bias learning rules, providing incremental updates after each presentation of a randomly presented input. The result of this approach is that the neurons in a given competitive layer will distribute themselves such that they are able to recognize commonly presented inputs. Therefore the network will return a zero for all neurons except for the winning neuron for which the network will return a value of one. This method allows for the very large wavelet based datasets to be successfully processed by an FFBP ANN and classified into different categories. The SOM does have some capability to classify targets itself, although in this case it was not able to provide a good result.

The real valued CWT is the first of the wavelet based methods that allowed for successful classification of data. The mother wavelets tested include the Daubechies, Morlet and Gaussian wavelets, with a particular focus on the Gaussian wavelets. This method shows itself to be effective in binary threat/non-threat classification with true positive classification rates approaching 100% when applied to the test set. When the individual object classifier is applied to the training set the true positive classification rate drops from close to 100% to around 83%. This reflects the additional complexity required to classify these objects individually, but is still a respectable figure.

The next logical step was to attempt to process the complex return data by using a complex approach as opposed to the real valued approach in the CWT. This and attempts to reduce the computational complexity of the CWT algorithm led to the decision to use the DTWT. This algorithm applies a discrete complex wavelet to the dataset, in order to maintain features of the dataset in the transformed signal. This method uses two stages of

filters, the first stage of which are nearly symmetric Farras filters [162] and all subsequent stages use Kingsbury Q shift filters [163]. The DTWT used as a binary threat/non-threat classifier shows some good results with true positive classification rates approaching 95% for the test set presented in Figure 75 and 98% in Figure 76 for data with PCA applied.

The inability of the DTWT to classify individual items led to work beginning on the CCWT, results of which can be found in section 6.2. The continuous complex wavelet transform. These results demonstrate that the CCWT has a number of advantages over the other methods presented.

7.3.5. Process timescale

The timescales for the analysis algorithm are critical. If it takes too long to process a target set the system will be of no practical use. A number of points need to be considered. Firstly, the use of an Field Programmable Gate Array (FPGA) based processor to perform the CWT could decrease the processing time from its current level of 3.2 seconds to less than 100 ms by parallelizing the processing of each individual scale. The size of the SOM used can also be altered. Current tests have shown a $4 \times 4n$ SOM to take 11 seconds to process, while a 2×2 SOM takes 3 seconds. The introduction of faster, more capable central processing units could also be used to accelerate the algorithm.

7.4. Future work and applications

7.4.1. Work program

Production of a practical weapon detection system would involve an extensive programme of hardware and software development with many trials to confirm its performance. This would include development of custom frequency control and data acquisition hardware, optimisation of process software and a wider range of training examples including target range, weapon type, body type, weapon position and covering clothing. As well as portal or walk past systems, several other potential applications have been identified and would be worth investigating:

1. A case study on luggage scanning:

Luggage scanning is a critically important security feature of modern air travel. LTR based security techniques lend themselves well to this type of application and so a wavelet based LTR scanner could be developed to meet this requirement. Using LTR for this would reduce the use of ionizing radiation sources such as x-rays currently employed by airports.

2. A case study on knife scanning:

Knife crime is a serious issue, commonly reported as in inner city areas and schools. The ability to detect these knives at standoff ranges would allow for effective screening in schools and shopping centres for example. Fixed installation wavelet based LTR screening systems at entrances could be applied to this scenario, with the potential for helping to reduce knife crime.

3. A case study on parcel scanning:

Transport of threat items through the postal system by unsuspecting staff is a very real possibility. LTR's non-invasive scanning could allow for these parcels to be checked prior to transport.

A number of potential areas for future work have been identified during the research project performed. These include:

- Design and development of a concurrently fed planar antenna array [159] [13]. This would assist in reducing the form factor of the system by reducing depth and allow for installation on flat surfaces such as walls.
- Introduction of a phased array system would allow for control of the radar beam via electronic beam steering/forming allowing for the range of the system to be increased and the location of the item on the body to be determined.
- An alternative method for focusing the beam would be to use a lens. For a fixed emplacement system based around a portal scanner this could be considered but for any other application would be impractical as the lens diameter would be > 2 m..
- The Empirical Mode Decomposition coupled with the Hilbert transform or Hilbert Huang Transform [77] as it is also known was developed by the National Aeronautics and Space Administration and is used for time-frequency analysis of meteorological data along with limited application to radar systems to date. This adaptive algorithm could potentially resolve some of the issues with computational complexity presented by the continuous wavelet based transforms while still resolving the frequency data accurately and potentially accounting for spurious data automatically. Conversely, its empirical based approach does allow for some error in the results provided which would need to be accounted for and the existing ANN's would need to be retrained to process this data.

References

- [1] S. J. Hutchinson, M. Fernando, D. Andrews, S. Harmer and N. Bowring, "Investigation of Late Time Response analysis for detection of multiple concealed objects," Dresden. Germany, 2013.
- [2] S. J. Hutchinson, M. Fernando, D. Andrews, S. Harmer and N. Bowring, "Investigation of LTR Analysis for Concealed Object Detection," Manchester, 2013.
- [3] C. T. Taylor, S. J. Hutchinson, N. A. Salmon, P. N. Wilkinson and C. D. Cameron, "Investigation of Radio Astronomy Image Processing Techniques for use in the Passive Millimetre-Wave Security Screening Environment," Baltimore, Maryland, USA, 2014.
- [4] S. J. Hutchinson, D. Andrews, M. Fernando, S. Harmer and N. Bowring, "Late Time Response Analysis for the Discrimination of Multiple Simulated Objects in concealed Threat Detection," Manchester, UK, 2014.
- [5] S. J. Hutchinson, C. T. Taylor, M. Fernando, D. Andrews and N. Bowring, "Investigation of the CLEAN deconvolution method for use with Late Time Response analysis of multiple objects," Amsterdam, 2014.
- [6] D. Fleisch, A Students Guide to Maxwell's Equations, 13 ed., Cambridge UK: Cambridge University Press, 2008.
- [7] J. C. Maxwell, "A Dynamical Theory of the Electromagnetic Field," *Phil. Trans. R. Soc. Lond*, no. 155, pp. 458-512, 1865.
- [8] P. A. Tipler and G. Mosca, Physics for Scientist and Engineers, 6 ed., New York: W.H.Freeman and company, 2008.
- [9] C. Hulsmeyer, "Patent DE165546 "The Telemobiloscope", " The German Patent and Trade Mark Office, Dusseldorf, 1904.
- [10] G. Marconi, "Radio Telegraphy," *Radio Engineers, Proceedings of the Institute of*, vol. 10, no. 4, pp. 215 - 238, 1922.
- [11] G. Galati, Advanced Radar Techniques and Systems, London: Peter Peregrinus Ltd, The Institution of Electrical Engineers, 1993.
- [12] A. J. Berni, "Target Identification by Natural Resonance Estimation," *IEEE Transactions on Aerospace and Electronic Sytems*, vol. 11, no. 2, pp. 147-154, 1975.
- [13] M. L. Skolnik, Introduction to Radar Systems, 3rd edition ed., Singapore: McGraw-Hill, 2001.
- [14] National Radio Astronomy Observatory, "The 43 Meter (140 Foot) Telescope," Available at: <http://www.gb.nrao.edu/43m/>, 1.0, 2011.
- [15] M. Skolnik, Radar Handbook, 3rd ed., New York: McGraw Hill, 2008.

- [16] United States Geological Survey, "Geologic Mapping," Available at: (<http://astrogeology.usgs.gov/PlanetaryMappingOld/VenusMappers/Overview.html>), 1.0, 2015.
- [17] Fraunhofer-Gesellschaft, "European space surveillance using phased array sensors," Available at: <http://www.fhr.fraunhofer.de/en/businessunits/space/European-space-surveillance-using-phased-array-sensors.html>, 1.0, 2015.
- [18] BBC News, "2003: Shoe Bomber Jailed for Life," http://news.bbc.co.uk/onthisday/hi/dates/stories/january/30/newsid_4081000/4081741.stm, 2003.
- [19] R. D. Hudson jr and J. Hudson, "The Military Applications of Remote Sensing by Infrared," *Proceedings of the IEEE*, vol. 63, no. 1, pp. 104 - 128, 1975.
- [20] N. C. Currie, F. J. Demma, D. D. Ferris Jr, B. R. Kwasowsky, R. W. McMillan and M. C. Wicks, "Infrared and Millimeter-wave sensors for military special operations and law enforcement," *International Journal of Infrared and Millimeter waves*, vol. Vol. 17, no. 7, pp. 1117-1138, 1996.
- [21] S. Cho and N. Tin, "Using Infrared Imaging Technology for Concealed Weapons Detection and Visualization," Fukuoka, 2010.
- [22] R. W. McMillan, O. j. Milton, M. C. Hetzler, R. S. Hyde and W. R. Owerms, "Detection of concealed weapons using far-infrared bolometer arrays," Beijing, 2000.
- [23] K. Hanton, M. Butavicius, R. Johnson and J. Sunde, "Improving infrared images for standoff object detection," Dubrovnik, 2009.
- [24] S. Annaduraj and V. Vaithiyanathan, "Concealed Weapon Detection Using Multiresolution Additive Wavelet Decomposition," *Research Journal of Applied Sciences, Engineering and Technology*, vol. Vol. 4, no. 20, pp. 4118-4121, 2012.
- [25] Z. Xue, R. S. Blum and Y. Li, "Fusion of Visual and IR Images for Concealed Weapon Detection," Annapolis, MD, USA, 2002.
- [26] P. K. Varshney, H. Chen, L. C. Ramac, M. Uner, D. Feris and M. Alford, "Registration and fusion of infrared and Millimeter wave images for concealed weapon detection," Kobe, 1999.
- [27] P. Kinahan, "Ultrasound," <http://courses.washington.edu/bioen508/Lecture6-US.pdf>, Washington, 2006.
- [28] J. E. DuChateau and M. Hinders, "Using Ultrasound in Concealed Weapons Detection," College of William and Mary, Williamsburg, Virginia, USA, 2005.
- [29] A. Achanta, M. Mckenna and J. Heyman, "Non-linear acoustic concealed weapons detection," Washington, DC, USA, 2005.
- [30] G. A. Vadakkal, "Detection of concealed weapons using acoustic waves," The University of Manchester, Manchester, UK, 2012.

- [31] C. L. Garrett, *Modern Metal Detectors*, Revised edition ed., RAM USA, publications and distribution, 1985.
- [32] C. V. Nelson, "Wide-area metal detection system for crowd screening," Orlando, Florida, USA, 2003.
- [33] D. K. Kotter, L. G. Roybal and R. E. Polk, "Detection and Classification of Concealed Weapons using a Magnetometer-base Portal," Orlando, Florida, USA, 2002.
- [34] S. F. Hallowell, "Screening people for illicit substances: a survey of current portal technology," *Talanta*, vol. 54, pp. 447-458, 2001.
- [35] C. Tillery, "Detecting Concealed Weapons: Directions for the Future," *NIJ Journal*, vol. 258, pp. 26-28, 2007.
- [36] A. Cavoukian, "Whole Body Imaging in Airport Scanners: Building in privacy by design," Information & Privacy Commissioner of Ontario, Toronto, Ontario, Canada, 2009.
- [37] British Broadcasting Corporation, "Manchester Airport's body scanners scrapped," BBC News, 2012.
- [38] Daily Mail, "TSA pulls ALL X-ray body scanners from airports over privacy concerns... but claims they were never a health risk to fliers," Daily Mail, 2013.
- [39] B. R. Abidi, Y. Zheng, A. V. Gribok and M. A. Abidi, "Improving Weapon Detection in Single Energy X-Ray Images Through Pseudocoloring," *IEEE Transactions on Systems, Man and Cybernetics, Part C: Applications and Reviews*, vol. 36, no. 6, pp. 784 - 796, 2006.
- [40] G. Smith, "Detection of contraband concealed on the body using X-ray imaging," Boston, 1997.
- [41] H. Chen, S. Lee, R. M. Rao, M. A. Slamani and P. K. Varshney, "Imaging for concealed weapon detection: a tutorial overview of development in imaging sensors and processing," *IEEE Signal Processing Magazine*, vol. 22, no. 2, pp. 52 - 61, 2005.
- [42] R. Sorrentino and G. Bianchi, *Microwave and RF Engineering*, 1st ed., Chichester: John Wiley and sons, 2010.
- [43] G. N. Sinclair, R. N. Anderton and R. Appleby, "Passive millimetre-wave concealed weapon detection," Boston, 2001.
- [44] S. W. Harmer, N. Bowring, D. R. N. D. Andrews and M. S. S. Southgate, "A Review of Nonimaging Stand-Off Concealed Threat Detection with Millimeter-Wave Radar," *IEEE microwave Magazine*, Vols. 1527-3342, no. 12, pp. 160-167, 2012.
- [45] D. I. McMakin, D. M. Sheen and H. D. Collins, "Remote Concealed Weapons and Explosives Detection on People Using Millimeter-wave Holography," Lexington, Kentucky, USA, 1996.

- [46] P. Keller, D. McMakin and D. M. Sheen, "Privacy algorithm for cylindrical holographic weapons surveillance system," *IEEE Aerospace and Electronic Systems Magazine*, pp. Vol.15, issue 2, 17-24, 6 February 2000.
- [47] D. O. Korneev, L. Y. Bogdanov and A. V. Nalivkin, "Passive millimeter wave imaging system with white noise illumination for concealed weapons detection," 2004.
- [48] R. Appleby and R. N. Anderton, "Millimeter-Wave and Submillimeter-Wave Imaging for Security and Surveillance," *Proceedings of the IEEE*, vol. 95, no. 8, pp. 1683-1690, 2007.
- [49] D. A. Andrews, S. W. Harmer, N. J. Bowring, N. D. Rezgui and M. J. Southgate, "Active Millimeter Wave Sensor for Standoff Concealed Threat Detection," *IEEE Sensors journal*, vol. 13, no. 12, pp. 4948-4954, 2013.
- [50] D. A. Andrews, S. Smith, N. Rezgui, N. Bowring, M. Southgate and S. Harmer, "A swept millimeter-wave technique for the detection of concealed weapons and thin layers of dielectric material with and without fragmentation," *Proc. of SPIE Passive Millimeter-Wave Imaging Technology*, vol. 7309, no. 73090H, pp. 1-10, 2009.
- [51] B. Kaplievich and M. Einat, "Detecting Hidden Objects on Human Body Using Active Millimeter Wave Sensor," *IEEE Sensors journal*, vol. 10, no. 11, pp. 1746-1752, 2010.
- [52] S. S. Ahmed, A. Schiessl, F. Gumbmann, M. Tiebout, S. Methfessel and L. P. Schmidt, "Advanced Microwave Imaging," *IEEE Microwave magazine*, Vol. 13, Issue. 6, pp. 26-43, 17 September 2012.
- [53] A. Elboushi and A. Sebak, "Active Millimeter-Wave imaging system for hidden weapons detection," Cairo, Egypt, 2012.
- [54] T. Crowe and D. Portefield, "Terahertz technology for imaging and spectroscopy," Orlando, Florida, USA, 2006.
- [55] W. Gao, X. Degang and Y. Jianquan, "Review of explosive detection using terahertz spectroscopy technique," Dalian, 2011.
- [56] K. B. Cooper, R. J. Dengler, N. Llombart, B. Thomas, G. Chattopadhyay and P. H. Siegel, "THz Imaging Radar for Standoff Personnel Screening," *IEEE Transactions on Terahertz Science and Technology*, vol. 1, no. 1, pp. 169-182, 2011.
- [57] S. Gu, C. Li, X. Gao, Z. Sun and G. Fang, "Terahertz Aperture Synthesized Imaging With Fan-Beam Scanning for Personnel Screening," *IEEE Transactions on Microwave Theory and Techniques*, vol. 60, no. 12, pp. 3877 - 3885, 2012.
- [58] R. Arusi, Y. Pinhasi, B. Kapilevitch, D. Hardon, B. Litvak and M. Anisimov, "Linear FM radar operating in the terahertz regime," Tel Aviv, 2009.

- [59] R. Appleby and H. B. Wallace, "Standoff Detection of Weapons and Contraband in the 100GHz to 1THz region," *IEEE Transactions on Antennas and propagation*, vol. 55, no. 11, pp. 2944-2956, 2007.
- [60] M. C. Kemp, "Explosives Detection by Terahertz Spectroscopy - A Bridge Too Far," *IEEE Transactions on Terahertz Science and Technology*, vol. 1, no. 1, pp. 282-291, 2011.
- [61] A. Atiah, "The Using of Late Time Response for Stand Off On- Body Concealed Weapon Detection," PhD thesis, Manchester Metropolitan University, Manchester Uk, 2011.
- [62] P. Goupillaud, A. Grossman and J. Morlet, "Cycle-octave and related transforms in seismic signal analysis," *Geoplotation Seismic Signal Analysis and Discrimination III*, vol. 23, no. 1, pp. 85-102, 1984.
- [63] S. Mallet, *A Wavelet Tour of signal Processing*, 3rd ed., Burlington: Academic Press, Elsevier, 2008.
- [64] I. Daubechies, *Ten Lectures on Wavelets*, 8th ed., Philadelphia: Society for Industrial and Applied Mathematics, 2004.
- [65] J. S. Marques, N. Perez de la Blanca and P. Pina, "Isotropic Gabor wavelets," in *Pattern Recognition and Image Analysis: Second Iberian Conference*, Estoril Portugal, Springer, 2005, pp. 336-338.
- [66] V. N. Fokin, M. A. Fokina and J. M. Sabatier, "Wavelet Analysis for Landmine Detection False Alarm discrimination," 2005.
- [67] Y. Sun and J. Li, "Adaptive Learning Approach to," *IEEE TRANSACTIONS ON AEROSPACE AND ELECTRONIC SYSTEMS*, vol. 41, no. 3, pp. 973 - 985, 2005.
- [68] A. Atiah and N. J. Bowring, "An Approach for on Body Concealed Weapon Detection Using Continuous Wavelet Transform," Stockholm, Sweden, 2013.
- [69] D. Gabor, "Theory of communication. Part 1: The analysis of information," *Electrical Engineers - Part III: Radio and Communication Engineering, Journal of the Institution of*, vol. 93, no. 26, pp. 429-441, 1946.
- [70] S. Mallat, *A Wavelet Tour of Signal Processing: The Sparse Way*, Burlington, MA, USA: Academic Press, Elsevier, 2009.
- [71] I. W. Selesnick, R. G. Baraniuk and N. G. Kingsbury, "The Dual-Tree Complex Wavelet Transform," *IEEE Signal Processing Magazine*, pp. 123 - 151, November 2005.
- [72] N. Kingsbury, "Complex Wavelets for Shift invariant Analysis and Filtering of Signals," *Applied and Computational Harmonic Analysis*, vol. 10, no. 3, pp. 234-253, 2001.
- [73] V. N. P. Raj and T. Venkateswarlu, "Denoising of Medical Images Using Dual Tree Complex Wavelet Transform," *Procedia Technology*, vol. 4, pp. 238-244, 2012.

- [74] T. Celik, H. Ozkaramanli and H. Demirel, "Facial feature extraction using complex dual-tree wavelet transform," *Computer Vision and Image Understanding*, vol. 111, no. 2, pp. 229-246, 2008.
- [75] K. J. Priya and R. S. Rajesh, "Local Statistical Features of Dual Tree Complex Wavelet Transform on Parallelogram Image Structure for Face Recognition with Single Sample," in *Recent Trends in Information, Telecommunication and Computing (ITC), 2010 International Conference on*, Kochi, Kerala, 2010.
- [76] N. E. Huang and S. S. Shen, *Hilbert - Huang Transform and its applications*, 1st ed., London: World Scientific Publishing Co, Pte, Ltd, 2005.
- [77] N. E. Huang, "Introduction to the HHT and its related mathematical problems," in *Hilbert-Huang transform and its Applications*, N. E. Huang, Ed., London, World Scientific Publishing Co, Pte, Ltd, 2005, pp. 1 - 26.
- [78] A. S. Grispino, G. O. Petracca and A. E. Dominguez, "Comparative Analysis of Wavelet and EMD in the Filtering of Radar Signal Affected by Brown Noise," *IEEE (Revista IEEE America Latina) Latin American Transaction*, vol. 11, no. 1, pp. 81 - 85, 2013.
- [79] B. Mijovi, M. De Vos, I. Gligorijevic and T. J., "Source Separation From Single-Channel Recordings by Combining Empirical-Mode Decomposition and Independent Component Analysis," *IEEE Transactions on Biomedical Engineering*, vol. 57, no. 9, pp. 2188 - 2196, 2010.
- [80] U. Maji, M. Mitra and S. Pal, "Automatic Detection of Atrial Fibrillation Using Empirical Mode Decomposition and Statistical Approach," *Procedia Technology*, vol. 10, pp. 45 - 52, 2013.
- [81] L. Shang, K. Shyu and Y. Lin, "A new secure communication based on EMD encryptions," New Taipei, 2012.
- [82] J. C. Cexus, A. O. Boudraa, L. Guillon and A. Khenchaf, "Sonar target analysis by Teager-Huang Transform," Marin, 2006.
- [83] C. Baum, "On the Singularity Expansion Method for the solution of electromagnetic interaction problems," *Air Force weapons lab interaction notes*, vol. 88, 1971.
- [84] S. W. Harmer, D. A. Andrews, N. D. Rezgui and N. J. Bowring, "Detection of Handguns by their Complex Natural Resonant Frequencies," *IET Microwaves, Antennas and Propagation*, vol. 4, no. 9, pp. 1182-1190, 2010.
- [85] M. Gashinova, M. Cherniakov and A. Vasalos, "UWB signature analysis for detection of body-worn weapons," Shanghai, 2006.
- [86] S. Harmer, D. Andrews, N. Bowring, N. Rezgui and M. Southgate, "Ultra wideband detection of on body concealed weapons using the out of plane polarized late time response," *Proc of SPIE*, vol. 7485, no. 748505, pp. 1-9, 2009.

- [87] S. W. Harmer, S. E. Cole, N. J. Bowring, N. D. Rezgui and D. Andrews, "On Body Concealed Weapon Detection Using A Phased Antenna Array," *Progress in Electromagnetics Research*, vol. 124, pp. 187-210, 2012.
- [88] L. Zhang, Y. Hao and C. G. Parini, "Natural Resonant Frequency Extraction for Concealed Weapon Detection at Millimeter Wave Frequencies," Edinburgh, Scotland, 2007.
- [89] A. Vasalos, R. Heung Gyoon, I. Vasalos and S. E. Fotinea, "Fast Concealed Weapon detection via LTR analysis," Kansas City, Missouri, USA, 2011.
- [90] IEEE Standards, C95.1-2005 - IEEE Standard for Safety Levels With Respect to Human Exposure to Radio Frequency Electromagnetic Fields, 3 kHz to 300 GHz, Revised 2005 Edition ed., IEEE Electromagnetic Compatibility Society, 2006.
- [91] J. J. McCombe, N. K. Nikolova, M. S. Georgiev and T. Thayaparan, "Clutter removal in the automatic detection of concealed weapons with late time responses," Nuremburg, 2013.
- [92] A. Vasalos, N. Uzunoglu, R. Heung-Gyoon and I. Vasalos, "Neural Network Target Classification for Concealed Weapon Radar Detection," Fira, 2013.
- [93] Y. Hua and T. K. Sarkar, "A discussion of E-pulse method and Prony's method for radar target resonance retrieval from scattered field," *IEEE Transactions on Antennas and Propagation*, vol. 37, no. 7, pp. 944-946, 1989.
- [94] C. Baum, "The singularity expansion method: Background and developments," *IEEE Antennas and Propagation Society Newsletter*, vol. 28, no. 4, pp. 14-23, 1986.
- [95] Y. Hua and T. Sarkar, "Generalized Pencil of Function Method for extracting the poles of an EM system from its transient response," *IEEE Trans. Antennas Propag*, vol. 37, no. 2, pp. 229-334, 1989.
- [96] F. Sarrazin, J. Chauveau, P. Poliguen, P. Potier and A. Sharaiha, "Accuracy of Singularity Expansion Method in Time and Frequency Domains to Characterize Antennas in Presence of Noise," *IEEE Transactions on Antennas and Propagation*, vol. 62, no. 3, pp. 1261-1269, 2014.
- [97] D. Rialet, S. K. Podilchak, M. Clenet, N. Essaïdi and Y. M. M. Antar, "Characterization of compact disc UWB monopole antennas using the Singularity Expansion Method," Syracuse, New York State, USA, 2012.
- [98] T. Chevgounov and A. Aleksandrov, "Ultra wideband radar targets discrimination using frequency domain E-pulse method," 2004.
- [99] L. Hoi Shun and N. V. Z. Shuley, "Radar Target Identification Using a "Banded" E-pulse Technique," *IEEE Transactions on Antennas and Propagation*, vol. 54, no. 12, pp. 3874-3881, 2006.
- [100] F. M. El Hefnawi, "Use of Prony's method for extracting the poles and zeros yielding a wideband window type response of circular antenna arrays," Colorado Springs. Colorado, USA, 1998.

- [101] A. J. Makay and A. Mcowen, "An improved pencil-of-functions method and comparisons with traditional methods of pole extraction," *IEEE Transactions on Antennas and Propagation*, vol. 35, no. 4, pp. 435-441, 1987.
- [102] T. Hauschild and R. Knochel, "Using the GPOF-algorithm in ground penetrating radar systems," Hamburg, 1999.
- [103] Y. Wang, I. D. Longstaff, C. J. Leat and N. V. Shauley, "Complex natural resonances of conducting planar objects buried in a dielectric half-space," *IEEE Transactions on Geoscience and Remote Sensing*, vol. 39, no. 6, pp. 1183-1189, 2001.
- [104] S. W. Harmer, S. E. Cole and N. J. Bowring, "Radar Identification of Hostile Fire by Means of the Electromagnetic Complex Natural Resonances of Projectiles," *Progress In Electromagnetics Research*, vol. 24, pp. 167-178, 2012.
- [105] C.-C. Chen, L. Peters Jr and W. D. Burnside, "Ground penetration radar target classification via complex natural resonances," Newport Beach, 1995.
- [106] M. P. Kolba and I. I. Jouny, "Buried land Mine Detection using Complex Natural Resonances on GPR data," Toulouse, 2003.
- [107] B. Borden, *Radar Imaging of Airborne Targets: A Primer for Applied Mathematicians and Physicists*, 1st ed., New York: Taylor and Francis, 1999.
- [108] W. L. Melvin, M. A. Richards, w. A. Holm and J. A. Scheer, *Principles of Modern Radar: Advanced Radar Techniques and Applications*, 2nd ed., Edison: IET SciTech Publishing inc, 2009.
- [109] C. O. Hargrave, N. V. Shuley, M. E. Bialkowski and J. C. Ralston, "Radar target identification of mining infrastructure for automated mine machinery navigation," Rome, 2011.
- [110] R. Rezaiesarlak and M. Manteghi, "Complex-Natural-Resonance-Based Design of Chipless RFID Tag for High-Density Data," *Antennas and Propagation, IEEE Transactions on*, vol. 62, no. 2, pp. 898-904, 2013.
- [111] M. Bani-Hasan, Y. M. Kadah and F. M. El-Hefnawi, "Identification of Cardiac Arrhythmias using Natural Resonance Complex Frequencies," *International Scholarly and Scientific Research & Innovation*, vol. 4, no. 1, pp. 1014-1020, 2010.
- [112] S. K. Davis, B. D. Van Veen, S. C. Hagness and K. Frederick, "Breast Tumor Characterization Based on ultra-wideband Microwave Backscatter," *IEEE TRANSACTIONS ON BIOMEDICAL ENGINEERING*, vol. 55, no. 1, pp. 237-246, 2008.
- [113] S. K. Hong, "Resonance-Based Techniques for Microwave Breast Cancer Applications," Virginia Polytechnic Institute and State University, Blacksburg, Virginia, 2012.

- [114] M. H. Bannis, F. M. El-Hafnawi, H. M. Abd El Kader, K. ElMahgoub and A. Z. Elsherbeni, "Breast Cancer Detection and Identification using Prony's method," Memphis, 2014.
- [115] The American Radio Relay League, The ARRL Handbook for Radio amateurs, 75th edition ed., The American Radio Relay League inc, 1997.
- [116] International Commision on Non-Ionizing Radiation Protection , "ICNIRP Guidelines for Limiting Exposure to Time-Varying Electric, Magnetic and Electromagnetic Fields (upto 300GHz)," *Health Physics*, vol. 74, no. 4, pp. 493-522, 1998.
- [117] H. F. Harmuth, *Advances in Electronics and Electron Physics: Nonsinusoidal Waves for Radar and Radio Communication*, 1st edition ed., Academic press, 1981.
- [118] M. A. Richards, *Fundamentals of Radar Signal Processing*, 2nd edition ed., New York: McGraw-Hill, 2014.
- [119] C. Wolff, "Radar Basics," *Radar Tutorial.eu*, 11 1998.
- [120] Rohde & Schwarz, "Fundamentals of Vector Network Analysis Primer," Rohde & Schwarz, USA, Colombia, MD, USA, 2014.
- [121] Anritsu EMEA Ltd, "System Optimization," in *The Essentials of Vector Network Analysis*, Luton, Bedfordshire, Anritsu Corporation, 2009, pp. 79-90.
- [122] N. J. Kinzie, "Ultra-Wideband Pulse Doppler Radar for Short-Range Targets," PhD Thesis, The University of Colorado, 2011.
- [123] J. Hogbom, "Aperture Synthesis with a Non-Regular Distribution of Interferometer Baselines," *Astronomy and Astrophysics Supplement*, vol. 15, pp. 417-426, 1976.
- [124] J. P. Burg, "Maximum Entropy Spectral analysis," Stanford University, Stanford, California, 1975.
- [125] B. G. Clark, "An Efficient Implementation of the Algorithm "CLEAN"," *Astronomy and Astrophysics*, no. 89, pp. 377-378, 1980.
- [126] R. G. Brown and P. Y. Hwang, *Introduction to Random signals and Applied Kalman Filtering*, Hoboken, NJ, USA: John wiley and sons, 2012.
- [127] T. Jenho and B. D. Steinberg, "Reduction of sidelobe and speckle artifacts in microwave imaging: the CLEAN technique," *IEEE Transactions on Antennas and Propagation*, vol. 36, no. 4, pp. 543 - 556, 1988.
- [128] R. Bose, "Sequence clean: A deconvolution algorithm useful for non-isolated radar target images with high sidelobes," University of Pennsylvania, Philadelphia, 1995.
- [129] M. Martorella, N. Acito and F. Berizzi, "Statistical CLEAN technique for ISAR imaging," *IEEE Transactions on Geoscience and Remote Sensing*, vol. 45, no. 11, pp. 3552 - 3560, 2007.

- [130] R. Bose, "Lean CLEAN: Deconvolution Algorithm for Radar Imaging of Contiguous Targets," *IEEE Transactions on Aerospace and Electronic Systems*, vol. 47, no. 3, pp. 2190 - 2199, 2011.
- [131] R. Bose, "Active CLEAN: A Modified CLEAN Algorithm for HRRPs of Contiguous Targets with Thinned Spectrum," *IEEE Transactions on Aerospace and Electronic Systems*, vol. 48, no. 2, pp. 930 - 939, 2012.
- [132] C. T. Taylor, N. A. Salmon and C. D. Cameron, "Applicability of radio astronomy techniques to the processing and interpretation of aperture synthesis passive millimetre-wave applications," Baltimore, 2012.
- [133] G. Strang, "The Fundamental Theorem of Linear Algebra," *The American Mathematical Monthly*, vol. 100, no. 9, pp. 848-855, 1993.
- [134] R. D. Fry and D. A. Gray, "CLEAN Deconvolution for Sidelobe Suppression in Random Noise Radar," Adelaide, SA, 2008.
- [135] T. Wagner, F. Reinhard and A. Stelzzer, "Cluster CLEAN: An Application of CLEAN to LFM CW Radar Systems," Rome, Italy, 2014.
- [136] J. Misiurewicz, K. S. Kulpa, Z. Czekala and T. A. Filipek, "Radar Detection of Helicopters with Application of CLEAN Method," *IEEE TRANSACTIONS ON AEROSPACE AND ELECTRONIC SYSTEMS*, vol. 48, no. 4, pp. 3525-3537, 2012.
- [137] J. S. Walker, *A Primer on Wavelets and Their Scientific Applications*, 2nd edition ed., Boca Raton Florida: Chapman and Hall/CRC, 2008.
- [138] M. Misiti, Y. Misiti, G. Oppenheim and J.-M. Poggi, *Matlab Wavelet Toolbox Users guide*, R2015a ed., Natick, Massachusetts, USA: The Mathworks inc, 2015.
- [139] A. Savitzky and M. J. E. Golay, "Smoothing and Differentiation of Data by Simplified Least Squares Procedures," *Analytical Chemistry*, vol. 36, no. 8, pp. 1627-1639, 1964.
- [140] J. Riordon, E. Zubritsky and A. Newman, "Top 10 Articles," *Journal of Analytical Chemistry*, vol. 72, no. 9, pp. 324A-329A, 2000.
- [141] R. W. Schafer, "What is a Savitsky-Golay filter?," *IEEE Signal Processing Magazine*, pp. 111-117, July 2011.
- [142] C. Hargrave, V. Clarkson, A. Abbosh and N. Shuley, "Radar Target Identification: Estimating the Start of the Late Time Response," Adelaide, SA, Australia, 2013.
- [143] Y. Hua and T. K. Sarkar, "Matrix Pencil Method for Estimating the Parameters of Exponentially Damped/Undamped Sinusoids in Noise," *IEEE Transactions on Acoustics, Speech and Signal Processing*, vol. 38, no. 5, pp. 814 - 824, 1990.
- [144] M. H. Beale, M. T. Hagan and H. B. Demuth, *Neural Network Toolbox Users guide*, a ed., Natick: The Mathworks inc, 2015.

- [145] B. Osgood, "The Fourier Transform and its Applications," Stanford University Engineering Everywhere, Stanford, California, USA, 2013.
- [146] E. W. Weisstein, "Fast Fourier Transform," *Wolfram Mathworld*, <http://mathworld.wolfram.com/FastFourierTransform.html> accessed 10/03/2013, 2013.
- [147] S. W. Smith, "Chapter 12 The Fast Fourier Transform," in *The Scientist and Engineers Guide to Digital Signal Processing*, San Diego, California, USA, California Technical Publishing, 1997, pp. 225-242.
- [148] Y. Wang and N. Shuley, "Complex resonant frequencies for the identification of simple objects in free space and lossy environments," *Progress in Electromagnetics Research*, vol. 27, pp. 1-18, 2000.
- [149] D. Wenbin and D. Weibo, "A method of extracting radar target poles," *IEEE GSMM*, pp. 449-452, 2012.
- [150] K. Pearson, "On Lines and Planes of Closest Fit to Systems of Points in Space," *Philosophical Magazine*, vol. 2, no. 6, pp. 559-572, 1901.
- [151] H. Hotelling, "Analysis of a complex of statistical variables into principal components.," *Journal of Educational Psychology*, vol. 24, no. 6, pp. 417-441, 1933.
- [152] P. Wallisch, M. E. Lusignan, M. D. Benayoun, T. I. Baker, A. S. Dickey and N. G. Hatsopoulos, *Matlab for Neuroscientists*, 2nd ed., London: Academic Press, 2014.
- [153] A. P. Bradley, "The Use of the Area Under the ROC curve in the evaluation of machine learning algorithms," *Pattern Recognition*, vol. 30, no. 7, pp. 1145-1159, 1997.
- [154] T. Wriedt and W. Hergert, *The Mie Theory*, Berlin: Springer-Verlag, 2012.
- [155] T. Kohonen, "Self-Organized Formation of Topologically Correct Feature Maps," *Biological cybernetics*, vol. 43, no. 1, pp. 59-69, 1982.
- [156] A. Turing, "The Chemical Basis of Morphogenesis," *Philosophical Transactions of the Royal Society of London*, vol. 237, no. 641, pp. 37-72, 1952.
- [157] W. H. Richardson, "Bayesian-based Iterative Method of Image Restoration," *Journal of the Optical Society of America*, vol. 62, no. 1, pp. 55-59, 1972.
- [158] L. Lucy, "An Iterative Technique for the Rectification of Observed Distributions," *The Astronomical Journal*, vol. 79, no. 6, pp. 745-754, 1974.
- [159] D. M. Pozar, *Microwave Engineering*, 4th Edition ed., Hoboken: John Wiley and sons inc, 2012.
- [160] H. A. Rahim, F. Malek and M. F. A. Malek, "The Influence of Textile Dielectric Propoerties in on-body Radio Communication Channel Performance at 2.45GHz," Stockholm, 2013.

- [161] M. T. Hagan, H. B. Demuth and M. H. Beale, *Neural Network Design*, volume 10 ed., Campus Pub. Service, University of Colorado Bookstore, 2002, 1996.
- [162] A. Farras Abdelnour and I. W. Selesnick, "Symmetric Nearly Orthogonal and Orthogonal Nearly Symmetric Wavelets," *The Arabian Journal for Science and Engineering*, vol. 29, no. 2c, pp. 3-16, 2004.
- [163] N. Kingsbury, "Design of Q-shift complex wavelets for image processing using frequency domain energy minimization," Barcelona, Spain, 2003.
- [164] R. M. Penha and J. W. Hines, "Using Principal Component Analysis Modeling to Monitor Temperature Sensors in a Nuclear Research Reactor," Knoxville, 2001.
- [165] R. Polkar, "The Wavelet Tutorial," <http://users.rowan.edu/~polikar/WAVELETS/WTpart1.html> accessed 08/07/2013, 1996.
- [166] K. Baker, "Singular Value Decomposition Tutorial," Ohio State University, 2005.
- [167] R. Kalman, "A New Approach to Linear Filtering and Prediction Problems," *Transactions of the ASME, Journal of Basic Engineering*, pp. 35-45, 1960.
- [168] R. Kalman and R. Bucy, "New Results in Linear Filtering and Prediction Theory," *Transactions of the ASME, Journal of Basic Engineering*, pp. 95-108, 1961.
- [169] U. Rau and T. Cornwell, "A multi-scale multi-frequency deconvolution algorithm for synthesis imaging in radio interferometry," *Astronomy and Astrophysics*, vol. 532, no. A71, pp. 1-17, 2011.
- [170] R. Rot and T. Kailath, "ESPRIT - Estimation of Signal Parameters via Rotational Invariance techniques," *IEEE Transactions on Acoustics, Speech and Signal Processing*, vol. 37, no. 7, pp. 984-995, 1989.
- [171] J. A. Fessler and A. O. Hero, "Space-Alternating Generalized Expectation-Maximization Algorithm," *IEEE Transactions on Signal Processing*, vol. 42, no. 10, pp. 2664-2677, 1994.
- [172] R. O. Schmidt, "Multiple Emitter Location and Signal Parameter Estimation," *IEEE Transactions on Antennas and Propagation*, Vols. AP-34, no. 3, pp. 276-280, 1986.
- [173] J. Burg, "Maximum Entropy Spectral Analysis," PhD Thesis, Dep. Geophysics Stanford Univ, 1975.
- [174] G. J. MacLachlan, *Discriminant Analysis and Statistical Pattern Recognition*, volume 544 Wiley series in probability and statistics ed., John Wiley and Sons, 2004.
- [175] J. MacQueen, "Some Methods for Classification and Analysis of Multivariate Observations," Berkeley, California, 1967.

- [176] C. E. Rasmussen and C. K. I. Williams, "Chapter 3 Classification," in *Gaussian Processes for Machine Learning*, Boston, The MIT Press, 2006, pp. 33-78.
- [177] S. W. Smith, "Chapter 17 Deconvolution," in *The Scientist and Engineers guide to Digital Signal Processing*, San Diego, California, USA, California Technical Publishing, 1997, pp. 297-310.
- [178] S. W. Smith, "Chapter 8 The Discrete Fourier Transform," in *The scientist and engineer's guide to digital signal processing*, San Diego, California, USA, California Technical Publishing, 1997, pp. 141-168.
- [179] S. W. Smith, "Chapter 6 Convolution," in *The Scientist and Engineers Guide to Digital Signal Processing*, San Diego, California, USA, California Technical Publishing, 1997, pp. 107-122.
- [180] M. Lazebnik and J. H. Booske, "Highly Accurate Debye Models for Normal and Malignant Breast Tissue Dielectric Properties at Microwave Frequencies," *IEEE Microwave and Wireless Components Letters*, vol. 17, no. 12, pp. 822-824, 2007.
- [181] A. Savitsky and M. J. E. Golay, "Smoothing and Differentiation of Data by Simplified Least Squares Procedures," *Analytical Chemistry*, vol. 36, no. 8, pp. 1627-1639, 1964.
- [182] A. Vasalos, I. Vasalos, R. Heung-Gyoon and F. Stavroula-Evite, "LTR Analysis and Signal Processing for Concealed Explosive Detection," Berlin, 2010.

Appendices

A.1. Gallery of target objects



Figure 92: Replica .44 calibre revolver



Figure 93: Gas powered target pistol



Figure 94: replica .38 calibre revolver



Figure 95: Keyring



Figure 96: Fujifilm camera



Figure 97: Kitchen knife



Figure 98: Steel rod



Figure 99: 6.5cm needle